REPORT DOCUMENTATION PAGE

Form Approved

AFRL-SR-AR-TR-03-
0065

REPORT DATE (DD-MM-YYYY)	2. REPORT TYPE
0-11-2002	Final

TITLE AND SUBTITLE	5a. CONTRACT NUMBER
nsteady Aerodynamics & Aeromechanics of Multi-Stage Turbomachinery Blading	
	5b. GRANT NUMBER F49620-97-1-0009
	5c. PROGRAM ELEMENT NUMBER

AUTHOR(S)	5d. PROJECT NUMBER
nford Fleeter	
	5e. TASK NUMBER
	5f. WORK UNIT NUMBER

PERFORMING ORGANIZATION NAME(S) AND ADDRESS(ES)	8. PERFORMING ORGANIZATION REPORT NUMBER
urdue Research Foundation 063 Hovde Hall est Lafayette, IN 47907-1063	

SPONSORING / MONITORING AGENCY NAME(S) AND ADDRESS(ES)	10. SPONSOR/MONITOR'S ACRONYM(S)
OSR/NA 015 Wilson Blvd. Room 713 rlington, VA 22203-1954	
	11. SPONSOR/MONITOR'S REPORT NUMBER(S)

DISTRIBUTION / AVAILABILITY STATEMENT

20030319 006

SUPPLEMENTARY NOTES

ABSTRACT An integrated experiment-theory approach included collaboration between Pratt & itney, Duke University, and Purdue University. A benchmark-standard multistage transonic search compressor was developed by modifying the Purdue High-Speed Axial Compressor to ature new IGV and stator rows representative of modern high pressure compressors. A antitative understanding and predictive capability for multi-stage blade row forced sponse was developed by analytically and experimentally investigating the fundamental flow enomena. Experiments at Purdue investigated and quantified the interacting blade row steady aerodynamics and resulting vane vibration and stress response. Duke University veloped a new computationally efficient unsteady aerodynamic analysis of multistage flows sociated with flutter and forced response. The inherently small damping of complex higher der modes was addressed by investigating techniques to control the flow induced vibrations. e issue of robustness was also considered.

SUBJECT TERMS

steady Aerodynamics, Aeromechanics, Turbomachinery, Forced Response

SECURITY CLASSIFICATION OF: nclassified			17. LIMITATION OF ABSTRACT	18. NUMBER OF PAGES	19a. NAME OF RESPONSIBLE PERSON Sanford Fleeter
EPORT	b. ABSTRACT U	c. THIS PAGE U	UU		19b. TELEPHONE NUMBER (include area code) 765 - 494 -1504

UNSTEADY AERODYNAMICS & AEROMECHANICS

OF MULTI-STAGE TURBOMACHINERY BLADING

AFOSR GRANT F49620-97-009

Final Performance Report

November 30, 2002
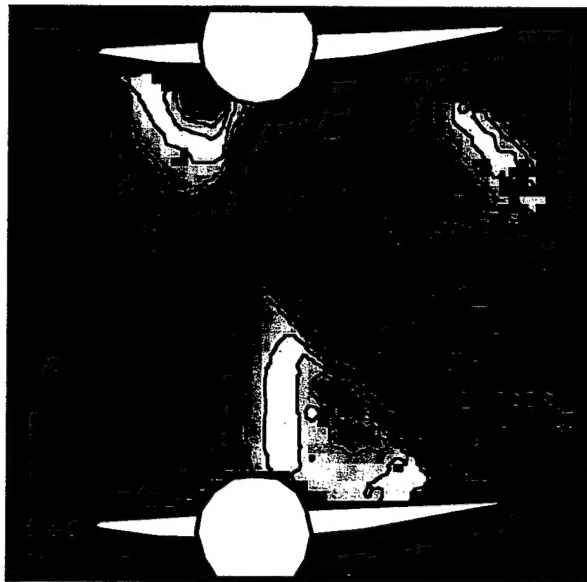
Sanford Fleeter

School of Mechanical Engineering
Purdue University
West Lafayette, Indiana 47907-1288

TABLE OF CONTENTS

INTRODUCTION

The advent of advanced turbomachines featuring closely spaced rows of highly loaded low-aspect ratio blading has resulted in the prediction of High Cycle Fatigue (HCF) being a fundamental weakness in the technology base for gas turbine engines. In fact, the loss of blades or disks due to HCF is currently the predominant surprise engine failure mode in the field.

The driving phenomenon for flow-induced vibrations and HCF is the blade row unsteady aerodynamics, with transonic compressors of particular interest. Specifically, a transonic rotor operates with a supersonic relative velocity with a subsonic axial component. Shocks thus form near the rotor blade leading edges, Figure 1. These shocks propagate upstream as the rotor moves and, thus, are a forcing function generating unsteady flow in the upstream vane row that can lead to HCF.
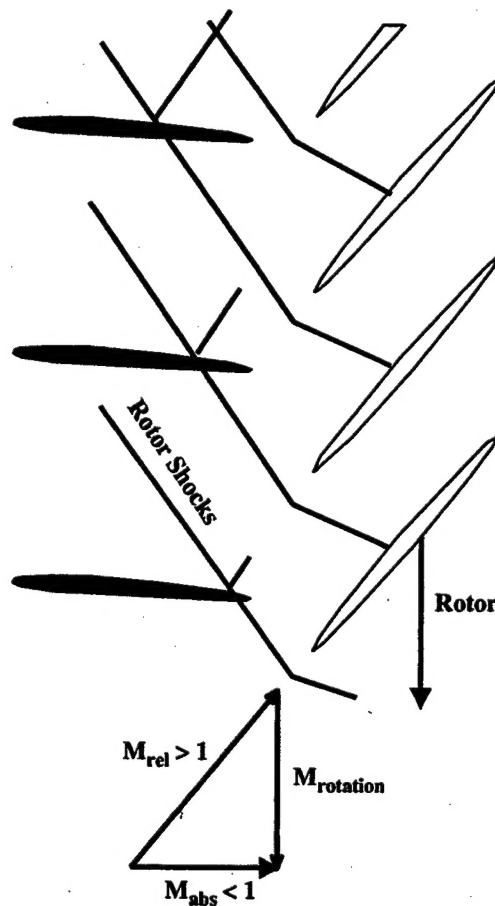
Figure 1. Upstream vane excitation due to rotor shocks

Wakes are the most common forcing functions, with rotor wakes an unsteady forcing function to the downstream stators. The reduction in the wake relative velocity causes an absolute velocity decrease and an incidence change to the downstream vanes, Figure 2. The resulting rotor-exit unsteady flow is the forcing function to the stator that can result in HCF.

Rotor   **Stator**

Figure 2. Stator excitation due to rotor wake

As airfoil row interaction unsteady aerodynamics is the driving phenomena for HCF blade failures, requirements to avoid HCF include an increased fundamental understanding of multi-blade row interaction phenomena. The key barrier research issues are: Multi-Stage Interaction Unsteady Aerodynamics Including Benchmark Standard Data, Multi-Stage Interactions Including Off-Design Unsteady Aerodynamics, Generating Additional Damping - Aerodynamic or Structural, and Variability & Nonlinearities.

RESEARCH OBJECTIVES

The overall research objective was to develop the technology needed to predict accurately significant blade row forced response in a multistage environment, thereby providing accurate predictions of HCF in turbine engine blade rows. Specific objectives included: development of a benchmark standard multistage transonic research compressor; providing a quantitative understanding and predictive capability for multi-stage blade row forced response; investigating techniques to control the flow induced vibrations; considering the issue of robustness including the role of variability and fluid-structure interactions.

TECHNICAL APPROACH

This multidisciplinary research program required an integrated experiment-theory approach, accomplished through collaboration between Pratt & Whitney, Duke University, and Purdue University.

First, a benchmark standard multistage transonic research compressor was developed, accomplished by modifying an existing research compressor. Specifically, in cooperation with Pratt & Whitney, the Purdue High Speed Axial Research Compressor was modified to feature new IGV and stator rows representative of those used in Pratt-designed modern high pressure compressors.

A quantitative understanding and predictive capability for multi-stage blade row forced response was developed. This includes investigating both analytically and experimentally the fundamental flow phenomena. This was accomplished through experiments that investigate and quantify interacting blade row unsteady aerodynamics as well as the resulting vane vibration and stress response. In addition, Duke University developed a new unsteady aerodynamic analysis of multistage flows in turbomachinery - especially those flows associated with flutter and forced response - capable of analyzing complex two and three-dimensional flows. The method is computationally much more efficient than the current generation of time-domain codes.

The inherently small damping of complex higher order modes was addressed by investigating techniques to control the flow induced vibrations. The issue of robustness - one engine may suffer HCF but a nominally identical one does not – was also considered. The inability to predict, or even understand, these failures is due to a poor understanding of the role of such issues as variability and fluid-structure interactions.

RESEARCH TRANSONIC COMPRESSOR

The Purdue Transonic Multistage Research Compressor features a 1&1/2 stage axial-flow geometry representative of that used in the front stages of aircraft engine high-pressure compressor designs. The drive system consists of a 400 horsepower AC motor, a variable speed magnetic clutch, and an 8:1 ratio gearbox, the output of which drives the compressor rotor. Atmospheric air is drawn into the test section through a converging bell-mouth inlet with a 16:1 contraction ratio and exits the test section through discharge piping which contains a butterfly throttle valve to regulate the flow rate.

The test section, Figure 3, has a constant hub-tip ratio of 0.67 with a tip diameter of 0.3 m (12.0 in.) and features an inlet guide vane (IGV) row, a blisk with 19 rotor blades, and a downstream stator. The rotor blades consist of NACA 65 series profiles on circular arc meanlines having a 5.08 cm (2.0 in.) chord and a thickness distribution varying from 10% at the root to 6% at the tip, with the sections stacked along their centers of gravity. The IGV and stator vanes are an advanced controlled diffusion airfoil (CDA) design with a 4.45 cm (1.75 in.) chord and a constant 7% thickness. The CDA sections are stacked along the maximum thickness locations, with the IGV trunnion located at 39% chord and the stator trunnion at 42% chord.
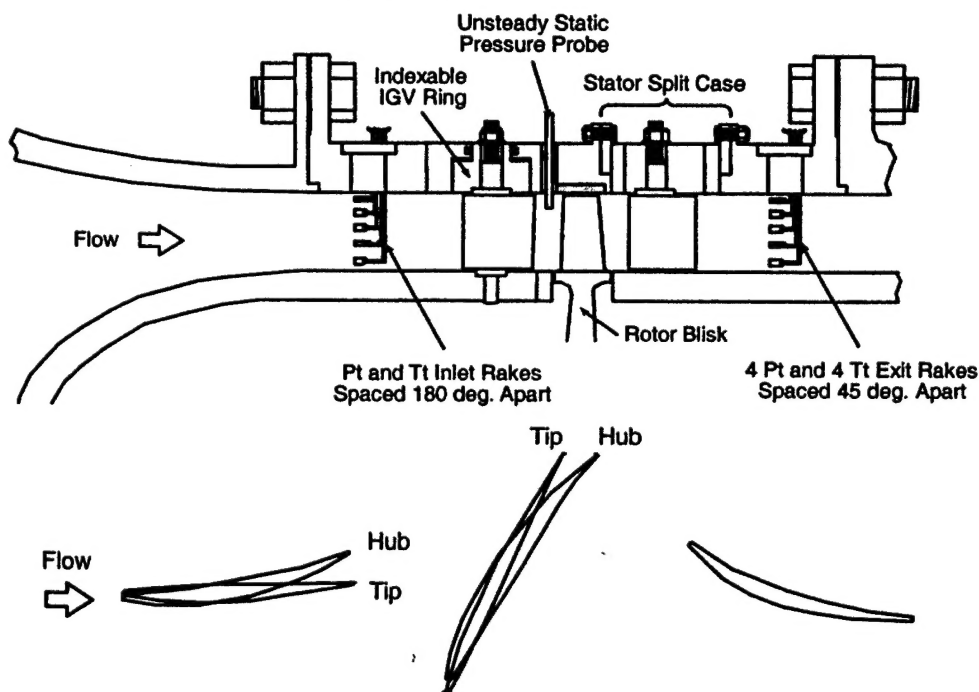
Figure 3. Research compressor test section

IGV ROW UNSTEADY INSTRUMENTATION

Measurements of the rotor generated unsteady aerodynamic forcing function and the resultant IGV steady and unsteady surface pressure distributions are made at 90% span. An unsteady static pressure probe is used to measure the potential flow generated forcing function upstream of the rotor, with vane mounted high-response Kulite XCS-093 5 psi sealed gage pressure transducers used to measure the resultant IGV unsteady surface

pressure response. These transducers are reverse mounted within the suction surface of one vane and the pressure surface of an adjacent vane, with the chordwise tap locations shown in Figure 4.

The rotor operates with a single detached leading edge shock wave which is a significant source of unsteady aerodynamic excitation to the upstream IGV row. Thus, the transducers are concentrated along the aft region of the IGV's since this is where strong interactions with the rotor tip shock system are expected. To minimize probe interference effects, the unsteady static pressure probe is located 21.4% vane chord downstream of the IGV trailing edge and circumferentially positioned at 44.55% pitch between the trailing edges of the vanes adjacent to the instrumented passage, Figure 4.

Very large unsteady pressures on the vane surfaces exceeding the quoted linearity range of the transducers are to be measured. Consequently, the transducers were statically calibrated over a pressure range from 0-7 psi, with the sensitivity found to be nearly linear over this pressure range. Accounting for nonlinearities, the maximum uncertainty in the unsteady pressure measurements is estimated to be 0.5%, with the frequency responses estimated to be 50kHz and 70kHz for the unsteady static pressure probe and instrumented vanes respectively.

Tap No.	1	2	3	4	5	6	7	8
% Chord	5.0	17.5	35.0	55.0	67.5	77.5	85.0	90.0
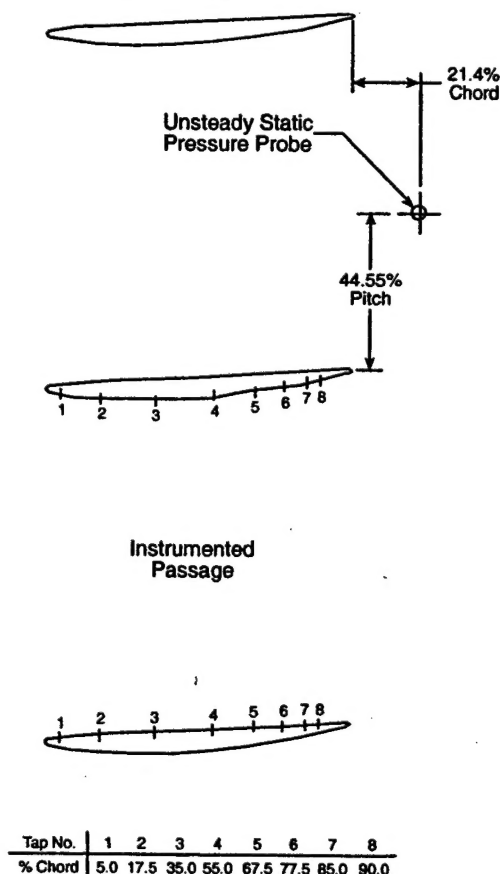
Figure 4. IGV 90% span instrumentation locations

STATOR ROW UNSTEADY INSTRUMENTATION

Measurements of the rotor wake generated unsteady aerodynamic forcing function to the downstream stator and the resultant stator steady and unsteady surface pressure distributions are made at mid-span. Miniature probes designed to access the confined regions between the blade rows are utilized to make inter-stage measurements at the stator inlet. These probes include a United Sensors DA-125 pneumatic five hole prism probe, a conventional total temperature probe, an unsteady static pressure probe, and a TSI Model 1240-20 cross hot-film anemometer probe. The probe measurement plane is 16.26% stator chord upstream of the stator leading edge and circumferentially positioned mid-way between the stator vane stacking axes, Figure 5.

The steady and unsteady stator vane mid-span pressure distributions are measured at the chordwise locations shown in Figure 5. The steady pressure distribution is measured using pneumatic taps, with the unsteady aerodynamic response measured on separate vanes with high response Kulite XCS-093 pressure transducers reverse mounted within the suction surface of one vane and the pressure surface of an adjacent vane. Both the transducers and lead wires are recessed into the vane to maintain the design intent vane profile. Note that the unsteady aerodynamic forcing function and vane response measurements are not made simultaneously. Rather, to minimize probe interference effects the vane response is measured with a clean inlet flow field. The instrumented stator assembly is then removed and separate forcing function measurements are made at the inlet to this same passage using each of the high-response probes. The maximum uncertainty in the unsteady pressure measurements is estimated to be 0.5%, with the frequency responses estimated to be 50kHz and 70kHz for the unsteady static pressure probe and instrumented vanes respectively.
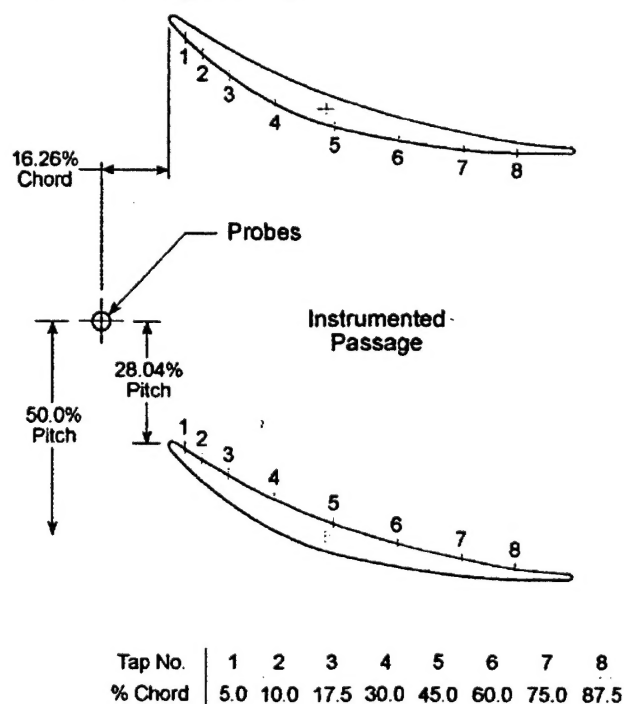

Tap No.	1	2	3	4	5	6	7	8
% Chord	5.0	10.0	17.5	30.0	45.0	60.0	75.0	87.5

Figure 5. Stator mid-span instrumentation locations

PARTICLE IMAGE VELOCIMETRY (PIV)

The DANTEC PIV system utilized consists of a 30 mJ NewWave Research Minilase III Nd:YAG laser, a high-resolution Kodak Megaplus ES 1.0 digital camera, and a dedicated personal computer (PC) controlled PIV-2100 Processor. The laser has twin oscillators and is capable of delivering a 5-7 ns duration pulse with a wavelength of 532 nm (visible green light) at a repetition rate of 10 Hz, with the time between pulses specified using software. The camera has a 1008 x 1018 CCD array operated in cross-correlation mode, with the images corresponding to the 1st and 2nd laser pulses recorded separately. Both images are then transferred to the PIV 2100 Processor that provides near real-time vector processing of the images using Fast Fourier Transform (FFT) correlation techniques. This unit also synchronizes the camera and laser, and is capable of resolving the particle displacement to within 1/10 of a pixel through the use of sub-pixel interpolation schemes. PC controlled software is used to perform off-line validation and post-processing of the vector maps, with directional velocity information unambiguously determined since the initial and final particle positions are recorded as separate images.

A thermal aerosol generator is used that produces a high volume of particles by discharging a heated and pressurized glycol based mixture into the atmosphere where it immediately vaporizes and then condenses into a fine mist of monodisperse particles. A uniform test section seeding density is achieved by introducing these particles upstream of the inlet and allowing them to disperse into the ambient air prior to being drawn through the facility.

The instantaneous IGV-to-IGV and stator vane-to-vane flows are measured for several time instants over one rotor blade-passing period. A once-per-revolution pulse from a photo-optic sensor on the shaft triggers the PIV 2100 Processor that then fires the lasers and records the camera CCD images. To record images at different points over one interaction cycle, the rotor speed is used to calculate the time delay to position the rotor at the desired angular location relative to the stationary vanes. This value is then programmed into a LaserStrobe 165 Phase Delay Generator, which can deliver an accurate time delay up to 999.9 μsec in 0.1 μsec increments.

The IGV-to-IGV 90% span flow is illuminated by a 1 mm thick light sheet introduced upstream through the bellmouth inlet using a combination of cylindrical and spherical lenses. Optical access to the IGV passage is provided with a 2 Plexiglas window contoured to the flow path O.D. The 50% span stator vane-to-vane flow is illuminated by a 1 mm thick sheet introduced downstream of the stator through an optical probe. The probe has a 7.94 mm O.D. and consists of a $45°$ high energy Nd:YAG mirror and a +4.0 mm plano-cylindrical lens. Prior to entering the probe, the laser beam is passed through an iris and a 1000 mm plano-convex lens located adjacent to the test section. To minimize disturbances produced by the probe, it is positioned ahead of the support strut leading edge 2.06-stator chords downstream of the stator trailing edge.

The images corresponding to the two laser pulses are divided into rectangular interrogation areas, with cross-correlation software used to determine an average particle displacement for each region. The FFT algorithm generates artificial cyclic background noise at the interrogation region edges. This can result in the loss of particle pairs due to

low signal-to-noise ratio at the boundaries, with particles near the edges not used in the velocity calculation. However, this information is recovered by over-sampling the images using overlapping interrogation regions. This does not increase the spatial resolution, but generates additional vectors as suitable interpolations. 32 x 32 pixel interrogation areas with 50% overlap are used, resulting in 3,844 raw velocity vectors per image.

RESULTS

The IGV and stator unsteady flow fields generated by rotor-IGV and rotor-stator interactions were experimentally investigated along the nominal operating line at transonic (N_c=20,000 rpm) and subsonic conditions (N_c=15,000 rpm), Figure 6. The downstream stator unsteady flow field was also investigated over a range of steady compressor loading conditions at the transonic design speed of 20,000 rpm. The three operating lines correspond to low steady loading near the choke boundary, nominal loading at the aerodynamic design point, and a highly loaded condition near the compressor stall line.
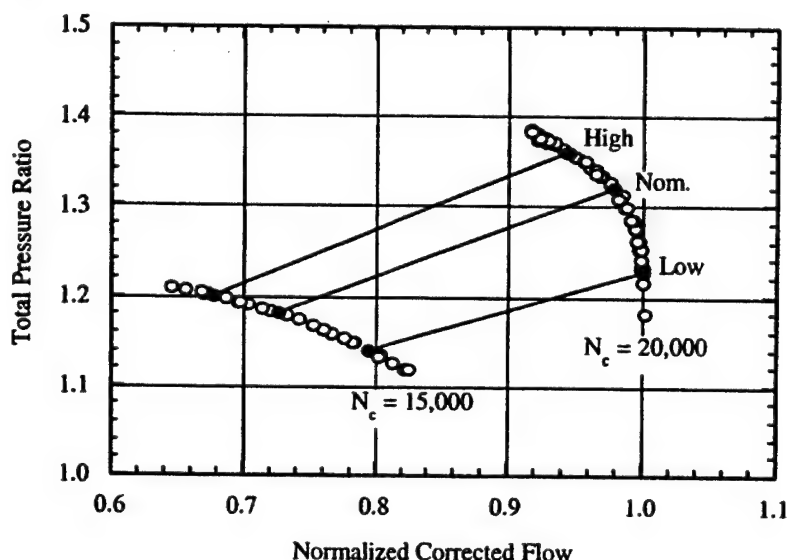

Figure 6. Purdue compressor performance map

IGV UNSTEADY AERODYNAMICS

Detailed benchmark rotor-IGV unsteady aerodynamic blade row interaction data are acquired at both design and part-speed operating conditions. These detailed data include IGV surface pressure data as well as PIV measurements of the instantaneous vane-to-vane flow field in the IGV passage at 90% span.

Rotor Generated Forcing Function to IGV's

The effect of steady compressor loading on the rotor generated unsteady static pressure field, i.e., the forcing function to the upstream IGV, is shown in Figure 7 for both design (transonic) and part-speed (subsonic) rotor operating conditions. Presented is the time-variant static pressure nondimensionalized by the time-average inlet total pressure, with time nondimensionalized by the blade-pass period. Note that the scales are different, with the maximum static pressure fluctuations at the transonic operating conditions 3.5 times larger than those for subsonic rotor flow.

These pressure fluctuations are very large, with peak-to-peak amplitudes up to 35% and 10% of the inlet total pressure for the transonic and subsonic rotor speeds respectively. The very large fluctuations at the transonic design speed are due to the shock waves generated by the rotor. Note that the forcing functions generated by subsonic rotor operation are by no means insignificant. Rather, they are small only in comparison to those generated at the transonic operating condition. Notice also that the waveforms are significantly different, transitioning from a saw tooth type pattern for subsonic rotor flow to a series of large amplitude periodic pulses at the transonic design speed. Steady compressor loading does not, however, have a strong effect on the forcing function, with the maximum amplitudes nearly identical for all operating conditions along a given speed line.

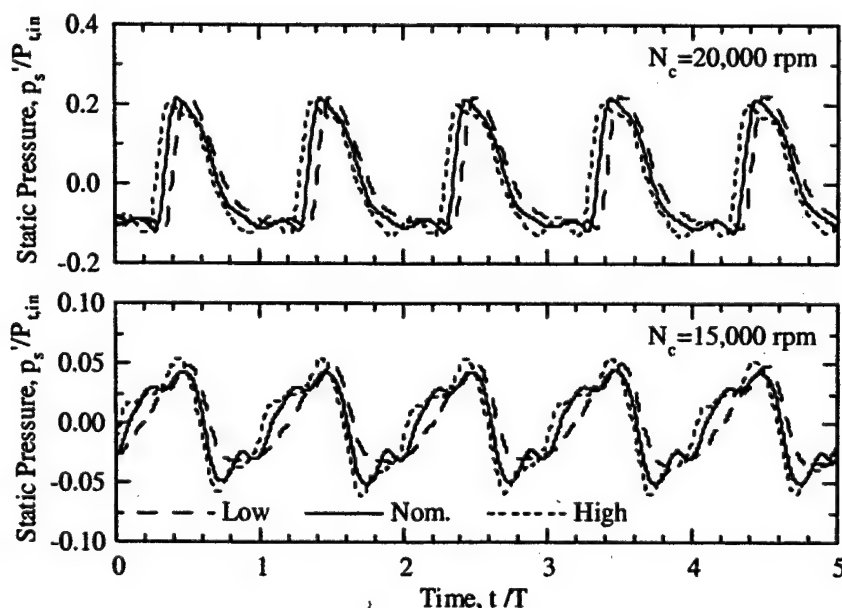

Figure 7. Effect of steady loading on rotor generated forcing function to IGV

IGV Unsteady Aerodynamic Response

The unsteadiness on the IGV surfaces is shown in Figure 8. Specifically, the vane surface unsteady pressure envelopes along with the time-average pressure distributions for the moderate and large axial spacings at the transonic and subsonic rotor operating conditions are shown.
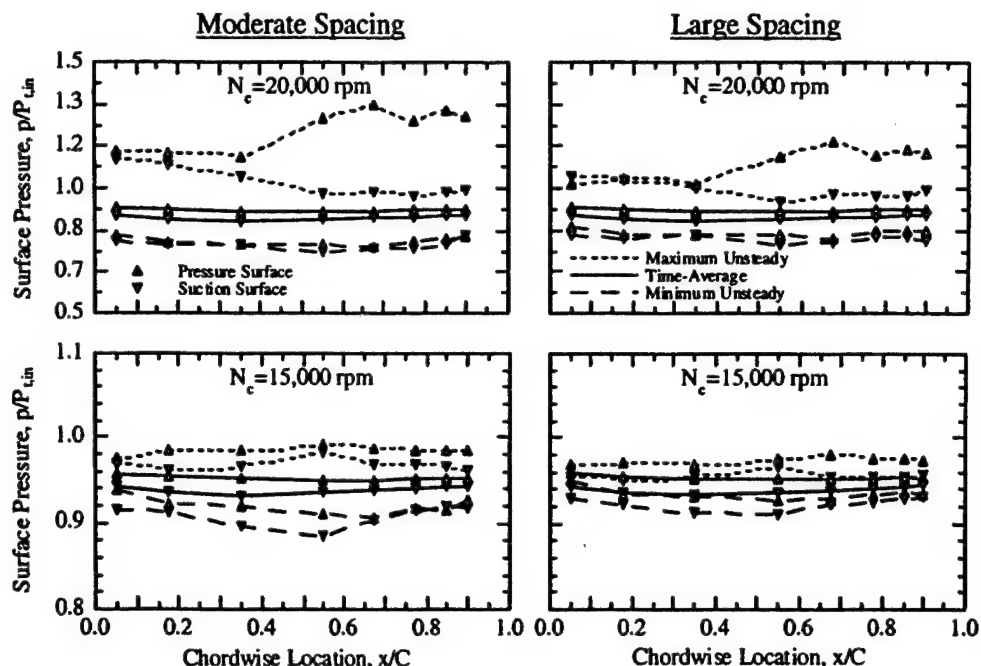
Figure 8. IGV unsteady pressure envelopes for nominal loading

At the transonic design speed, the maximum unsteady pressure surface loading is highest along the aft 30% chord, decreasing as one moves forward from 70 to 30% chord, and then remaining relatively constant over the front 30% of the chord. Note that the suction surface exhibits the opposite trend, with the unsteady loading highest near the leading edge, decreasing in a nearly linear fashion to 60% chord, and then remaining nearly constant over the aft 40% chord. This unsteadiness is very significant, reaching amplitudes as high as 60% (maximum – minimum) of the inlet total pressure in the trailing edge region at the moderate spacing. Increasing the axial spacing reduces the magnitude of the unsteady loading, but the loading still reaches levels as large as 40% of the inlet total pressure, which corresponds to nearly 1/2 of the steady loading in the trailing edge region. Also notice that the vane suction surface unsteadiness begins to increase at roughly the same chordwise location as that at which the pressure surface unsteadiness begins to decrease, with the unsteadiness the same order of magnitude near the vane leading edge on both vane surfaces.

The unsteady vane loading is considerably reduced at the subsonic rotor operating condition, with the maximum peak-to-peak pressure fluctuations at the moderate spacing only around 10% of the inlet total pressure. Additionally, the pressure fluctuations are highest over the central portion of the vane on both airfoil surfaces. This is in contrast to the data at the transonic rotor speed where the fluctuations were highest in the vane pressure surface trailing edge region and in the suction surface leading edge region. Since the forcing function generated by subsonic rotor operation decays exponentially with axial distance, it might be expected that the vane response would be highest in the IGV trailing edge region at this operating condition. The data, however, indicate that the unsteadiness is the same order of magnitude in the vane leading and trailing edge regions and highest over the central portion of the vane. This may be due to acoustic phenomena, with the rotor-IGV interactions generating acoustic modes which propagate upstream

through the vane passage. These acoustic modes are contained in both the forcing function and vane response data since they occur at harmonics of blade-pass frequency and are phase-locked to the rotor. Also note that the forcing function generated in the transonic flow regime is 3.5 times larger than that generated by subsonic rotor operation. However, the maximum unsteady loading on the IGV at the design speed as a result of this interaction is six times larger than that at part-speed. It will be shown that this dramatic increase in unsteady loading at transonic speeds is due, in part, to nonlinear interaction effects in the vane trailing edge region, with these effects not present for subsonic rotor operating conditions.

To gain insight into the unsteadiness evolution, the time-variant IGV surface pressures generated at the transonic design speed over one periodic cycle are examined. Figure 9 shows the phase-lock averaged surface pressure distributions at ten equally spaced increments over one blade-passing period. Also shown for reference in the center of the figure is the rotor generated unsteady aerodynamic forcing function. Recall that this forcing function is measured at approximately mid-pitch, and lags the measurements at the upper vane trailing edge by 58.5% of the blade-pass period. To compensate for this time delay, the pressure fluctuations associated with the passing of the rotor shock at each time increment are indicated on the forcing function waveform by the open symbols for one vane response cycle.
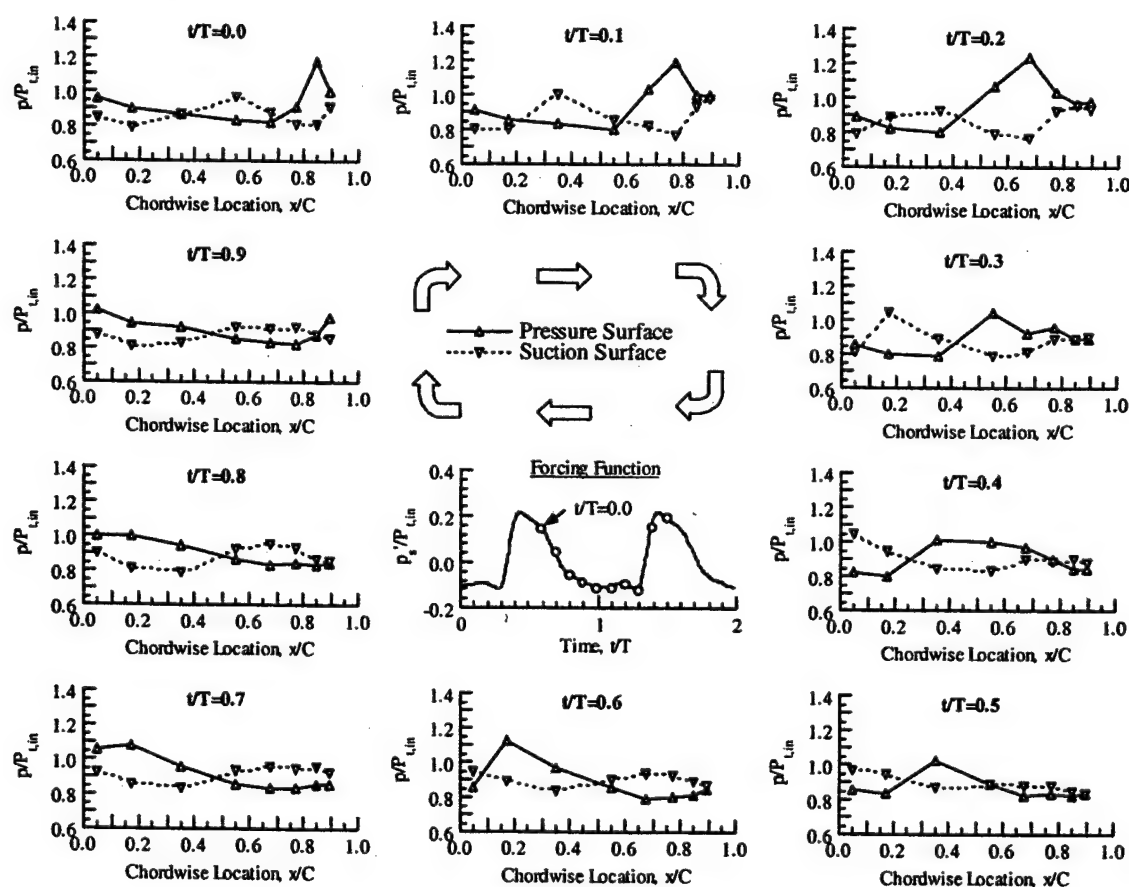

Figure 9. Time-variant IGV loading at 20,000 rpm

Upstream traveling wave phenomena are evident, with the pressure and suction surface responses nearly $180°$ out-of-phase along most of the chord. This behavior is attributed to a time-dependent wave pattern being generated in the IGV passage due to the interaction of the rotor shock waves with the upstream vane row. The rotor shocks periodically impact the trailing edge region of the upstream vanes, with a reflection of the incident shock wave occurring on the pressure (upper) surface and diffraction occurring on the suction (lower) surface as the shock bends around the trailing edge, Figure 10.

The reflection of the shock by the vane pressure surface causes a significant increase in the static pressure (overpressure zone) to occur in the region aft of the reflection point ($p_3 > p_2$). Since the IGV flow field is subsonic, a pressure wave is generated in the trailing edge region which equalizes the pressure in the overpressure zone with the lower pressure region aft of the diffracted shock on the suction surface. This process is periodic since the shock waves translate with the rotor, with the reflection point moving upstream along the chord and the reflected shock segment continuing to propagate upstream toward the suction surface of the adjacent vane as the cycle progresses. As the reflection point moves past the nose of the airfoil, another pressure wave is generated in the leading edge region in order to equalize the pressure on the upper and lower surfaces and the reflected shock segment is diffracted as it bends around the nose. Note that cascade effects can cause secondary reflections to occur, with the reflected shock segments impacting the surface of adjacent vanes or the multiple leading edge shocks generated by the rotor as they propagate upstream.

Shock Interaction with V ane Trailing Edge
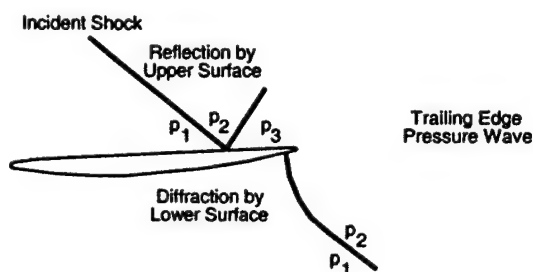
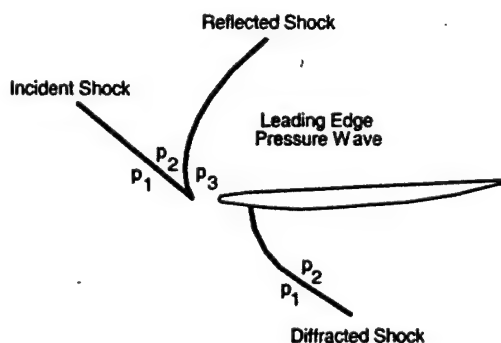**Shock Interaction with V ane Leading Edge**

Figure 10. Shock wave interaction with an isolated IGV

The maximum pressure fluctuation associated with the rotor generated forcing function occurs at $t/T=0.8$, while the vane response to this forcing function is first evident at $t/T=0.9$. This time lag is due to the rotor leading edge shock waves being inclined to the axial direction, with the axial separation distance between the last transducer and unsteady static pressure probe 31.4% vane chord. At $t/T=0.9$, the impact of the rotor shock causes an increase in the unsteady pressure surface loading in the trailing edge region of the vane. Note that a suction surface response to the rotor shock is not yet evident at this time for the 90% chord transducer location due to the diffraction of the shock by the lower surface of the vane.

At the next time instant, the overpressure caused by the shock reflection on the pressure surface is clearly visible, with the suction surface of the vane also beginning to respond to the passing of the rotor shock. The unsteady loading generated by the reflected shock is very significant, with the maximum unsteady pressure difference across the vane nearly 50% of the time-average inlet total pressure. Note that the pressure surface loading decreases sharply aft of the reflection point, with the loading on both vane surfaces approaching the same value as the trailing edge is approached.

As the reflection point moves upstream, the unsteady pressure surface loading aft of the reflection continues to increase to a maximum at $t/T=0.2$, after which it decreases and then remains about the same throughout the remainder of the cycle. This behavior is attributed to the decay of the incident shock waves as they interact with the upstream vane row and dissipate energy through the reflection and diffraction process. The reflected shocks, however, continue to propagate upstream as the cycle progresses. At $t/T=0.3$, the shock reflected by the pressure surface of the adjacent vane during the previous cycle has traveled across the vane passage and impacts the suction surface of the reference vane in the leading edge region, causing the unsteady loading near 20% chord to increase noticeably.

Analogous results for the moderate axial spacing at the subsonic rotor speed are shown in Figure 11. Here the entire pressure and suction surfaces of the vane smoothly respond to the passing of the rotor at each time instant, with essentially no unsteady loading occurring at $t/T=0.4$ and the maximum unsteady loading occurring at $t/T=0.7$. Notice that a pressure wave is generated on the vane suction surface near the trailing edge at $t/T=0.6$ which propagates upstream along the vane chord and reaches the leading edge about halfway though the cycle at $t/T=0.1$. The effects of this on the unsteady loading are, however, much less noticeable than those which occurred at the transonic rotor speed, in which upstream traveling wave phenomena were distinctly evident on both vane surfaces over the entire cycle.
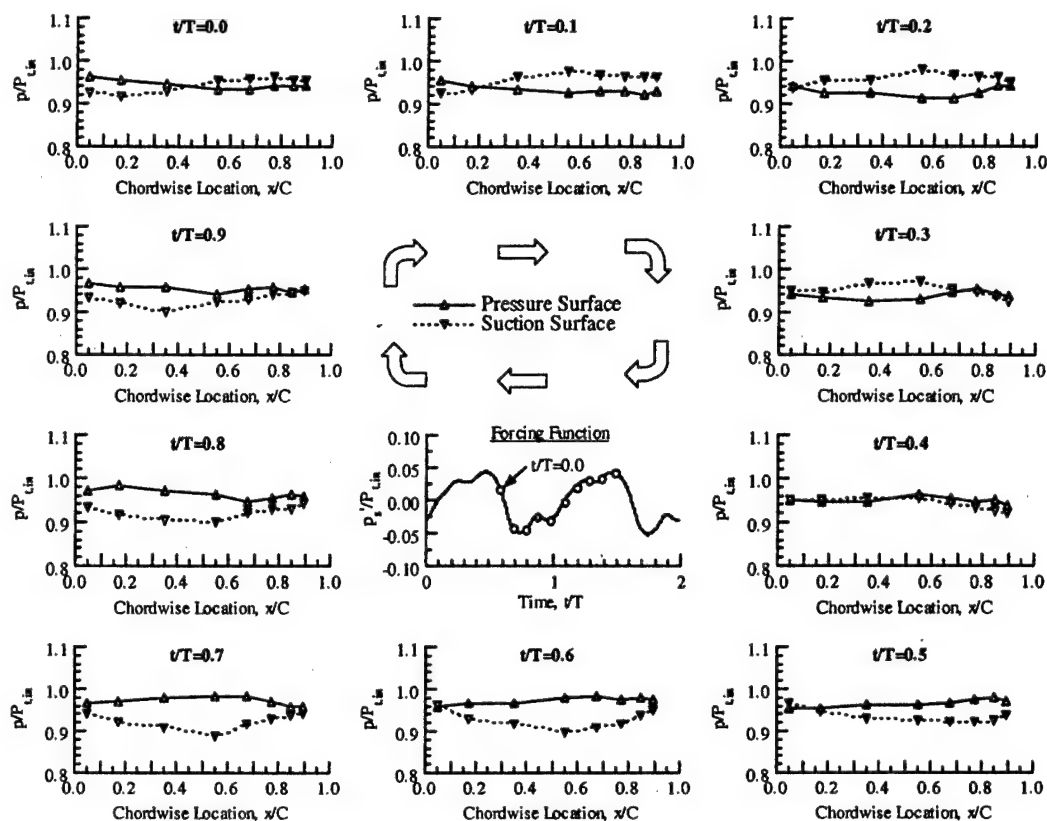
Figure 11. Time-variant IGV loading at 15,000 rpm

IGV-to-IGV Time-Variant Flow Field

The time-variant IGV-to-IGV flow field is measured at 90% span using PIV, with ensemble averaged snapshots of the periodic unsteady flow field generated by rotor-IGV interactions presented for ten equally spaced increments over one blade-passing period. Figures 12 and 13 show the time-average and unsteady Mach number contours over one interaction cycle respectively for the transonic rotor speed.
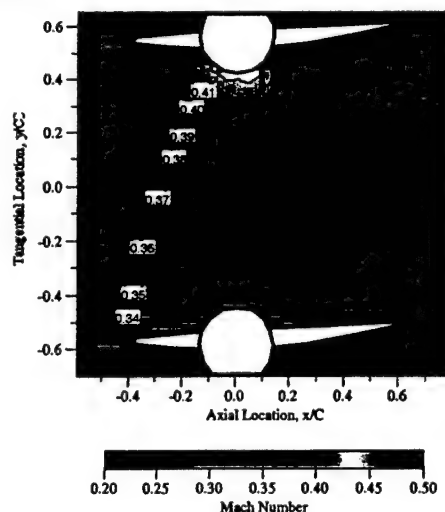
Figure 12. Time-average IGV flow field for nominal loading at 20,000 rpm

The time-averaged PIV data at the IGV leading edge plane are in excellent agreement with the average inlet Mach number of 0.37 calculated from the surface pressure data. The instantaneous snapshots of the flow field demonstrate the highly unsteady nature of the flow field generated by the transonic rotor-IGV interactions and reveal several complicated interaction phenomena. First, the rotor leading edge shock waves are reflected and diffracted as they impact the IGV trailing edge. The reflection point moves upstream as the cycle progresses, with the incident shock decaying as it propagates through the IGV passage. The reflected shock segment however, travels across the vane passage as it propagates upstream, interacting with the shock of the adjacent rotor blade before it eventually impacts the suction surface of the upper vane in the leading edge region.

At $t/T=0.9$, the rotor leading edge shock wave is just about to impact the lower vane in the passage. Note however, that the shock of the adjacent rotor blade has already impacted the upper vane in the passage due to the unequal blade-vane count. The blade-vane count ratio sets the spatial periodicity of unsteady flow phenomena in the passage, with interactions which occur on the upper vane leading those on the lower vane by the interblade phase angle. For the present geometry with 18 IGV's and 19 rotor blades, the interblade phase angle is $380°$. It thus takes any given rotor blade 1.06 blade-passing periods to traverse the IGV passage, with the rotor-IGV interactions for each vane periodic at blade-pass frequency.

At $t/T=0.0$, the rotor shock impacts the lower vane and is diffracted as it bends around the trailing edge. At the next time instant, the point of impact has moved upstream and the shock is reflected by the vane pressure surface. A pressure wave is also generated at the trailing edge to equalize the overpressure region aft of the reflected shock with the lower pressure region on the suction surface behind the diffracted shock. The reflected shock segment continues to propagate upstream toward the suction surface of the upper vane in the passage as the cycle progresses, with the incident shock decaying as the reflection point moves further upstream along the vane chord and no longer visible at $t/T=0.7$.

At $t/T=0.4$, a pressure wave is also visible just ahead of the diffracted shock on the upper vane suction surface. This pressure wave continues to grow and begins interacting with the shock segment reflected by the lower vane at $t/T=0.6$. This interaction between the pressure wave and the reflected shock segment continues as the cycle progresses, with the reflected shock also beginning to interact with the incident shock generated by the adjacent rotor blade at $t/T=0.8$. This complex interaction continues as the cycle repeats up until $t/T=0.3$, at which point the shock segment reflected by the lower vane during the previous cycle has traveled across the passage and impacts the suction surface of the upper vane in the leading edge region.

A low velocity high pressure region characterizes the IGV flow field aft of the reflected shock on the vane pressure surface. After passing through the reflected shock segment, fluid particles are smoothly accelerated to a velocity higher than the free stream prior to being again decelerated as they pass through the incident shock generated by the adjacent rotor blade. Note that a similar process also occurs on the suction surface of the upper vane in the passage aft of the secondary reflection point.
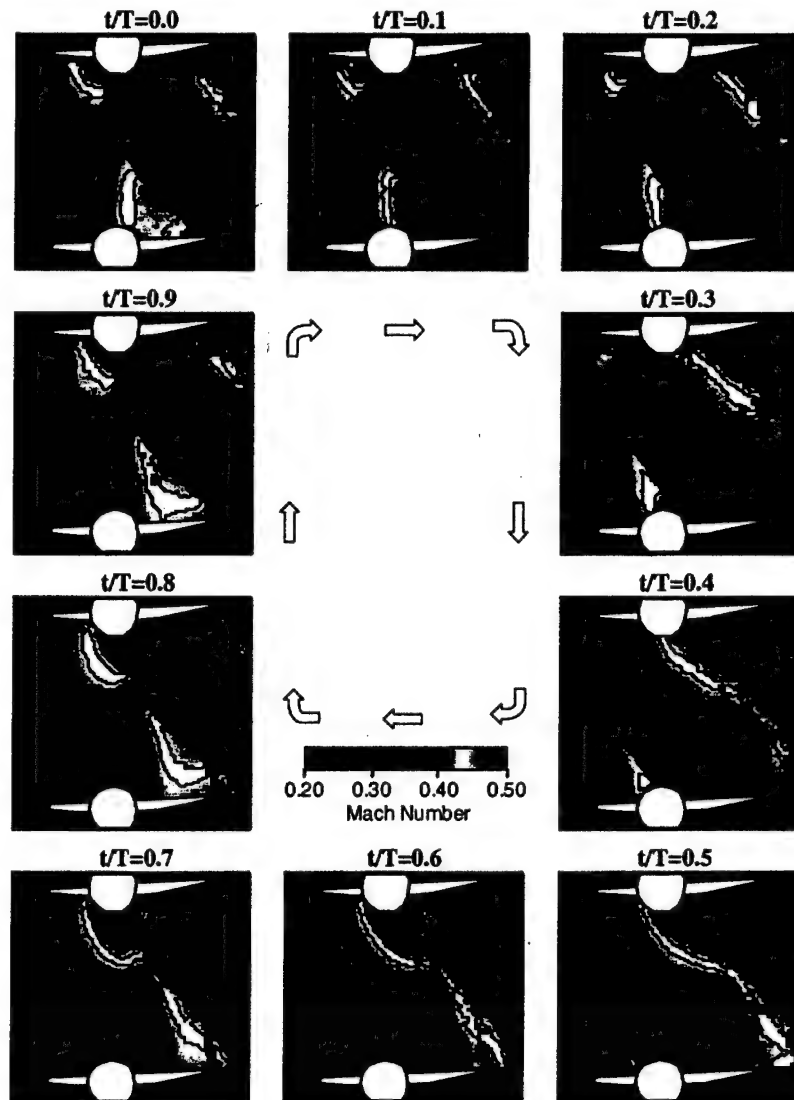
Figure 13. Time-variant IGV flow field for nominal loading at 20,000 rpm

Figures 14 and 15 show the time-average and unsteady Mach number contours at the same ten time instants for the part-speed subsonic rotor operating condition. The time-average subsonic and transonic rotor generated IGV flow fields are similar, with the time-averaged PIV data at the IGV leading edge plane again in excellent agreement with the average inlet Mach number of 0.27 calculated from the surface pressure data. The time-variant snapshots of the flow closely resemble the time-average flow throughout the entire interaction cycle. This is due to the subsonic rotor potential field imposing a moderate unsteady backpressure variation on the upstream IGV row, with the flow through the IGV passage smoothly responding to the passing of the rotor at each time instant. This is in contrast to the highly unsteady flow field generated at the transonic

rotor speed in which the rotor leading edge shocks were reflected and diffracted as they interacted with the upstream vane row, creating sharp unsteady velocity gradients.
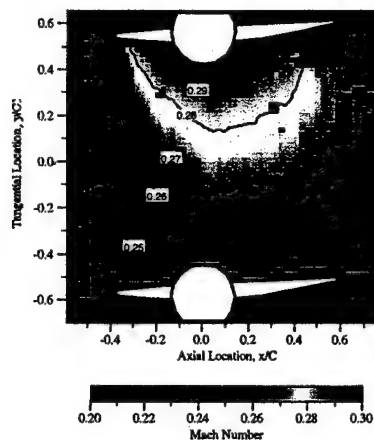

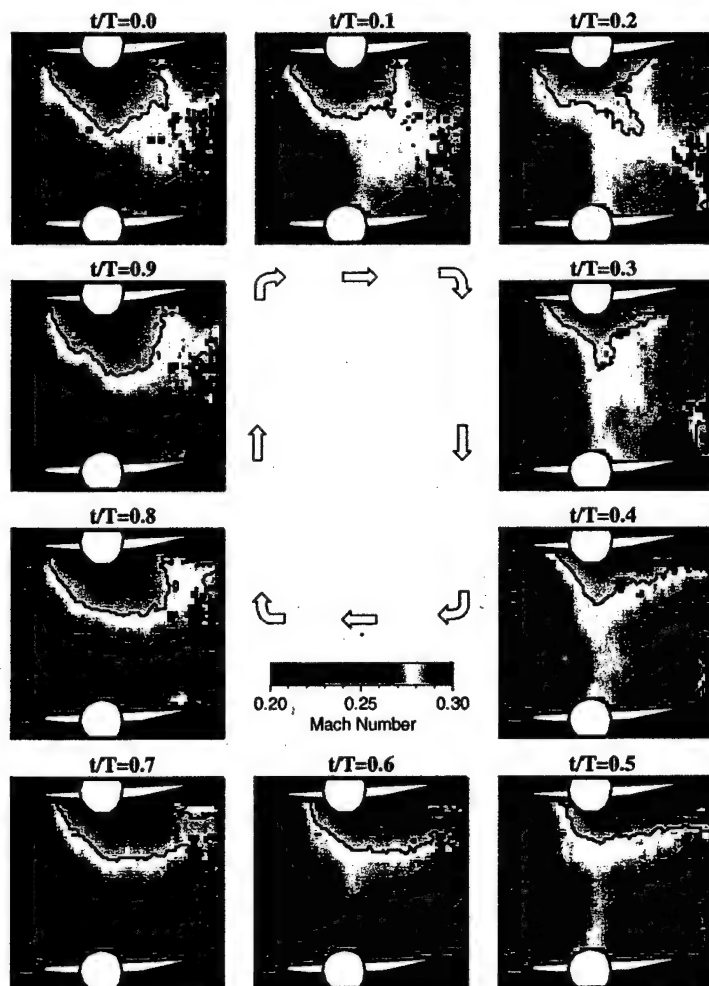Figure 14. Time-average IGV flow field for nominal loading at 15,000 rpm

Figure 15. Time-variant IGV flow field for nominal loading at 15,000 rpm

Conclusions

The rotor generated shocks resulted in very large pressure fluctuations, i.e., forcing functions to the upstream IGV's, with peak-to-peak amplitudes to 35% of the inlet total pressure. The resulting vane unsteady aerodynamic loading was very significant, with the maximum peak-to-peak static pressure fluctuations over the aft region as large as 60% of the inlet total pressure.

For the part-speed rotor operating condition, the time-variant IGV flow field closely resembled the time-average flow throughout the entire cycle. This was due to the subsonic rotor potential field imposing a mild unsteady backpressure variation on the upstream vane row, with the flow through the IGV passage smoothly responding to the passing of the rotor at each time instant.

The time-variant IGV flow field at the transonic design speed differed markedly from the time-average vane-to-vane flow. The impact of the rotor leading edge shocks with the vane trailing edge resulted in the incident shock being reflected by the pressure surface and diffracted by the suction surface. The reflection point moved upstream as the cycle progressed, with the incident shock decaying due to its interaction with the vane row as it propagated upstream through the vane passage. The reflected shock segment however, did not decay and traveled across the vane passage as it propagated upstream, interacting with the incident shock of the adjacent rotor blade before it eventually impacted the suction surface of the upper vane in the leading edge region. This interaction resulted in a complicated time-dependent wave pattern being established in the vane passage, with steep velocity gradients occurring across both the incident and reflected shocks.

The reflection of the rotor shock by the upstream vanes generated a high overpressure zone aft of the reflection point on the vane pressure surface. This high-pressure region caused the flow to accelerate around the trailing edge and the stagnation point to periodically move from the upper to the lower surface of the vane over the course of a single blade-passing period.

STATOR ROW UNSTEADY AERODYNAMICS

Rotor Wake Generated Forcing Function to Stators

The subsonic rotor wake generated forcing function is shown in Figure 16. Presented are the rotor relative Mach number, relative flow angle, absolute Mach number, absolute flow angle, and unsteady static pressure normalized by the compressor inlet total pressure for one complete rotor revolution. The subsonic rotor wakes are narrow compared to the rotor pitch, with blade-to-blade differences present in the phase-lock averaged waveforms. The blade-to-blade wake variability is large compared to the size of the wake deficit, with the relative Mach number deficits ranging from 13.6% to 17.7% of the free stream Mach number over one rotor revolution.
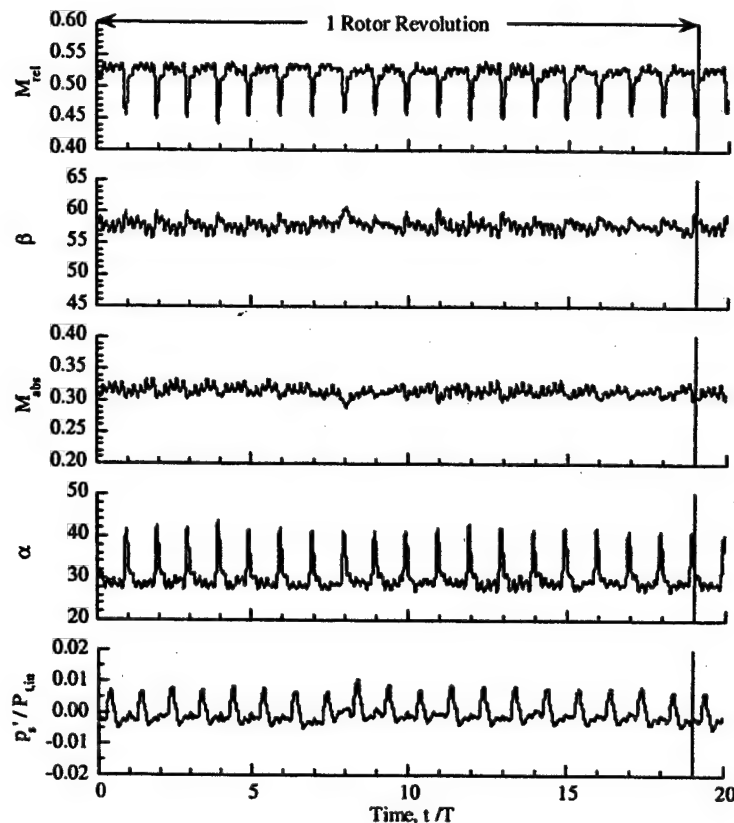
Figure 16. Subsonic rotor wake generated forcing function ($\Delta S/S=0.0$)

In the reference frame of the downstream stator, the rotor wakes manifest themselves mainly as absolute flow angle fluctuations, with the absolute Mach number fluctuations much smaller. In fact, the waveforms for the absolute Mach number and flow angle closely resemble the inverted relative flow angle and relative Mach number waveforms respectively. This causes the vane incidence angle to fluctuate from -15.0° to +1.9° over one rotor revolution, which is a considerable fluctuation. Also note that the variability in the rotor wake velocity deficits causes the maximum, or peak, phase-lock averaged incidence angle to the downstream stator to vary by as much as 2.8° over one rotor revolution, which will generate significant variability in the periodic stator loading.

Also notice that the static pressure fluctuations are approximately 180° out-of-phase with the rotor wake velocity deficits. These static pressure fluctuations are attributed to the spinning acoustic modes generated by interactions between the stationary and rotating blade rows, with an infinite number of these spinning pressure patterns generated at harmonics of blade-pass frequency. These patterns are generated both upstream and downstream of the interacting blade rows, with the number of lobes and phase speed of each pattern set by the blade-vane count ratio. Only certain modes are cut-on and propagate unattenuated to the far field where they are perceived as discrete frequency noise, with the majority of the modes cut-off in which they decay exponentially with axial distance. In the near field, the effects of both the cut-on as well as the cut-off modes are present, with the superposition of a number of patterns rotating at different phase speeds resulting in a signal level that varies with circumferential position.

Additionally, since the probe is placed in the inter-stage region between the rotor and stator, both the downstream propagating rotor-IGV interaction modes as well as the upstream propagating rotor-stator modes are contained in the data since both sets of modes occur at blade-pass frequency harmonics.

To investigate the spatial variation in the static pressure fluctuations generated by these interactions, the static pressure probe is traversed across the inlet to one full vane passage. The circumferential traverse used for this survey is located at top dead center 90° (4.5 vane spacings) from the reference stator passage, with the results presented in Figure 17. Here $\Delta S/S$ denotes the circumferential location of the probe relative to the center of the reference stator passage measured in the direction of rotor rotation normalized by the stator vane-to-vane spacing. Thus, the probe is located at the same circumferential position relative to the downstream vane passages for $\Delta S/S=0.0$, $\Delta S/S=-1.0$, $\Delta S/S=-2.0$, $\Delta S/S=-3.0$, $\Delta S/S=-4.0$, and $\Delta S/S=-5.0$.
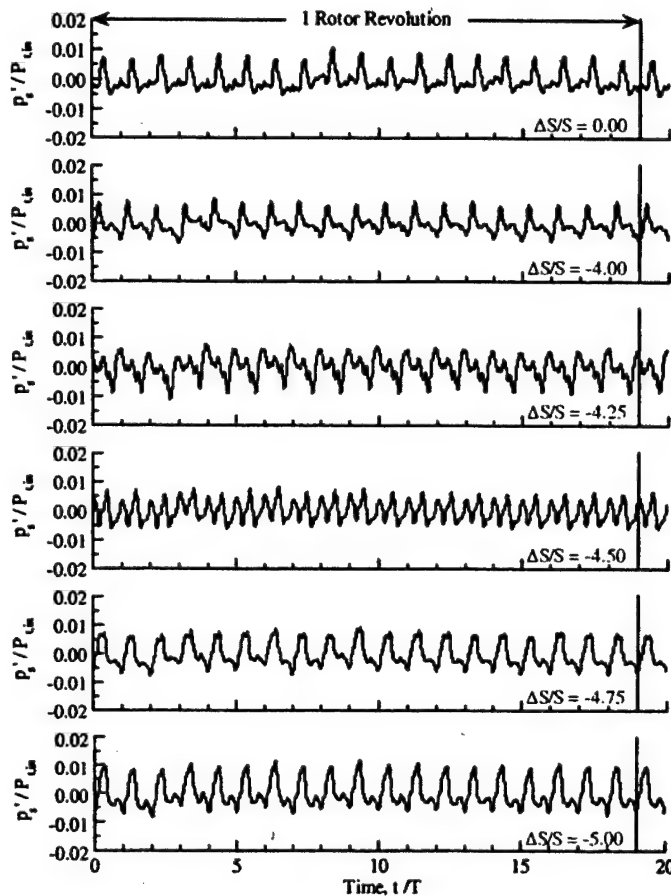
Figure 17. Circumferential variation in subsonic rotor wake unsteady static pressure

However, the waveforms for $\Delta S/S=0.0$, $\Delta S/S=-4.0$, and $\Delta S/S=-5.0$ are noticeably different, indicating that the unsteady static pressure field varies from vane-to-vane around the compressor annulus. The waveform character changes even more markedly as the probe is traversed across an individual stator passage, i.e., from $\Delta S/S=-4.0$ to $\Delta S/S=-5.0$. In fact the waveform corresponding to $\Delta S/S=-4.5$ has a visibly different harmonic

content than the waveforms at $\Delta S/S$=-4.0 and $\Delta S/S$=-5.0. These spatial variations are due to the superposition effect of the infinite number of modes generated at blade-pass frequency harmonics in the near field region between the rotor and stator where the measurements are made. Since these modes occur at the same frequency but travel at different phase speeds, they constructively and destructively interfere with one another they as they spiral around the compressor annulus, with the degree of interference dependent upon circumferential as well as axial location.

The spatial periodicity of these acoustic interactions is over the entire annulus of the machine due to the unequal numbers of blades and vanes in the compressor, with the amplitude of the acoustic excitation to the stator varying from vane-to-vane around the compressor annulus. Time-accurate multi-blade row CFD simulations commonly scale the geometry such that the computational domain of each airfoil row is represented by at most a few passages. This greatly reduces the computation time and storage requirements but alters the fundamental periodicity of the blade row interaction phenomena, i.e., the characteristics of the interaction acoustic modes are drastically altered due to the interblade phase angle change. Thus, the impact of this assumption on the unsteady aerodynamic flow field must be considered when comparing the results of multi-blade row CFD analyses to the data presented herein.

Analogous results for the transonic rotor speed are presented in Figure 18. The transonic rotor wakes are very broad and deep, with their circumferential extent spanning almost the entire rotor pitch. These characteristics are due to off-design operation of the current rotor, which features subsonic NACA 65 series airfoil profiles. The wake velocity deficits generated by transonic rotor operation are significantly deeper than those at the subsonic rotor speed, with the average wake deficit 25.7% of the free stream Mach number. Blade-to-blade wake variability is again present in the phase-lock averaged waveforms, with the rotor wake relative velocity deficits ranging from 23.6% to 26.7 % of the free stream Mach number over one rotor revolution.

The absolute flow angle fluctuations to the downstream stator are also nearly sinusoidal and much more severe for the transonic rotor speed, with the vane incidence angle fluctuating from–23.2° to +2.0° over one rotor revolution. The rotor wake variability again causes the maximum, or peak, phase-lock averaged incidence angle to the downstream stator to differ by as much as 1.7° over of one rotor revolution. Also notice that the time-average vane incidence is nearly the same for both the subsonic and transonic rotor speeds (-6.5° versus -7.1°). However, the change is rotor speed has a marked impact on the time-variant characteristics of the stator incidence fluctuations.

Transonic rotor operation also results in much larger static pressure fluctuations than those that occurred at part-speed. Here, the minimum static pressure occurs very near the wake centerline, with the peak-to-peak fluctuations around 4% of the compressor inlet total pressure. These static pressure fluctuations are again attributed to the spinning acoustic modes generated by blade row interactions.

Figure 19 shows the circumferential variation in the unsteady static pressure. The changes in waveform character with probe location are similar to those noted for the

subsonic rotor speed, with the superposition field characterized by a signal which varies with circumferential position in the inter-stage region between the rotor and stator.
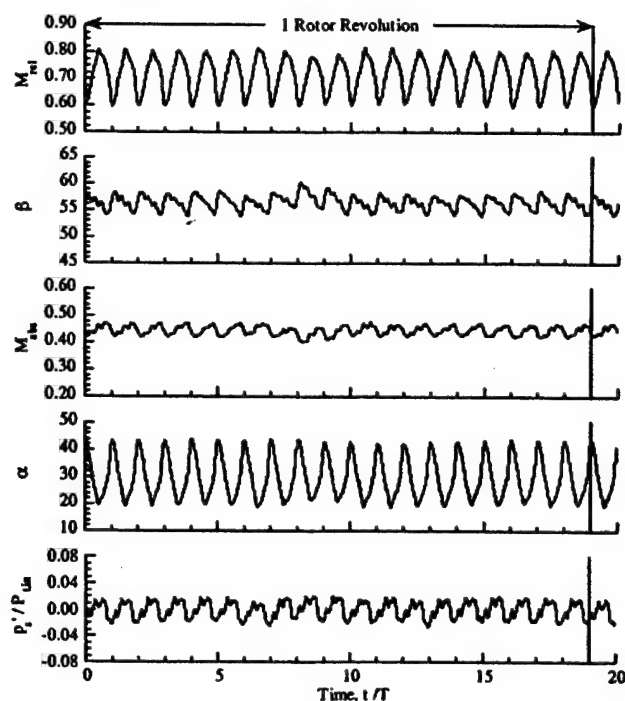

Figure 18. Transonic rotor wake generated forcing function ($\Delta S/S=0.0$)
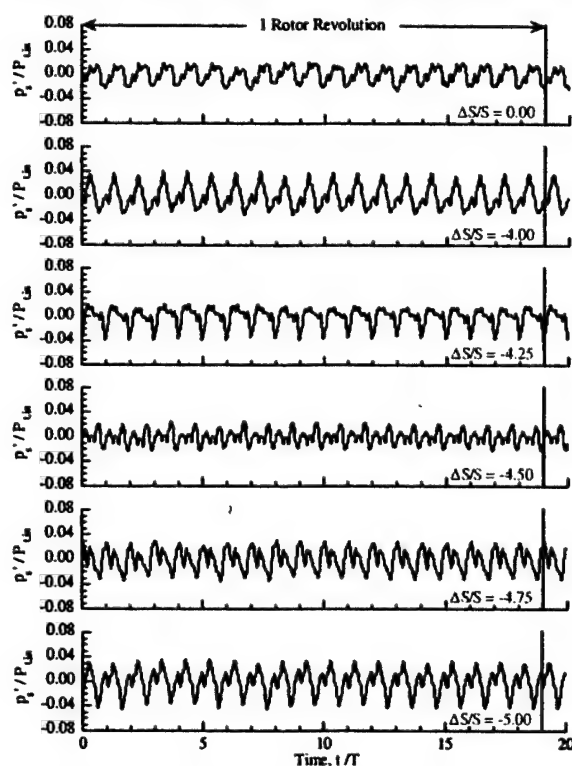

Figure 19. Circumferential variation in transonic rotor wake unsteady static pressure

Stator Unsteady Aerodynamic Response

The vane surface phase-lock averaged unsteady pressure envelopes along with the time-average pressure distributions for the subsonic and transonic rotor operating conditions are shown in Figure 20. For the subsonic rotor speed, the pressure fluctuations on the vane suction surface are smallest at the leading edge and increase to a maximum at 30% chord, which corresponds to approximately the point at which the steady pressure gradient switches from favorable to adverse. The pressure fluctuations remain relatively constant between 30% and 80% chord, and then begin to decrease aft of 80% chord as the trailing edge is approached, with the maximum peak-to-peak pressure fluctuations around 3% of the compressor inlet total pressure. The magnitude of the pressure surface unsteadiness, however, is nearly constant across the entire chord, with the peak-to-peak pressure fluctuations as large as 3.6% of the inlet total pressure.

At the transonic rotor speed, the deeper rotor wake velocity deficits cause the periodic unsteadiness to increase significantly on both vane surfaces (note the difference in scales for the two rotor speeds). The vane suction surface unsteadiness is now highest in the leading edge region and decreases with chordwise distance. The suction surface unsteadiness is again considerably reduced aft of 30% chord, which corresponds approximately to the location at which the steady pressure gradient changes from favorable to adverse. These pressure fluctuations are very significant, with the peak-to-peak amplitudes as large as 10.3% of the compressor inlet total pressure in the leading edge region and decreasing to around 4% in the aft region of the vane.
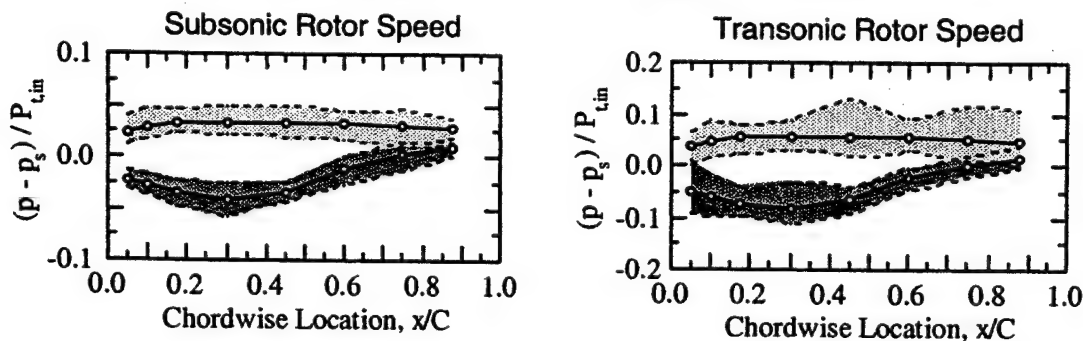
Figure 20. Stator unsteady surface pressure envelopes

The unsteadiness on the vane pressure surface at the transonic rotor operating condition follows a noticeably different trend than that which occurred at the subsonic rotor speed. Here the pressure fluctuations increase significantly from the leading edge and reach a maximum at 45% chord. Notice that the unsteadiness at this chordwise location is higher than that which occurs on the vane suction surface, with the peak-to-peak pressure fluctuations as large as 11.3% of the compressor inlet total pressure. Aft of this location, the unsteadiness attenuates slightly but is still very significant along the aft half of the vane.

The steady vane incidence is nearly the same for both the transonic and subsonic rotor speeds (-6.5° versus -7.1°). However, the rotor wake characteristics are markedly different for the two speed regimes, with the subsonic rotor wakes narrow compared to the blade pitch while the transonic rotor wakes have much broader and deeper profiles

that are nearly sinusoidal in character. The impact of this on the vane response is twofold. First, the incidence angle fluctuations are much more severe at the transonic rotor speed, resulting in higher levels of periodic unsteadiness on both vane surfaces relative to those at the subsonic rotor speed. At part-speed, the stator incidence angle fluctuates from $-15.0°$ to $+1.9°$ while at the transonic rotor speed the stator incidence angle fluctuates from $-29.8°$ to $+2.4°$ over one rotor revolution. Thus, the transonic rotor wakes cause highly negative incidence angle swings that result in a high level of periodic unsteadiness on the pressure surface of the vane.

The wake character also has a marked impact on the vane response due to unsteady phenomena associated with the intra-stator transport of the chopped rotor wake segments. In the stator reference frame, the rotor wakes have a slip velocity relative to the mean flow that causes the low momentum wake fluid to migrate across the vane passage and accumulate on the vane pressure surface as the chopped wake segments are convected downstream, Figure 21.

The transonic rotor wakes are much broader and deeper than those associated with subsonic rotor flow, which results in more low momentum wake accumulating on the stator pressure surface during this transport process due to the higher slip velocity in the wake regions. The interaction of this low momentum wake fluid with the airfoil boundary layer thus results in significantly higher levels of pressure surface unsteadiness at the transonic rotor operating condition. The particle image velocimetry (PIV) data presented in Part I of this paper confirm this phenomena, and quantifies the stator vane-to-vane flow field differences at the subsonic and transonic rotor speeds which lead to vane response differences noted herein.
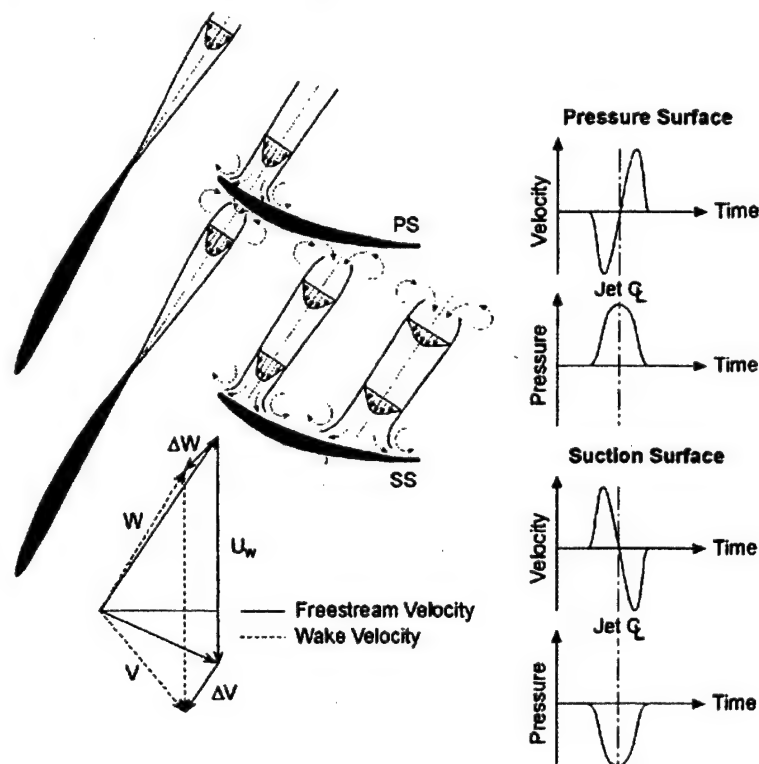
Figure 21. Intra-stator transport of chopped rotor wake segments

To gain insight into the evolution of the wake-generated periodic unsteadiness on the vane surfaces, the time-variant chordwise pressure distributions generated over one periodic cycle are examined. At the subsonic rotor speed, the time-variant vane surface pressure distributions for both vane surfaces resemble the time-average loading distributions throughout the cycle, with the entire surface of the vane responding to the incidence change resulting from the passing of the rotor wakes at each time instant, Figure 22. This behavior indicates that the vane response is mainly due to the time-variant airfoil circulation distribution resulting from the incidence fluctuations generated by the passing of the rotor wakes. Also notice that the pressure and suction surface responses are almost $180°$ out-of-phase with one another, with the minimum and maximum pressure difference across the chord occurring at approximately $t/T=0.2$ and $t/T=0.7$ respectively.
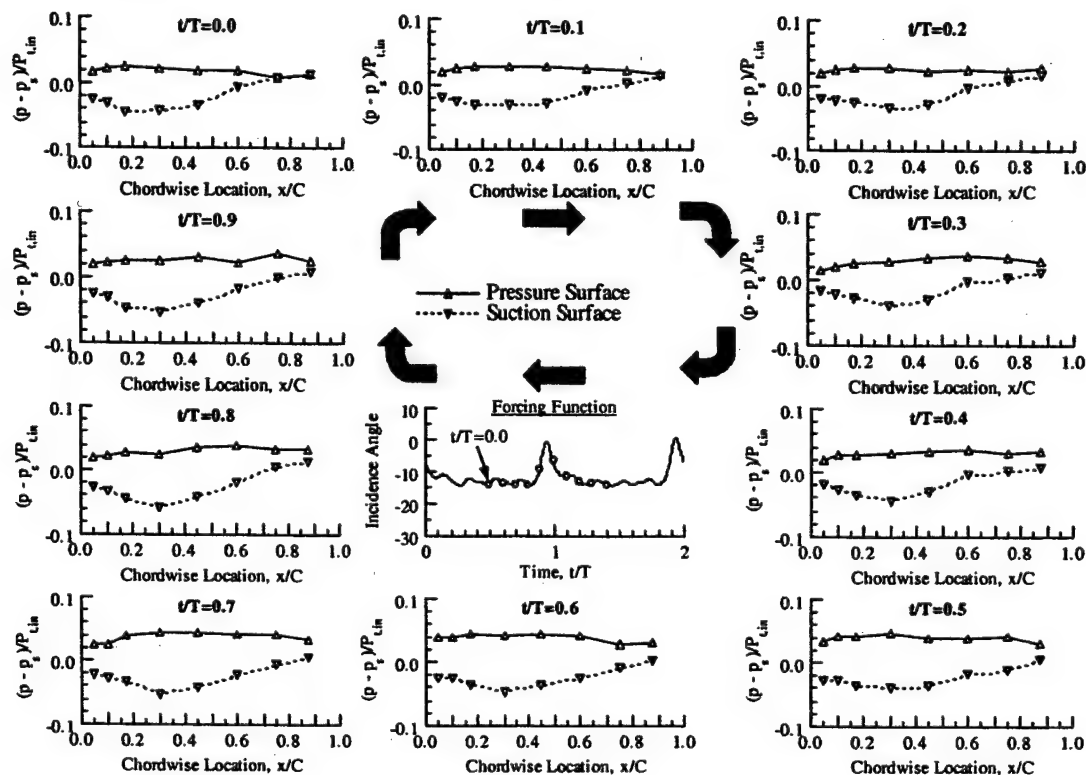
Figure 22. Time-variant stator loading at subsonic rotor speed

Figure 23 presents analogous results for the transonic rotor operating condition. At $t/T=0.5$ there are two local depressions in the pressure surface loading at 30% and 75% chord. These depressions are due to the chopped transonic rotor wake segments collecting on the vane pressure surface as they are transported through the vane passage. The rotor wake segments act as "negative jets" after they are chopped by the downstream stator vanes due to the wake slip velocity. As the wake fluid is transported from the suction to the pressure side of the passage, it creates a low-pressure region on the suction surface of the airfoil and a high-pressure region on the pressure surface at the impingement location. Two counter rotating vortices are generated on each side of the

high-pressure region as the wake fluid interacts with the pressure surface of the vane at the impingement location. A similar set of counter rotating vortices are generated near the low pressure region on the suction surface of the airfoil as high momentum free stream fluid replaces the low momentum wake fluid that has migrated toward the pressure surface of the vane.

These vortices are an additional source of unsteadiness for both airfoil surfaces, with their low-pressure cores causing local depressions in the surface pressure distribution on each side of the chopped wake segments as they are transported through the vane passage. The PIV data presented in Part I of this paper confirm that vortical flow structures are generated by the migration of the low momentum wake fluid across the vane passage, with these vortices convected along the vane pressure surface by the mean flow. It should be pointed out that these vortices are generated by nonlinear effects associated with the migration of wake fluid across the vane passage, with their presence not accounted for in linearized analyses which utilize the frozen gust assumption.
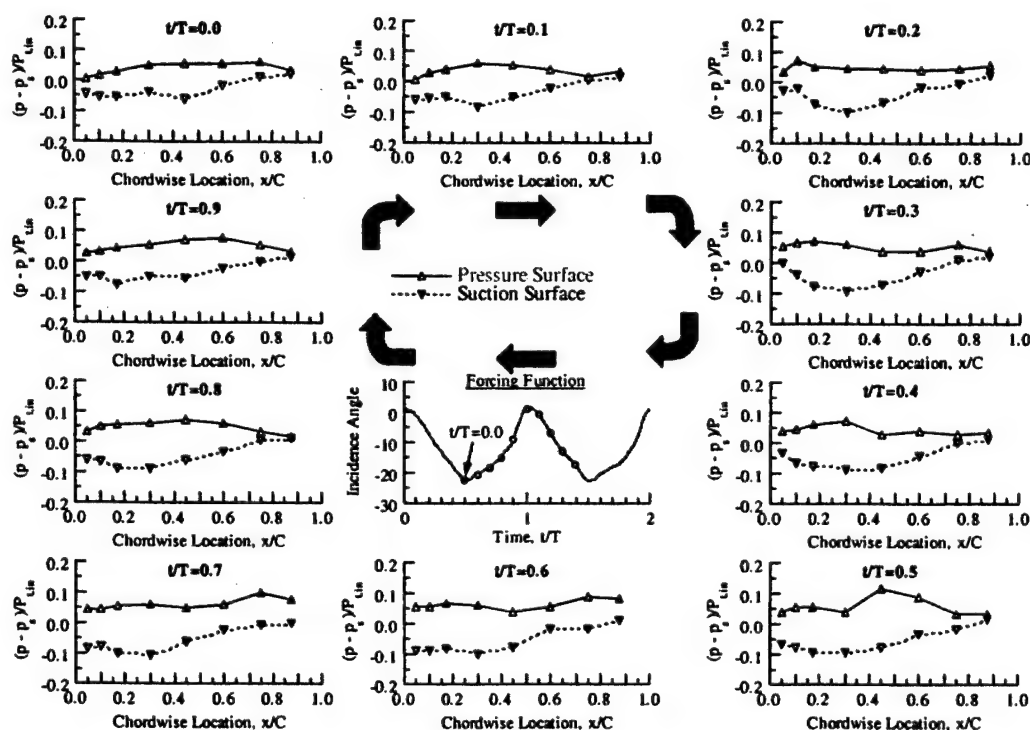
Figure 23. Time-variant stator loading at transonic rotor speed

As the cycle progresses, the low-pressure troughs due to the vortex cores on each side of the chopped wake segment are convected downstream with the mean flow. Notice however, that distinct troughs are not present at each and every time instant. This may be an artifact of displaying the instantaneous loading at only ten discrete time instants, with significant changes also occurring during the time instants that were not displayed. Additionally, the chopped wake segments interact with the pressure surface boundary layer as the wakes collect on the pressure surface, with more and more low momentum wake fluid entrained within the boundary layer as the wakes convect further downstream. This process is highly nonlinear and dominated by viscous effects, with flow field

structures having time scales different from blade-passing events possibly generated by these interactions that are removed by the phase-lock averaging process. This interaction phenomenon was not evident at the part-speed operating conditions due to the narrow subsonic rotor wakes having a much lower velocity deficit and hence slip velocity.

Notice that the effects of the low-pressure vortex cores are not evident in the vane suction surface loading distributions. Here the entire suction surface loading distribution is smooth at all ten time instants and there is no indication of the counter rotating vortices being convected along the suction surface of the vane. This may be due to the suction side vortices being generated away from the vane surface. Once the wake segment is chopped by the leading edge of the airfoil, the wake fluid begins its migration toward the pressure surface of the vane. This may cause the suction side vortices to be generated further and further away from the vane suction surface as the wakes convect downstream, which may be enhanced by the fact that the present airfoils are front-loaded. Thus, the vortices do not affect the suction surface loading and the character of the suction surface pressure distribution more closely resembles that which occurs at the subsonic rotor speed, which is in sharp contrast to the pressure surface unsteadiness.

Notice also that the interaction of the rotor wakes with the vane row results in the generation of a pressure wave in the trailing edge region that propagates upstream along the suction surface of the vane as the cycle progresses. This wave was not present at the part-speed subsonic rotor operating condition and its effects are superimposed on the unsteady loading induced by the time-variant circulation distribution, with this pressure wave first evident along the aft region of the suction surface at t/T=0.6. The suction surface loading changes noticeably as this wave propagates upstream along the chord between t/T=0.6 and t/T=0.2, at which point the suction surface loading distribution remains similar throughout the remainder of the cycle.

Stator Vane-to-Vane Flow Field

The time-variant downstream stator mid-span vane-to-vane flow field is measured using PIV, with ensemble averaged snapshots of the periodic unsteady flow field generated by rotor-stator interactions presented for ten equally spaced increments over one blade-passing period. The time-average of the unsteady flow field is also presented, with this vector field calculated by arithmetically averaging the ensemble averaged flow field over one complete interaction cycle. Since it was not possible to obtain valid data at every point in the flow field, the time-average is calculated only for interrogation regions that had valid velocity vectors at all ten time instants.

The time-average stator mid-span Mach number contours are shown in Figure 24 for the subsonic and transonic compressor operating conditions respectively. These time-average PIV data are in excellent agreement with the steady surface Mach number distributions. Specifically, the steady surface Mach number distributions for the subsonic rotor speed indicate that the average inlet and exit Mach numbers are 0.30 and 0.25 respectively, with the pressure surface Mach number nearly constant at 0.23 and the suction surface Mach number peaking at 0.38 at 30% chord. At the transonic rotor speed, the average inlet and exit Mach numbers determined from the pneumatic surface pressure data are 0.39 and 0.34, with the pressure surface Mach number nearly constant at 0.30

and the suction surface Mach number peaking at 0.51 at 30% chord. These values are in excellent agreement with the time-average PIV data for both rotor speeds.
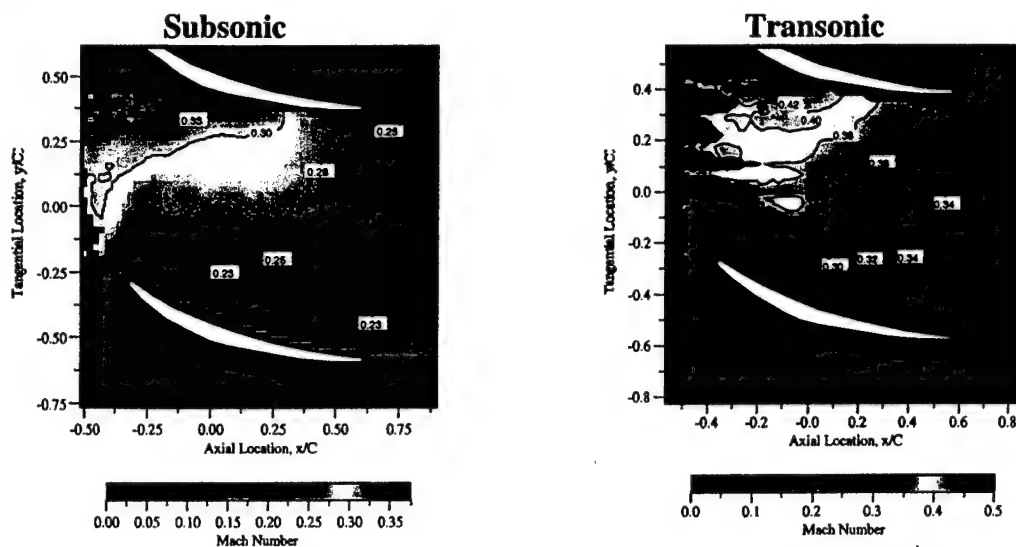
Figure 24. Time-average stator flow field at subsonic rotor speed

Two unsteady flow phenomena occur as the rotor wakes are chopped and transported through the downstream stator passages. First, the circulation around the stator vanes enhances the decay rate of the rotor wakes due to an inviscid straining of the wake fluid as the chopped wake segments are convected downstream, Figure 25. For an incompressible inviscid two-dimensional flow, Kelvin's theorem requires that the circulation associated with the incoming wake segment remain constant as it is transported through the vane passage. Thus, the length of the chopped wake segment increases and its width is reduced as it convects downstream to maintain the same vorticity. Since the velocity deficit is proportional to the width of the wake for a fluid with constant vorticity, the straining of the wake fluid by the vane row potential field causes the chopped wake segments to decay faster than they would behind an isolated blade row. This inviscid straining occurs in addition to viscous dissipation and is commonly referred to as wake recovery, which is a reversible process that reduces the viscous mixing losses.

Second, the low momentum rotor wake fluid has a slip velocity relative to the free stream that causes it to drift across the vane passage and accumulate on the vane pressure surface as the chopped rotor wake segments are transported downstream, Figure 26. This slip velocity causes the low momentum rotor wake fluid to drift across the vane passage and collect on the airfoil pressure surface as the chopped wake segments are transported downstream. This results in a local broadening of the wake segment near the pressure surface and a thinning near the suction surface due to "negative jet" effects. Recirculating flow patterns are also generated as high momentum free stream fluid is drawn into the chopped wake segment near the suction surface to replace the low momentum wake fluid that has drifted across the passage. As the low momentum rotor wake fluid accumulates on the vane pressure surface, it will interact with the airfoil boundary layer and eventually end up appearing in the stator wake regions.
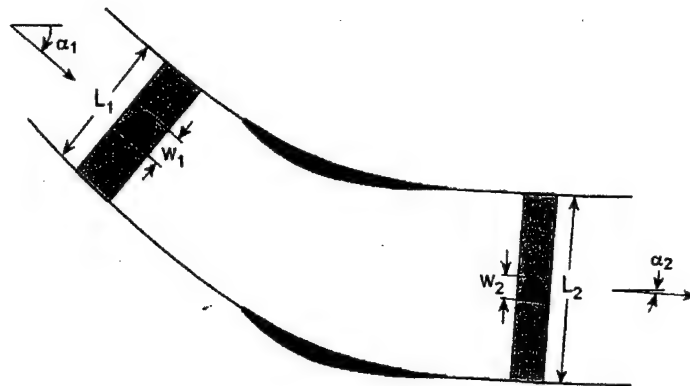
Figure 25. Inviscid wake recovery process for a stator row
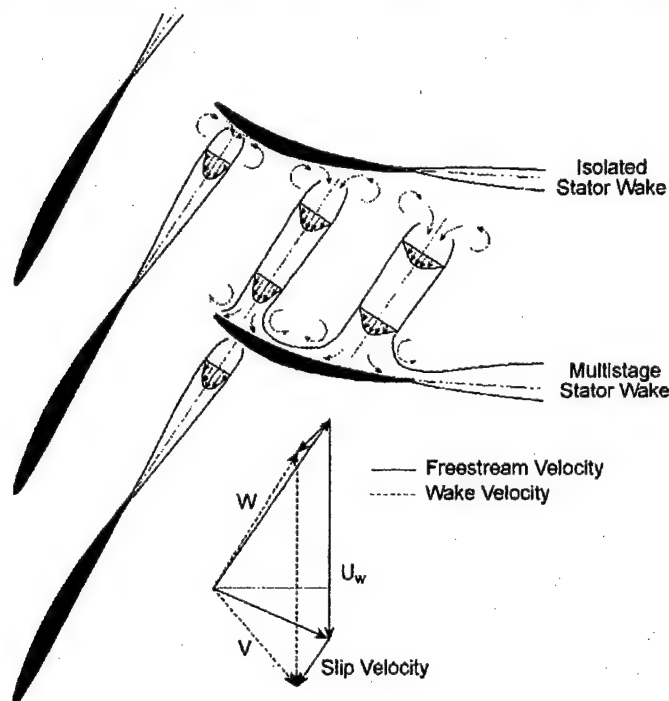
Figure 26. Intra-stator transport of chopped rotor wake segments

These unsteady phenomena are investigated by examining the downstream stator time-variant mid-span vorticity and axial Mach number contours at ten time instants over one blade-passing period. The time-variant vorticity field is shown in Figures 27 and 28 for the subsonic and transonic rotor speeds respectively. The vorticity is calculated from the ensemble averaged velocity using central differencing and is normalized by the compressor inlet stagnation speed of sound and stator chord length, with the calculation performed only if there are valid velocity vectors present for all four neighboring interrogation areas. The shear flow in the rotor wake causes the vorticity to be negative on the suction side of the wake and positive on the pressure side. Thus, the chopped wake segments appear as alternating bands of positive and negative vorticity that extend across the vane passage and are convected downstream with the mean flow.

The reduced frequency is defined as the ratio of the time it takes a fluid particle to convect through the vane row to the time scale of the wake-generated unsteadiness.

Thus, this parameter provides an indication of the number of chopped wake segments residing within the vane passage at any given instant in time. The reduced frequencies based on the mass averaged mid-span stator inlet velocity are 2.42 and 2.45 for the subsonic and transonic rotor speeds respectively, indicating that it takes approximately 2.5 blade-passing periods for one chopped wake segment to be completely transported through the vane row.
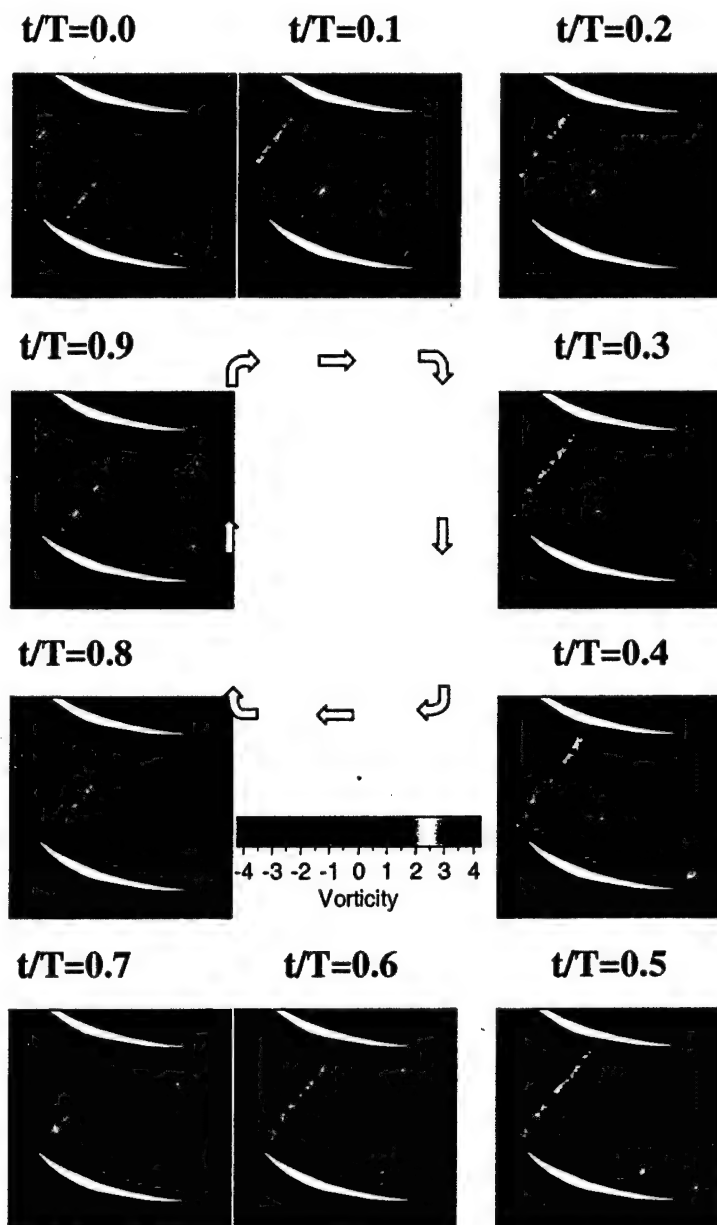
Figure 27. Time-variant stator vorticity at subsonic rotor speed
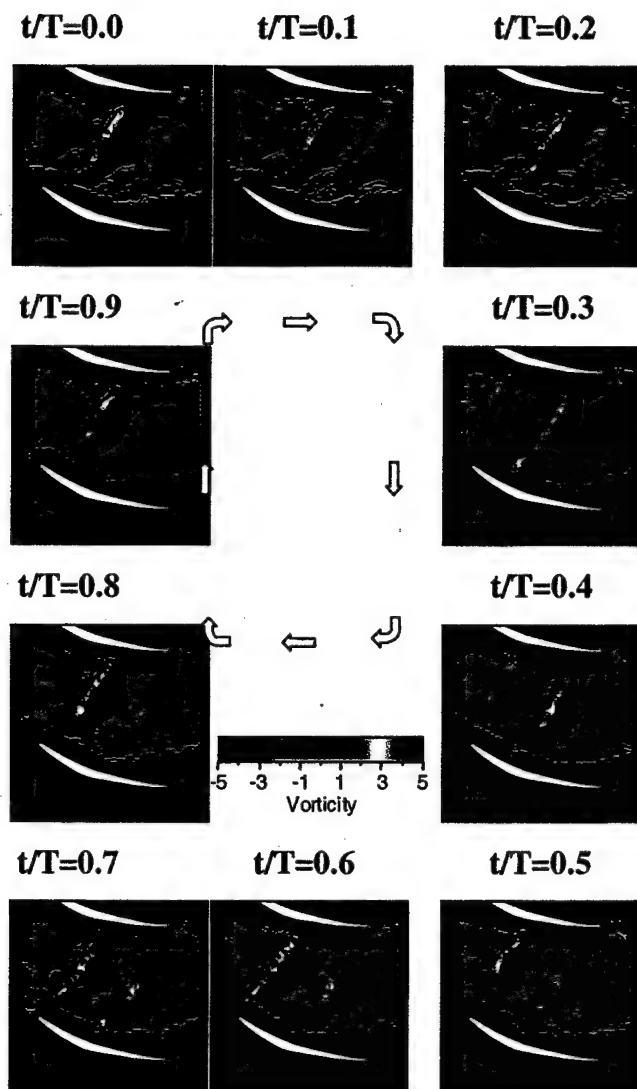
Figure 28. Time-variant stator vorticity at transonic rotor speed

For both rotor speeds, the rotor wake is in the process of being cut by the lower vane between t/T=0.5 and t/T=0.8. Notice that this wake was cut by the upper vane in the passage at an earlier time, with the blade-vane count ratio setting the spatial periodicity of the wake chopping and transport process. For the present geometry with 19 rotor blades and 18 stator vanes, the interblade phase angle is 380°. Thus, the rotor wake was cut by the upper vane 1.06 blade-passing periods earlier, with the resulting unsteady flow in the vane passage periodic at blade-pass frequency.

After being cut by the vane, the chopped wake segment acts a "negative jet", with the slip velocity in the wake region causing low momentum wake fluid to drift across the vane passage and collect on the pressure surface as it convects downstream. The effects of this are first visible at t/T=0.8 for both rotor speeds, with the chopped wake segment becoming noticeably broader along the pressure surface of the lower vane and thinner near the suction surface of the upper vane in the passage. Both viscous dissipation and the inviscid straining of the wake fluid by the vane row potential field cause it to decay as

it is transported through the vane passage, with the vorticity of the wake segment thus reduced as the cycle progresses.

The subsonic rotor wakes decay very rapidly after they are chopped and ingested into the stator passage. This decay is evident by examining the vorticity contours for the first chopped wake segment between $t/T=0.8$ and $t/T=0.2$, with the dispersion of the chopped wake segment very noticeable. The chopped wake segment continues to disperse as the cycle progresses, with both the wake width increasing and the vorticity decreasing considerably by the time it exits the stator passage 2.5 blade-passing periods after being initially cut. Note however, that even though the subsonic rotor wakes decay considerably as they are chopped and transported through the stator, the chopped rotor wake segments are still clearly evident downstream of the stator trailing edge.

The chopped rotor wakes appear to disperse much more rapidly at the transonic rotor speed, and are not evident downstream of the stator trailing edge as they were for the subsonic compressor operating condition. This result is surprising considering that the transonic rotor wakes are much larger than those generated by subsonic flow, with the transonic rotor wake velocity deficit 25.7% of the free stream relative Mach number versus 15.2% at the subsonic rotor speed. Thus, it might be expected that the transonic rotor wakes would persist for longer distances downstream of the rotor. However, the reasons for the more rapid decay of the rotor wakes at the transonic rotor speed are due to unsteady flow effects. Specifically, the slip velocity in the rotor wakes causes low momentum fluid to drift across the stator passage as the chopped wake segments are transported downstream, with this rotor wake fluid accumulating on the vane pressure surface and thus appearing in the stator wake regions during the transport process. This unsteady intra-stator wake transport process is more significant at the transonic rotor speed due to the much deeper and broader rotor wakes generated by transonic compressor operation.

This intra-stator wake transport process is further investigated by examining the axial Mach number contours for the subsonic and transonic rotor speeds, Figures 29 and 30 respectively. Notice that the low velocity regions associated with the chopped wake segments do not extend across the entire passage as did the vorticity contours, with this evident in the data for both rotor speeds. This is due to the wake segments being cut by the upper vane 1.06 blade-passing periods earlier, with a significant portion of the low momentum wake fluid drifting toward the pressure surface during this time. Also recall that the chopped wake segments act as "negative jets" as they are transported downstream. Thus, high momentum free stream fluid is drawn into the wake segments on the suction side of the passage to replace the low momentum wake fluid that has drifted toward the pressure surface during this time interval. It is this transport process which causes the low velocity regions to be concentrated only on the pressure side of the passage.
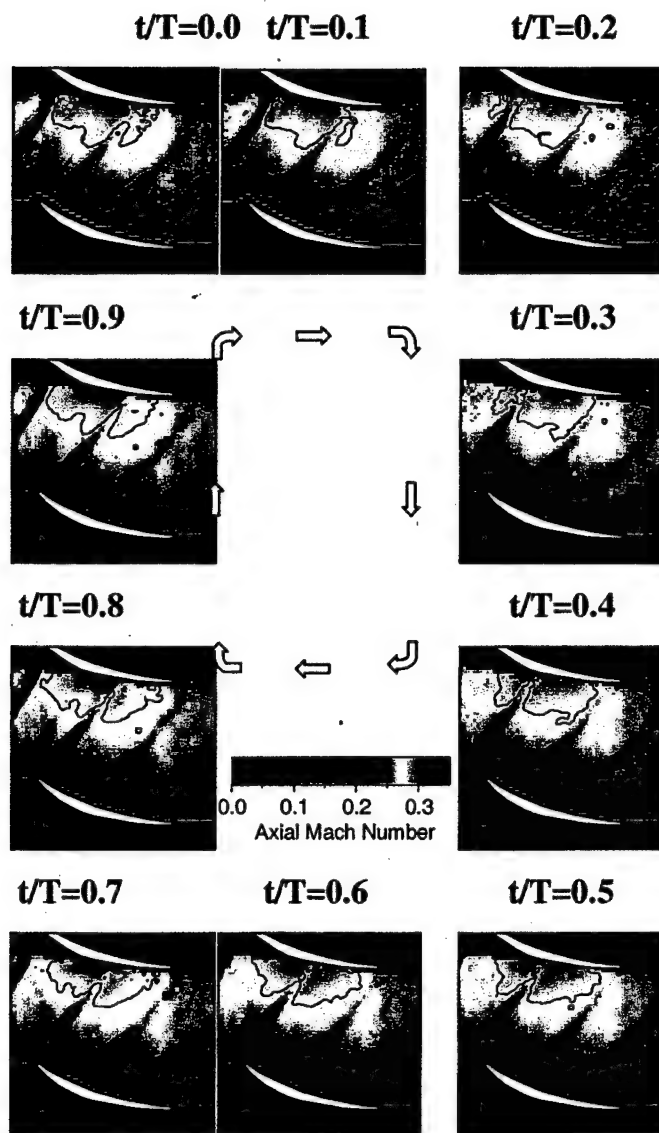
Figure 29. Time-variant stator axial mach number at subsonic rotor speed
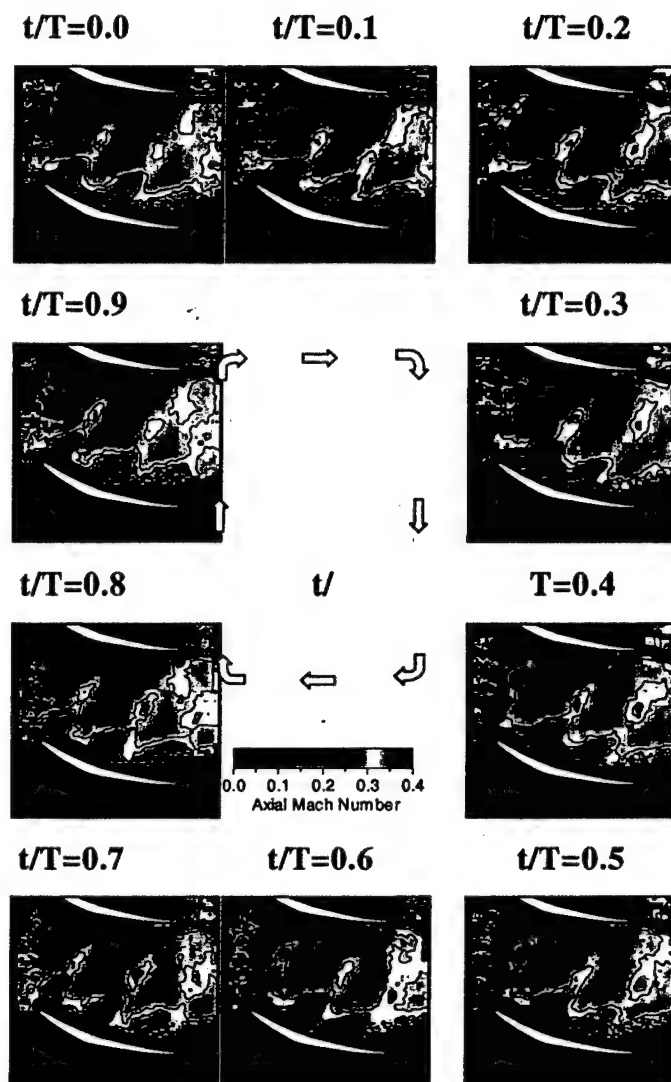
Figure 30. Time-variant stator axial mach number at transonic rotor speed

At the subsonic rotor speed, the low velocity regions associated with the chopped wake segments are superimposed on the steady flow field, with the time-variant flow field outside of the wake regions very similar to the time-average flow field at each time instant. Additionally, very little low momentum rotor wake fluid accumulates on the stator pressure surface as the chopped wake segments are transported through the vane row. This is consistent with the surface pressure data presented which show the convection of the chopped wake segments through the vane passage have a low order effect on the vane response at the subsonic rotor operating condition. In fact, the stator response at this operating condition is mainly due to changes in the airfoil circulation distribution due to the incidence change associated with the passing of the rotor wakes.

This is not the case for the transonic rotor speed, in which the higher slip velocity in the rotor wakes causes a significant amount of low momentum wake fluid to accumulate on the vane pressure surface as the chopped wake segments convect downstream, Figure 14. Also notice that distinct low velocity regions associated with the

various chopped wake segments are only evident in the leading edge region at the beginning of the wake chopping cycle between t/T=0.5 and t/T=0.1. For times t/T=0.2 to t/T=0.5, the low velocity regions of the two adjacent chopped wake segments have begun to merge and encompass a significant portion of the airfoil pressure surface. This is due to the chopped wake segments becoming broader as they convect further downstream, with more and more low momentum wake fluid accumulating on the vane pressure surface as the cycle progresses. This is again consistent with the surface pressure data presented in Part II of this paper, with the intra-stator transport of the chopped rotor wake segments through the vane passage significantly impacting the character of the vane pressure surface response at the transonic rotor speed.

To examine the detailed unsteady flow field generated by the accumulation of low momentum rotor wake fluid on the stator vane pressure surface at the transonic rotor speed, PIV images were also acquired focusing on the pressure surface leading edge flow field. The wake migration process is depicted in Figure 31, which shows the unsteady velocity vectors superimposed on the time-variant axial Mach number contours for the transonic rotor operating condition. This unsteady velocity field was calculated by subtracting the time-average velocity and shows how the steady flow field is perturbed at each time instant during the wake chopping cycle.

The slip velocity is largest prior to the wake being cut by the vane (t/T=0.4). Once the wake has been cut, this slip velocity causes the low momentum rotor wake fluid to accumulate on the airfoil pressure surface as the chopped wake segment is transported downstream. Notice that the wake slip velocity is reduced as the cycle progresses and the chopped wake segment is convected further downstream. This is due to both viscous dissipation and wake recovery effects enhancing the rotor wake decay rate, as can be seen by examining the length of the velocity vectors in the wake region as the cycle progresses onward from t/T=0.5.

As the wake fluid collects on the vane pressure surface, counter-rotating vortices that are evident throughout the entire cycle are generated near the airfoil. These vortices are convected downstream along with the chopped wake segments and are an additional source of unsteady aerodynamic excitation to the stator vanes. Recirculating flow patterns are also established away from the vane surface on each side of the chopped wake segment as high momentum free stream fluid is drawn into the wake region to replace the low momentum wake fluid which has migrated toward the airfoil pressure surface. Also notice that these vortices actually appear to distort the chopped wake segment. This distortion, however, may be an artifact of a large radial velocity component in the convected wake regions that cannot be measured using conventional two-dimensional PIV techniques that only measure the axial and tangential velocity components. These three-dimensional effects may also be responsible for the lack of data near the vane pressure surface, with the radial velocity component at the impingement point on the airfoil surface probably significant.

t/T=0.0 t/T=0.1 t/T=0.2

t/T=0.9 t/T=0.3

t/T=0.8 t/T=0.4

0.0 0.1 0.2 0.3 0.4
Axial Mach Number

t/T=0.7 t/T=0.6 t/T=0.5
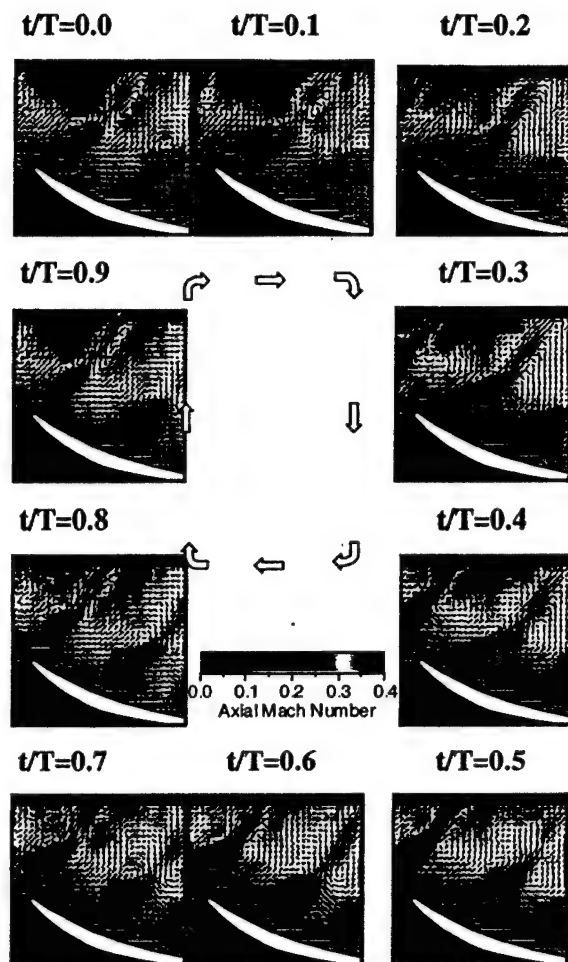
Figure 31. Unsteady stator pressure surface velocity vectors at transonic rotor speed

Conclusions

Two unsteady flow phenomena occurred as the rotor wakes were chopped and transported through the downstream stator passages. First, the circulation around the stator vanes enhanced the decay rate of the rotor wakes due to an inviscid straining of the wake fluid as the chopped wake segments were transported through the vane row. This inviscid stretching, or wake recovery, occurred in addition to viscous dissipation and enhanced the rotor wake decay rate. Second, the chopped rotor wake segments acted as "negative jets" after being cut by the downstream vanes. This was due to the slip velocity in the wake region causing low momentum wake fluid to drift across the stator passage and collect on the vane pressure surface as the chopped rotor wake segments were transported through the vane row.

The rotor wakes decayed very rapidly after they were chopped and ingested into the downstream stator passage, but were still evident downstream of the vane trailing edge for the subsonic rotor operating condition. This was not the case at the transonic rotor speed, in which the chopped rotor wakes dispersed much more rapidly and were no longer evident by the time they reached the stator exit. This increased decay rate was due

to the much higher levels of unsteadiness at the transonic operating condition. In fact, even though the rotor wakes were much deeper at the transonic rotor speed, the higher slip velocity in the wake region caused more low momentum fluid to drift across the stator passage and accumulate on the vane pressure surface as the chopped rotor wake segments were transported downstream.

As the low momentum wake fluid collected on the vane pressure surface, counter-rotating vortices were generated on each side of the chopped wake segment. These vortices were convected downstream by the mean flow and acted as an additional source of unsteadiness to the vane pressure surface. It should be noted that the presence of these vortices are not accounted for in linearized analyses that utilize the frozen gust assumption since they are generated by a nonlinear process. These interaction phenomena were not evident in the PIV data at the part-speed compressor operating conditions due to the subsonic rotor wakes having a much lower velocity deficit and hence slip velocity, with the intra-stator wake transport process dominated by the convective action of the inviscid free stream flow at the subsonic rotor speed.

Finally, since the rotor wake fluid ultimately tends to appear in the stator wake regions, the characteristics of the wake-generated forcing function to a downstream rotor in a multistage compressor would be significantly impacted by this unsteady intra-stator wake transport process. Thus, these multi-blade row interaction effects must be accounted for to accurately predict the forced response characteristics of multistage turbomachinery.

Rotor speed had a marked impact on the characteristics of the wake generated forcing function to the downstream stator. The subsonic rotor wakes generated at the part-speed compressor operating condition were characterized by narrow wake profiles relative to the blade pitch with moderate velocity deficits. Transonic rotor operation resulted in much broader and deeper wake profiles that were nearly sinusoidal in character. This was due to off-design operation of the current rotor. In the absolute reference frame of the downstream stator, the passing of the rotor wakes caused significant fluctuations in the incidence angle to the downstream vane row for both rotor speed regimes, with the fluctuations in the absolute inlet Mach number much smaller in comparison.

Significant static pressure fluctuations were also measured at the stator inlet which were attributed to the spinning acoustic modes generated by both rotor-IGV and rotor-stator interactions. The spatial periodicity of these acoustic interactions was over the entire annulus of the machine due to the unequal numbers of blades and vanes in the compressor, with the amplitude of the acoustic excitation to the downstream stator varying from vane-to-vane around the compressor annulus. This spatial variation was due to the superposition of the infinite number of modes that occur in the near field at harmonics of blade-pass frequency but travel at different phase speeds as they spiral around the compressor annulus, with the degree of interference dependent upon circumferential position.

The steady vane incidence was nearly the same for both the subsonic and transonic rotor speeds, with the steady stator mid-span surface pressure distributions

nearly scaling with the change in rotor speed squared. The stator unsteady aerodynamic response was, however, significantly different for the two rotor speed regimes due to the markedly different rotor wake characteristics associated with transonic rotor operation. For the subsonic rotor speed, the downstream stator unsteady aerodynamic response was mainly due to changes in the airfoil circulation distribution, with the maximum pressure fluctuations occurring at nearly the same instant in time across the entire chord. Here, the velocity fluctuations associated with the convection of the chopped wake segments through the vane passage had small order effect on the vane response.

This was not the case for the transonic rotor speed in which unsteady phenomena associated with the intra-stator transport of the chopped rotor wake segments were significant. In the stator reference frame, the rotor wakes have a slip velocity relative to the mean flow that causes the low momentum wake fluid to migrate across the vane passage and accumulate on the vane pressure surface as the chopped wake segments are transported downstream. The transonic rotor wakes were much broader and had a higher slip velocity than those associated with subsonic rotor operation, which resulted in more low momentum wake accumulating on the stator pressure surface during this transport process.

The interaction of the transonic rotor wakes with the downstream vane row also resulted in the generation of an upstream propagating pressure wave in the vane trailing edge region. This pressure wave propagated upstream along the vane suction surface as the cycle progressed, with its effects superimposed on the unsteady loading induced by the time-variant circulation distribution. The suction surface loading changed noticeably as this wave propagated upstream along the airfoil chord. This phenomenon was not evident at the subsonic rotor speed, in which the vane response was predominantly due to changes in the airfoil circulation resulting from the incidence angle fluctuations associated with the passing of the rotor wakes.

STEADY LOADING EFFECTS ON ROTOR-STATOR INTERACTIONS

Rotor Wake Generated Forcing Function

The rotor wakes are the primary unsteady aerodynamic excitation to the downstream stator. The rotor wake velocity deficit causes the absolute velocity and flow angle to the stator vanes to fluctuate over a blade-passing period. Rotor-IGV and rotor-stator interactions also result in the generation of spinning acoustic modes at blade-pass frequency harmonics that propagate both upstream and downstream. The unsteady aerodynamic forcing function to the downstream stator is thus characterized by measurements of both the rotor wake velocity deficits and the unsteady static pressure fluctuations at the stator inlet.

The effect of steady compressor loading on the rotor wake generated forcing function is shown in Figures 32-34. Presented are the rotor relative Mach number, relative flow angle, and unsteady static pressure normalized by the inlet total pressure for one complete rotor revolution. The transonic rotor wakes are very broad and deep for all three operating conditions, with their circumferential extent spanning almost the entire rotor passage, Figure 32. These characteristics are due to off-design operation of the current rotor which features subsonic NACA 65 series airfoil profiles. The transonic

rotor wake velocity deficits for all three loading conditions are very large, with the average wake deficit 25.4% of the free stream Mach number at the low, 25.7% at the nominal, and 32.2% at the highly loaded operating conditions. Also, there is significant blade-to-blade wake variability. This is most notable at the lowest loading condition since this is where the rotor is most off-design, i.e., the rotor inlet Mach number is highest. Also note that the blades which generate the largest and smallest wakes change with compressor loading indicating that the wake variability is aerodynamic in origin.
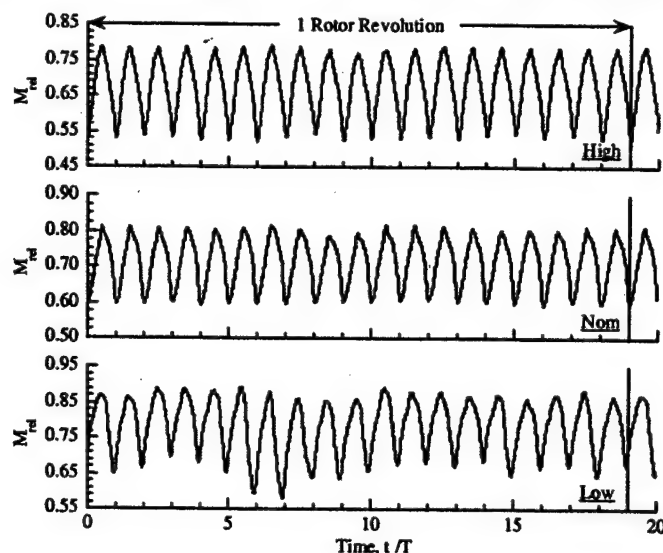
Figure 32. Steady loading effect on rotor wake relative Mach number

The rotor wake relative flow angle fluctuations are shown in Figure 33. The under-turning in the wake region increases as the compressor loading is increased, with the maximum rotor relative exit flow angle fluctuations across the wake 4.1°, 4.6°, and 7.3° for the low, nominal, and highly loaded operating conditions. Significant blade-to-blade differences are also evident.
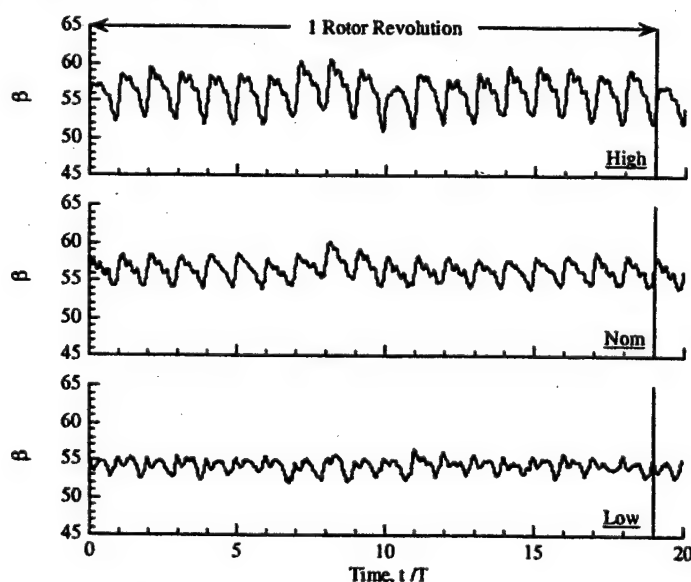
Figure 33. Steady loading effect on rotor wake relative flow angle

Figure 34 presents the unsteady static pressure fluctuations at the stator inlet as a function of compressor loading, with sharp pressure fluctuations associated with the passing of the 19 rotor blades clearly visible. These static pressure fluctuations are attributed to the spinning acoustic modes generated by both rotor-IGV and rotor-stator interactions and represent a significant source of unsteady aerodynamic excitation to the downstream stator vanes. Additionally, since the probe is in the rotor-stator inter-stage region, both the downstream propagating rotor-IGV interaction modes as well as the upstream propagating rotor-stator modes are contained in the data since both sets of modes occur at blade-pass frequency harmonics.
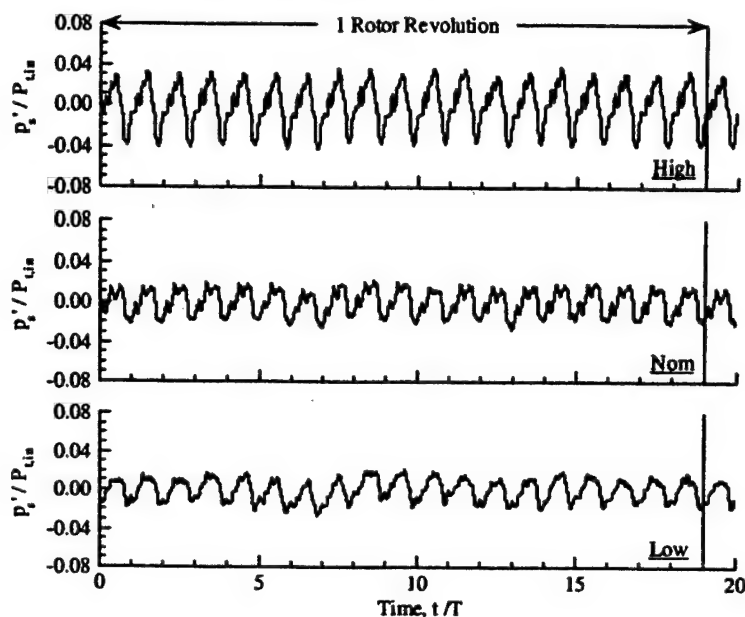
Figure 34. Steady loading effect on rotor wake unsteady static pressure

Stator Unsteady Aerodynamic Response

Figure 35 displays the corresponding phase-lock averaged stator unsteady surface pressure envelopes for the low, nominal, and highly loaded compressor operating conditions. For all three loading conditions, the vane suction surface unsteadiness is highest in the leading edge region and decreases with chordwise distance. At the low and nominal operating conditions, the unsteadiness is considerably reduced aft of 45% chord, which corresponds approximately to the location at which the steady pressure gradient changes from favorable to adverse. These pressure fluctuations are very significant, with the peak-to-peak amplitudes as large as 9.6% and 10.3% of the compressor inlet total pressure in the leading edge region and decreasing to around 4% in the aft region of the vane for the low and nominal loading conditions respectively. The chordwise attenuation of the unsteadiness is much less pronounced at the high loading condition.
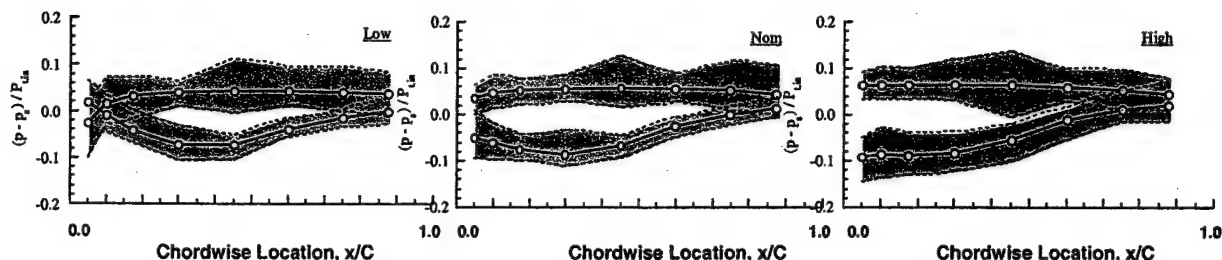
Figure35. Unsteady stator surface pressure envelope

The unsteadiness on the vane pressure surface follows a noticeably different trend than that noted for the suction surface. Here the pressure fluctuations increase significantly from the leading edge and reach a maximum at 45% chord for all three loading conditions. Notice that the periodic unsteadiness at this chordwise location is considerably higher than that which occurs on the vane suction surface. Aft of this location, the unsteadiness attenuates slightly but is still very significant. Also note that much higher levels of unsteadiness are generated in the vane leading edge region for the low operating line due to the highly negative incidence angle variations.

Time-Variant Stator Flow Field

The effect of steady loading on the time-average stator mid-span Mach number contours is shown in Figure 36, with this vector field calculated by arithmetically averaging the phase-lock averaged PIV data over one complete rotor-stator interaction cycle. As the compressor flow rate is reduced and the loading increases, a low velocity region forms on the pressure surface of the vane. This low velocity region first becomes evident at the nominal operating condition and is even more significant at the highly loaded condition. It will be shown that this low velocity region forms as a result of unsteady flow processes associated with the transport of the chopped rotor wake segments through the vane passage.

Low Loading   **Nominal Loading**   **High Loading**
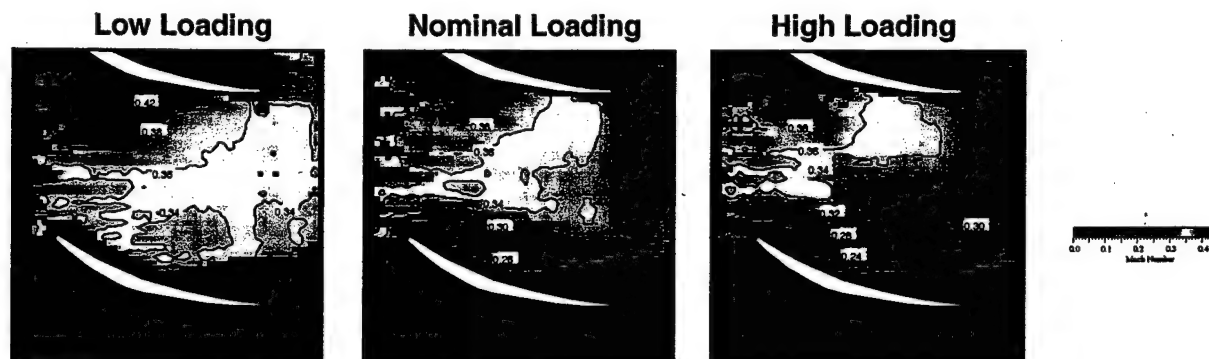
Figure 36. Compressor loading effect on time-average absolute Mach number

The time-variant vorticity field at a time instant for all three loading conditions is shown in Figure 37. The shear flow in the rotor wake causes the vorticity to be negative on the suction side of the wake and positive on the pressure side. Thus, the chopped rotor wake segments appear as alternating bands of positive and negative vorticity that extend across the vane passage and are convected downstream with the mean flow.

The fundamental physics of the wake chopping and transport process are very similar for all loading conditions. As the compressor loading is increased, a region of high vorticity forms near the pressure surface of the vane, with this region extending from the leading to the trailing edge of the vane at the highly loaded operating condition. This region is also present at the nominal loading condition but to a much lesser extent. This region is attributed to the slip velocity in the rotor wakes causing the low momentum wake fluid to drift across the vane passage and accumulate on the pressure surface as the chopped wake segments are transported downstream. This results in the rotor wake fluid tending to appear in the stator wakes, with the amount of entrained rotor wake fluid increasing as the compressor loading is increased.

Low Loading   **Nominal Loading**   **High Loading**
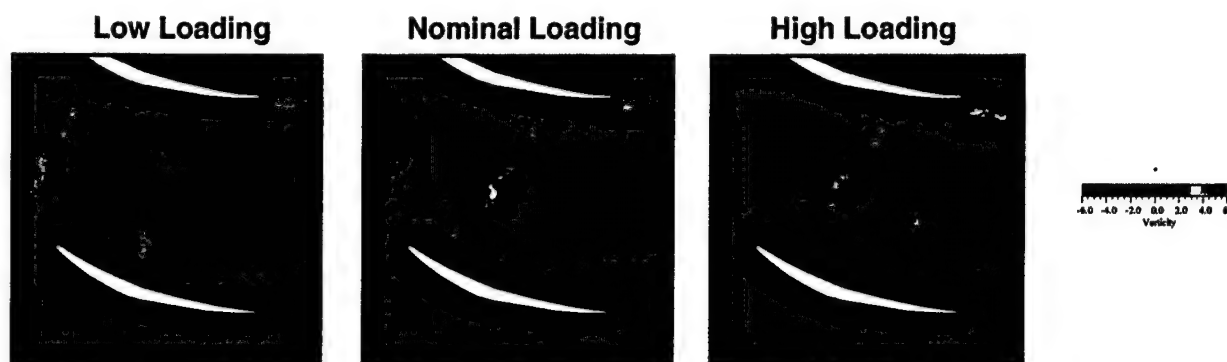
Figure 37. Effect of Compressor Loading on the Time-Variant Vorticity (t/T=0.0)

The reduced frequency is defined as the ratio of the time it takes a fluid particle to convect through the vane row to the time scale of the wake-generated unsteadiness. Thus, this parameter provides an indication of the number of chopped wake segments residing within the vane passage at any given instant in time. The reduced frequencies based on the mass averaged mid-span stator inlet velocity are 2.27, 2.46, and 2.65 for the low, nominal, and highly loaded operating conditions respectively, indicating that it takes between two and three blade-passing periods for one chopped wake segment to be completely transported through the vane passage. The combination of a longer transport time and a higher slip velocity due to deeper wakes at the higher loading conditions thus results in more low momentum rotor wake fluid accumulating on the stator pressure surface during the rotor-stator interaction cycle. It is the interaction of this low momentum rotor wake fluid with the airfoil boundary layer that generates the high vorticty region near the pressure surface of the vane.

The increased compressor loading also causes the rotor wake segments to disperse more rapidly after they are chopped and ingested into the vane passage, with the enhanced decay rate due to both increased viscous dissipation and stronger inviscid wake recovery effects. The enhanced wake recovery is due to the airfoil circulation causing the chopped wake segments to convect past the suction surface faster than they do past the pressure surface, with the amount of wake stretching increasing with compressor loading. This can be seen by comparing the snapshots of the flow field at each of the three loading conditions, with the tilting of the first chopped wake segment increasing with compressor loading due to the higher stator vane circulation, with this wake stretching partly responsible for the enhanced decay rate.

The effect of compressor loading on the axial Mach number contours is shown in Figure 38 for single time instant, with the characteristics of the unsteady flow field similar for all three operating conditions. Increasing the compressor loading results in both deeper rotor wake velocity deficits and lower convection velocities due to the decreased flow rate through the machine. Thus, more low momentum rotor wake fluid accumulates on the stator pressure surface as the chopped wake segments are transported downstream, as evident by the increased size of the low velocity region near the vane pressure surface for the higher loading conditions. The extent of this low velocity region increases with compressor loading due to both the higher wake slip velocity and the fact that the chopped wake segments reside in the passage longer due to the reduction in flow rate.

Low Loading　　　**Nominal Loading**　　　**High Loading**
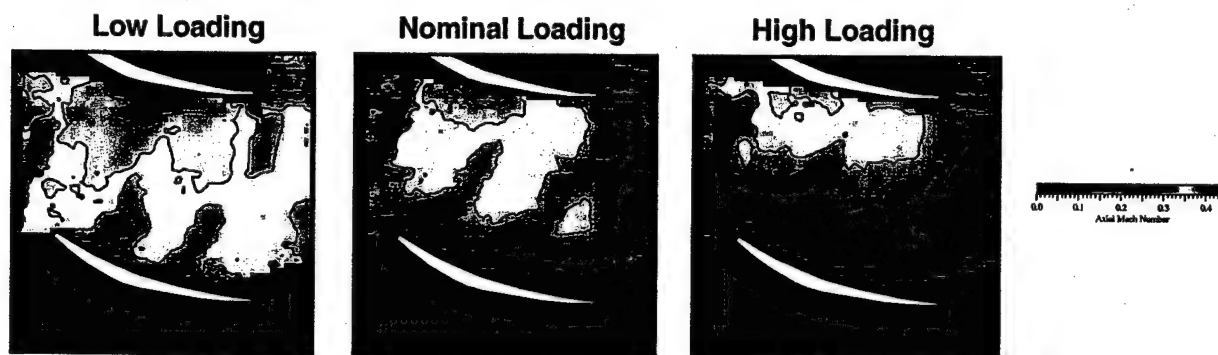
Figure 38. Compressor loading effect on the time-variant axial Mach number (t/T=0.0)

At the highest loading condition, this low velocity region extends from the leading to the trailing edge of the vane pressure surface. Recall that this low velocity region was also evident in the time-average Mach number contours for this operating condition and to a lesser extent at the nominal loading condition. Thus, the unsteady wake chopping and transport processes that occur within multistage turbomachines can significantly affect the time-average flow through downstream airfoil rows. Additionally, since the rotor wake fluid tends to appear in the stator wakes, this intra-stator wake transport process can significantly affect the character of the wake-generated forcing function to a downstream rotor in a multistage turbomachine.

To examine the detailed unsteady flow field generated by the wake chopping and transport process, PIV images were also acquired focusing on the stator leading edge region flow field near the vane pressure surface. Figure 39 shows the unsteady velocity vectors superimposed on the time-variant axial Mach number contours including the effects of steady loading for the same time instant at which the passage flow data were presented. This unsteady velocity field was calculated by subtracting the time-average velocity and shows how the steady flow field is perturbed at each time instant throughout the rotor-stator interaction cycle.

Figure 39 shows the effects of steady loading on the unsteady velocity vectors, with the vectors clearly showing the high slip velocity associated with each of the chopped rotor wake segments. Once the wake has been cut, this slip velocity causes the low momentum rotor wake fluid to drift across the vane passage and accumulate on the airfoil pressure surface as the chopped wake segment is transported downstream. As the

wake fluid collects on the vane pressure surface, counter-rotating vortices are generated near the airfoils which are present throughout the entire cycle. These vortices are convected downstream along with the chopped wake segments and are an additional source of unsteady aerodynamic excitation to the stator vanes. Recirculating flow patterns are also established away from the vane surface on each side of the chopped wake segment as high momentum free stream fluid is drawn into the wake region to replace the low momentum wake fluid which has migrated toward the airfoil pressure surface.

As the compressor loading is increased, the size of the low velocity region that forms as the wake fluid collects on the pressure surface also increases. This causes the counter-rotating vortices to be generated further away from the airfoil surface as can be seen comparing the snapshots of the flow field for the three loading conditions. Also notice that at the nominal and highly loaded operating conditions these vortices actually appear to distort the chopped wake segment. However, this distortion may be an artifact of a large radial velocity component in the wake regions that cannot be measured using conventional two-dimensional PIV techniques.

Low Loading   **Nominal Loading**   **High Loading**
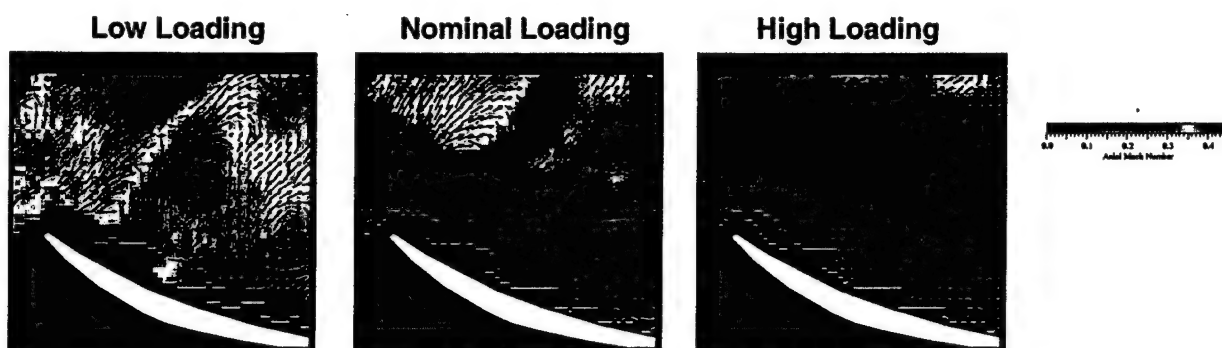
Figure 39. Compressor loading effect on unsteady velocity vectors (t/T=0.0)

Conclusions

For all three loading conditions the suction surface unsteadiness was highest in the leading edge region and decreased with downstream distance. The pressure surface unsteadiness followed a noticeably different trend. Here the pressure fluctuations increased significantly from the leading edge and reached a maximum at 45% chord for all three loading conditions. Aft of this location, the unsteadiness attenuated slightly but was still very significant along the aft half of the vane. Increasing the compressor loading resulted in higher levels of unsteadiness on both vane surfaces, with the peak-to-peak pressure fluctuations very significant.

The PIV data indicated that the high levels of pressure surface unsteadiness were due to viscous effects associated with the intra-stator transport of the chopped rotor wake segments through the vane row. Specifically, the low momentum rotor wake fluid had a slip velocity relative to the free stream that caused it to drift across the vane passage and accumulate on the vane pressure surface as the wakes convected downstream. As the compressor loading was increased, the extent of the low velocity region on the vane

pressure surface became larger due to the deeper wakes and lower convection velocities at the higher loading conditions.

Counter-rotating vortices were generated on each side of the chopped wake segment as the low momentum wake fluid accumulated on the vane pressure surface. These vortices were convected downstream along with the chopped wake segments and were an additional source of unsteady aerodynamic excitation to the stator vanes. Recirculating flow patterns were also established away from the vane surface on each side of the chopped wake segment as high momentum free stream fluid is drawn into the wake region to replace the low momentum wake fluid that had migrated toward the airfoil pressure surface. As the compressor loading was increased, the size of the low velocity region that formed on the vane pressure surface increased, causing the counter-rotating vortices to be generated further away from the airfoil surface.

The PIV data also illustrated the effects of steady loading on the inviscid wake recovery process. This was due to the circulation around the stator vanes enhancing the decay rate of the rotor wakes due to an inviscid straining of the wake fluid as the chopped wake segments were transported through the vane row. This inviscid stretching occurred in addition to viscous dissipation and is a reversible process that causes the rotor wakes to decay faster than they would in isolation. This phenomenon became more pronounced as the flow rate was reduced, with the increased vane loading partially responsible for causing the wakes to disperse more rapidly.

ROTOR WAKE VARIABILITY & ITS EFFECT ON VANE RESPONSE

Rotor wakes are the aerodynamic forcing function to the downstream stator. However these wakes are not steady in the rotor relative frame due to the interaction of the rotor with the upstream IGV row and the potential field of the downstream stator row. To quantify these multistage interaction effects on the rotor wake, the IGV row is circumferentially clocked over one vane spacing relative to the stationary instrumentation and downstream stator at a corrected speed of 15,000 rpm. Since the data acquisition is always initiated at the same absolute rotor shaft position, the temporal variations over one complete rotor revolution measured by the stationary probes are generated by the same rotor blades, regardless of IGV clocking position. However, by clocking the IGV row, the interaction between the IGV and the rotor is shifted in the time domain, thereby resulting in different rotor wake characteristics. Thus, multistage interaction effects are assessed by comparing the time-variant signals from the stationary probes at the different IGV clocking positions. In the unclocked position, the stacking axes of the IGV and the stator airfoils coincide at the same circumferential position, Figure 40.
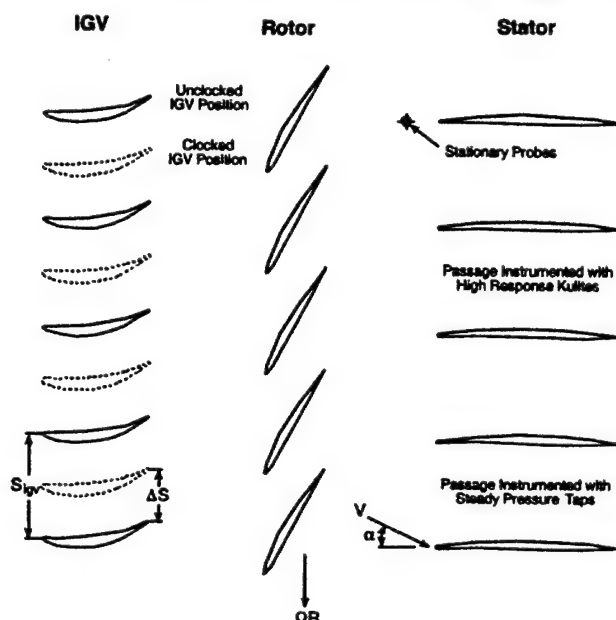
Figure 40. Stage geometry showing instrumentation locations and vane clocking

Figures 41-43 show the rotor exit time-variant mid-span velocity, flow angle, and static pressure over one rotor revolution as a function of IGV clocking position for 20° IGV stagger. This is the inlet flow field to the vane row, with the 19 rotor-blade wakes readily apparent. The 1st blade wake is also shown at the beginning of the second rotor revolution to illustrate that the fundamental temporal periodicity of these multistage interactions is over one complete rotor revolution.

Both the rotor blade wake deficits and the free stream velocities change noticeably as the IGV row is clocked, Figure 41. This is attributed to multistage interactions, with the chopped IGV wake segments most visible in the free stream region at the ¼-cycle IGV position. The wake velocity deficit is similar for the unclocked and 1/2-cycle IGV positions, with the wakes for the 1/2 cycle position narrower than those in the unclocked

position. The wakes for the ¼- and ¾-cycle IGV positions are also similar, with the velocity deficits approximately 5% smaller than those in the unclocked position. The ½-cycle IGV data also reveal a very interesting phenomenon. Namely, the magnitudes of the velocity deficits are nearly the same as those in the unclocked position, but the blade-to-blade wake variability is markedly different. In the unclocked position blade-to-blade variability is apparent. However, in the ½-cycle IGV position, the wakes are fairly uniform from blade-to-blade except for a rogue wake with a velocity deficit roughly 2.5% larger than the other blades between the 17th and 18th blade pass periods. This rogue wake is also evident in the ¾- cycle IGV clocking position and to a lesser extent in the ¼-cycle position. Also, the free stream velocity magnitude is similar for the unclocked and the full-cycle IGV positions. However, the waveforms exhibit small differences, with the suction side of the rotor blade wake thicker in the unclocked position. Note that for each clocking position the temporal periodicity is one complete rotor revolution, with the wake generated by the 1st blade identical for the 1st and 2nd rotor revolutions.
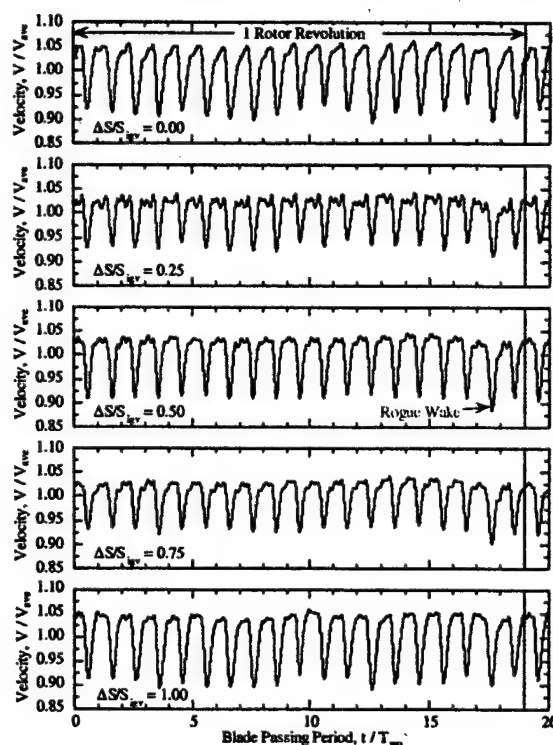
Figure 41. Velocity magnitude as a function of IGV clocking, θ_{igv}= 20°, N_c= 15,000 rpm

Figure 42 shows that blade-to-blade wake differences in the absolute flow angle of up to 3° exist at each IGV clocking position. However, this wake variability as well as the magnitudes of the flow angle variations are very similar for each IGV clocking position, not exhibiting the differences seen in the velocity data. The most notable difference is in the time-average flow angle that varies from -0.9° to -2.6° as the IGV is clocked over one cycle. Also, the time-average flow angle is different for the unclocked and full-cycle positions, indicating that the fundamental spatial periodicity is over the entire compressor annulus and not just a single vane spacing.
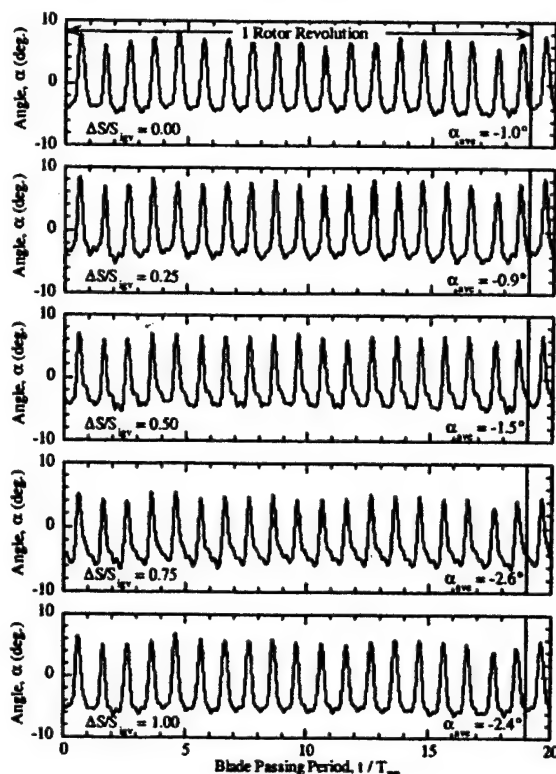
Figure 42. Flow angle as a function of IGV clocking, $\theta_{igv} = 20°$, $N_c = 15,000$ rpm

The static pressure coefficient data of Figure 43 were acquired 66% rotor chord downstream of the rotor. Hence, the steady rotor potential-flow field is expected to be negligible and not contribute to the unsteady static pressure. However, the data exhibit large pressure perturbations at blade-pass-frequency harmonics. Also, both the waveform character and its phase change with IGV clocking position, with the waveforms for the unclocked and full cycle IGV positions significantly different.

These pressure perturbations are attributed to acoustic interactions. Rotors and stators interact and generate spinning acoustic modes at multiples of blade-pass frequency. Depending on the axial wave number, these modes either decay exponentially or propagate unattenuated. These interactions lead to frequency shifting and mode scattering, with a single excitation frequency in the rotor frame producing a multiplicity of frequencies and interblade phase angles in the stator frame.

That the static pressure waveforms differ at the unclocked and full-cycle IGV positions supports the hypothesis that these pressure perturbations are due to acoustic interactions, i.e., the pressure perturbations due to these spinning acoustic modes vary with circumferential position and depend upon the mode order. The clocking of the IGV row results in a shifting of the IGV-rotor interaction in the time-domain. Hence, the phase of the acoustic modes generated by this IGV-rotor interaction are also shifted. In addition, the interaction between the rotor and downstream stator generates a second set of acoustic modes, with the phase of these modes independent of IGV clocking position. Since the probe measures the total interaction field, both sets of acoustic interaction modes are contained in the data, with possible constructive or destructive interference

between the two sets of modes occurring as the IGV is clocked over one cycle. Thus, this multistage interaction also contributes to the rotor wake differences resulting from IGV clocking.
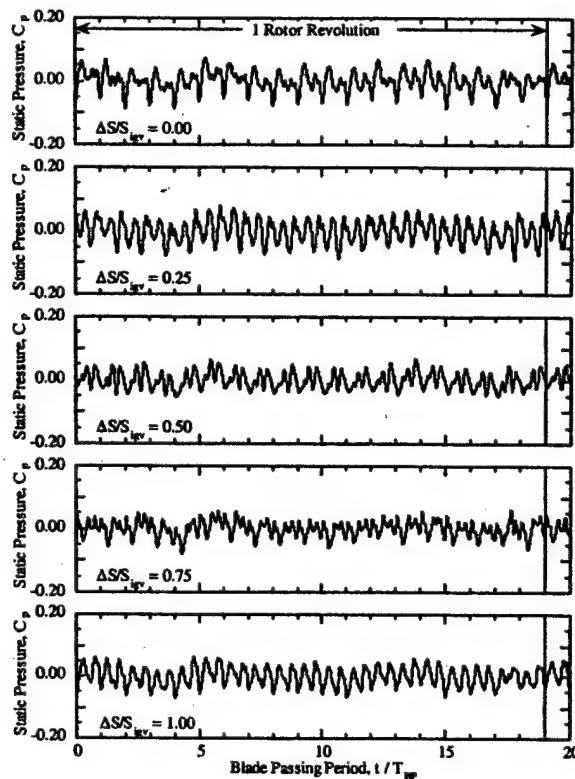
Figure 43. Static pressure as a function of IGV clocking, $\theta_{igv} = 20^\circ$, $N_c = 15,000$ rpm

Figures 44 - 46 show analogous results for the 10° IGV stagger. The rogue wake is more pronounced and clearly evident at all IGV clocking positions, with its velocity deficit nearly twice that of the other wakes in the unclocked position. The free stream region ripples are the chopped IGV wake segments, which are much more pronounced than in Figure 41. This is due to the IGV incidence increase from -3.4° to -13.4° in going from the 20° to the 10° IGV stagger resulting in larger IGV wakes. At the 3/4-cycle IGV position, these chopped IGV wake segments have actually merged with the rotor wakes, resulting in a markedly different wake profile from those at the other clocking positions. Also, the unclocked and full cycle IGV results are not identical, with the deficits associated with the wakes of the 3rd, 11th, and 14th blades differing. The temporal periodicity at each clocking position is again over one complete rotor revolution, with the spatial periodicity over the entire annulus due to the differences noted for the unclocked and full cycle IGV positions. The rotor exit absolute flow angle variability is nearly independent of IGV clocking, Figure 46. However, the flow angle fluctuations are about 1° larger for the 1/2 cycle versus the other IGV clocking positions. The time-average flow angles for the clocked and full cycle IGV positions are also identical, in contrast to the 20° IGV stagger results.
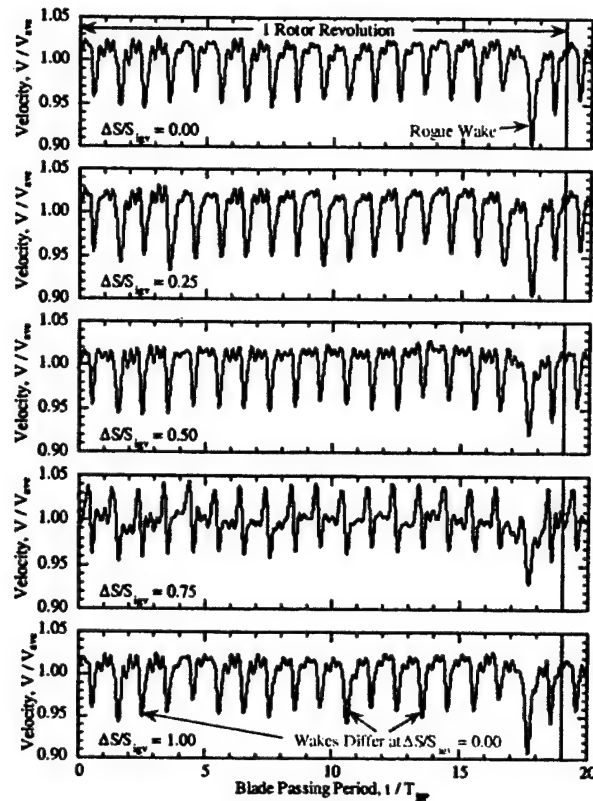
Figure 44. Velocity magnitude as a function of IGV clocking, $\theta_{igv}= 10^o$, $N_c= 15,000$ rpm

Figure 45. Flow angle as a function of IGV cocking, $\theta_{igv}= 10^o$, $N_c= 15,000$ rpm

Figure 46 shows the rotor exit unsteady static pressure coefficient as a function of IGV clocking position. As per the 20° IGV stagger, the waveform character and phase change with IGV clocking. However, the waveforms for the unclocked and full cycle positions are nearly identical and the pressure fluctuations are larger than those at the 20° IGV stagger. Also, both the character and phase of the ¾- and full-cycle waveforms are similar to the 20° IGV stagger unclocked and 1/4-cycle positions of Figure 43.
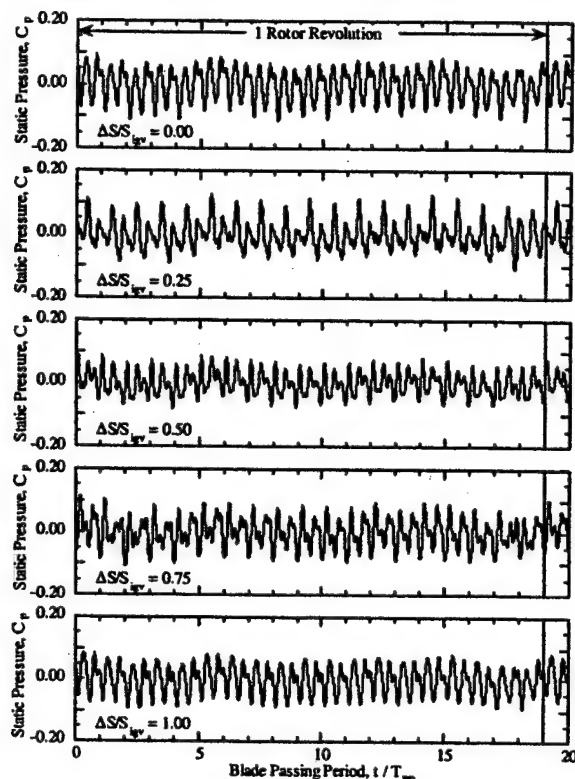
Figure 46. Static pressure as a function of IGV clocking, θ_{igv}= 10°, N_c= 15,000 rpm

Vane Unsteady Aerodynamic Response

The unsteady aerodynamic response of the downstream vane row over one complete rotor revolution is also examined. To illustrate the fundamental temporal periodicity, the response data are presented for 20 rotor blade pass periods. These detailed response data are acquired at corrected speeds of 15,000 and 18,000 rpm for IGV staggers of 10° and 20° with the IGV row in the unclocked position. The steady vane pressure distributions are presented in Figure 47. The pressure distributions for angles-of-attack of -1.0° and 8.5° are in good qualitative agreement with the results obtained in a linear oscillating cascade with the airfoils staggered at 60°.
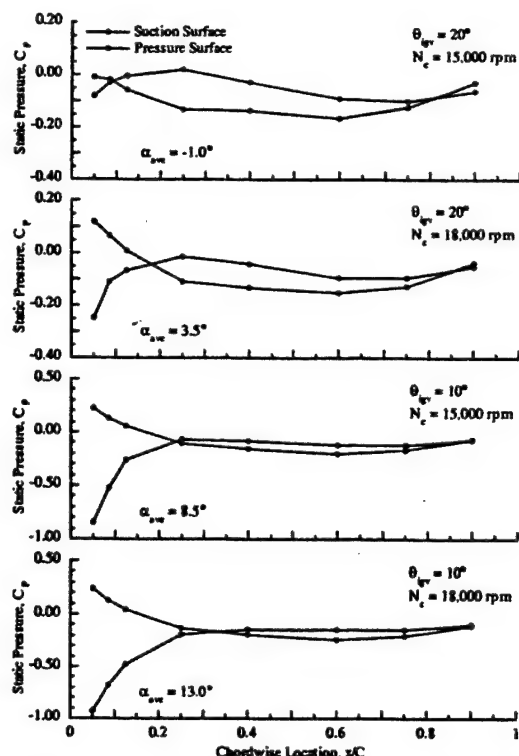
Figure 47. Steady vane pressure distributions

Figures 48 and 49 show the rotor wake generated forcing function and the resultant vane row unsteady aerodynamic response at corrected speeds of 15,000 and 18,000 rpm for the 20° IGV stagger. Presented are the rotor wake velocity deficit, flow angle, and static pressure together with the resulting vane unsteady lift and moment, with the two speeds corresponding to design (subsonic) and off-design (transonic) rotor flow.

At 15,000 rpm, the rotor wake velocity deficit and flow angle variations are on the order of 15% and 12°, with blade-to-blade wake variability of approximately 5% and 2°, Figure 48. The stator response exhibits considerable variability over one complete rotor revolution, most notable in the unsteady lift. Also, the responses over the 1st and last (20th) blade pass periods are identical. This shows that blade-to-blade wake variability results in variability in the unsteady aerodynamic response of a downstream row, with the fundamental periodicity of both the forcing function and the resultant vane response one complete rotor revolution. Also, the shape and phase of the unsteady lift and moment waveforms closely resemble the unsteady static pressure measured 18.75% stator chord upstream of the vane. This suggests that part of the static pressure variation is indeed due to an acoustic interaction generated by the stator response to the rotor wakes.

At 18,000 rpm, the rotor wake velocity deficit is much more erratic, with the blade-to-blade wake differences of the same magnitude as the wakes themselves, Figure 49. The flow angle variation is much more uniform, but the profiles differ from blade-to-blade and are much wider than at 15,000 rpm. The stator response as well as the unsteady static pressure upstream of the vane also exhibit erratic behavior, with the variability much more pronounced than at 15,000 rpm. The erratic vane response is attributed to the erratic behavior of the forcing function, with the temporal periodicity over one complete

rotor revolution. Again, the phase and shape of the unsteady static pressure upstream of the vane closely resemble the vane unsteady aerodynamic response.
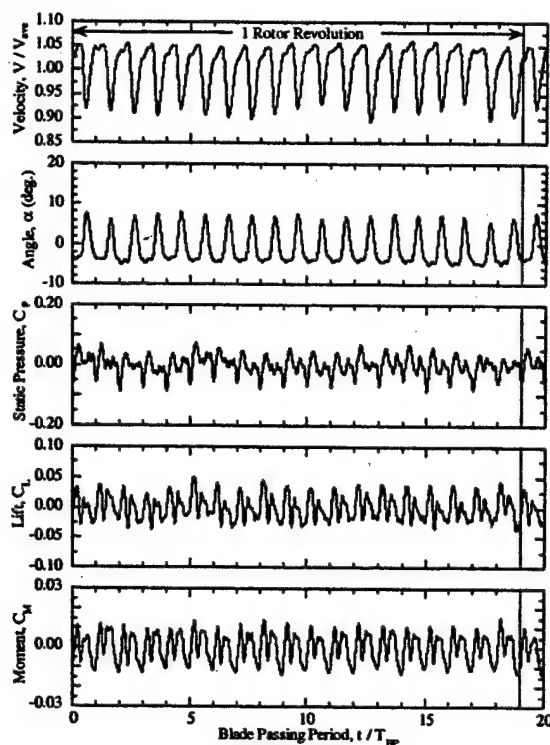
Figure 48. Rotor wake and vane response, $\Delta S/S_{igv}= 0.00$, $\theta_{igv}= 20^\circ$, $N_c= 15,000$ rpm
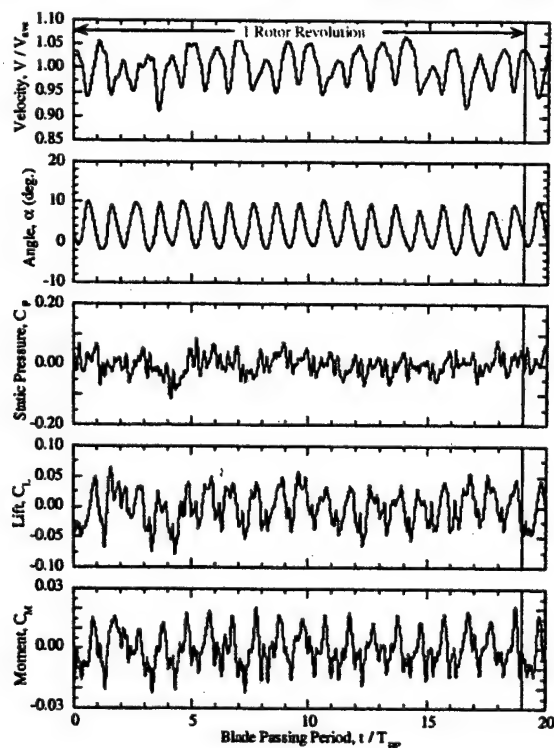
Figure 49. Rotor wake and vane response, $\Delta S/S_{igv}= 0.00$, $\theta_{igv}= 20^\circ$, $N_c= 18,000$ rpm

Figures 50 and 51 show the rotor wake and resultant stator vane unsteady aerodynamic response at corrected speeds of 15,000 and 18,000 rpm for the 10° IGV stagger. The rogue wake is clearly evident at 15,000 rpm, with the velocity deficit nearly twice as large as the other wakes, Figure 50. However, the rogue wake flow angle variation is the same as the other wakes. In fact, there is considerable variability in the velocity deficit but the flow angle is fairly uniform from blade-to-blade. There is also large variability in the vane response, again most pronounced for the unsteady lift. However, the stator does not respond to the rogue wake. This may be due in part to the signal conditioning, with the pressure transducer signals high-pass filtered at 500 Hz and the rogue wake having a passing frequency of 250 Hz. Also, the responses for the first and last (20th) blade pass periods differ slightly. This may be due to errors associated with the integration of the discrete pressure data and also the phase-lock averaging procedure, with 500 ensembles possibly insufficient to average out all random unsteadiness due to the high steady vane loading at this IGV stagger.
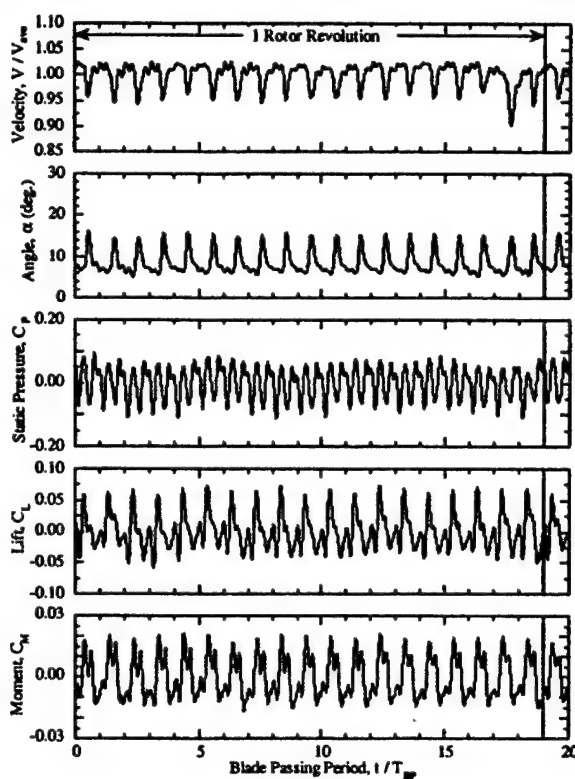
Figure 50. Rotor wake and vane response, $\Delta S/S_{igv}$= 0.00, θ_{igv}= 10°, N_c= 15,000 rpm

At 18,000 rpm, the wakes are wider and deeper, Figure 51. However, the rotor exit flow is not as erratic as at 20° IGV stagger. This is because the rotor inlet relative Mach number is lower at the 10° IGV stagger due to less inlet pre-swirl. The rogue wake is also much less pronounced, with the rogue wake wider but the velocity deficit only a few percent larger than the other wakes. In contrast to the 15,000-rpm results, the blade-to-blade wake flow angle variability is large, on the order of 5°. From the flow angle data, the wakes of the 15th, 16th, and 17th blades also appear much wider than those of the other blades. The variability of the unsteady lift and moment has also increased relative

to the corresponding 15,000 rpm results, attributed to the larger blade-to-blade wake variability. Also, the responses for the first and last blade pass periods are identical, again indicating that the fundamental periodicity is one complete rotor revolution.
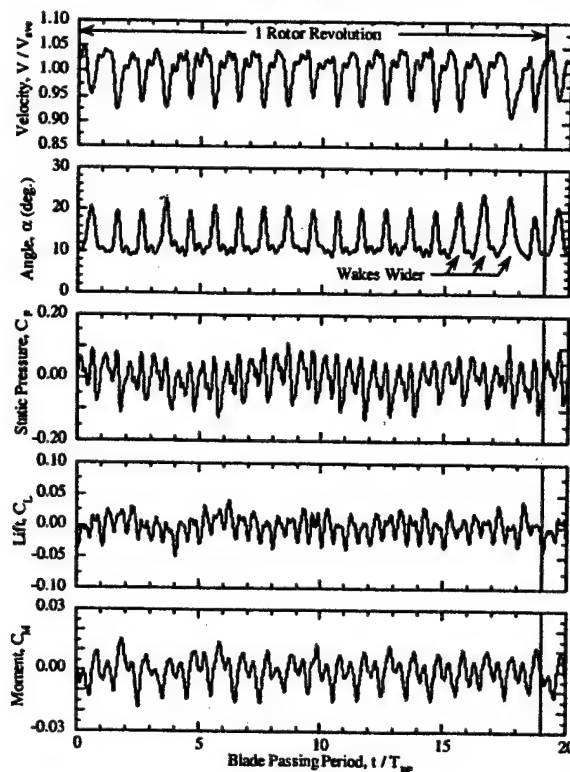
Figure 51. Rotor wake and vane response, $\Delta S/S_{igv} = 0.00$, $\theta_{igv} = 10°$, $N_c = 18,000$ rpm

Blade-to-Blade Wake & Response Variability

The variability in the phase-lock averaged wake velocity deficit and stator vane unsteady aerodynamic lift are also quantified with the IGV in the unclocked position. To obtain an integer number of data points per blade pass period, a new sampling rate was defined based on the measured rotor speed and the waveforms interpolated. This allows all 19 rotor wakes and the corresponding stator vane unsteady aerodynamic response to each wake to be directly compared to one another and the statistical variations determined, with the mean and standard deviation calculated by averaging corresponding points along each of the 19 wake and vane response blade pass periods.

Figures 52 and 53 present the 19 rotor wakes and the vane unsteady lift response to each wake for corrected speeds of 15,000 and 18,000 rpm at the 20° IGV stagger. The average or mean wake and vane response are denoted by the solid symbols, with the vertical bars representing ±2 standard deviations (±2σ) from the mean. The wake and corresponding vane response between the 17th and 18th blade pass periods are also shown by dashed lines since this was the time interval associated with the rogue wake.

At the design speed of 15,000 rpm, the largest variability is on the rotor wake suction side, with the pressure side of the wake and free stream region fairly uniform from blade-to-blade, Figure 52. This variability is quite large, with the average velocity

deficit approximately 13%, and the 2σ bands about ±5%, ±2%, and ±1% of the time-average velocity for the suction side, pressure side, and free stream respectively. For this clocking position, the rogue wake is not evident in the time traces. However, the wake that occurs between the 17th and 18th blade pass periods exhibits the greatest variability from the mean. Thus, even in the unclocked position, the rotor blade that generates the rogue wake has a higher loss than the other blades. Also, the deeper wakes exhibit larger suction side semi-wake widths, indicating that the rotor loss varies from blade-to-blade.

Figure 52. Wake & vane response variability, $\Delta S/S_{igv}= 0.00$, $\theta_{igv}= 20°$, $N_c= 15,000$ rpm

The vane response variability is even more marked, with the 2σ bands ±0.015 nearly half the maximum of the average unsteady lift coefficient over one blade pass period. Thus, small blade-to-blade differences in the wake forcing function lead to even greater variability in the resultant vane response. This indicates that the vane row does not respond to individual rotor blade wakes in a quasi-steady manner. Rather, the fundamental forcing function period is one rotor revolution.

At 18,000 rpm, there is considerable variability over the entire blade passage due to transonic flow effects, Figure 53. This variability is very significant, with the 2σ bands for the free stream, pressure side, and suction side of the wake ±4%, ±2%, and ±5% respectively, with the average profile having a velocity deficit of 8%. The vane response variability is also much more marked than at 15,000 rpm, with the 2σ bands as large as ±0.047, 160% of the maximum average unsteady lift over one blade pass period. This large vane response variability is attributed to the increased blade-to-blade variability of the forcing function generated by off-design rotor operation, with this variability spread out over the entire 2σ band.
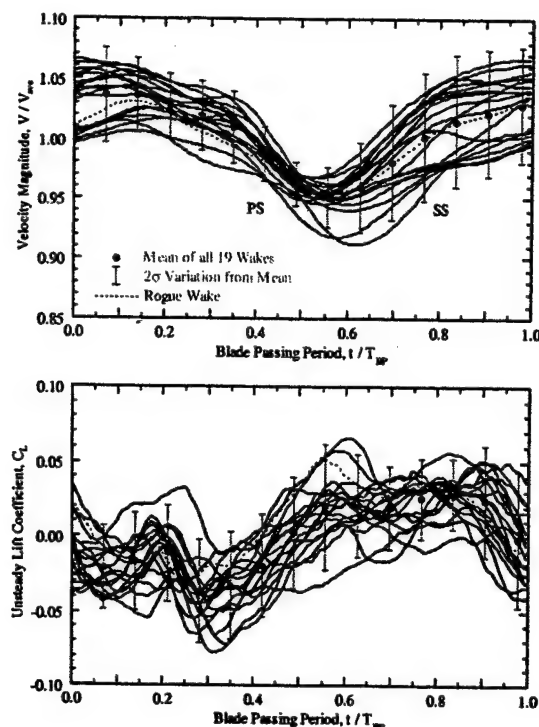
Figure 53. Wake & vane response variability, $\Delta S/S_{igv}= 0.00$, $\theta_{igv}= 20^o$, $N_c= 18,000$ rpm

Figures 54 and 55 show the forcing function and vane response for the 10° IGV stagger. At 15,000 rpm, the blade-to-blade variability in the velocity deficit is fairly small except for the rogue wake, Figure 54. Since the rogue wake has a velocity deficit almost twice as large as the mean for all 19 blades, it contributes substantially to the standard deviation. The 2σ bands for the free stream, pressure side, and suction side of the wake are near $\pm1\%$, $\pm1.5\%$, and $\pm4\%$ respectively, and the average velocity deficit is near 6%. Also, the rogue wake is outside the 2σ band. Thus, it is not part of the Gaussian distribution describing the statistical variations of the wake. In fact, with the exclusion of the rogue wake, the variability associated with the suction side of the wake is on the order of $\pm1\sigma$. The vane response variability for this configuration is smaller than that at 20° IGV stagger, but is still large, with the 2σ bands ±0.021, nearly 1/3 of the maximum average unsteady lift occurring over one blade pass period.

At 18,000 rpm, the rogue wake is much less pronounced but is still outside the 2σ band, Figure 55. The variability is also smaller than at the 20° IGV stagger, with the average velocity deficit 9% and the 2σ bands $\pm2\%$, $\pm3\%$, and $\pm4\%$ for the free stream, pressure side, and suction side of the wake respectively. The vane response variability is also very pronounced, with the 2σ bands as large as ±0.021, nearly 90% of the maximum average unsteady lift.
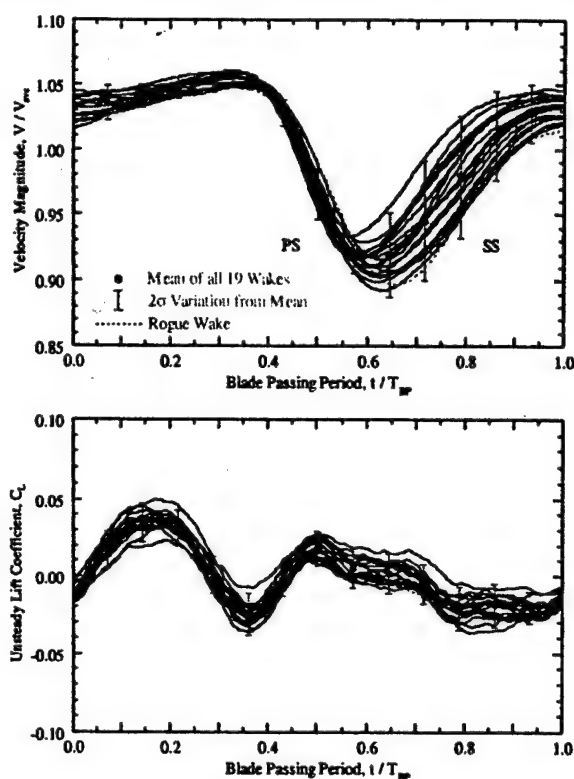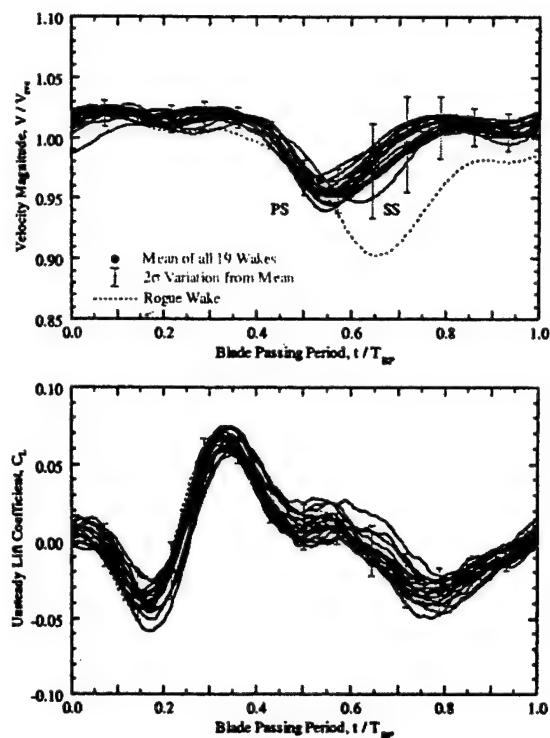
Figure 54. Wake & vane response variability, $\Delta S/S_{igv}$= 0.00, θ_{igv}= 10°, N_c= 15,000 rpm
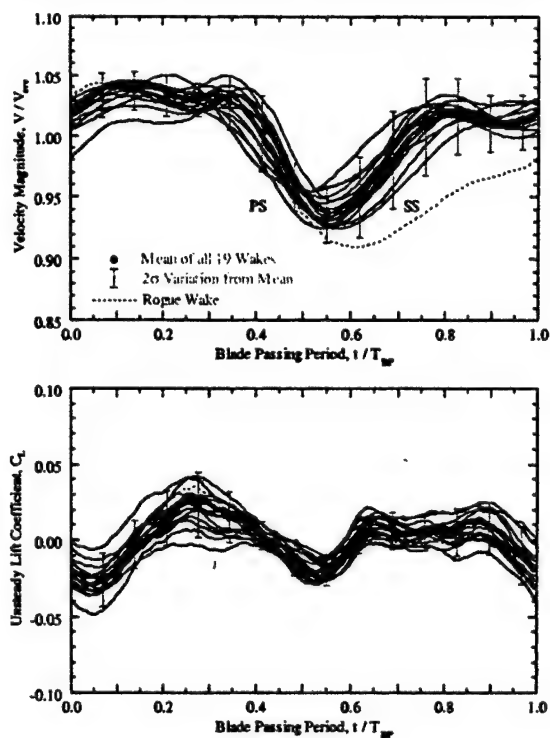
Figure 55. Wake & vane response variability, $\Delta S/S_{igv}$= 0.00, θ_{igv}= 10°, N_c= 18,000 rpm

Conclusions

High-speed rotor blade-to-blade wake variability and the resultant unsteady aerodynamic response of a downstream stator were experimentally investigated. The rotor wake changed markedly with IGV clocking, with both the wake character and the blade-to-blade variability affected. This was attributed to both wake chopping and transport of the IGV wake segments by the rotor and also the spinning acoustics modes generated by blade row coupling. At certain IGV clocking positions, the chopped IGV wake segments merged with the rotor wakes, thereby resulting in a very different forcing function to the downstream stator. A rogue wake was also generated by these multistage interactions, with the velocity deficit dependent upon IGV clocking position and IGV stagger. The temporal periodicity of these multistage interactions was shown to be one complete rotor revolution due to the unequal number of blades and vanes. The time-variant waveforms corresponding to the unclocked and full cycle IGV positions were also different, showing that the fundamental spatial periodicity of these interactions was over the entire annulus.

The variability in the unsteady aerodynamic response of the downstream stator over one complete rotor revolution was also investigated. Off-design rotor operation resulted in the largest blade-to-blade wake variability, which generated the largest variability in the vane response. The unsteady static pressure waveform upstream of the vane was markedly similar to the downstream vane unsteady response waveforms, indicating that the measured unsteady pressure field is due in part to the vane acoustic response to the rotor wakes.

The blade-to-blade rotor wake and resultant vane response variability were quantified. The wake width and depth exhibited considerable variability, most notably on the wake suction side. In fact, this variability can be of the same order as the average velocity deficit. Off-design rotor operation resulted in the largest variability, with the free stream region exhibiting almost as much variability as the wakes themselves. The rogue wake velocity deficit was also greater than 2σ from the mean. The vane response variability was even more pronounced, with the unsteady lift variability ranging from 33% to 160% of the maximum average unsteady lift.

In summary, IGV clocking alters the rotor wake, demonstrating it may be a viable passive stator vibration control technique. Multistage interactions also contributed to rotor blade-to-blade wake variability and to the generation of a rogue wake. Typically, data are acquired over only a few wake-passing periods. However, to accurately assess multistage interaction phenomena and determine if rouge wakes exist, data corresponding to one complete rotor revolution must be acquired since this is the fundamental periodicity of these interactions. Also, CFD analyses must correctly account for unequal numbers of blades and vanes in the machine in order to accurately predict multistage interactions. Finally, small blade-to-blade wake differences lead to large variations in the downstream vane row unsteady aerodynamic response. Thus, models are needed to address aerodynamic mistuning effects on airfoil response, including rogue wake effects.

FLUID-STRUCTURE INTERACTION SIMULATIONS

TAM-ALE3D (Turbomachinery Aero-Mechanics Arbitrary Lagrangian Eulerian 3D) is a three-dimensional Euler solver using a finite element scheme. The equations stating conservation of mass, momentum and energy are marched forward in time, with the physical domain discretized by an unstructured assembly of finite elements. These elements are not required to move with the material, nor must they remain stationary, making the scheme an "Arbitrary" Lagrangian Eulerian (ALE) scheme. For each step forward in time, there are three distinct calculation procedures: (1) The Lagrange calculation, (2) mesh relaxation, and (3) the advection calculation.

The elements move with the material with no flux of mass or energy through the element faces in the Lagrange calculation. Thus, conservation of mass requires that the mass of the elements be constant during this calculation. Conservation of momentum is

$$\frac{D}{Dt}\int_V \rho u_i dV = -\int_S (P+q)n_i dS + \int_V \rho b_i dV \tag{1}$$

where summation notation is used with i representing the three coordinate directions, and D/Dt is the material derivative showing that the control volume moves with the material and the term q is a mathematical device that smears shocks over distances comparable to the mesh interval.

To discretize the conservation equations, the integration volumes are taken to be the finite elements. Physical quantities are assigned to staggered locations in the element. Velocities and accelerations are stored at the nodes (vertices) and are assumed to vary linearly over the element. The pressure, energy, and q term are stored at the center and are constant over the element. The element mass is stored at both the center and element nodes, with the nodal mass being one-eighth the sum of the surrounding element masses.

In the time discretization, the velocities and the q terms are taken at half time levels, denoted by superscript "n±1/2", while all other quantities are evaluated at full time levels. Evaluating the velocities and q terms at half time levels produces difference equations that are centered in space and are thus second order accurate. The body force per unit mass b_i is required to account for Coriolis and centripetal accelerations in a rotating reference frame.

In Equation 1, the density of the volume is constant in space and time, so the left-hand-side is the product of mass and acceleration. Since acceleration is stored at the element nodes, it is convenient to discretize Equation 1 by using a "node-centered" element. The pressure and q term acting on the surfaces of this element are considered in the evaluation of the surface integral of Equation 1. In discretized form, Equation 1 is

$$a_i^n = \frac{1}{M'^n}\sum_e \left(P^n - q^{n-1/2}\right)n_i' \Delta S' + b_i^n + \frac{1}{M'^n}F_i^{hg} \tag{2}$$

where M' is the mass of a node; n_i' and $\Delta S'$ are the outward normal and surface area of the node-centered element contained within element e; and the subscript e on the summation denotes summation over all the elements surrounding the node, eight

elements for an interior node or four, two, or one element for a boundary node. The F_i^{hg} term represents the hourglass viscous force required to damp the hourglass modes.

After finding the nodal acceleration from Equation 2, a centered-difference formula is used to find the velocity at time level n+1/2. The centered-difference formula is again applied to the velocity to find the new position of the node at time level n+1.

Using energy conservation to update the elemental energy completes the Lagrange step. For a control volume with no energy flux through its faces, energy conservation is

$$\frac{D}{Dt}\int_{V}\rho E dV = -\int_{V}(P+q)u_{i,i}dV$$

The average velocity divergence of a finite element is the non-dimensional rate of change of volume of the element, i.e. $(1/V)(DV/Dt)$. Substituting this for $u_{i,i}$, and substituting the equation of state for a fluid for P gives

$$\frac{D\rho EV}{Dt} = -\big[(\gamma-1)\rho E+q\big]\frac{DV}{Dt}$$

If q were zero, this could be integrated in closed form. However, since q is not necessarily zero, a third-order Runge-Kutta method is used to integrate this to find the elemental energy at time level n+1.

In the Lagrange calculation, the elements change position. Clearly, the fluid elements cannot continue moving in a Lagrangian fashion; otherwise the solution will be destroyed as the elements exit the solution domain. Therefore, before proceeding to the next time step it is necessary to relax the finite element mesh to a new position and calculate new elemental and nodal quantities via an advection calculation. In this study, solid boundaries such as blades and vanes are not moving. Thus, mesh relaxation is accomplished with a straightforward placement of the elements back to their original position at the beginning of the Lagrange step.

As an element moves from its position at the end of the Lagrange calculation to its new position after mesh relaxation, there is a flux of mass, momentum, and energy through the six faces of the element. The mass, momentum, and energy of the element are updated by simply summing the flux of these quantities through the element faces.

Consider a single face of an element that moves from its old position to its new position after mesh relaxation. The volume between the old and new face positions, termed the face-swept volume and denoted by ΔV_f, is positive if the face moves into the element. The change in mass, momentum, and energy of the element is then

$$\Delta M = -\sum_{j=1}^{6}\big(\rho^{*}\Delta V_f\big)_{j} \qquad \Delta(M'u_i) = -\sum_{j'=1}^{6}\Big[(\rho u_i)^{*}\Delta V_f'\Big]_{j'} \qquad \Delta(ME) = -\sum_{j=1}^{6}\Big[(\rho E)^{*}\Delta V_f\Big]_{j}$$

where the summation is over the six faces of the element.

The starred quantities in these equations are the values at the center of the face-swept volume and are determined with a second-order upwinding scheme. The scheme requires information from the two elements upwind of the face and the one element

downwind of the face. Monotonic limiters are employed to assure that the starred quantities are never greater or less than the corresponding quantities in the upwind and downwind elements. The momentum advection calculation is performed with the node-centered element since the velocities are stored at the element nodes.

The airfoils are modeled with immovable shell elements. At the end of both the Lagrange and advection calculations, the fluid nodes adjacent to the airfoils could be away from the surface due to airfoil curvature. They are thus projected normally onto the airfoil at the end of these two calculations. In addition, at the end of both calculations, the velocity of the nodes next to the airfoil is made tangent to the surface.

During the Lagrange calculation, the exit static pressure and inflow velocity are specified. As the mesh is relaxed after each Lagrange step the inflow boundary moves into the region upstream of the domain. Consequently, the advection step requires the specification of two other boundary conditions at inflow, namely ρ^* and $(\rho E)^*$. The momentum flux $(\rho u_i)^*$ at inflow is deduced from the previously defined inflow velocity. To minimize reflections at the inflow and outflow boundaries, one-dimensional partially non-reflecting unsteady boundary conditions are used.

Modeling the 18/19-airfoil count of the IGV-rotor geometry would require the simulation of the complete annulus. To alleviate this difficulty, the vane count of the IGV row is altered so that IGV and rotor rows each have 19 airfoils, enabling them to be modeled with one passage per row. Increasing the IGV vane count by one changes the geometry of the IGV passage, but does not affect the rotor blade pass period.

IGV Response to Rotor-Generated Forcing Functions

Part-Speed

The downstream rotor potential field is the forcing function generating the upstream IGV unsteady aerodynamic response and is determined in both the experiment and the simulation. Experimentally this is accomplished by an unsteady static pressure probe at 90% span, 21.4% vane chord downstream of the IGV trailing edge and halfway between vane stacking axes. Care must be taken when situating an equivalent simulated static pressure probe since the simulation has 19 IGV's while the experiment has 18. The vane surface pressures from both the simulation and experiment are compared on the upper vane. Thus a simulated static pressure probe is located in the same position relative to the upper vane, i.e. 10° below the upper vane.

The predicted and measured forcing functions are shown in Figure 56, with the mean pressure subtracted. The initial vane-blade position at t = 0 corresponds to a rotor stacking axis being midway between experimental vane stacking axes, equivalent to the rotor stacking axis being aligned with the static pressure probe. Note that the rotor blade pass frequency is the largest frequency component in both the simulation and experiment. However, the experimental forcing function has a significant higher frequency component at two times blade pass frequency. The source of this higher frequency component is unclear, although it could be related to the IGV viscous wake periodically altering the rotor potential field, with this effect not being captured by the inviscid TAM-ALE3D

model. Nevertheless, overall agreement between the experimental and simulated forcing function is good.
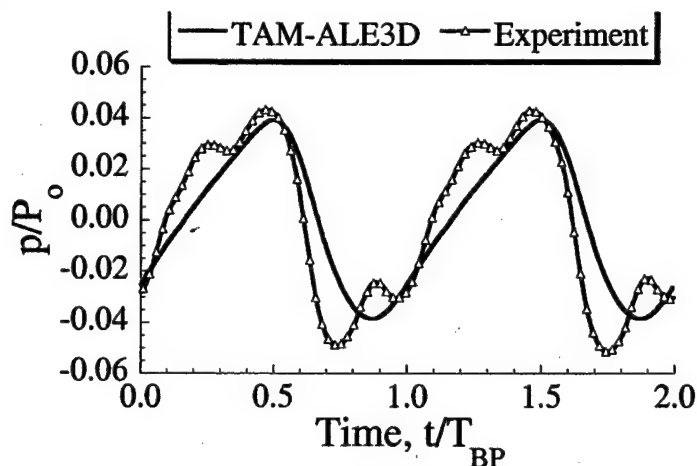
Figure 56. Rotor-generated forcing function at 15,000 rpm

The time-averaged IGV surface pressures are shown in Figure 57. The simulation over-predicts the pressure on the suction side and also on the aft half of the pressure surface. However, this over-prediction is slight, never exceeding a 0.6% difference.
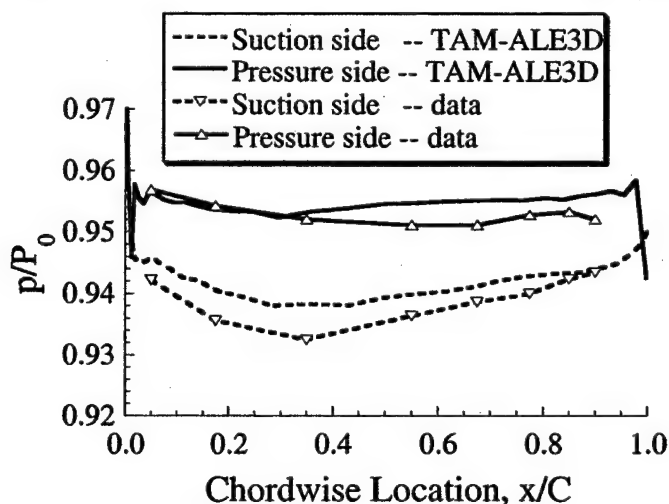
Figure 57. Time-averaged IGV surface pressure at 15,000 rpm

The time-averaged vane-to-vane flow field colored by Mach number is shown in Figure 58. The dark spots in these PIV data are areas where flow field information is not resolved due to high flow gradients or laser reflections. The IGV trunnion is also visible in the data, preventing flow field visualization near the vane at mid-chord. Note that the IGV vane-to-vane spacing is smaller for the TAM-ALE3D results than for the data because of the increased vane count used in the simulation. There are very similar flow field structures in the simulated and experimental time-averaged results, with the Mach number increasing in the vane passage due to the blockage of the vanes and a localized high Mach number region evident on the suction side of the IGV.
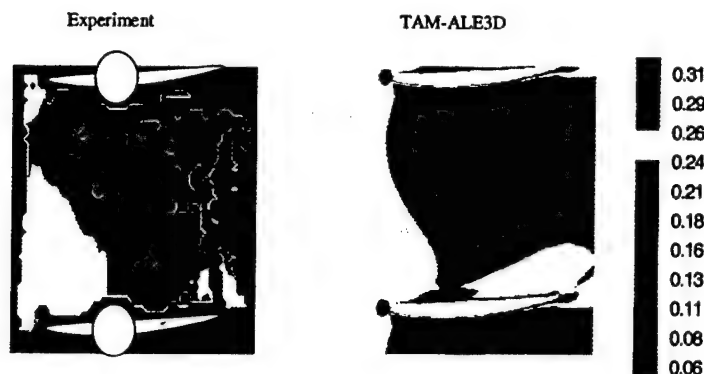
Figure 58. IGV time-averaged vane-to-vane flow colored by Mach number

Both experimental and simulated vane surface pressures are shown at ten time instants during one rotor blade pass period in Figure 59. The relationship between the IGV loading and the pressure just aft of the IGV trailing edge is shown via the forcing function plot in the figures. Recall that the forcing function probe is located 10° below the vane on which the surface pressure data are referred. Thus the probe's static pressure measurement lags the static pressure aft of the upper vane trailing edge by 0.585 times the blade pass period. The vertical lines in the forcing function denote the expected static pressure directly aft of the IGV 21.4% chord downstream for the times $t/T_{BP} = 0.0$, 0.1, etc, in the surface pressure results.

The trends predicted by TAM-ALE3D and exhibited by the data are similar, but TAM-ALE3D tends to predict larger unsteady pressure fluctuations over the entire IGV chord. In both the prediction and the experiment, the suction side loading begins to be larger than that on the pressure surface over the aft chord starting at $t/T_{BP} = 0.0$. From this time until $t/T_{BP} = 0.5$ the suction side loading is larger than the pressure side loading over most of the chord. At $t/T_{BP} = 0.5$, both predicted and experimental loadings begin to cross over again, with the pressure side loading larger from $t/T_{BP} = 0.6$ to $t/T_{BP} = 0.9$. Although it appears that the suction side of the vane has higher loading over the majority of the cycle, the vane surface pressure plot showed that the pressure side has the higher loading on a time-averaged basis.
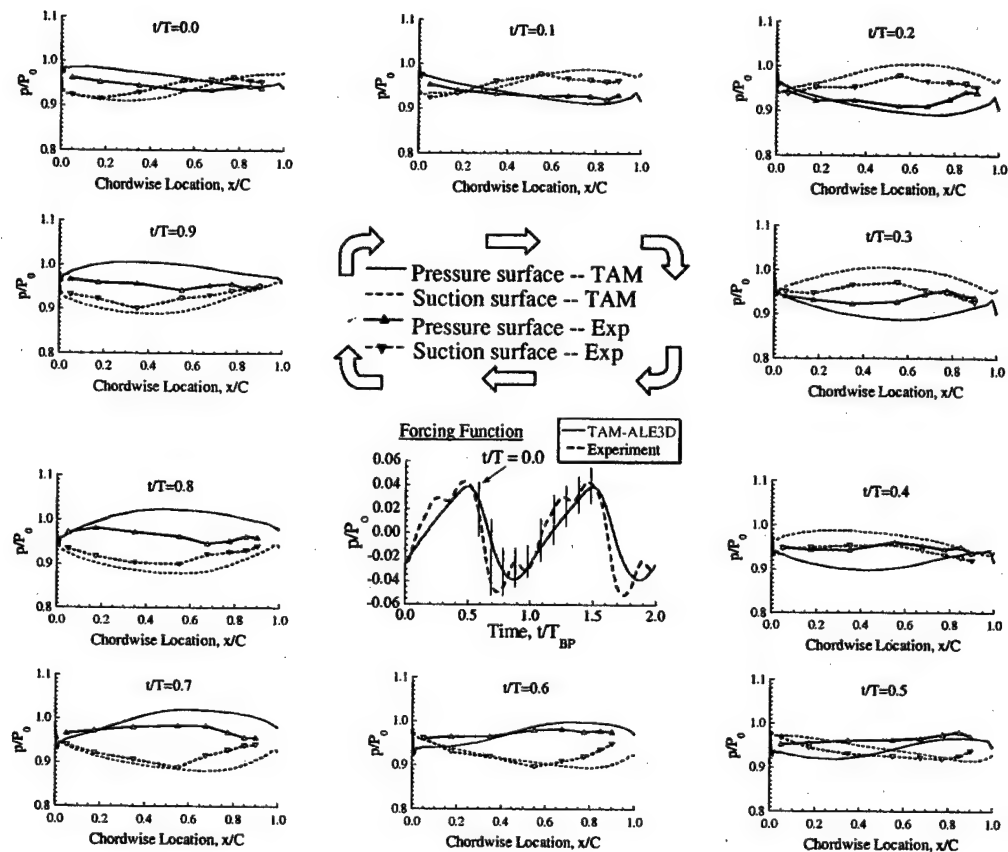
Figure 59. Predicted and measured time-variant IGV surface pressures at 15,000 rpm

The predicted and measured overall lift per unit span experienced by the vane tip at part-speed is shown in Figure 60, with the nondimensional time-averaged lift per unit span shown on the left. The instantaneous lift is normalized by the time-averaged lift, i.e. the instantaneous TAM-ALE3D predicted lift by the TAM-ALE3D time-averaged lift and the experimental instantaneous lift by the experimental time-averaged lift.
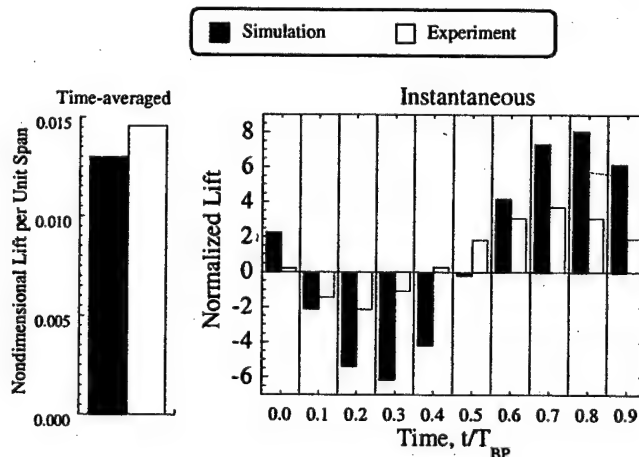
Figure 60. Time-averaged and time-variant IGV lift per unit span

For the time-averaged lift, TAM-ALE3D predicts 12% less lift than the data. This is partially due to the differing vane counts, i.e. the spacing between vanes is 5.3% less for the simulation than for the experiment. A linearized cascade analysis at similar conditions gives a decrease in steady lift of 6% for this same decrease in spacing.

For the instantaneous lift, the magnitude of the simulated lift is often over 100% larger than the measured lift, but the relative phase between the data and the prediction is similar. This large difference in unsteady lift magnitude can also be attributed to the scaling of the geometry in the simulation.

Figure 61 shows the vane-to-vane Mach number field at ten instants of time during one rotor blade pass period.
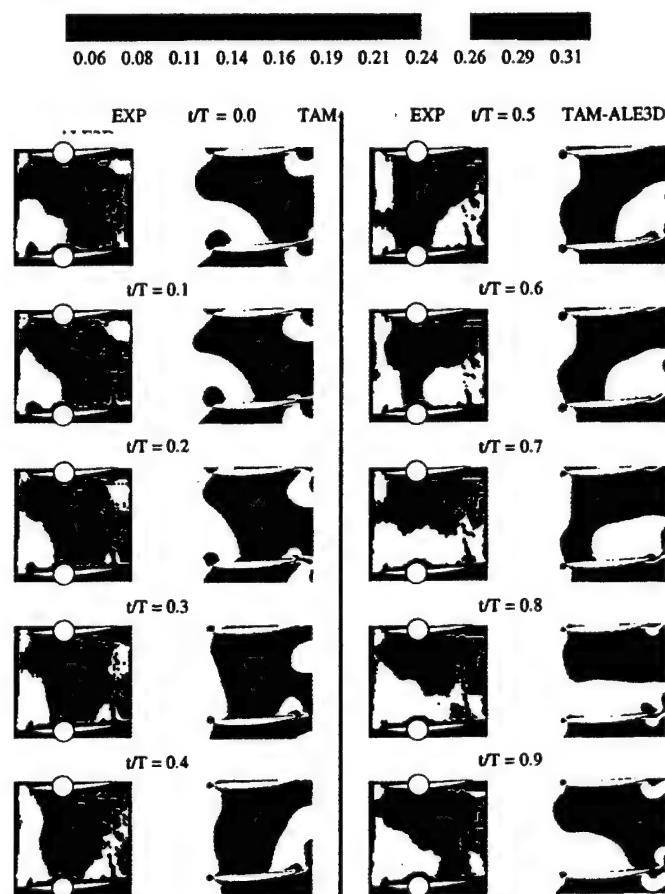
Figure 61. IGV vane-to-vane flow colored by Mach number at 15,000 rpm

There is good agreement between the predicted and measured flow fields, with the potential field from the downstream rotor affecting the entire IGV passage flow. A slightly higher Mach number region associated with an acoustic wave is seen to propagate upstream through the IGV passage. This high Mach number region enters the IGV passage at $t/T_{BP} = 0.8$, and continues propagating upstream through the passage until it leaves the IGV passage at $t/T_{BP} = 0.6$. The TAM-ALE3D simulation captures this acoustic disturbance well.

Figure 62 shows the predicted and measured time variation of the vane surface pressure at several locations along the chord – 5%, 55%, and 90% chord from the leading edge. The vertical scales in all plots are the same, so it is evident that the unsteady effects are largest in the mid-chord region.

The trend of the prediction matches that of the data. There are, however, quantitative differences. The biggest difference is the presence of higher harmonics in the data, while only the blade pass frequency is evident in the predictions. The best agreement between prediction and data is at mid-chord on the suction side of the vane, with the poorest agreement at 90% chord on the suction side. Here the data have a relatively small blade-pass frequency component, while the blade-pass frequency is dominant in the prediction.
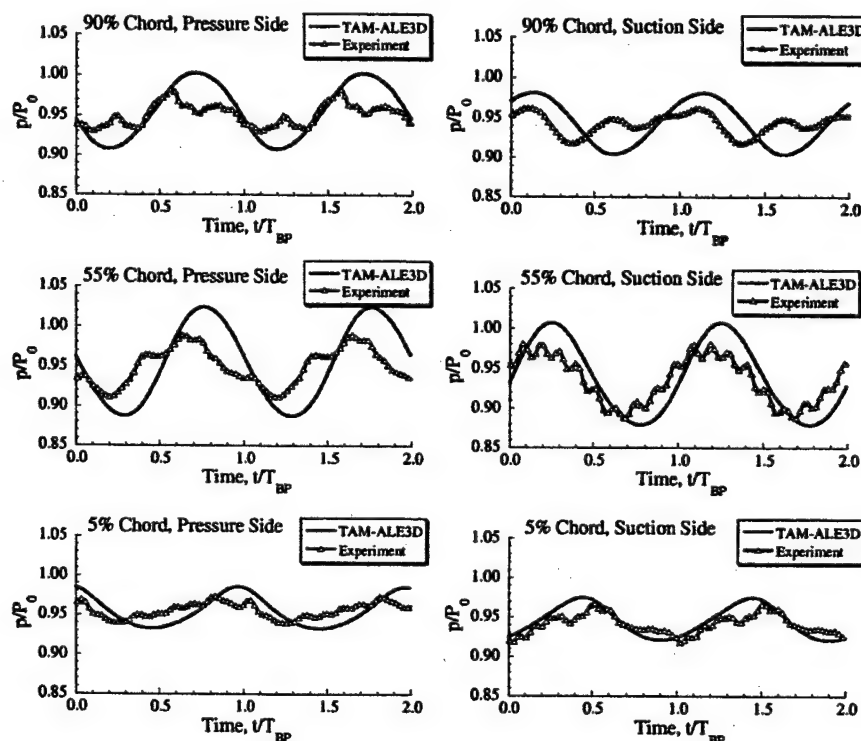
Figure 62. Predicted & measured vane surface pressures, 15,000 rpm

The trend of the prediction matches that of the data. There are, however, quantitative differences. The biggest difference is the presence of higher harmonics in the data, while only the blade pass frequency is evident in the predictions. The best agreement between prediction and data is at mid-chord on the suction side of the vane, with the poorest agreement at 90% chord on the suction side. Here the data have a relatively small blade-pass frequency component, while the blade-pass frequency is dominant in the prediction.

Design-Speed

The design-speed flow field is transonic, with a shock located on the upper half of the rotor blade. In the simulation, the location of the rotor shock differs from that in the experiment. The rotor shock structure is approximated as a straight line based on the PIV

data and the static pressure probe measurement. The simulated shock structure is obtained directly from IGV and rotor flow field visualization tools. This simulated shock is curved and is located further aft on the rotor.

For the design-speed operating point, the predicted and measured forcing functions are shown in Figure 63, with the mean pressure subtracted. The simulated shock impacts the probe 5% of a blade pass period earlier than the experimental shock. This is consistent with the shock structure shown in Fig. 13 since the simulation time zero has been adjusted to be two-tenths of a blade pass period later than experimental time zero. With this adjustment, both shocks impact the IGV at the same time and place, but the curvature of the simulated shock causes it to impact the static pressure probe before the experimental shock.
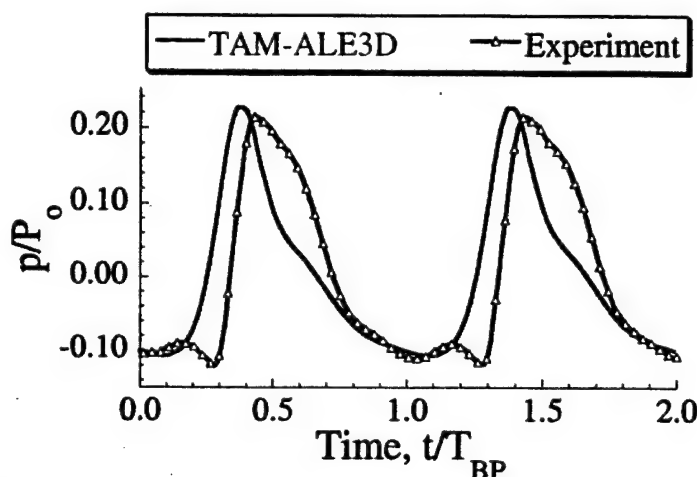
Figure 63. Rotor-generated forcing function at 20,000 rpm

The saw-tooth pattern indicative of the shock emanating from the downstream transonic rotor flow is evident in both the prediction and data. The peak-to-peak unsteady forcing function pressure is 30% of the upstream stagnation pressure and is 300% larger than the corresponding unsteady forcing function pressure at part-speed.

The time-averaged IGV surface pressures for simulation and experiment are shown in Figure 64. The prediction and data are very close over the suction side. Over the pressure side of the vane, the prediction under-predicts the pressure, with the maximum difference between prediction and data 1.2% near the leading edge.
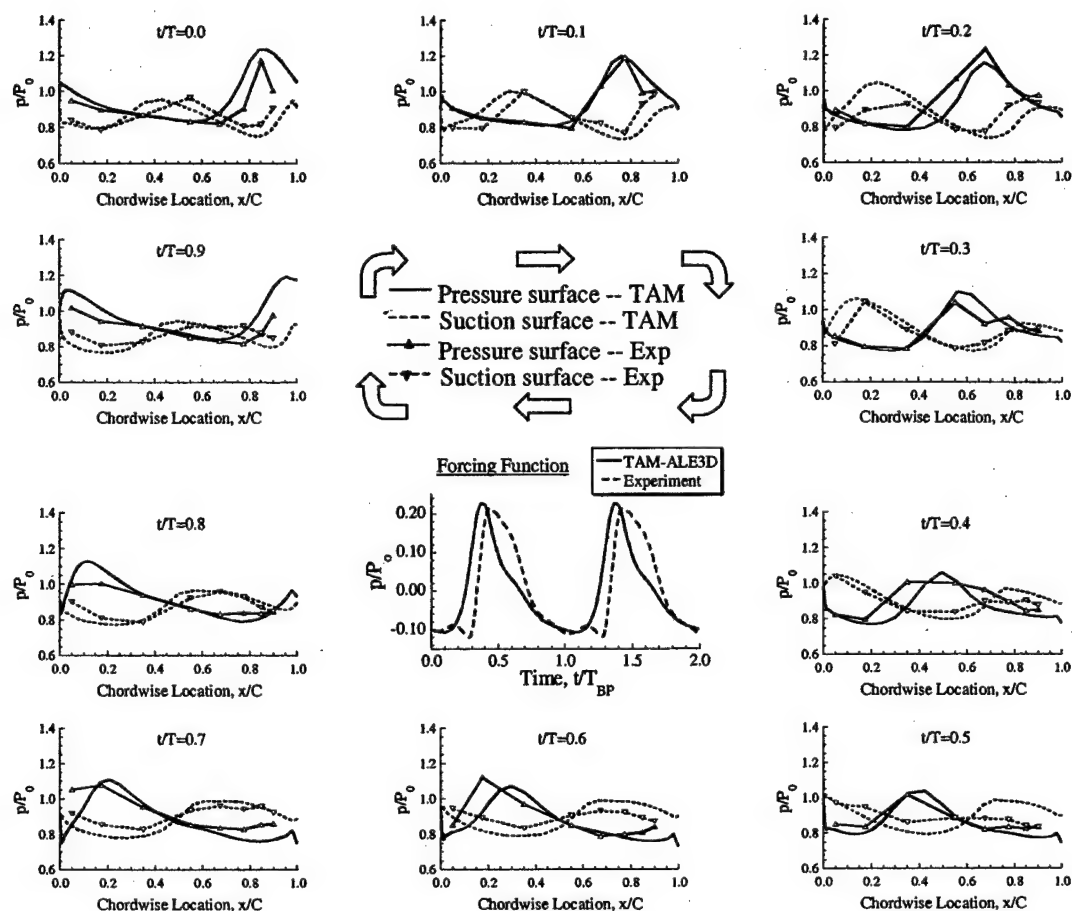
Figure 64. Predicted and measured time-variant IGV surface pressures at 20,000 rpm

The time-averaged vane-to-vane flow field colored by Mach number is shown in Figure 65. There are very similar flow field structures in the simulated and experimental time-averaged results, with a high Mach number region evident on the suction side of the IGV. Within the passage, the simulation has a slightly higher Mach number. This is expected because the increased vane count creates more blockage and thus higher velocities through the passage are required for the same mass flow rate.
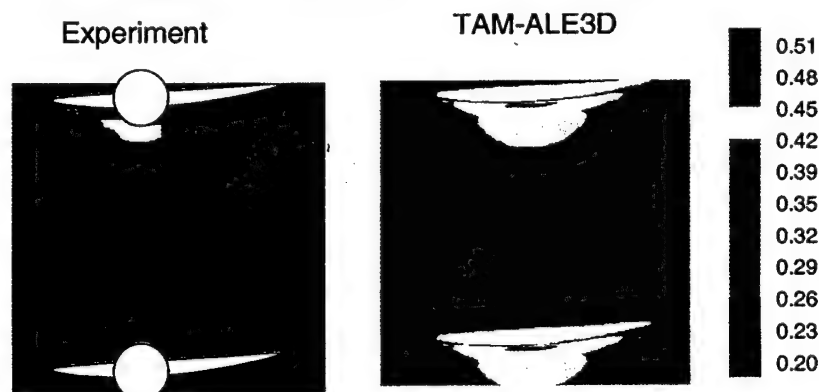
Figure 65. IGV time-averaged vane-to-vane flow colored by Mach number – 20,000 rpm

The predicted and measured overall lift per unit span experienced by the vane tip is presented in Figure 66, with these lifts normalized as before. The time-averaged lift prediction is 19% lower than the data, partially explained by the geometry scaling. With regard to the instantaneous lift, first note that the differences between the instantaneous time-averaged lift are smaller at design-speed than at part-speed. This is understood by noting that the instantaneous lift is proportional to the area between the suction side and pressure side loading curves versus chord. Because of the large variations in IGV loading along the chord at design-speed, the net area between the curves varies relatively little from one time to the next. In contrast, at part-speed, the loading varies relatively slowly along the chord. Thus, although these curves do not have localized loadings as large as at design speed, the total area between the suction and pressure side curves (i.e. the lift) becomes relatively large. Thus, in terms of net lift on the vane, part-speed has more unsteadiness than does the design-speed condition. However, in terms of localized loadings along the chord, the design-speed flow produces more unsteadiness.
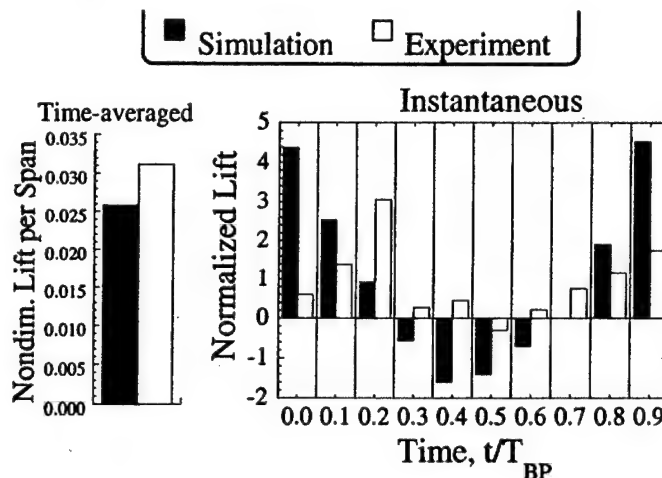
Figure 66. Time-averaged and time-variant IGV lift per unit span at 20,000 rpm

The predicted and measured instantaneous lift differ significantly at times and are in good agreement at times, with the best agreement at t/T_{BP} = 0.1 and 0.8. This is associated with the large pressure variations along the chord. Namely, with the large spatial variations in the surface instantaneous loading, small variations can cause large differences in the instantaneous lift. Hence, very accurate unsteady pressure predictions are necessary to accurately predict the instantaneous lift. Specifically, the simulated lift tends to follow a simple sinusoidal pattern in time. In contrast, the data have a more complicated time history, containing significant higher harmonic contributions.

Figure 67 shows the Mach number field at ten time instants during one rotor blade pass period. The strong shock from the transonic downstream rotor, indicated by the dark green regions just aft of the high Mach number red regions, is seen to propagate through the IGV passage. At t/T_{BP} = 0.0, the shock impacts the IGV trailing edge. The shock reflection by the IGV pressure surface at later times causes a large increase and then a large decrease in Mach number along this surface. This large gradient region propagates upstream along the pressure surface until it reaches the IGV leading edge at t/T_{BP} = 0.8 and exits the passage. The reflected shock on the pressure surface makes an angle equal

and opposite to the incident shock angle, and thus angles back toward the downstream direction. Starting at $t/T_{BP} = 0.2$, this reflected shock breaks the high Mach number region in the middle of the passage into two parts. The simulation shows excellent agreement with the data in the context of these highly complex flow phenomena.
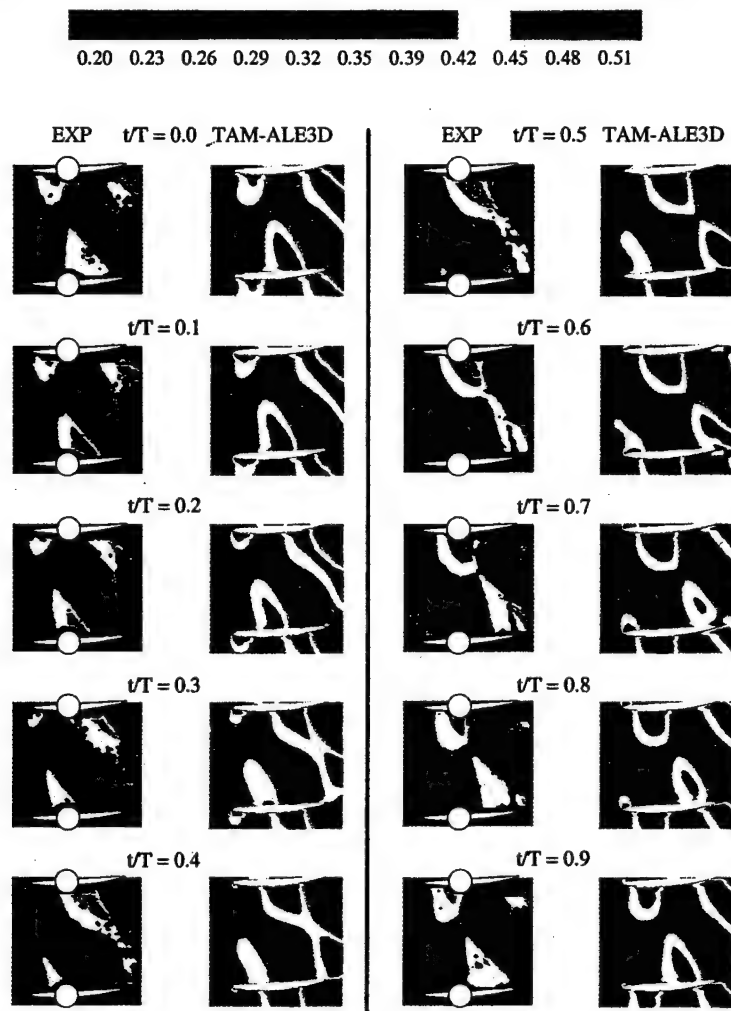
Figure 67. IGV vane-to-vane flow colored by Mach number at 20,000 rpm

Figure 68 shows the predicted and measured time variation of the vane surface pressure at locations 5%, 55%, and 90% chord from the leading edge. Note that the variation in pressure on the vane pressure side is much larger than on the suction side. On both suction and pressure sides, a significant difference between the prediction and the data is the higher harmonics in the data.
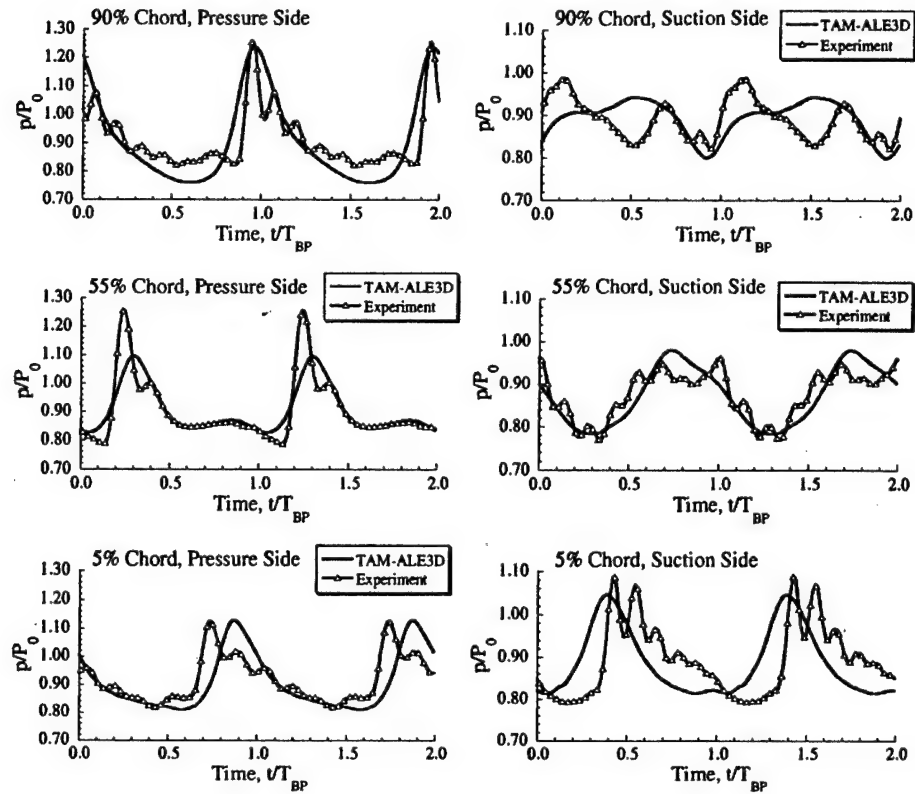
Figure 68. Predicted and measured vane surface pressures - 20,000 rpm

On the vane pressure side, the movement of a large pressure disturbance is evident over the entire chord. This is the incident shock and its reflection propagating from downstream to upstream. The peak in pressure in the simulation and experiment occurs at a similar time at 90% chord. However, this pressure pulse appears to move upstream more slowly in the simulation than in the experiment. The magnitude of this peak is similar between experiment and simulation at 90% chord, but at 55% chord the simulation peak drops approximately 15% while the experimental peak remains the same. Between 55% and 5% chord the experimental peak drops 15% and the simulated peak remains about the same, so they have approximately equal magnitude at 5% chord.

On the vane suction side there is poor agreement between experiment and simulation at 90% chord. This could be attributed to inadequate mesh resolution in the trailing edge region. Surprisingly, the agreement improves at 55% and 5% chord. Both in the experiment and in the simulation, the suction side disturbance increases in strength as it moves from trailing edge to leading edge.

Vane Row Mistuning For Hcf Minimization

This study is directed at coupled fluid-structure HCF prediction in a multi-stage environment, with a special emphasis on detuning strategies for HCF minimization. This is accomplished utilizing TAM-ALE3D, a finite element model that solves the three-dimensional Euler equations to simulate the blade row interaction generated unsteady flow and vibration phenomena in the IGV row of the Purdue Transonic Compressor. A trailing edge flapping mode in the IGV's is excited by the downstream rotor operating subsonically (15,000 rpm). Two detuning strategies are evaluated: (1) decreasing the rotor-generated forcing function to the upstream IGV's, accomplished by detuning the rotor by unequal blade tangential spacing and (2) altering the IGV-rotor unsteady aerodynamic interactions, thereby decreasing the IGV modal forcing. These two strategies are quantified by the unsteady aerodynamic modal force and internal IGV stresses, with the unsteady stresses a key HCF metric.

The IGV's experienced cracking during operation at 15,000 rpm, Figure 69. These cracks are due to excitation of the trailing edge flapping mode, with the 4,750 Hz excitation from the downstream 19-bladed rotor potential field. The frequency of this flapping mode is 4,200 Hz, close enough to the excitation frequency to cause HCF problems. This case is ideal for the application and evaluation of HCF passive detuning techniques that reduce aerodynamically induced unsteady stresses while minimally impacting performance and reliability. Two detuning strategies are evaluated: (1) decreasing the rotor-generated forcing function to the upstream IGV's, accomplished by a 4° shift in the tangential location of every other rotor blade and (2) decreasing the IGV modal forcing by altering the IGV-rotor unsteady aerodynamic interactions through a 4° shift in the tangential location of every other vane.
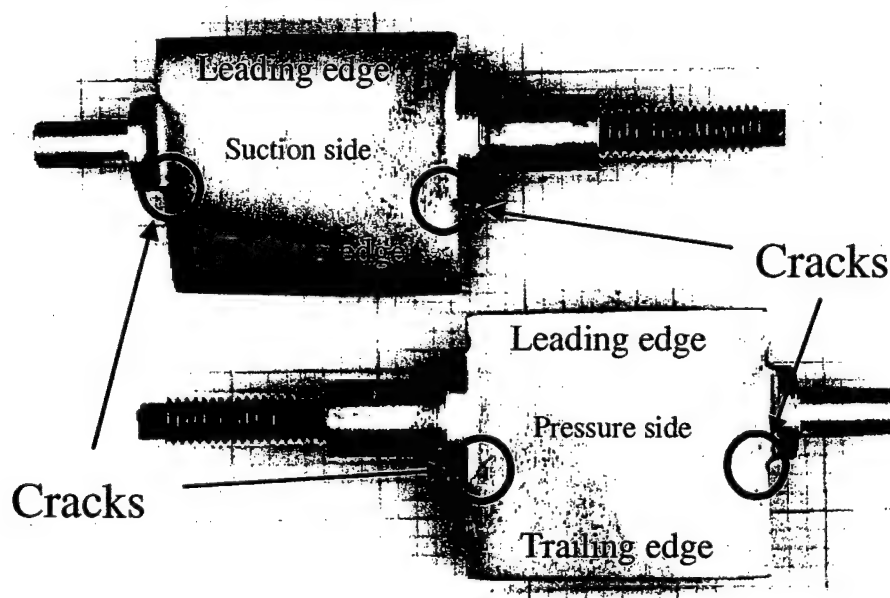
Figure 69. IGV cracking experienced at 15,000-rpm operation

Although not required for the TAM-ALE3D analysis, dynamic characterization of the IGV without aerodynamics is appropriate to verify that the IGV dynamic behavior is

similar to that observed in experiment, especially for the trailing edge flapping mode. The TAM-ALE3D IGV-only model is a mesh having 2,204 hexahedron elements and 3,000 nodes. Four elements across the thickness are needed for acceptable natural frequency results. Special effort is made to pack elements around the four high stress regions where cracking occurred, Figure 70.
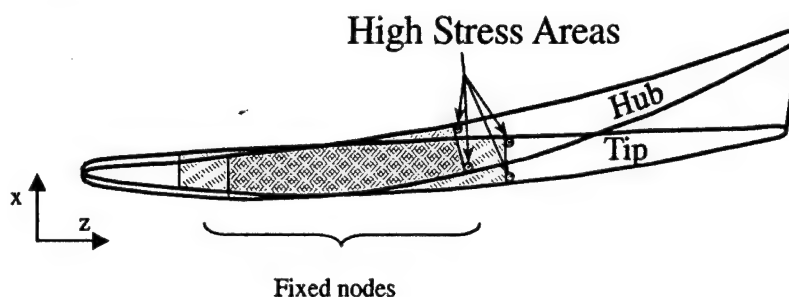
Figure 70. High stress areas on the IGV.

Characteristics of the IGV trailing edge flapping mode are obtained by applying an impulse from hub-to-tip at the vane trailing edge. After the impulse, the vane is allowed to respond freely for 4 milliseconds. The resulting mode shape is captured by sampling the displacement of the nodes at vane mid-thickness at a time when the vane displacement is largest. The frequency of the mode is deduced from this time trace at 4,024 Hz, close to the 4,200 Hz frequency observed in experiment.

For the baseline case, only one airfoil passage for each airfoil row is analyzed, with periodic boundaries accounting for the presence of the other vanes/blades in the rows. Each passage is modeled with an unstructured assembly of hexahedron elements, with the IGV fluid mesh having 9,680 hexahedron elements and 11,688 nodes. The IGV structural mesh is the same as that used for the IGV structural analysis. The rotor fluid mesh has 9,152 elements and 11,064 nodes. The steel rotor blade is modeled with 532 elements and 900 nodes. There are 11 layers of elements in the spanwise direction for the rotor and IGV fluid meshes. These relatively coarse meshes are required because of the small time steps and thus large CPU times necessary for these fluid-structure interaction studies.

The computational procedure is as follows. The airfoils are modeled as rigid while the flow is established using a 0.25 microsecond time step. The IGV's are then allowed to move freely in response to the flow and the time step is reduced by an order of magnitude to 0.016 microseconds to capture the vane short time scale response. The aerodynamics and response of the IGV's are simulated for 11 milliseconds which requires approximately 10 days on two SGI RS10000 processors running in parallel.

The four HCF failure locations on the IGV, Figure 70, are investigated by writing out the stress tensor at these locations throughout the simulation. Transforming these stresses to an equivalent Von-Mises stress yields the four stress time-histories shown in Figure 71. The beating pattern in the stresses is due to the proximity of the forcing frequency (4,500 Hz) to the mode natural frequency (4,024 Hz). The response at the mode natural frequency is damped and accounts for the decay in the signals. Ideally, the simulation would be run until the natural frequency response is negligible, resulting in the

periodic steady state stress at the forcing frequency. However, computational resources dictate that the simulation run for a short time period (10 days), with post-processing tools used to extract the periodic steady state stress amplitude.
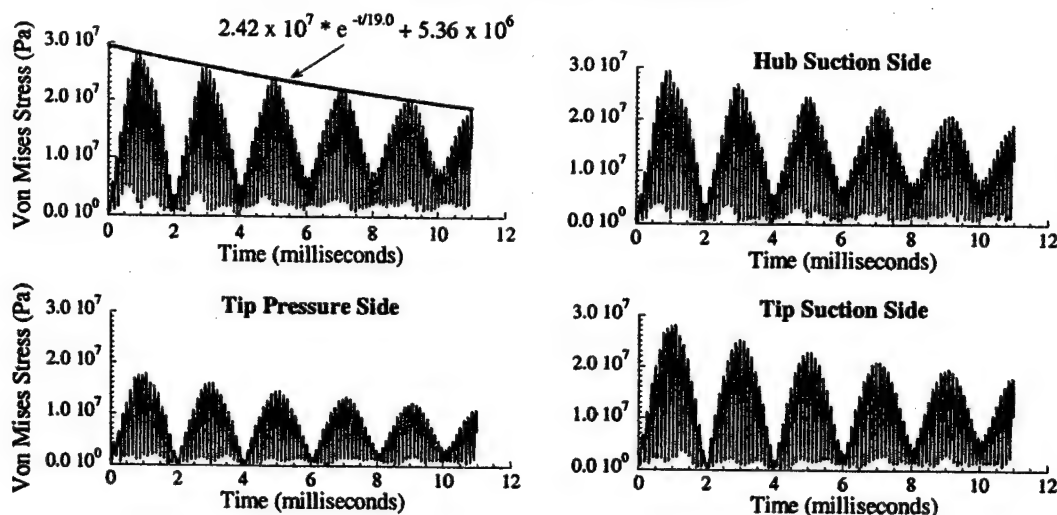
Figure 71. Stress time-histories for four high stress locations on the IGV

The peaks of the stress time form envelopes that follow

$$A_h e^{-t/\tau} + A_p$$

where A_h is the decaying homogeneous solution amplitude and A_p is the steady state stress amplitude and are found by a least squares curve fit.

The periodic steady state stress amplitude A_p is the unsteady stress experienced by the airfoil for $t \to \infty$, and thus is a key HCF metric. The upper left-hand plot 4 shows the calculated envelope for the IGV pressure side at the hub. The periodic unsteady Von-Mises stress amplitude as $t \to \infty$ is 5.36 MPa.

Rotor-Spacing Detuning

The rotor detuning strategy offsets every other blade 4° tangentially. With this approach, the aerodynamic forcing function to the IGV's, i.e. the rotor-generated potential field, will have less energy at the dominant blade pass frequency (4,500 Hz). This is desirable since any energy near the IGV trailing edge flapping mode natural frequency (4,024 Hz) contributes to HCF.

With this rotor-spacing detuning, the fundamental spatial period of the flow is two airfoil passages. Thus, the TAM-ALE3D simulation is accomplished by placing two IGV passages side-by-side and two rotor passages side-by-side, with periodic boundaries accounting for the remainder of the row. The number of elements and nodes per passage is the same as the baseline. The simulation time is 24 CPU-days, over twice that of the baseline because of the doubling of the domain sizes.

After the flow has converged to a periodic steady state and before the airfoils are allowed to respond, the aerodynamic flow field is analyzed. The unsteady pressure 21.4% of the IGV chord downstream of the IGV is sampled and plotted in the frequency

domain for the baseline and detuned configurations, Figure 72. The BPF component for the detuned geometry is 89% of that for the baseline geometry. Note that some of the energy for the detuned potential field has moved to 2,250 Hz.
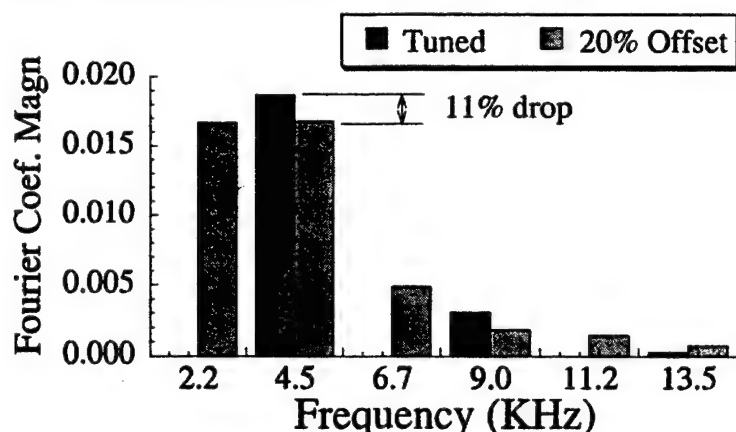
Figure 72. TAM-ALE3D predicted frequency spectra for tuned and rotor-spacing detuned geometries.

Figure 73 shows the vertical axis of Figure 5 along the horizontal axis and the modal forcing at BPF for the IGV flapping mode on the vertical axis. The red line is an IGV-rotor axial spacing study which demonstrates that the IGV modal forcing decreases as IGV-rotor axial spacing increases. The single solid triangle is the rotor-spacing detuning result. Unfortunately, the rotor-spacing detuning, while decreasing the excitation source at BPF, decreases the IGV modal forcing at BPF less than that observed by an equivalent increase in axial spacing.
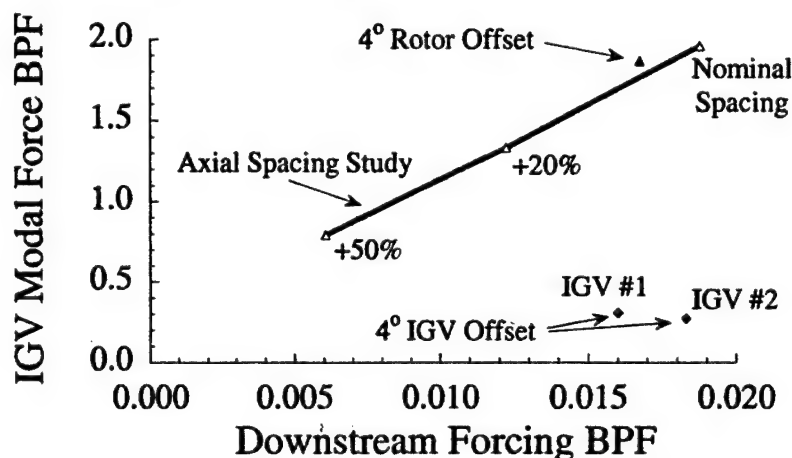
Figure 73. IGV modal force versus downstream forcing

The results of the full fluid-structure interaction simulation are shown in Figure 74, with the periodic unsteady Von-Mises stress amplitude and a comparison to the baseline results given in Table 1. The last column shows that the rotor-spacing detuning actually increases the periodic steady state stress amplitude by about 70%. It is likely that although the 4,500 Hz component decreases with the rotor-spacing offset, the new 2,250

Hz component adds enough energy to the IGV flapping mode to make this detuning strategy undesirable.
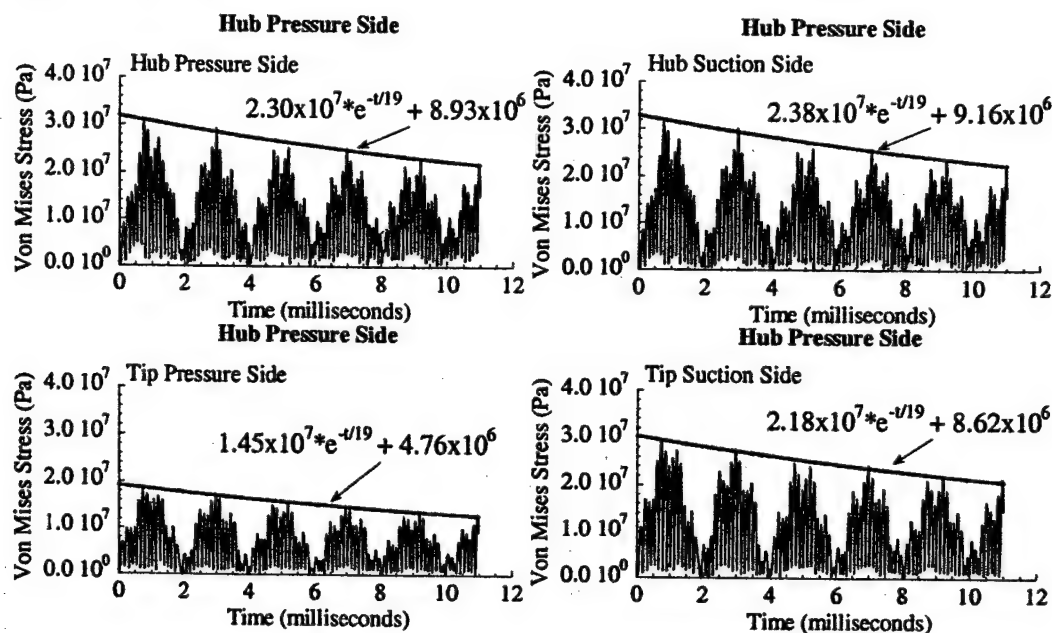
Figure 74. IGV stress time-histories for rotor-spacing detuned geometry

	Tuned	Detuned	Ratio detuned/tuned
Hub Pressure Side	5.36	8.93	1.67 ↑
Hub Suction Side	5.65	9.16	1.62 ↑
Tip Pressure Side	2.59	4.76	1.84 ↑
Tip Suction Side	4.92	8.62	1.75 ↑

Table 1. Periodic unsteady stress amplitude (MPa) with rotor-spacing detuning

IGV-Spacing Detuning

The second detuning strategy is to offset every other IGV by 4° tangentially. With this approach, the IGV-rotor unsteady aerodynamic interactions are altered, providing a substantial decrease in the IGV modal forcing. Having equal numbers of airfoils corresponds to a zero interblade phase angle, with the effect of this acoustic excitation on the IGV unsteady forcing analyzed by a two dimensional linear detuned aerodynamic model developed by Sawyer and Fleeter. The model superimposes the linear solutions from two flat plate cascades having different geometries, thus providing the unsteady loadings for a single detuned cascade. The upwash boundary condition is specified as an upstream-going acoustic wave with zero interblade phase.

Figure 75 shows the IGV loading versus detuned spacing ratio, i.e. the ratio of the tangential spacing. A spacing ratio of 0.5 represents a uniformly spaced or tuned cascade and a spacing ratio of 0.4 represents a 4° offset for the 18-vaned IGV row. Cascade A and B are the two cascades comprising the single detuned cascade in this linear model. There is a significant decrease in the unsteady IGV loading away from the tuned

condition, indicating that the detuning disrupts the acoustic wave. The unsteady loading decreases by a factor of approximately five for the 4° offset.
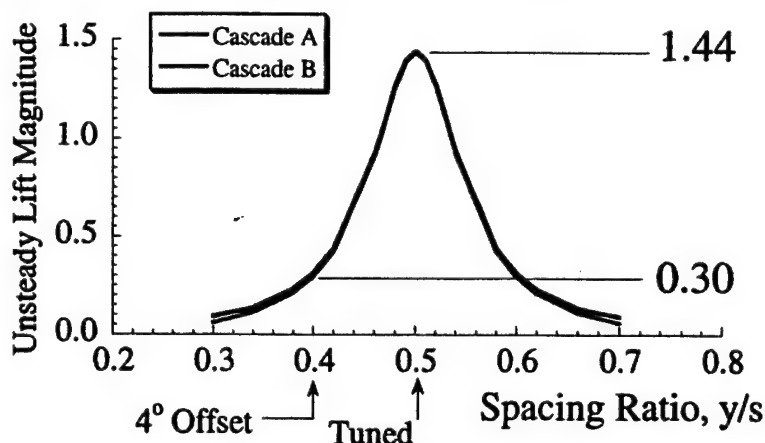
Figure 75. IGV unsteady loading versus detuned spacing ratio. Excitation provided by upstream propagating zero-lobed IGV-rotor interaction acoustic mode

The TAM-ALE3D model uses the same number of elements for the two IGV and two rotor passages as used in the rotor-spacing detuning study. An analysis of the periodic steady state aerodynamics of the TAM-ALE3D simulation is performed before allowing the airfoils to respond, with the resulting IGV modal forcing versus the downstream forcing at BPF. Because of the loss of symmetry, the forcing at two downstream positions are considered, each 21.4% IGV chord downstream and tangentially centered in adjacent IGV passages. In addition, the modal forcings for two adjacent IGV's are shown as the solid diamonds. As expected, the IGV-detuning does not decrease the downstream generated forcing, but the average IGV modal forcing decreases by a factor of approximately 6.5 over the baseline, thus corroborating the linear detuned model predictions.

The full fluid-structure interaction simulation is performed with TAM-ALE3D by allowing the IGV and rotor airfoils to respond to the aerodynamic forces. This simulation is performed for 11 milliseconds, with the resulting internal IGV stress time-histories monitored and post-processed. The periodic unsteady Von-Mises stress amplitudes at the four critical stress locations on two adjacent IGV's are given in Table 2. The detuned stress amplitude decreased from the baseline by a factor of approximately six, thus validating that IGV-spacing detuning is an excellent strategy for alleviating the large HCF stresses in the IGV's at the 15,000-rpm operating condition.

	Tuned	Detuned		Ratio
		IGV #1	IGV #2	tuned/detuned
Hub Pressure Side	5.36	0.984	0.778	5.4/6.9 ↓
Hub Suction Side	5.65	0.956	0.897	5.9/6.3 ↓
Tip Pressure Side	2.59	0.314	0.459	8.2/5.6 ↓
Tip Suction Side	4.92	0.507	0.981	9.7/5.0 ↓

Table 2. Periodic unsteady stress amplitude (MPa) with IGV-spacing detuning

Conclusions

This study was directed at coupled fluid-structure HCF prediction in a multi-stage environment, with a special emphasis on detuning strategies for HCF minimization. This was accomplished utilizing TAM-ALE3D, a finite element model that solves the three-dimensional Euler equations, to simulate the blade row interaction generated unsteady flow and vibration phenomena in the IGV row of the Purdue Transonic Compressor. Aerodynamic excitation to the IGV's is caused by the downstream rotor row operating at subsonic conditions, which excites a trailing edge flapping mode in the IGV's. Two detuning strategies were evaluated: (1) decreasing the rotor-generated forcing function to the upstream IGV's, accomplished by detuning the rotor by unequal blade tangential spacing and (2) altering the IGV-rotor unsteady aerodynamic interactions, thereby decreasing the IGV modal forcing. Evaluation of these strategies was quantified by the unsteady aerodynamic modal force and internal IGV stresses, with the unsteady stresses a key HCF metric.

The rotor-spacing detuning was aimed at decreasing the BPF component of the unsteady forcing, which is near the IGV flapping mode frequency. This detuning did decrease the BPF component, but it also created a component at ½ of the BPF. The full fluid structure TAM-ALE3D simulation showed that the unsteady internal IGV stresses actually increased due to rotor-spacing detuning, with the ½ BPF component likely contributing to this increase.

The IGV-spacing detuning was aimed at disrupting the zero interblade phase IGV-rotor interaction mode. A two dimensional linear analysis predicted a factor of five decrease in the IGV loading by offsetting every other IGV 4°. The TAM-ALE3D simulation showed the unsteady internal IGV stresses decreased by a factor of approximately six due to this passive IGV detuning strategy.

Flutter Suppression Via Structural Mistuning

Structural mistuning, defined as small structural differences between blades in a row, has long been known to have a favorable effect with regard to flutter. Whitehead showed that this result is valid regardless of nature of the aerodynamic coefficients, as long as the coefficients linearly relate the airfoil displacement or velocity to the aerodynamic force. This has led to the concept of designed structural differences between rotor blades, i.e. intentional structural mistuning, for passive control of flow-induced vibrations.

The effects of mistuning on blade row flow-induced vibrations were initially analyzed with lumped parameter models. More recently, component mode synthesis and receptance techniques combined with finite element models have been developed. These structural mistuning models do not, however, utilize unsteady aerodynamic analyses to calculate the unsteady aerodynamic forces generated by the blade motion. Unfortunately, blade row unsteady aerodynamics play a key role in flow-induced vibrations. Namely, the driving phenomena for these vibrations are the blade row unsteady aerodynamics. Hence, for accurate prediction of mistuned blade row flow-induced vibrations, it is necessary to incorporate an unsteady aerodynamics model with the structural mistuning model.

In the classical flow-induced vibration approach, the fluid and airfoil motion are not coupled, i.e., the fluid and airfoil structure are modeled separately. They are coupled by specifying the kinematic boundary conditions at the fluid-airfoil boundary, with the airfoil motion specified as a boundary condition to the unsteady flow analysis. Thus, the fluid and structure are coupled only in that the unsteady aerodynamic forces and airfoil state are passed between each model after each time step. Unfortunately, this uncoupling of a truly coupled fluid-structure interaction problem introduces errors, specifically this pseudo-coupling produces phase-lagging errors that can act as energy sources or sinks in the system.

The analysis of blade row flow-induced vibrations is, in fact, a coupled fluid-structure interaction problem. Namely, the blade row unsteady aerodynamics is dependent on the airfoil motion and, in turn, the airfoil motion is dependent on the unsteady aerodynamics. Thus, instead of utilizing separate fluid and structural models, a coupled interacting fluid-structures analysis is needed to accurately predict flow-induced vibrations of both tuned and mistuned turbomachine blade rows,. Such an analysis would enable quantitative intentional mistuning issues for passive flutter control to be addressed, for example the level of mistuning and the mistuning pattern needed to increase the flutter velocity by a certain percentage

A fluid-structure interaction model that predicts the energy exchange between the fluid and structure is obtained by modeling both the fluid and structure with consistent numerical schemes. The TAM-ALE3D finite element model maintains this consistency by modeling both the fluid and structure with the same finite elements and simultaneously marching them forward in time. This consistent approach makes the TAM-ALE3D analysis suitable for flutter calculations, wherein accurate modeling of the energy exchange between the fluid and structure is essential for flutter boundary prediction.

In this paper, the 1st torsion-mode flutter boundary for a baseline-tuned rotor is first predicted utilizing TAM-ALE3D, with the flutter boundary determined by impulsing the blading and observing its oscillatory growth/decay rate. This is accomplished by marching the fluid equations of motion forward in time with the blades fixed until the flow has reached steady state. The blades are then released and allowed to respond freely, thereby enabling the flutter boundary, specifically the nondimensional damping factor to be determined. The airfoil row is then intentionally structurally mistuned by changing the Young's modulus of every other blade from its nominal value. The structurally mistuned rotor dynamics and unsteady aerodynamics are then analyzed utilizing TAM-ALE3D.

TAM-ALE3D Flutter Simulation

Preliminary design of the baseline rotor with a 1st torsion mode flutter instability was accomplished utilizing the linearized unsteady aerodynamic analysis LINSUB. It predicts that the tuned rotor design, Table 3, will be unstable in its 1st torsion mode for an interblade phase angle of 90° with an oscillation frequency less then 565 Hz.

The TAM-ALE3D simulations in a vacuum for this aluminum blade with a Young's modulus of 0.717 Mbars, a Poisson's ratio of 0.368, and density of 2.793x10^3 kg/m^3 show that the blade oscillates with a 1st torsion natural frequency of 373 Hz. This

is well below the LINSUB stability limit of 565 Hz, so the blade row should be unstable in its 1st torsion mode with an interblade phase angle of 90°.

Baseline Tuned Rotor Geometry	
Blade Chord	0.07 m
Blade thickness	0.004 m
Radius hub/tip	0.2 m / 0.4 m
Stagger hub/mid-span/tip	43.0° / 54.4° / 61.8°
Number of blades	72

Table 3. Unstable tuned rotor properties

To allow for a 90° interblade phase angle in TAM-ALE3D, four blade passages are modeled simultaneously, with four processors each running a single blade passage. Figure 76 shows a schematic of the rotor including the four blade passages that are simulated.
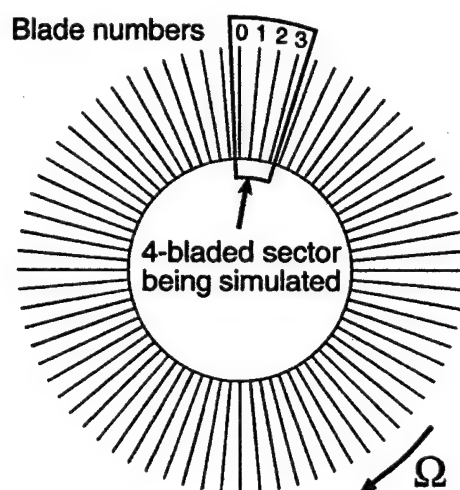
Figure 76. Front view of unstable rotor and the four blade passages being simulated

The mesh for the metal blade has 2,262 elements, 39 spanwise, 29 chordwise, and 2 across the thickness. Each blade passage for the fluid mesh has 772 elements for a constant radius sheet with 19 elements spanwise for a total of 14,668 elements. This relatively coarse fluid mesh is required to reduce run times for the computationally intensive fluid-structure interaction simulations.

The first step in the TAM-ALE3D simulation is to march the fluid equations forward in time with the blade fixed until the fluid has reached steady state. The blades are then allowed to respond freely to the aerodynamic and centripetal forces until they reach their steady state position, with the time step reduced since the short time scales in the responding aluminum blades must be captured. The blade motion is stopped at key instants to damp unwanted vibrations and accelerate the blade movement to their equilibrium positions.

To accelerate the initiation of self-induced oscillations, Blade 0 is impulsed with a nose-down moment while Blade 2 is simultaneously impulsed with a nose-up moment. Blades 1 and 3 are not impulsed. The impulse is a force of 5 Newtons applied for 0.2

milliseconds to each of the four nodes at the blade tip. The response of the leading edge of the four blades in the form of displacement time histories is shown in Figure 77. There are two major frequency components in the response after 20 milliseconds, with the amplitude of both growing in time. The lower frequency component corresponds to the 1st bending mode, while the higher one corresponds to the 1st torsion mode. By 85 milliseconds, the displacements have become as large as 2 millimeters, or 2.8% of the chord. The interblade phase angle for the 1st bending mode response is 90°, with post-processing tools showing that the 1st torsion mode response also has a 90° interblade phase angle. The instability in the 1st torsion mode response is expected from the LINSUB analysis, but the instability in the 1st bending mode was not predicted by LINSUB.
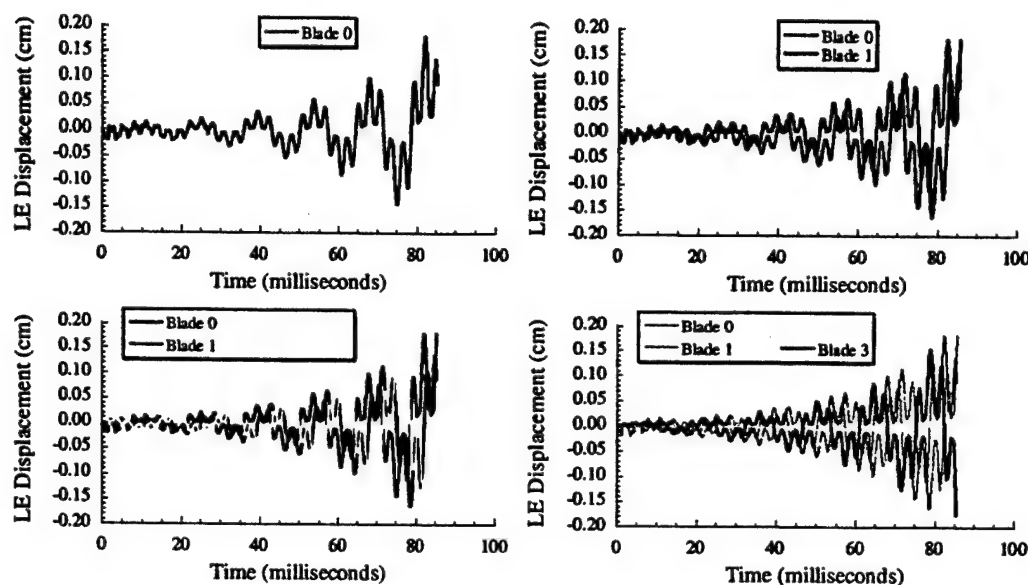
Figure 77. Blade displacement normal to chord

Mistuning strategies to stabilize blade response are most needed in the vicinity of the rotor neutrally stable point. Thus, the blade stiffness in the TAM-ALE3D model is gradually increased until the turned rotor blading becomes stable, accomplished by increasing Young's modulus from its value for the previous case of 0.717 Mbars.

By considering the response of the leading and trailing edges of Blade 0 for various Young's modulus, it is determined that the 1st torsion mode is dominant for Young's modulus of 1.25 Mbars and larger, and it is this mode that is the focus of this study. The 1st torsion mode response is analyzed by: (1) isolating this response by filtering in the frequency domain, (2) identifying and storing the peaks and troughs of the response, (3) determining the mean frequency with its standard deviation and the growth/decay rate based on these peaks and troughs. A band pass filter is used in Step 1, with the band-center frequency set to the torsion natural frequency and the band half-width set to 200 Hz. For Step 3, the initial part of the response is not included so that transient effects are excluded.

The 1st torsion mode exponential decay envelope, $e^{-\omega \zeta t}$ where ω is the natural frequency in-flow, is shown in Figure 78. In-flow, the neutrally stable point occurs at 576

Hz, approximately 11 Hz above the neutrally stable point predicted by LINSUB. The two stable cases correspond to Young's modulus of 2.0 and 2.8 Mbars or natural frequencies of 595 Hz and 706 Hz.
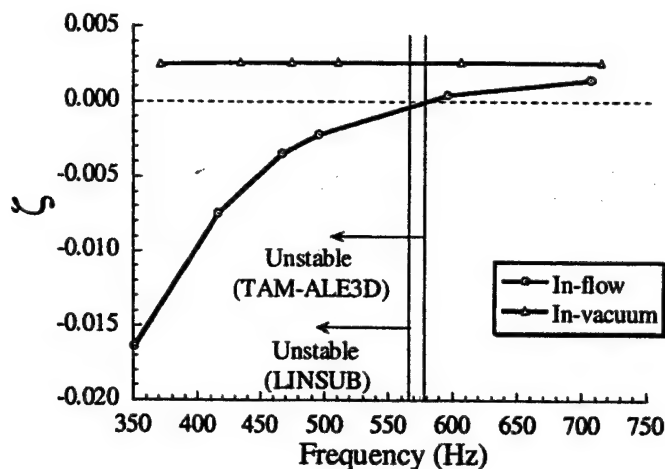
Figure 78. Decay rate for 1st torsion mode, e$^{-\square\square}$

With Young's modulus = 1.4 Mbars, the tuned rotor is near the neutrally stable point. Hence, this case is examined in detail. First it is observed that the torsion mode response has an interblade phase angle of 90°, Figure 79.
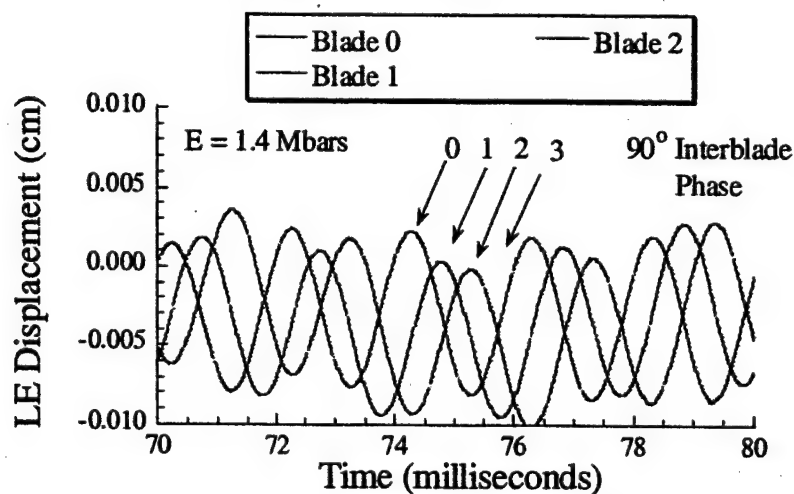
Figure 79. Tuned rotor blade leading edge displacement showing 90° interblade phase angle

The time-variation of the unsteady moment for Blade 0 about mid-chord is shown in Figure 80 as the blue line. Also shown as the red line is the time-variation of the blade pitch angle for one cycle of pitching oscillation. Both the unsteady moment and pitch angle vary harmonically in time, with the moment leading the pitch angle. This is an indication that the this tuned rotor is unstable from an unsteady aerodynamics point of view since a component of the unsteady moment is in phase with the pitching velocity.
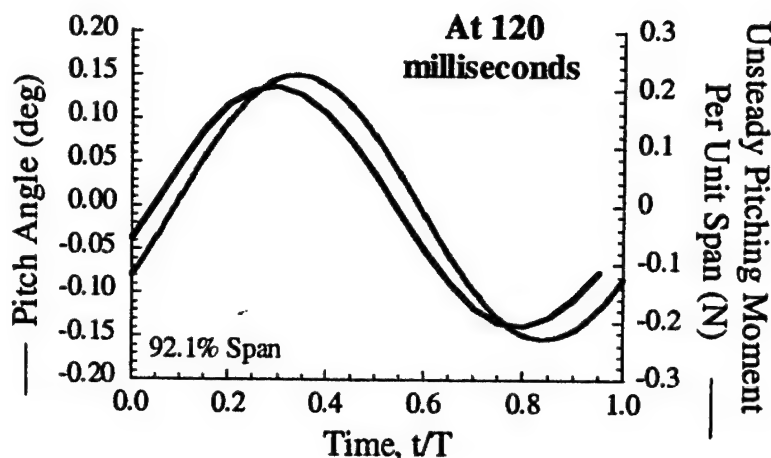
Figure 80. Unsteady moment and pitch angle versus time

Intentional Structural Mistuning

Intentional structural mistuning is considered to stabilize the baseline-tuned rotor that has been shown to be unstable in torsion for blades with a torsion natural frequency less than 580 Hz. The structural mistuning strategy is to alternate Young's modulus around the rotor. Blades 0, 2, 4, ... have a Young's modulus of 1.4 Mbars, while Blades 1, 3, 5, ... have a Young's modulus of 1.2 Mbars. The stiffer set of blades has a torsion natural frequency of 495 Hz, while the "softer" ones have a torsion natural frequency of 457 Hz, an 8% difference. Both blade sets are well within the unstable region for the tuned rotor.

Before impulsing this mistuned rotor, the blades are relaxed to their equilibrium state. The simulation time required to reach equilibrium for this mistuned rotor is approximately three times longer than that for the tuned rotor. The reason is traced to the mistuned steady aerodynamics. Starting from the first stop at 2.3 milliseconds, the blades with the smaller Young's modulus, Blades 1 and 3, have been displaced more toward the pressure side than Blades 0 and 2. Thus the flow passages between Blades 0 and 1 and Blades 2 and 3 are narrower than the flow passages between Blades 3 and 0 and Blades 1 and 2. Under these conditions, the steady aerodynamics creates a mismatch in pressure from blade passage-to-passage, the wide passages having higher pressure and the narrow passages having lower pressure. These non-equal pressures tend to bend the blades further so that the wide passages are widened and the narrow passages narrowed. This aerodynamic mistuning effect creates an equilibrium blade position that features blade spacing mistuning. The equilibrium spacing at the tip for the wide passages is 3.525 cm, and that for the narrow passages is 3.457 cm, a 1.9% difference from blade passage-to-passage.

After reaching their equilibrium positions, Blades 0 and 2 are impulsed with a nose-down and nose-up impulse. The resulting displacement time history for the blade trailing edges, Figure 81, shows that the blade vibration is damped and the mistuned rotor is stable. Recall that the natural frequencies for the two blade sets used on this mistuned rotor are well within the unstable region for a tuned rotor. Thus, the intentional

mistuning strategy of alternating Young's modulus around the rotor is effective for increasing the stability of a rotor near its flutter boundary.
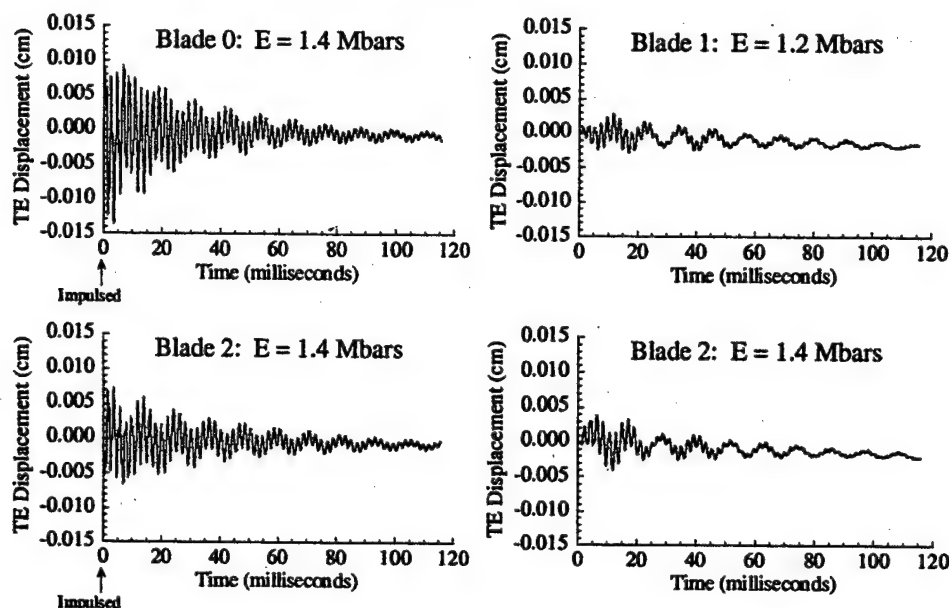
Figure 81. Displacement time history after impulse for mistuned rotor

The mistuned rotor unsteady aerodynamics is examined to determine the mechanism that stabilizes the mistuned rotor. Figure 82 shows the blade leading edge displacement. The dominant frequency component for Blades 0 and 2 is from the 1st torsion mode, with the vibration of these two blades 180° out of phase. By comparison, the 1st torsion mode is only slightly visible for Blades 1 and 3, indicating that the pitching mode is only marginally excited for these blades. The pitching motion of Blade 3 is approximately in phase with that of Blade 0, and the pitching motion of Blade 1 is approximately in phase with Blade 2.
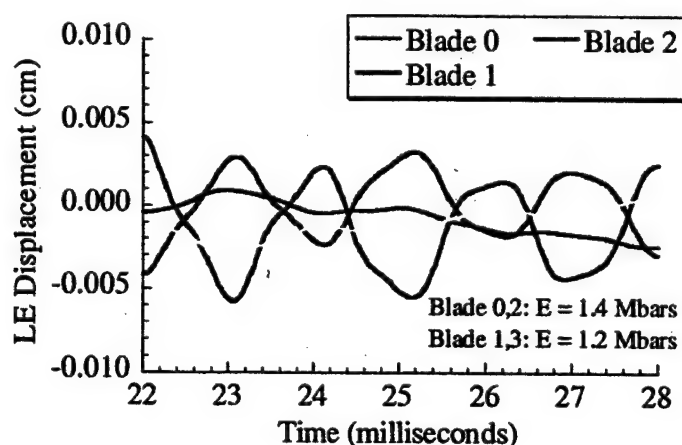
Figure 82. Close-up of leading edge displacement for mistuned rotor

A band-pass filter so that only the torsion mode is passed is applied to the mistuned rotor displacements , , with the result shown in Figure 83.   The mean

frequencies and standard deviations for Blades 0 and 2 are 492 Hz (4.3 Hz) and 491 Hz (2.9 Hz) respectively. The natural frequency for Blades 0 and 2 on a tuned rotor in-flow is 496 Hz, with these blades thus responding to the initial impulse at their natural frequency. The mean frequencies and standard deviations for Blades 1 and 3 are 490 Hz (14.5 Hz) and 491 Hz (13.4 Hz), respectively. The natural frequency for Blades 1 and 3 on a tuned rotor is 457 Hz, with these blade thus responding to the aerodynamic forcing generated by the motion of their neighboring blades. The beating is a result of the external aerodynamic forcing at 490 Hz being close to the 458 Hz natural frequency of these blades.
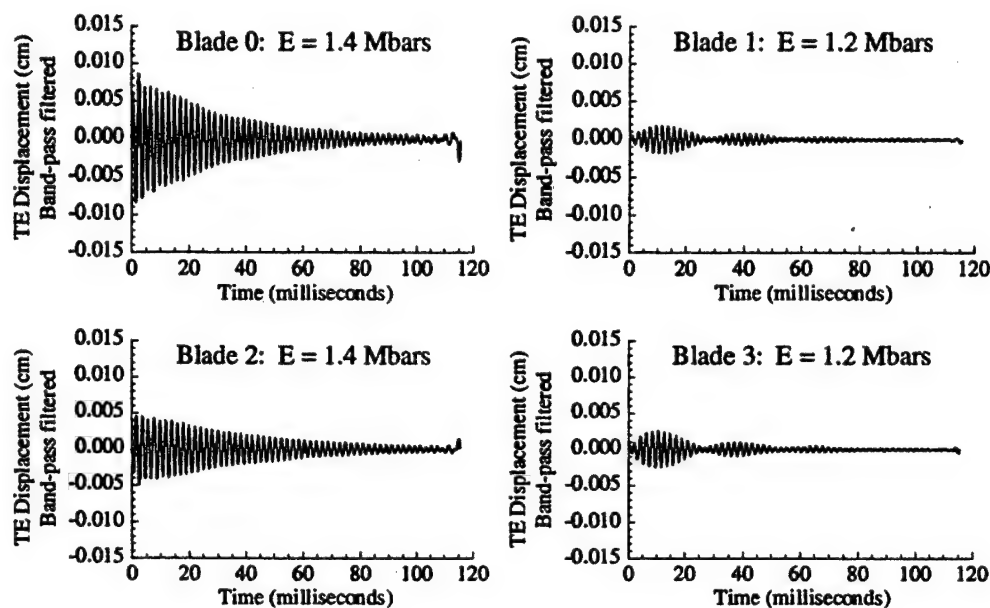
Figure 83. Displacement for mistuned rotor with bending frequency removed

The nondimensional damping factor ζ for Blades 0 and 2 is 0.0097 and 0.0082, much larger than the values for the tuned rotor studies. Table 4 summarizes ζ for the unstable tuned rotor and the stable mistuned rotor, where the value for the mistuned rotor is the average value from Blades 0 and 2.

	$\square$	
Tuned, E = 1.2 Mbars	-0.0034	Unstable
Tuned, E = 1.4 Mbars	-0.0022	Unstable
Mistuned, E = 1.2 Mbars/1.4 Mbars	0.0090	Stable

Table 4. Quantitative stability improvement resulting from mistuning

Figure 84 shows the unsteady moment and pitch angle for the mistuned rotor blades. The pitching amplitude is largest for Blade 0, approximately 0.20°, with Blade 2 amplitude not much smaller - 0.14°. These are the two blades that were initially impulsed. In contrast, the pitching amplitude for Blades 1 and 3 is 0.03°, nearly an order of magnitude smaller. Similarly, the unsteady moment is much smaller for Blades 1 and 3 than for Blades 0 and 2. The unsteady moment is essentially in phase with the pitch

angle for Blades 0 and 2, while it is approximately 180° out of phase for Blades 1 and 3. Having an unsteady moment in phase or 180° out of phase with the pitch angle corresponds to a neutrally stable condition. However, the decaying response indicates that a component of the unsteady pitching moment is out of phase with the pitching velocity the majority of the time.
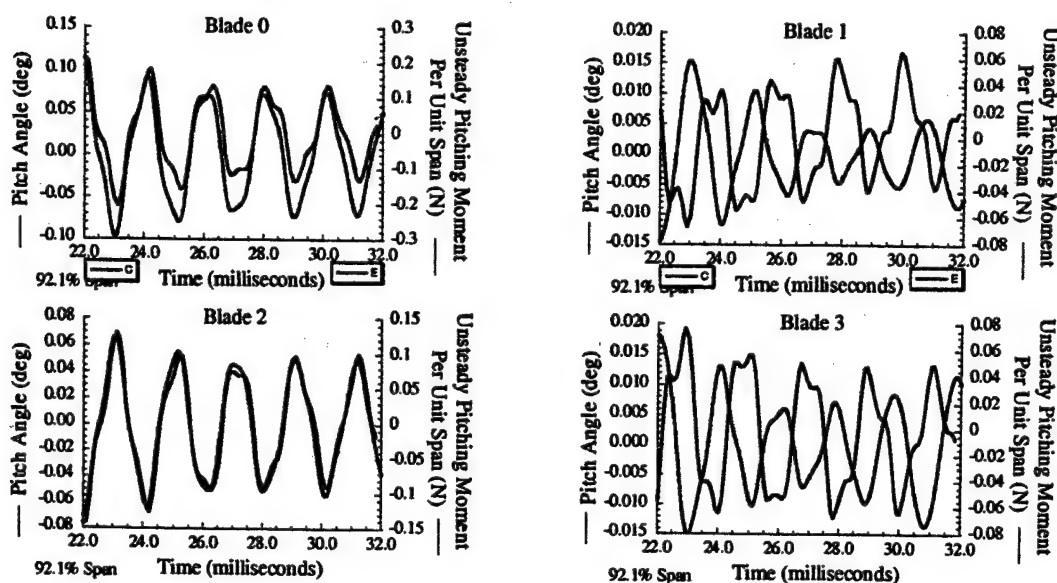
Figure 84. Unsteady moment and pitch angle for mistuned rotor

The blade surface pressures are Fourier decomposed to extract the unsteady pressure at the pitching natural frequency for the tuned and mistuned rotors. The pitching frequency for the tuned rotor is 496 Hz and the average of the four blades - 491 Hz. - for the mistuned rotor. The tuned and mistuned rotor blade surface unsteady pressure magnitudes are shown in Figure 85. The pressure surface unsteady pressure distributions on mistuned rotor Blades 0 and 2 are similar to that of the tuned rotor. Blades 1 and 3, on the other hand, have much less unsteady forcing on their pressure surfaces. On the suction surface, Blades 1 and 3 have a peak in the unsteady forcing at about mid-chord, a feature also seen for the tuned rotor blades. However, Blades 0 and 2 do not have this peak.
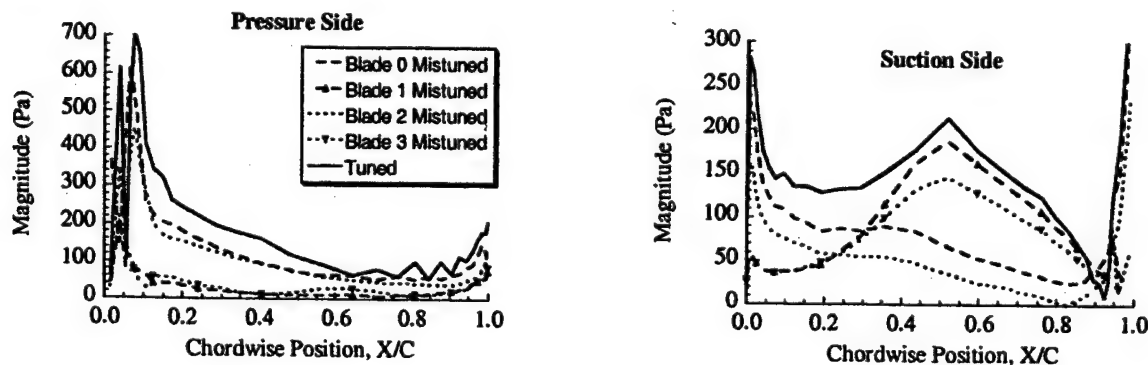
Figure 85. Blade unsteady pressure magnitude

Figure 86 illustrates the regions of large unsteady aerodynamic effects and thus qualitatively explains the results of Figure 85. The pitching motion of all the tuned rotor blades causes relatively large unsteady pressures in the forward half of the blade row. However, for the mistuned rotor, the pitching of Blades 0 and 1 creates large aerodynamic unsteadiness in a region that extends from their own pressure sides near the leading edge to the mid-chord region of the adjacent blades. Hence the unsteady forcing on the mistuned blades looks similar to the tuned rotor for the pressure sides of Blades 0 and 2 and the mid-chord suction sides of Blades 1 and 3.
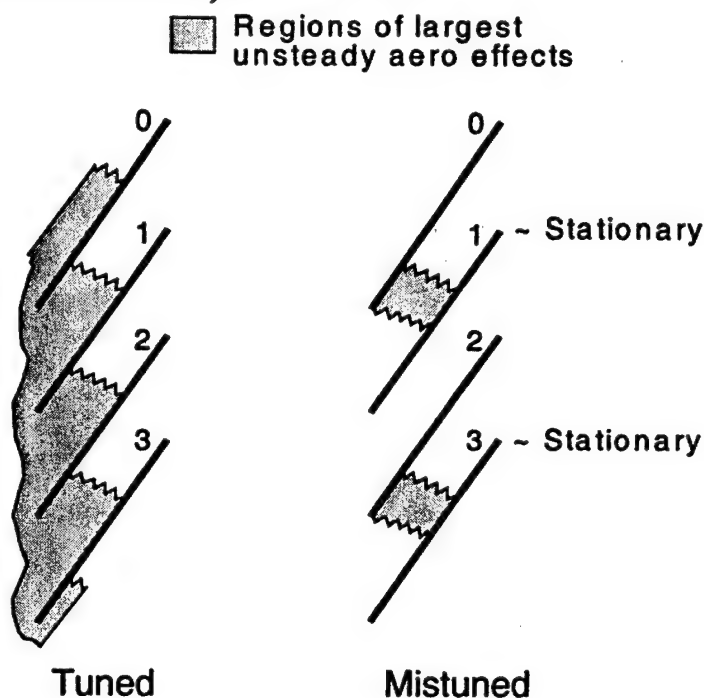
Figure 86. Regions of large unsteady aerodynamic effects for tuned and mistuned rotors

Conclusions

The TM-ALE3 simulation demonstrated that this mistuning strategy was very effective in stabilizing the baseline tuned rotor. Specifically, the 1st torsion natural frequencies for the two types of blades were such that they would be unstable as part of a tuned rotor, i.e. both types of blades on this structurally mistuned rotor within the tuned rotor unstable region. However, when incorporated into the mistuned rotor, these blades become stable. The precise increase in stability was quantified by the nondimensional damping factor for the tuned and mistuned rotors. The technique presented herein and made possible by the TAM-ALE3D analysis can be applied to other mistuning patterns, e.g. every fourth blade mistuned, and other mistuning amounts, e.g. 20% change in frequency, with the precise stability enhancement the result predicted by the simulation.

SHUNTED PIEZOELECTRICS FOR PASSIVE VIBRATION CONTROL

The application of shunted piezoelectric elements to provide passive structural damping is investigated by means of a series of experiments performed in the Purdue High Speed Axial Compressor Research Facility. Piezoelectric elements are bonded to three airfoils in the stator row. The airfoils are excited by the wakes generated by an upstream rotor. As the wakes drive the airfoil vibrations, the piezoelectrics experience a strain and in response produce an electric field. Tuned electrical circuits connected to the piezoelectrics as shunts dissipate this electrical energy. This electrical energy dissipation and the corresponding reduction in the airfoil mechanical energy result in a reduction in the magnitude of the resonant vibrations.

Piezoelectric Model and Theory

Piezoelectric materials have the ability to transform electrical energy to mechanical energy and visa versa. Thus, they can provide passive damping by using electrical impedance as a dissipating shunt. This is accomplished by bonding a piezoelectric element to a structure such as a plate or beam. As the structure vibrates, the piezoelectric experiences a strain and in response produces an electric field. The electrical shunt in turn dissipates the electrical energy, thereby reducing the systems mechanical energy. The conversion of mechanical energy to electrical energy causes a reduction in the resonant vibrations of the structure.

Figure 87 illustrates a thin piezoelectric material element representing those that could be bonded to or embedded in surface of an airfoil. In this model, direction "3" is the direction through which the electric field and current act on the element, or the poling direction, and is perpendicular to directions "1" and "2" which lie along the surface of the host structure. It is generally assumed that the properties in the "1" and "2" directions are isotropic, and symmetry is used throughout the derivation. An understanding of the relationship between the deformed shape of the piezoelectric and its electrical response allows for an analysis of the vibratory motion of the airfoil by coupling its motion to that of the attached piezoelectric element.
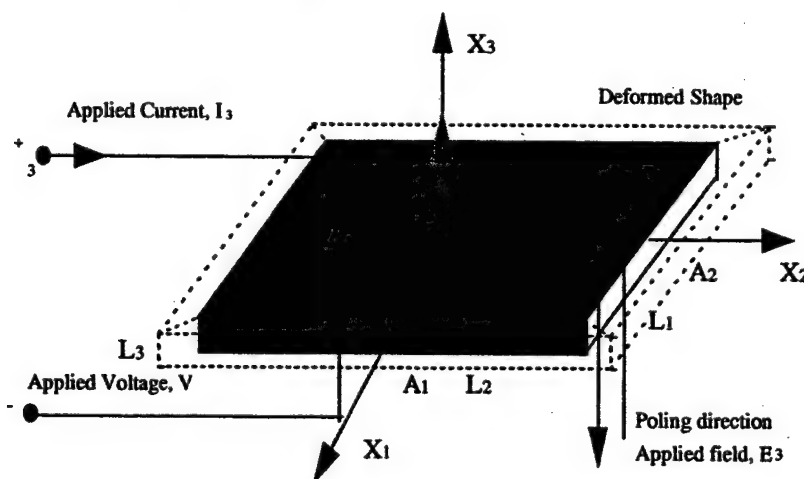
Figure 87. Piezoelectric element model

   To develop this coupling of electrical and mechanical properties, three constitutive relationships are defined. The constant "d" is the piezoelectric strain constant and is defined as the relation between material strain and the applied field. The constant "g" represents the relation between charge density and applied strain. The constant "k" is the electromechanical coupling term, which defines the electrical-mechanical energy transfer properties of the material. Numerically, the square of k is equal to the ratio of electrical energy, which is converted to mechanical energy to the input electrical energy. The general expression for the material constants of a linear piezoelectric is

$$\begin{bmatrix} D \\ S \end{bmatrix} = \begin{bmatrix} \varepsilon^T & d \\ d_t & s^E \end{bmatrix} \begin{bmatrix} E \\ T \end{bmatrix} \tag{1}$$

where D is the electrical displacement vector (charge/area), E is the electrical field vector, S is the strain vector (volts/meter), T is the material stress vector (force/area), ε is the permittivity (farad/meter), s is the elastic compliance (meter^2/newton), and d is the piezoelectric strain constant.

   The form of the vectors D and S are

$$D = \begin{bmatrix} D_1 \\ D_2 \\ D_3 \end{bmatrix} = \begin{bmatrix} \varepsilon_1 E_1 + d_{15} T_5 \\ \varepsilon_1 E_2 + d_{15} T_4 \\ \varepsilon_3 E_3 + d_{31}(T_1 + T_2) + d_{33} T_3 \end{bmatrix} \tag{2a}$$

$$S = \begin{bmatrix} S_1 \\ S_2 \\ S_3 \\ S_4 \\ S_5 \\ S_6 \end{bmatrix} = \begin{bmatrix} s_{11}^E T_1 + s_{12}^E T_2 + s_{13}^E T_3 + d_{31} E_3 \\ s_{11}^E T_2 + s_{12}^E T_1 + s_{13}^E T_3 + d_{31} E_3 \\ s_{13}^E (T_1 + T_2) + s_{33}^E T_3 + d_{33} E_3 \\ s_{44}^E T_4 + d_{15} E_2 \\ s_{44}^E T_5 + d_{15} E_1 \\ s_{66}^E T_6 \end{bmatrix} \tag{2b}$$

and the E and T vectors conform to standard nomenclature for stress and electrical vectors.

$$E = \begin{bmatrix} E_1 \\ E_2 \\ E_3 \end{bmatrix} \qquad T = \begin{bmatrix} T_{11} \\ T_{22} \\ T_{33} \\ T_{23} \\ T_{13} \\ T_{12} \end{bmatrix} \tag{2c,d}$$

where the superscript T denotes the property measured under constant stress conditions and the superscript E that the property was measured in a constant electrical field.

The first equation of Equation 1 represents the direct piezoelectric effect, or the creation of an electrical charge due to the application of a stress to the material. The second equation represents the converse effect or a stress resulting from the application of an electrical charge.

To perform an analysis using the traditionally defined concepts of admittance and impedance, the electrical field vector (E) and the electrical displacement vector (D) must be replaced by current (I) and voltage (V). Using standard definitions,

$$V_i = \int_0^{L_i} \mathbf{E} \cdot dx_i \qquad\qquad I = \int_{A_i} \mathbf{D} \cdot da_i \qquad (3)$$

and assuming uniform fields and displacements throughout the piezoelectric, a transfer to the Laplace domain yields

$$\mathbf{V}(s) = \mathbf{L} \cdot \mathbf{E}(s) \qquad\qquad \mathbf{I}(s) = s\mathbf{A} \cdot \mathbf{D}(s) \qquad (4)$$

where L is the diagonal matrix of the lengths of the piezoelectric element in the ith direction, A is the diagonal matrix of the areas of the surfaces of the piezoelectric element orthogonal to the ith direction, and s is the Laplace parameter.

Taking the Laplace transform of Equation 1 in conjunction with these definitions leads to the following expression for the piezoelectric in terms of external current and the applied voltage.

$$\begin{bmatrix} \mathbf{I} \\ \mathbf{S} \end{bmatrix} = \begin{bmatrix} s\mathbf{A}e^T\mathbf{L}^{-1} & s\mathbf{A}\mathbf{d} \\ \mathbf{d}_i\mathbf{L}^{-1} & s^E \end{bmatrix} \begin{bmatrix} \mathbf{V} \\ \mathbf{T} \end{bmatrix} \qquad (5)$$

Defining the capacitance between perpendicular surfaces in the ith direction as

$$C_{pi}^T = \frac{A_i \varepsilon_i^T}{L_i} \qquad (6)$$

and grouping the components into a $\mathbf{C}_p^T$ matrix, Equation 5 can be written in the form

$$\begin{bmatrix} \mathbf{I} \\ \mathbf{S} \end{bmatrix} = \begin{bmatrix} \mathbf{Y}^D(s) & s\mathbf{A}\mathbf{d} \\ \mathbf{d}_i\mathbf{L}^{-1} & s^E \end{bmatrix} \begin{bmatrix} \mathbf{V} \\ \mathbf{T} \end{bmatrix} \qquad (7)$$

where $\mathbf{Y}^D(s) = s\mathbf{C}_p^T$ and is defined as the open circuit admittance of the piezoelectric. The open circuit admittance relates the voltage applied across the materials electrodes to the external current input to the piezoelectric.

Piezoelectric Shunting

For shunting, a passive electrical circuit is placed between the electrodes of the piezoelectric element. The circuit is parallel to the capacitance of the piezoelectric and therefore the total admittance of the device, $\mathbf{Y}^{EL}$, is the sum of the individual admittances from the device, $\mathbf{Y}^D$, and the shunt, $\mathbf{Y}^{SU}$, or $\mathbf{Y}^{EL} = \mathbf{Y}^D + \mathbf{Y}^{SU}$.

To find the overall effect on the system, or effective impedance of the piezoelectric shunt, their properties must be combined with the properties of the other

damping elements acting on the system. Using the method of combining viscoelastic damping elements, the relationship between the loss factor of damping components and the loss factor of the overall structure can be expressed as an average of the component loss factors multiplied by their fraction of the total strain energy. Defining U_i as the strain energy in the ith component of the structure, the total loss factor is

$$\eta^{TOT} = \sum_{i=1}^{n} \frac{\eta_i U_i}{\sum_{i=1}^{n} U_i} \tag{8}$$

Maximizing the loss factor for the piezoelectric device does not necessarily maximize the loss factor for the structure. The total damping of the system consists of a combination of all damping methods in the system, weighted by their fraction of the strain energy dissipated.

One method of determining the system damping is to consider the piezoelectric shunt as a viscoelastic material with frequency dependent properties. For the resistive shunted device, the properties are similar to those of a linear solid. However, for the resonant shunted device, the properties are non-linear functions of frequency and the tuning parameters. As a result, a prior knowledge of the properties must exist to effectively predict the effect of the resonant shunt on the system.

The second method of obtaining the system damping is to represent the system by a simple 1-DOF system including the piezoelectric device. The mass and stiffness of this 1-DOF system can represent a particular mode of a multi-DOF system. In the Laplace domain, the modal velocity of the system can be expressed as

$$v(s) = \frac{F(s)}{Ms + \left(\dfrac{K}{s}\right) + Z_{jj}^{RES}(s)} \tag{9}$$

where F(s) is the magnitude of the forcing function and Ms, K/s, and $Z_{jj}^{RES}(s)$ are the impedances associated with the modal mass, stiffness, and resistive shunt respectively. The impedance of an element is the inverse of its admittance.

Nondimensionalization and reduction results in the following transfer function.

$$\frac{x}{\left(F/K_{tot}\right)} = \frac{(r\gamma+1)}{(r\gamma^3 + \gamma^2 + r(1+K_{ij}^2)\gamma + 1)} \tag{10}$$

where Ktot is the total modal stiffness of the system, $K_{ij}^2 = \left(\dfrac{K_{jj}^E}{K+K_{jj}^E}\right)\left(\dfrac{k_{ij}^2}{1-k_{ij}^2}\right)$ is the

generalized electromechanical coupling coefficient, $\omega_n^E = \sqrt{\dfrac{(K+K_{jj}^E)}{M}}$, and $\gamma = \dfrac{s}{\omega_n^E}$ and

$r = R_i C_{pi}^S \omega_n^E = \rho\big|_{\omega=\omega_n^E}$ are the nondimensional frequency and the electric damping ratio.

The generalized electromechanical coupling coefficient describes the fraction of the modal strain energy, which is converted into electrical energy, and therefore serves as a direct measurement of the shunt's effect on the system. A miscalculation of this energy fraction greatly affects the circuit sizing. Noting that the natural frequency of the structure changes as the damping due to the piezoelectric elements varies, the effect of short versus open shunting circuit can be seen in the frequency of vibration. The open circuit and short circuit natural frequencies are

$$\omega_n^D = \sqrt{\frac{\left\{ K + \frac{K_p^E}{1 - k_{ij}^2} \right\}}{M}}$$

(11)

$$\omega_n^E = \sqrt{\frac{\left\{ K + K_p^E \right\}}{M}}$$

(12)

where K is the effective stiffness of the underlying structure, K_p^E is the effective stiffness of the piezoelectric elements, and M is the mass of the system.

Combining Equations 11 and 12

$$K_{ij}^2 = \frac{\left(\omega_n^D\right)^2 - \left(\omega_n^E\right)^2}{\left(\omega_n^E\right)^2}.$$

(13)

Utilizing this method of determining the generalized electromechanical coupling coefficient, most variables due to construction of the system can be taken into account. With the various natural frequencies known, and thus the generalized electromechanical coupling coefficient determined, the shunting circuit can be designed.

Due to the nonlinear dependence of the resonant shunted effective natural properties on the frequency and tuning parameter, optimization by considering energy dissipation is difficult. Hence, optimization must be based on another criteria. A common method in the transfer function technique wherein the transfer function is evaluated at an electric damping ratio of zero, r=0, and where the ratio goes to infinity. A quadratic expression is found for their intersection points. In proof mass dampers, these points are termed the S and T locations. From the sum of the roots of this quadratic expression, the optimal tuning parameter is determined to be

$$\delta_{TF}^{opt} = \sqrt{1 + K_{ij}^2}$$

(14)

When the optimal tuning parameter is specified, the optimal damping in the electrical circuit can be determined. A convenient method for optimization sets the amplitude of the transfer function at the desired operating frequency to that of the system at the S and T points. The resulting analysis shows that the optimum circuit damping is

$$r_{TF}^{opt} = \frac{1.414 K_{ij}}{1 + K_{ij}^2}.$$

(15)

In resistive shunting, a resistor is placed in the circuit parallel to the inherent capacitance of the piezoelectric element. The resistor provides a means for dissipation of the electrical energy developed through the vibration of the underlying structure.

Returning to the nondimensional electrical impedance and identifying that the shunted impedance is the value of the resistor

$$Z_i^{SU}(s) = R_i \tag{16}$$

the nondimensional electrical impedance for resistive shunting is

$$\overline{Z}_i^{EL}(s) = \frac{R_i C_{pi}^T s}{\left(R_i C_{pi}^T s + 1\right)} \tag{17}$$

Substituting into the piezoelectric nondimensional mechanical impedance, the nondimensional impedance of a resistive shunted piezoelectric is determined.

$$\overline{Z}_{ij}^{RES}(s) = 1 - \frac{k_{ij}^2}{(1 - i\rho_i)} \tag{18}$$

where $\rho_i = R_i C_{pi}^S \omega = \sqrt{1 - k_{ij}^2}$ is the nondimensional frequency.

In resonant circuit shunting, a resistor and an inductor are placed in series with the inherent capacitance of the piezoelectric element to create an L-R-C circuit. The electrical resonance of the new circuit can be tuned to the frequency of the mechanical vibration. The electrical resonance greatly increases the modal damping ratio. It has been shown that the effect of resonant piezoelectric shunting is similar to a mass damper or a resonant vibration absorber.

The electrical impedance of the resonant shunt is a function of both the resistor and inductor values. Substituting into the nondimensional mechanical impedance

$$\overline{Z}_{ij}^{RES}(s) = 1 - k_{ij}^2\left(\frac{\delta^2}{\gamma^2 + \delta^2 r\gamma + \gamma^2}\right) \tag{19}$$

where r is the damping parameter, $\delta = \dfrac{\omega_e}{\omega_n}$ is the nondimensional tuning frequency, $\gamma = \dfrac{\omega}{\omega_n}$ is the nondimensional frequency and

$$\omega_n^E = \frac{1}{\sqrt{LC_{pi}^S}} \tag{20}$$

is the electrical resonant frequency.

With the relationships between the electrical and mechanical properties of the shunted system determined, the following summarizes the equations needed to practically apply the technique. Before a shunt can be applied, the basic properties of the system, piezoelectric elements, and their interactions must be understood. The inherent capacitance of each piezoelectric element is determined.

$$C_{pi}^T = \frac{A_i \varepsilon_i^T}{L_i} \qquad (6)$$

The open and short circuit natural frequencies of the shunted system are determined experimentally. Using a vibration driver, the system is excited to determine its resonant response frequency with the piezoelectric elements. For the open circuit configuration, a peak voltage output from the piezoelectric elements can be used to determine the resonant location. For the short circuit configuration with the leads of the piezoelectric elements connected, a peak current reading is appropriate.

With these natural frequencies determined, the generalized electromechanical coupling coefficient is calculated .

$$K_{ij}^2 = \frac{\left(\omega_n^D\right)^2 - \left(\omega_n^E\right)^2}{\left(\omega_n^E\right)^2} \qquad (13)$$

The optimal tuning parameter and the circuit damping can now be determined.

$$\delta_{TF}^{opt} = \sqrt{1 + K_{ij}^2} \qquad (14)$$

$$r_{TF}^{opt} = \frac{1.414 K_{ij}}{1 + K_{ij}^2} \qquad (15)$$

For a resistive shunt, the required resistance is.

$$\rho_i = R_i C_{pi}^S \omega = \sqrt{1 - k_{ij}^2} \qquad (18)$$

For a resonant shunt, the required inductor and resistor values are

$$\omega_n^E = \frac{1}{\sqrt{L_i C_{pi}^S}} \qquad (20)$$

$$r = R_i C_{pi}^S \omega_n^E = \rho\Big|_{\omega = \omega_n^E} \qquad (10)$$

Forced Response Experiments

The application of shunted piezoelectric elements to provide passive structural damping to turbomachine blade rows is investigated by means of a series of experiments performed in the Purdue High Speed Axial Compressor Research Facility. Piezoelectric elements are bonded to three airfoils, in the stator row. The airfoils are excited by upstream rotor generated wakes. The piezoelectrics experience a strain and in response produce an electric field, with tuned electrical circuits connected to the piezoelectrics as shunts designed to dissipate this electrical energy.

Three vanes with bonded piezoelectric elements are evaluated. The volume of the piezoelectric elements are the same on two of the vanes, with a single large element bonded on one vane and two smaller elements mounted on the other. The third vane has a piezoelectric element approximately 20% larger extending completely across the span. For the two vanes with a single element, the piezoelectric element is placed to cross two

nodal lines, whereas on the vane with two elements, each element acts across a large strain area independently. For reference, the vanes with the same piezoelectric volume are known as the SPE vane for the vane with the single piezoelectric element and as the 2PE vane for the vane with the two piezoelectric elements. The third vane, with the larger piezoelectric volume is known as the LPE vane. The location and dimensions of the piezoelectric elements is presented in Figure 88.

Pressure Surface of Stator vanes
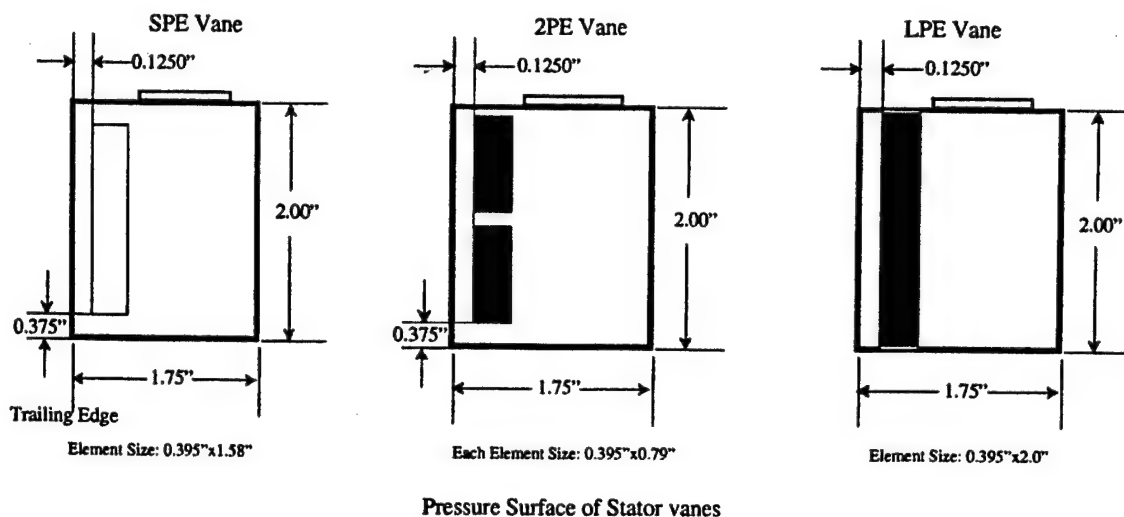
Figure 88. Location and dimensions of piezoelectric elements

The piezoelectric stator airfoils are excited by the rotor wakes. The piezoelectric patches bonded to the airfoils are lead zirconate titanate G1195. Based on the vane dimensions, the effective capacitance of the piezoelectric elements for each configuration was determined. For the SPE and 2PE vanes, an effective capacitance of $2.79*10^{-8}$ Farads was calculated and for the LPE vane the capacitance was $3.532*10^{-8}$ Farads.

In applying the design criteria for the resonant shunting circuit, a critical issue arises in evaluating the generalized electromechanical coupling coefficient. As defined, the generalized electromechanical coupling coefficient K_{ij} describes the fraction of the modal strain energy converted into electrical energy, and therefore is a direct measurement of the effect of the shunt on the system. As previously discussed, the miscalculation of this energy fraction greatly affects the circuit sizing. Noting that the natural frequency of the structure changes as the damping due to the piezoelectric elements varies, the effect of short versus open shunting circuits is seen in the frequency of vibration. Hence, the electromechanical coupling coefficient is determined experimentally.

With the open and short circuit airfoil natural frequencies measured, the general parameters needed to size the resonant shunting circuit can be calculated. Based on holographically recorded resonant frequencies, the generalized electromechanical coupling coefficient K_{ij} for the SPE vane is determined to be 0.0031. For the 2PE vane, it is also 0.0031, and for the LPE vane it is 0.0032.

Assuming a value of 0.0031 for each case, the optimum circuit tuning parameter δ^{opt} for the vanes is 1.0015, and the optimum circuit damping, r^{opt} is 0.0785. The

variation in circuit tuning and circuit damping values based on generalized electromechanical coupling coefficients ranging from 0.0031 to 0.0032 is indistinguishable.

Based on the experimentally determined tuning parameter and circuit damping, the resistance and inductor values are calculated for the passive damping circuits. Based on the effective capacitance of the SPE and 2PE vanes, the required resistance for a resistive shunt is 6,900 $\tilde{\Omega}$With the resonant shunt, the required resistance and inductance are 530 Ω and 1.3 H. For the LPE vane, the required resistance for a resistive shunt is 5,500 Ω and for the resonant shunt, the required resistance and inductance is 435 Ω and 1.1 H.

Experiments incorporating shunted piezoelectric elements to damp the vibratory motion of stator vanes are performed in the Purdue High Speed Compressor Facility. With the upstream rotor providing the aerodynamic forcing function excitation, shunted piezoelectric passive damping effectiveness is demonstrated. Finite element codes and laser holography were used to structurally and dynamically analyze the stator row with bonded piezoelectric elements. The analyses and data were evaluated to determine placement of strain gages and piezoelectric elements for sensing and damping of the airfoil vibrations.

For these experiments, three stator vanes with bonded piezoelectric elements are evaluated for passive flow induced vibration control with various passive electrical shunting circuits. A speed transient that crosses a stator resonant mode at 5,333 Hz is obtained for each configuration of vane and circuit. Due to the sharpness of the resonant excitation band for this mode, Figure 89, an extremely slow transient was utilized to capture the vane response. For the transient extending from 15,000 rpm to 17,000 rpm, the rotor speed is increased at a rate of 25 rpm/second. Three transients are obtained for each vane: a baseline response with no circuit connected to the piezoelectric; a resistively shunted response; and a resonant shunted response. The effect of each circuit on the vane response is determined through strain gages located at the vane trailing edge and the electrical output of the piezoelectric elements.
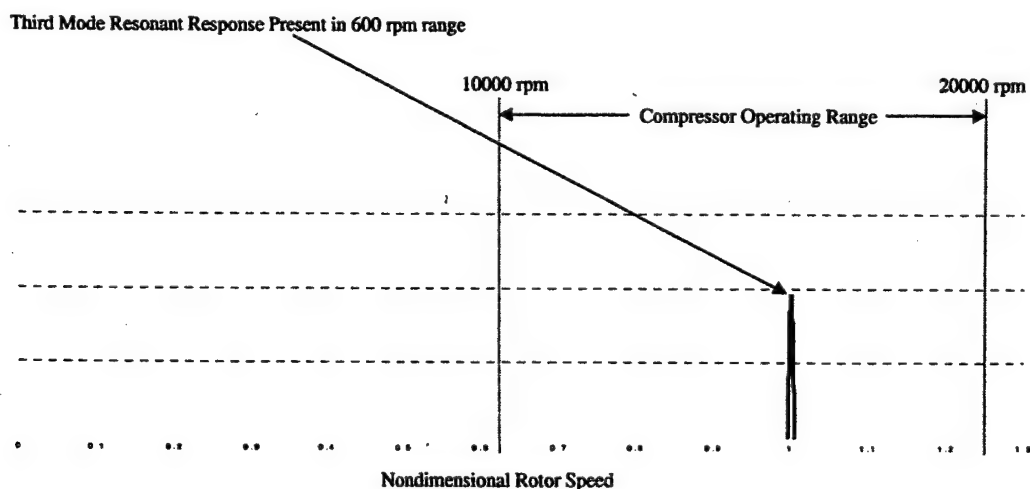
Figure 89. Resonant condition with respect to compressor operating range

The baseline response and the effect of the resistive and resonant damping shunts on the vibratory response of the SPE vane, as determined by the strain gages, are presented in Figure 90. For this vane, the decrease for both the resistive and resonant shunts is nearly identical. Application of the resistive shunt to the SPE vane results in an amplitude reduction of 8%, with a 9% reduction for the resonant shunt. Based on the relationship between the stress at the strain gage location and the maximum dynamic stress, a reduction of 9% in the strain gage signal is estimated to result in a reduction of 1.4 ksi in the maximum dynamic stress as compared to the baseline piezoelectric vane. Due to the increased stiffness of the piezoelectric vanes, the total reduction in maximum dynamic stress is estimated to be 4.8 ksi compared to the baseline steel vane.
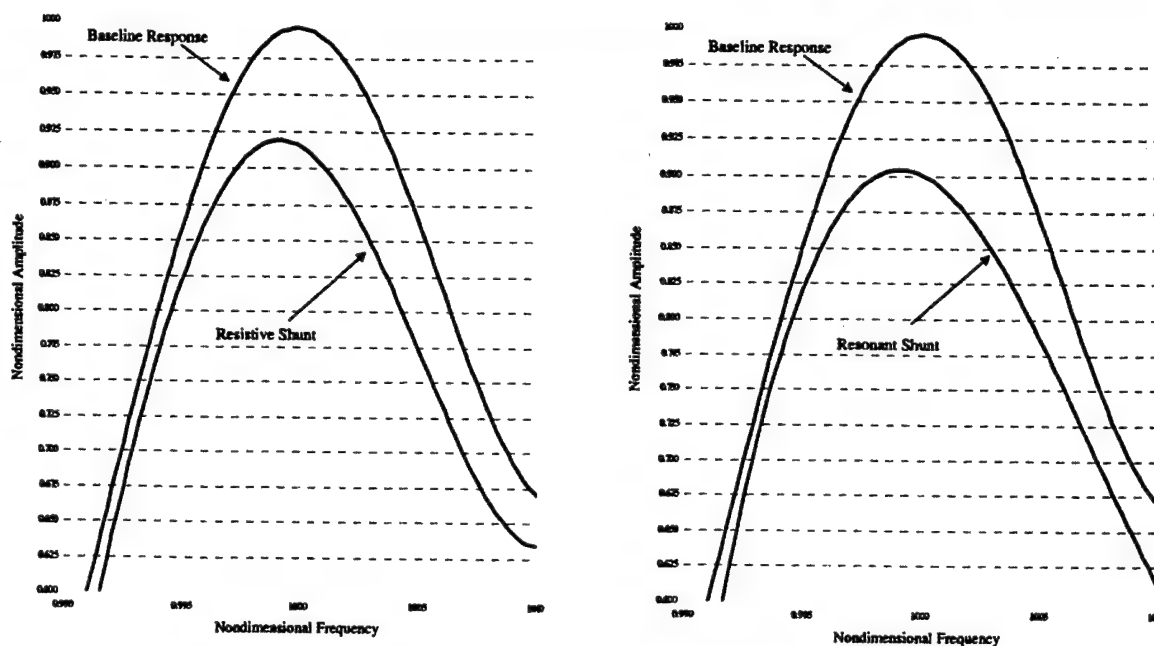
Figure 90. Piezoelectric controlled response of SPE vane

The reduction in the electrical output of the piezoelectric element is approximately 17% for the resistive circuit and 19% for the resonant circuit. The electromechanical coupling relationship for this system verifies that these values correspond to the strain gage reduction values achieved.

The results near the resonant peak show the traditional peak shift that occurs as damping is increased. In each case, a system damping increase results in the resonant peak shifting to a lower frequency. Due to the sharpness of the peak, and the magnification needed to compare the peak responses, a valid estimate of the frequency shift is not practical. The half power bandwidth method estimate of the damping ratio of the baseline system is 0.0079. With the shunts attached to the airfoil, an increase in damping ratio is present for all circuits. The increase in damping ratio for the resistive and resonant circuits is 0.0005 and 0.0007.

The baseline response and the effect of the resistive and resonant damping shunts on the vibratory response of the 2PE vane are presented in Figure 91. The decrease for the resonant shunt is approximately twice that of the resistive shunt. Application of the

resistive shunt to the 2PE vane results in an amplitude reduction of 3%, with a 6% reduction for the resonant shunt. Based on the relationship between the stress at the strain gage location and the maximum dynamic stress, a reduction of 6% in the strain gage signal is estimated to result in a reduction of 0.9 ksi in the maximum dynamic stress as compared to the baseline piezoelectric vane. Due to the increased stiffness of the piezoelectric vanes, the total reduction in maximum dynamic stress is estimated to be 4.3 ksi compared to the baseline steel vane.
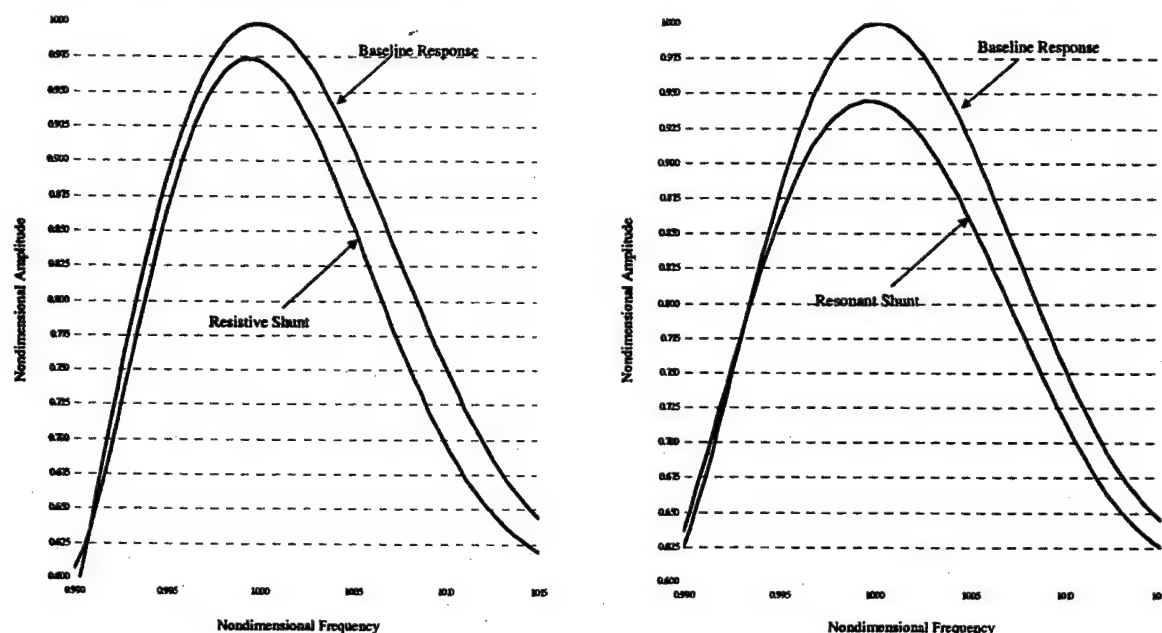
Figure 91. Piezoelectric controlled response of 2PE vane

The reduction in the electrical output of the piezoelectric element is approximately 6% for the resistive circuit and 13% for the resonant circuit. As for the SPE vane, the electromechanical coupling relationship for this system verifies that these values correspond to the strain gage reduction values achieved. The half power bandwidth method estimate of the damping ratio of the baseline system is 0.0095. With the shunts attached to the airfoil, an increase in damping ratio is present for all circuits. The increase in damping ratio for the resistive and resonant circuits is 0.0004 and 0.0008.

The baseline response and the effect of the resistive and resonant damping shunts on the vibratory response of the LPE vane are presented in Figure 92. Application of the resistive shunt to the LPE vane results in an amplitude reduction of 8%, with a resonant shunt reduction of approximately 11%. Based on the relationship between the stress at the strain gage location and the maximum dynamic stress, a reduction of 11% in the strain gage signal is estimated to result in a reduction of 1.7 ksi in the maximum dynamic stress as compared to the baseline piezoelectric vane. Due to the increased stiffness of the piezoelectric vanes, the total reduction in maximum dynamic stress is estimated to be 5.1 ksi compared to the baseline steel vane.
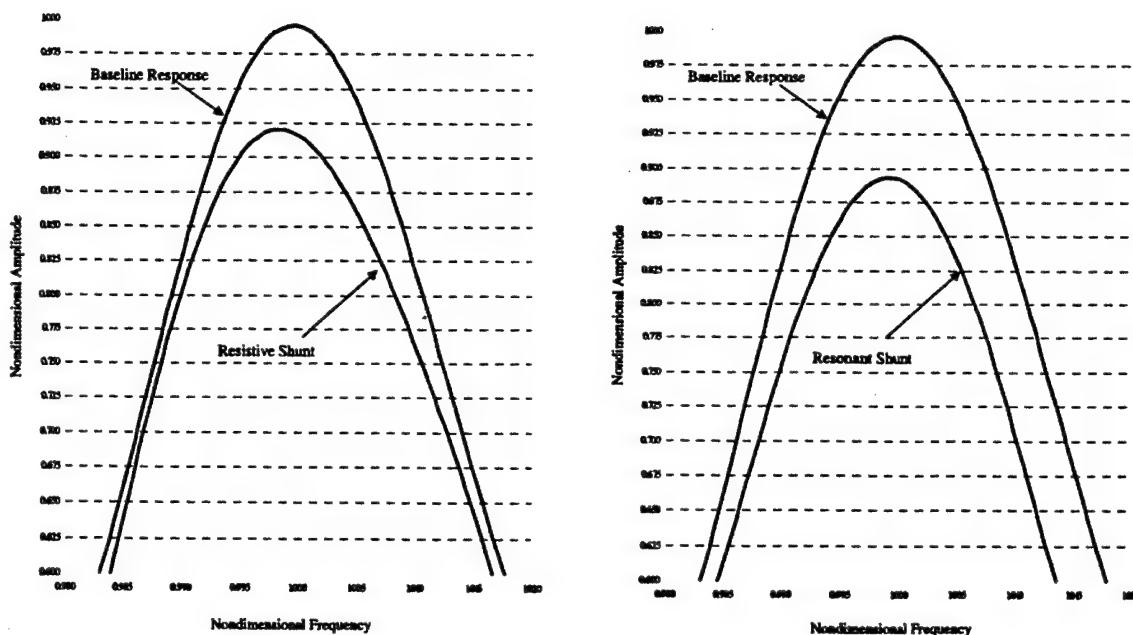
Figure 92. Piezoelectric controlled response of LPE vane

The reduction in the electrical output of the piezoelectric element is approximately 17% for the resistive circuit and 23% for the resonant circuit. Once again, the electromechanical coupling relationship for this system verifies that these values correspond to the strain gage reduction values achieved. The half power bandwidth method estimate of the damping ratio of the baseline system is 0.0132. With the shunts attached to the airfoil, an increase in damping ratio is present for all circuits. The increase in damping ratio for the resistive and resonant circuits is 0.0007 and 0.0014.

Conclusions

These passive vibration control experiments demonstrate that shunted piezoelectrics have significant damping capability and could be practical for the elimination or minimization of gas turbine fan and compressor blading flow induced vibrations. The use of a single large element is shown to be more effective than a series of smaller elements for this application. In comparing the SPE and 2PE results, vanes with identical piezoelectric volume but different element configurations, the single large element is more effective than two small elements in converting the kinetic energy of the vibratory motion to electrical energy. Additionally, in comparing the effectiveness of the two large element vanes, SPE vs. LPE, it appears that for the resonant shunt, the effectiveness is strongly coupled to the volume of piezoelectric material present in the system. The LPE vane has a 20% larger piezoelectric volume than the SPE vane and an increase of approximately 20% in amplitude reduction over the SPE vane.

Acknowledgement/Disclaimer

Research Assistants

Albert Sanders, Ph.D., Purdue University, currently at Honeywell Phoenix

John Papalia, M.S.M.E., Purdue University, completing Ph.D. at Purdue

Dana Gottfried, Ph.D., Purdue University, currently Post-Doctoral Researcher at Purdue

Yoon Choi, M.S.M.E., Purdue University, currently Ph.D. candidate at Purdue

Xiaoguang Li, Ph.D., Purdue University, Rolls Royce, General Electric

Doug Boyd, M.S.M.E., Purdue University, currently at Rolls Royce

Steve Szczap, M.S.M.E., Purdue University, currently at Williams International

Kishore Ramakrishnan, M.S.M.E., Purdue University, currently Ph.D. Candidate

Siowmen Litingtung, M.S.M.E., Purdue University, currently at Rolls Royce

Chihang Lin, M.S.M.E., Purdue University

Natalia Smelova, Duke University

Publications

Sanders, A.J. and Fleeter, S., "Experimental Investigation of Rotor-IGV Interactions in a Transonic Axial-Flow Compressor," *AIAA Journal of Propulsion and Power*, Vol. 16, No. 3, May-June 2000, pp. 421-430.

Sanders, A.J., Papalia, J. and Fleeter, S., "Multi-Blade Row Interactions in a Transonic Axial Compressor Part I: Stator Particle Image Velocimetry (PIV) Investigation," *ASME Journal of Turbomachinery*, Vol. 124, No. 1, January 2002, pp. 10-18.

Sanders, A.J. and Fleeter, S., "Rotor Blade-To-Blade Wake Variability and Its Effect on Downstream Vane Response," *AIAA Journal of Propulsion and Power*, Vol. 18, No. 2, March-April 2002, pp. 456-464.

Richman, M. and Fleeter, S., "Nonlinear Turbo Euler Simulation of IGV - Transonic Rotor Interactions," *International Journal of Rotating Machinery*, Vol. 8, No. 4, 2002, pp. 259 - 274.

Gottfried, D. A. and Fleeter, S., "Unsteady Cascade Aerodynamics in the Time Domain," *AIAA Journal of Propulsion and Power*, Vol. 18, No. 3, May-June 2002, pp. 519-527.

Cross, C.J. and Fleeter, S., "Shunted Piezoelectrics for Passive Control of Turbomachine Blading Flow Induced Vibrations," *Smart Materials and Structures*, Vol. 11, 2002, pp. 239-248.

Boyd, D.M. and Fleeter, S., "Axial Compressor Blade-To-Blade Unsteady Aerodynamic Variability," *AIAA Journal of Propulsion and Power*, in press.

Li, Xiaoguang Li, "Dynamic Stall Generated Airfoil Oscillations," *International Journal of Turbo & Jet Engines*, in press.

Sanders, A. and Fleeter, S., "Blade-to-Blade Wake Differences Including Effects on Vane Response," *AIAA 97-2753*, July 1997.

Gottfried, D. A. and Fleeter, S., "Unsteady Cascade Aerodynamics in the Time Domain," *AIAA 98-1852*, April 20-23, 1998.

Cross, C.J. and Fleeter, S., "Passive Control of Flow Induced Vibrations Using Shunted Piezoelectrics," *AIAA 98-1952*, April 20-23, 1998.

Li, X. and Fleeter, S., "Stall Flutter and Dynamic Stress Prediction for Cascaded Airfoils," *AIAA 98-1853*, April 20-23, 1998.

Gottfried, D.A. and Fleeter, S., "Prediction of Unsteady Cascade Aerodynamics by An Arbitrary Lagrangian-Eulerian Finite Element Method," *AIAA 98-3746*, July 12 - 15, 1998.

Sanders, A.J. and Fleeter, S., "An Experimental Investigation of IGV-Rotor Interactions In A Transonic Axial-Flow Compressor," *AIAA 98-3291*, July 12 - 15, 1998.

Sanders, A.J. and Fleeter, S., "Forcing Function Variability and Its Effect on Airfoil Response," *AIAA 98-3898*, 1998.

Sanders, A.J., and Fleeter, S., "Transonic Axial-Flow Compressor IGV-Rotor Interactions," *4th National Turbine Engine High Cycle Fatigue Conference*, February 1999.

Cross, C.J. and Fleeter, S., "Flow Induced Vibration Control of Stator Vanes Utilizing Shunted Piezoelectrics," *4th National Turbine Engine High Cycle Fatigue Conference*, February 1999.

Cross, C.J. and Fleeter, S., "Shunted Piezoelectric Control of Airfoil Vibrations," *ASME Paper 99-GT-385*, June 1999.

Sanders, A. and Fleeter, S., "A PIV Investigation of Transonic IGV-Rotor Interactions, *AIAA Paper 99-2674*, June 1999.

Richman, M. and Fleeter, S., "Nonlinear Turbo/TurboAE Simulation of Transonic IGV-Rotor Interactions, *AIAA Paper 99-2675*, June 1999.

Gottfried, D. and Fleeter, S., "Aerodynamic Damping Prediction for Turbomachine Blade Rows Using A Three-Dimensional Time Marching Simulation," *AIAA Paper 99-2810*, June 1999.

Papalia J. and Fleeter, S., "PSP Measurement of Subsonic Rotor-Stator Interactions," *7th Annual Pressure Sensitive Paint Workshop*, October 1999.

Sanders, A.J. and Fleeter, S., "Unsteady Blade Row Interactions in a Transonic Multistage Compressor," *5th National Turbine Engine High Cycle Fatigue Conference*, March 2000.

Richman, M.S., and Fleeter, S., "Simulation and Correlation of Rotor-IGV Interactions in A Transonic Compressor," *5th National Turbine Engine High Cycle Fatigue Conference*, March 2000.

Gottfried, D. A. and Fleeter, S. "A New Approach for Aerodynamic Damping Predictions In Turbomachine Blade Rows," 5th National Turbine Engine High Cycle Fatigue Conference, March 2000.

Richman, M.S., and Fleeter, S., "Nonlinear Turbo Simulation Of IGV - Transonic Rotor Interactions," 8th *International Symposium on Transport Phenomena and Dynamics of Rotating Machinery*, March 2000.

Gottfried, D. and Fleeter, S., "Turbomachine Blade Row Interaction Predictions With A Three-Dimensional Finite Element Method," *AIAA Paper 2000*-3226, July 2000.

Richman, M.S., and Fleeter, S., "Navier-Stokes Simulation of IGV-Rotor-Stator Interactions In A Transonic Compressor," *AIAA-2000-3379*, July 2000.

King, A. and Fleeter, S. "3-D Linearized Euler Simulation and Evaluation of Rotor-IGV Interactions," *AIAA-2000-3225*, July 2000.

Gottfried, D. A. and Fleeter, S. "Vane Row Mistuning For HCF Minimization," 6th *National Turbine Engine High Cycle Fatigue Conference*, March 2001.

Sanders, A.J., and Fleeter, S., "Stator Row Unsteady Aerodynamics Generated by a Transonic Rotor," 6th *National Turbine Engine High Cycle Fatigue Conference*, March 2001.

Sanders, A.J., Papalia, J. and Fleeter, S., "Multi-Blade Row Interactions in a Transonic Axial Compressor Part I: Stator Particle Image Velocimetry (PIV) Investigation," *ASME Paper 2001-GT-0268*, July 2001.

Sanders, A.J., and Fleeter, S., "Multi-Blade Row Interactions in a Transonic Axial Compressor Part II: Rotor Wake Forcing Function and Stator Unsteady Aerodynamic Response," *ASME Paper 2001-GT-0269* July 2001.

Gottfried, D.A. and Fleeter, S., "Fluid-Structure Interaction Simulation of Flutter Suppression Via Structural Mistuning," 7th *National Turbine Engine High Cycle Fatigue (HCF) Conference*, May 2002.

Sanders, A. J., Papalia, J. and Fleeter, S., "Steady Loading Effects On Rotor-Stator Interactions In A Transonic 1&1/2 Stage Axial-Flow Compressor," 7th *National Turbine Engine High Cycle Fatigue (HCF) Conference*, May 2002.

Richman, M. and Fleeter, S., "3-D Navier-Stokes Simulation of Rotor-Stator Interactions in 1&1/2 Stage Axial-Flow Compressor," *AIAA Paper 2002-3546*, July 2002.

Gottfried, D.A. and Fleeter, S., "Passive Mistuning for HCF Reduction," *AIAA Paper 2002-3634*, July 2002.

Choi, Y., Gottfried, D.A. and Fleeter, S., "Aerodynamic Effects on Mistuned Bladed Disks," *AIAA Paper 3639*, July 2002.

Honors and Awards

Sanford Fleeter: Fellow, American Institute of Aeronautics and Astronautics, (Awarded 2000).

Sanford Fleeter: 2000 International Society of Rotating Machinery Research Award (ISORMAC).

Sanford Fleeter: 2001 ASME Propulsion Flag Award

ASME Joint Propulsion Best Paper: Sanders, A. and Fleeter, S., "A PIV Investigation of Transonic IGV-Rotor Interactions, *AIAA Paper 99-2674*, June 1999 (Awarded 2000).

ASME Joint Propulsion Best Paper, Richman, M.S., and Fleeter, S., "Navier-Stokes Simulation Of IGV-Rotor-Stator Interactions In A Transonic Compressor," *AIAA-2000-3379*, July 2000 (Awarded 2001).

APPENDIX

Multistage Analysis of Unsteady Flows In Turbomachinery

Natalia Smelova
Graduate Research Assistant

Kenneth C. Hall (PI)
Professor and Chair

and

Earl H. Dowell (Co-PI)
J. A. Jones Professor

Department of Mechanical Engineering and Materials Science
School of Engineering
Duke University, Durham, NC 27708-0300

Abstract

The interactions between stationary and rotating blade rows in turbomachinery lead to unsteady aerodynamic forces acting on the blades. These unsteady forces may cause blade fatigue and structural failure. A number of methods have been developed to predict the interaction within a coupled rotor-stator pair. However, because of their high computational cost, most of these methods cannot currently be used efficiently in design and development. An alternative method based on the time-linearized approach is developed in this report for three-dimensional inviscid flows. The flow is represented as a sum of a time-averaged nonlinear mean flow and a small perturbation unsteady flow resulting from blade vibration or an incoming gust. The small perturbation unsteady flow is identified with a finite set of discrete fluid modes called "spinning modes" each with a distinct frequency and an interblade phase angle. The mean multistage flow is first computed using the Euler equations and conventional fluid dynamics techniques. To couple the solutions from the different blade rows, the circumferentially averaged flow quantities are matched at the inter-row boundaries at each radial station. To find the small perturbation unsteady flow, the linearized Euler equations are solved for each pair of frequency and an interblade phase angle associated with spinning modes concurrently using a pseudo-time time-marching finite-volume Lax-Wendroff scheme. At each iteration, information is exchanged among various spinning mode solutions at the inter-row computational boundaries. The time-linearized equations are solved in the frequency domain, time does not appear explicitly in the governing equations. Instead, frequency appears as a parameter. Since the "steady-state" solution of the linearized Euler equations is desired, the discretized equations are not marched time-accurately. Therefore, local time stepping and multigrid acceleration techniques can be employed, significantly increasing the convergence rate. A number of numerical examples are presented to validate the method and to demonstrate the influence of neighboring blade rows on aerodynamic damping of a cascade of blades. In addition, it is shown that a good estimation of aerodynamic damping can be obtained retaining a small number of spinning modes in the model.

Chapter 1

Introduction

1.1 Statement of the Problem

Turbomachinery blades are subjected to unsteady aerodynamic forces arising from inlet distortions, interactions between stationary and rotating blade rows, random excitations and motions of the blades themselves. These unsteady pressure loads produce vibratory motion of the blades which may lead to a blade's structural fatigue and subsequent failure. Blades in rotors are particularly susceptible to high cycle fatigue (HCF) because of the large mean stress resulting from centrifugal forces. To predict the life of the blade, and to design blades for longer high cycle fatigue life, one must be able to estimate accurately the unsteady aerodynamic forces acting on the blades.

A simplified view of the forces acting on a blade is shown in Fig. 1.1. The basic equation of motion describing this system is

$$\mathbf{M}\ddot{\mathbf{x}} + \mathbf{C}\dot{\mathbf{x}} + \mathbf{K}\mathbf{x} = \mathbf{F}_{\text{motion}}(\mathbf{x}, \dot{\mathbf{x}}, \ddot{\mathbf{x}}, ...) + \mathbf{F}_{\text{gust}}(t) \tag{1.1}$$

where $\mathbf{x}$ represents the vector of the blade's displacement and the dots correspond to the differentiation with respect to time. The structural dynamic properties of the blade are contained in the mass matrix $\mathbf{M}$ and the stiffness matrix $\mathbf{K}$. The structural damping is represented by the matrix $\mathbf{C}$. The aerodynamic forces are divided into external forces, $\mathbf{F}_{\text{gust}}$, and self-induced forces, $\mathbf{F}_{\text{motion}}$. External forces, $\mathbf{F}_{\text{gust}}$, that are independent of the displacement of a blade are generated by air flow nonuniformities called "gusts". In practice, these gusts can be attributed to a number of sources including potential fields produced by neighboring blade rows, inlet distortions, and viscous wakes. The external forcing induces a response which in some cases may lead to high cycle fatigue failure of the blade, and is referred to as *forced response*. Self-induced forces, $\mathbf{F}_{\text{motion}}$, are created as a result of the blade displacement. These forces are functions of the displacement, velocity and acceleration of the blade itself. If the work of these self-induced forces on the blade is positive, then the blade will absorb the energy from the airstream as the blade vibrates. If the energy absorbed from the airstream is greater than that dissipated by the structural damping, then the blade vibratory amplitude will increase exponentially with time. This phenomenon is called *flutter*.

6

Unsteady Aerodynamic Forces, $F_m + F_g$
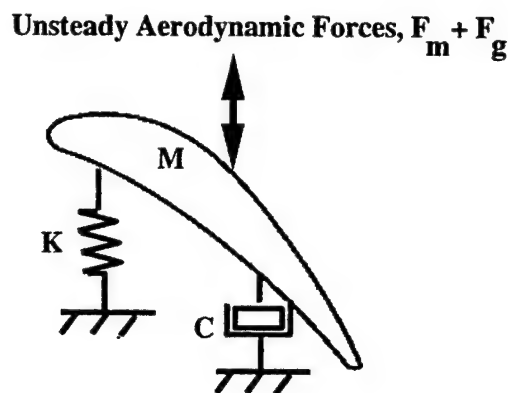
Figure 1.1: Turbomachinery blade model.

A prediction of forced response and flutter in the design and development stage requires an accurate knowledge of the unsteady flowfields that result from blade motion and gusts. Since the flow physics of modern compressors and turbines is extremely complex, developing the computational models of these flows is a challenging task. Generally, these flows are three-dimensional, viscous, and compressible. Moreover, since blade rows in a real turbomachinery are typically placed a fraction of a chord apart, multistage effects are likely to be important.

A number of methods have been developed to model complex multistage flows of turbomachinery. Most of these methods are based on time-marching techniques. In this approach, the governing equations of fluid motion are "marched" in time from one time level to the next simulating the flow through the turbomachine. This approach is very powerful and is also computationally very expensive. An alternative approach is the time-linearized technique. In this technique, the time-averaged mean flow is computed first. Then, one linearizes the governing equations assuming that the unsteadiness is small compared to the mean flow and is harmonic in time. The linearized equations are solved numerically using conventional finite element of finite volume techniques. The main advantage of the time-linearized approach is that it is very efficient compared to time marching methods.

Several methods capable of modeling unsteady flows through multiple blade rows machines are available now. Among them are time-marching methods by Rai [51, 52], Giles [17]; and time-linearized methods by Kaji and Okazaki [39], Hanson [28, 29], Buffum [5], Hall and Silkowski [26, 55, 56], Namba [45]. Most of above time-linearized methods are applied to two-dimensional configurations. The objective of this report is to develop an efficient numerical method for modeling three-dimensional flows through a multistage turbomachinery. The presented method is based on the time-linearized approach. The computational time is much smaller than the current time-domain calculations making it desirable for use in aeroelastic design.

1.2   Previous Work

For the past several decades, unsteady aerodynamic models of flows in turbomachin-
ery have been extensively developed. Fig. 1.2 classifies mathematical models that can
be used to simulate turbomachinery flows. They appear in the figure roughly in the
order of their complexity. At the extreme left there are flat plate cascade models;
at the extreme right there are nonlinear unsteady Navier-Stokes multistage models.
As models become more sophisticated, the computational cost increases dramatically.
At the present time, computational cost associated with nonlinear unsteady three-
dimensional methods is high, so that these methods, while very general, cannot be
easily used in routine design computations.

Historically, analytical and semi-analytical models of flows in turbomachinery
known as classical were developed first. A common simplification is to treat the blades
as flat plates. The resulting mean flow is uniform and all unsteady disturbances can
be considered small in comparison to the mean flow. These assumptions reduce the
equations governing the unsteady flow to linear constant coefficient equations. These
simplified equations are then solved using classical analytical techniques. Whitehead
[61, 62, 63] studied unsteady flows about two-dimensional flat plate cascades isolated
in infinitely long duct. He constructed solutions from combinations of singularities
for incompressible and compressible subsonic flows. Similar approach was applied to
supersonic flows by Verdon and McCune [38], Nagashima and Whitehead [46], and
Adamczyk and Goldstein [2]. It is possible to extend the semi-analytical approach
to incompressible flows with mean flow turning [63]. However, it is difficult to define
singularity solutions and their related kernel functions for flows that are both com-
pressible and contain mean flow nonuniformities. The main advantage of the classical
approach is its computational efficiency. However, these methods are limited to cases
unrealistic for turbomachinery aeroelasticity.

The numerical methods for modeling turbomachinery flows can be divided into
time-linearized and time-marching techniques. In the time-linearized approach, one
first solves for the time averaged "steady" flow through the turbomachine using the
governing nonlinear fluid equations. Then, one linearizes the governing equations
assuming that the unsteadiness in the flow is small compared to the mean flow, is
harmonic in time, and has a fixed interblade phase angle. As a result, one can
discretize the equations on a single blade passage and solve a problem for each in-
terblade phase angle and frequency. This technique provides a good compromise
between computational efficiency and modeling fidelity of the flow physics. Typically
the linearized approach requires several orders of magnitude less computer time than
time marching the nonlinear equations. The linearized approach was applied suc-
cessfully to single blade row computations by Hall and Crawley [23], Hall and Clark
[22], Holmes and Chuang [32] (two-dimensional linear Euler codes); Hall and Lorence
[24] (three-dimensional linear Euler codes), Clark and Hall [9] (two-dimensional linear
Navier-Stokes code).

In time-marching techniques, the governing nonlinear equations of fluid motion
are solved using a time-accurate discretization of the time-dependent terms. The
approach was applied to two-dimensional Euler equations by Huff [35], He [41] and
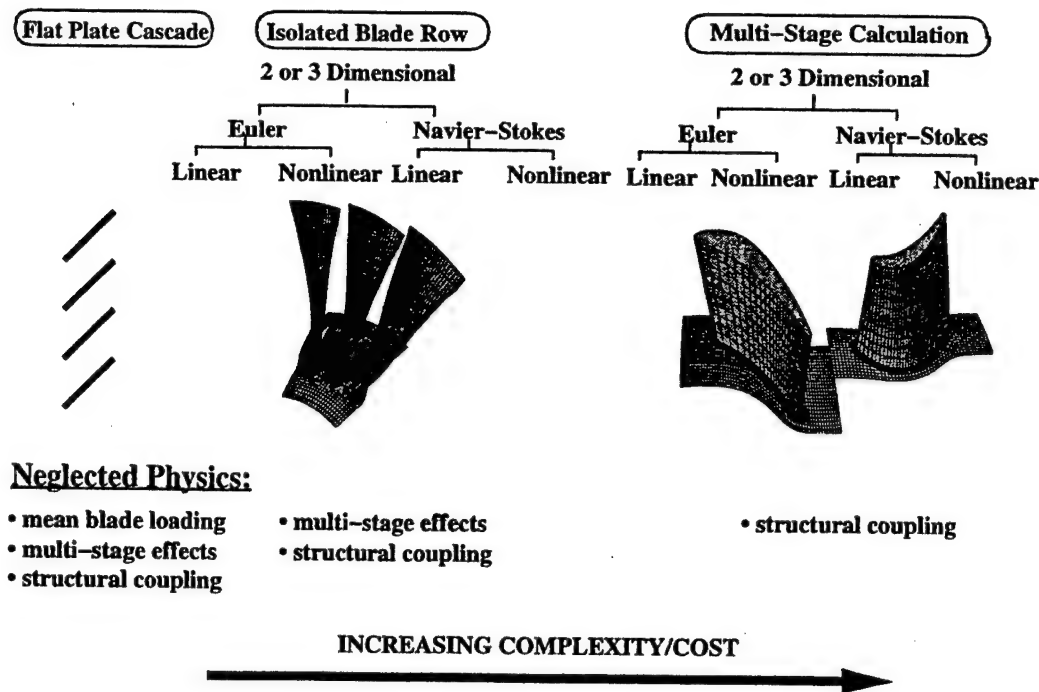
Figure 1.2: Modeling strategy (after Clark [??])

to three-dimensional Euler equations by Gerolymos [16], He [30]. It is also possible to include boundary layer effects by a process known as viscous-inviscid interaction [31]. In this technique, viscous effects are modeled only near the solid boundaries and inviscid equations are solved in the rest of the domain. Thus, viscous effects can be modeled without resorting to the full Navier-Stokes equations reducing significantly the computational time.

All of the above mentioned methods have been applied, for the most part, to an isolated blade row in an infinite duct. However, the isolated blade row model does not represent the actual operating environment and may lack the essential physics of real machines, such as unsteady potential, wake and shock wave interactions between neighboring blade rows. These interactions between neighboring blade rows may significantly alter the unsteady flowfield of a given blade row. Recently, several investigations which model multistage blade row interactions in turbomachinery have been reported in the literature.

The most common approach is to perform direct time marching simulations of the flow field. This approach was implemented by Giles [17] (two-dimensional Euler equations), Rai [50] (two-dimensional Navier-Stokes equations), Giles and Saxer [54] (three-dimensional Euler equations), and Rai [51, 52] (three-dimensional Navier-Stokes equations). In these methods, separate grids are generated for the stator and for the rotor with a common interface between the blade rows. The equations are marched in time, and at each time step of the simulation the information at stator/rotor interface is exchanged. A key issue in these methods is how to model this interface boundary. An assumption in Rai's work [51, 52] is that the blade pitches of the two blade rows are equal or integer ratios. In case of integer ratios, calculations

are performed on a domain including multiple blades which increases significantly the computational cost. Giles [17], on the other hand, introduces a "time-inclining" technique whereby a space-time transformation is made on the governing flow equations that allows unequal pitches for the stator and the rotor to be modeled using just a single blade passage from each row (under some circumstances).

Several time-linearized methods have been likewise developed for multiple blade row machines. In a time-linearized analysis for an isolated blade row, one assumes that the initial flow disturbance has a fixed frequency and a fixed interblade phase angle. As this initial disturbance interacts with the blade row, it *scatters* into multiple pressure, vortical, and entropy waves with the same frequency and phase shift over one blade pitch. When two or more blade rows are involved, the relative motion due to the rotation of the rotors produces a *shifting* of the frequencies of waves as they propagate from one blade row to the next. This frequency shift is analogous to the familiar Doppler effect. When the fluid waves impinge on another blade row, they will act as an excitation in this second blade row, and will scatter into another set of waves which propagate upstream and downstream. Some of these waves impinge on the original blade row and the entire process repeats. The final result is that a multiplicity of waves with different frequencies and wavelengths interact with one another, violating the original assumption of a single frequency and an interblade phase angle.

Among time-linearized models for multistage turbomachinery are the semi-analytical methods by Kaji and Okazaki [39], Hanson [28], Namba [45]. In these analyses, flat-plate rotors and stators are modeled by distributed singularities. Kaji and Okazaki retained one harmonic in the coupling. Hanson and Namba included several harmonics and incorporated the concept of scattering. These semi-analytical methods are extremely fast, and are useful for understanding the importance of multistage effects in turbomachinery. Unfortunately, analytical solution techniques cannot be easily applied to realistic geometries, i.e. blades with thickness and camber.

Hall and Silkowski [26, 55, 56], Hanson [29], and Buffum [5] have developed an alternative method for modeling the influence of multistage effects on the unsteady aerodynamic response of (two-dimensional) compressors and turbines. In this method, the different blade rows are coupled through the spinning modes - pressure, vorticity and entropy waves at discrete frequencies and nodal diameters that propagate between blade rows. Each blade row is modeled by a set of transmission/reflection/scattering coefficients calculated using conventional frequency domain solvers for an individual blade row. These coefficients provide the information on how individual spinning modes interact with a given blade row. The isolated blade row influence coefficients, explicit inter-row coupling relationships and appropriate boundary conditions are all assembled into a linear system of equations, which is solved by lower upper (LU) matrix decomposition.

The described above method by Hall and Silkowski [56] (later referred to as Coupled Mode Method or CMM) is computationally very efficient. Furthermore, it offers some flexibility because the influence coefficients may be calculated by using any isolated blade row solver (e.g., Euler, Navier-Stokes, etc.). The only disadvantage of this method that it cannot be easily extended to three-dimensional cases. Note that

in this method the influence coefficients are computed by running code separately for each spinning mode for each blade row. In three dimensions, accounting for radial eigenmodes in addition to circumferential modes increases the computational cost of the problem significantly. Additionally, in two dimensions the eigenmodes of unsteady flow are book kept by frequency and interblade phase angle, whereas in three dimensions one has to find radial eigenmodes and axial wavenumbers (eigenvalues) numerically, which also contributes to the total computational cost.

In this work, a new unsteady aerodynamic analysis of multistage flows in turbomachinery is presented that is capable of efficiently analyzing complex three-dimensional flows.

1.3   Summary of Present Research

The objectives of this work are to develop an efficient method for modeling multistage flows in turbomachinery, and to study flutter vibration in a modern three-dimensional compressor.

The present method is based on the time-linearized approach. We assume that the initial unsteady excitation (e.g. vibration of rotor blades, incoming gust) has a fixed frequency and a fixed number of nodal diameters. This initial excitation shifts and scatters into a multiplicity of frequencies and wavelengths because of relative motion of adjacent blade rows in turbomachinery. Hence, the unsteady flow is given as an infinite sum of fluid modes (*spinning modes*) identified by a frequency and a number of nodal diameters. In practice, this sum is truncated. We assume and demonstrate later that the unsteady solution converges as more modes are added to a model.

The outline of the method is given as the following. First, we generate separate computational grids for each individual blade row. Only one blade passage for each blade row is needed for computations because the flow is periodic in the circumferential direction. Then, the steady multistage flow is computed using the Euler equations and conventional fluid dynamic techniques. At the interface boundaries, the circumferentially averaged flow variables are matched at each radial station. This insures that mass, momentum, and energy are conserved. This matching procedure is similar to the "mixing planes" technique developed by Denton and Singh [15], Dawes [13], Denton [14], and Hall [20].

Once a mean nonlinear flow is obtained, the Euler equations are linearized. Then, we discretize and solve the linearized Euler equations on each computational grid for each spinning mode solution concurrently. A time-linearized technique [24] that has been developed for an isolated blade row is used to compute each of these solutions. At each iteration of flow solver, information is exchanged among solutions at the inter-row boundaries coupling together the various spinning modes. This iteration procedure continues until convergence is reached. Note, that mode coupling in the present method is performed by matching the circumferential Fourier modes of flow variables rather than characteristic waves, which are used in the influence coefficients methods [56].

There are several features of the present method that make the calculations more

efficient. First, while calculating the mean steady and unsteady flows, only steady-state solution are obtained (unsteady flows are solutions of time-linearized Euler equations where the term $\partial/\partial t$ is replaced by the term $j\omega$, so time is not explicitly present in the equations). This allows us to use local time stepping and multi-grid acceleration techniques.

Finally, the overall size of numerical problem is a function of a number of blade rows and the number of modes retained in a computational model. It will be shown that a good estimation of the unsteady pressure on a blade surfaces can be obtained by keeping in the model only the neighboring blade rows and a few spinning modes. This reduces the size of the problem significantly.

1.4 Outline

In Chapter 2, the three-dimensional Euler equations governing the motion of an inviscid compressible flow are presented in a Cartesian reference system rotating at a constant angular speed. From this form, the equations in absolute frame (stator) of reference are easily derived. Next, the process whereby the unsteady flow is decomposed into a nonlinear mean flow and a harmonically varying small perturbation is developed. Finally, the linearized Euler equations used to solve the unsteady flow model are presented.

In Chapter 3, the numerical algorithm used to integrate the governing equations is developed. A Lax-Wendroff scheme developed by Ni [47, 48] is presented. The conservation, accuracy and stability properties of this scheme are discussed next. Finally, the numerical smoothing and model convergence acceleration techniques are addressed.

In Chapter 4, the boundary conditions required to solve steady and unsteady conservation equations for a single blade row are developed. These conditions are divided into near-field and far-field. Near-field conditions include the boundary conditions at the solid walls and the periodic boundaries. Far-field conditions are developed to minimize spurious reflections from the upstream and downstream computational boundaries.

In Chapter 5, the kinematic behavior of unsteady flows through multiple blade rows is discussed. Then, the method for modeling these flows is presented with a detailed discussion on the algorithm used to couple solutions at the inter-row boundaries.

In Chapter 6, a number of test cases are presented to validate the multistage linearized Euler analysis and to demonstrate the multistage effects on unsteady flows. All cases in this chapter are designed to demonstrate the significance of the multistage effects. First, simple two-dimensional configurations are considered and validated against available two-dimensional multistage methods. Second, we examine a three-dimensional stage composed with flat helical plates, which enables us to validate the present method againt a semi-analytical multistage three-dimensional method. Finally, one and one-half stages of a modern three-dimensional compressor is considered.

In Chapter 7, the contributions of the present work are outlined and the possible extensions for future research are discussed.

Chapter 2

Governing Equations

In this Chapter, the governing nonlinear and liner Euler equations are presented. In Section 2.2, the nonlinear Euler equations in both integral and differential forms are introduced. In Section 2.3, the computational grid is linearized about a fixed position, so that the grid continuously deforms with the blade. In Section 2.4, the Euler equations are linearized in a frame of reference attached to the moving grid.

2.1 Nomenclature

c_v, c_p	specific heats
E	total rotary internal energy per unit mass
e	internal energy per unit mass
$\bar{e}_x, \bar{e}_y, \bar{e}_z$	basis vectors of Cartesian coordinate system
$\bar{e}_x, \bar{e}_\theta, \bar{e}_R$	basis vectors of cylindrical coordinate system
$\mathbf{F}, \mathbf{G}, \mathbf{H}$	flux vectors in the x, y and z directions
f, g, h	grid perturbation in the x, y and z directions
I	rothalpy
$[\mathbf{J}]$	Jacobian matrix of transformation from physical to computational coordinates
j	$\sqrt{-1}$
p	pressure
$\mathbf{S}$	vector of source terms (centripetal and Coriolis forces)
T	temperature
t	time
$\mathbf{U}$	vector of conservation variables
u, v, w	components of velocity in Cartesian coordinates
u_x, u_θ, u_R	components of velocity in cylindrical coordinates
$\mathbf{X}$	vector of spatial coordinates (x, y, z)
x, y, z, t	Cartesian coordinate system - physical domain
x, R, θ, t	cylindrical coordinate system - physical domain

14

ξ, η, ζ, τ	Cartesian coordinate system - computational domain
γ	specific heat ratio
ρ	density
$\bar{\Omega}, \Omega$	angular velocity of a rotor
ω	frequency
$()_{abs}$	quantity in absolute frame of reference
$()_{rel}$	quantity in relative frame of reference
$\bar{()}$	"steady" (mean) quantity
$()'$	small perturbation quantity

2.2 Three-Dimensional Euler Equations

We consider the time-dependent and three-dimensional adiabatic flow, with negligible body forces, of a non-heat conducting perfect gas through a turbomachinery. For many flows of practical interest the Reynolds number (Re), is sufficiently high that viscous effects are concentrated in relatively thin layers. Outside these regions, the gas is assumed to be inviscid.

The Euler equations governing the inviscid flow describe the conservation of mass, momentum and energy. The conservation laws are derived for either a fixed or a moving control volume in space, see for instance Refs. [4, 42]. The differential form of the Euler equations is obtained from the integral form by shrinking the control volume to a point and applying the divergence theorem. For a detailed development of the three-dimensional Euler equations, the reader is referred to Ref. [44].

The algorithm developed in this report solves the flow fields associated with non-rotating and rotating blade rows in their own Cartesian coordinate systems. The rotating and non-rotating blade rows are called rotors and stators respectively. Absolute values (subscripted *abs*) are used in the stators, fixed frame of reference, whereas rotor-relative quantities (subscripted *rel*) are used in the rotating coordinate system. After finding the flow through all rotors and stators, appropriate transformations are applied at the stator/rotor interface boundaries to match the flow fields from the both sides.

Consider a Cartesian coordinate system with its x axis aligned with the axis of rotation of an engine. The y and z axes rotate about the x axis with angular speed $\bar{\Omega} = \Omega \bar{i}$. The governing Euler equations will be written in the in the rotating frame of reference. The integral form of the equations for an arbitrary control volume V with a surface area A is given by

$$\frac{\partial}{\partial t} \iiint_V \mathbf{U} dV + \iint_A \left(\mathbf{F} - \mathbf{U}\frac{\partial \hat{f}}{\partial t}, \mathbf{G} - \mathbf{U}\frac{\partial \hat{g}}{\partial t}, \mathbf{H} - \mathbf{U}\frac{\partial \hat{h}}{\partial t} \right) \cdot d\mathbf{A} = \iiint_V \mathbf{S} dV \quad (2.1)$$

where $\hat{f}$, $\hat{g}$, and $\hat{h}$ describe the displacement of the control volume in x, y, and z directions respectively; dV is the elemental volume of the control volume; and $d\mathbf{A}$ is the elemental surface vector.

The differential form of the equations is given by

$$\frac{\partial \mathbf{U}}{\partial t} + \frac{\partial \mathbf{F}}{\partial x} + \frac{\partial \mathbf{G}}{\partial y} + \frac{\partial \mathbf{H}}{\partial z} - \mathbf{S} = 0. \tag{2.2}$$

In Eqs. (2.1)-(2.2), $\mathbf{U} = (\rho, \rho u, \rho v, \rho w, \rho E)_{rel}^T$ is the vector of flow conservation variables where ρ is the density and the vector $(u, v, w)_{rel}^T$ is the flow velocity. The total rotary internal energy per unit mass E is defined as

$$E_{rel} = e + \frac{1}{2}(u^2 + v^2 + w^2)_{rel} - \frac{1}{2}\Omega^2 R^2, \quad R = \sqrt{y^2 + z^2}. \tag{2.3}$$

Here e is the internal energy per unit mass. It is defined as $e = c_v T$. The symbol c_v denotes the specific heat at constant volume and T is the static temperature.

The vectors $\mathbf{F}, \mathbf{G}, \mathbf{H}$ represent fluxes of mass, momentum and energy in x, y and z directions. They are given by

$$\mathbf{F} = \begin{pmatrix} \rho u \\ \rho u^2 + p \\ \rho u v \\ \rho u w \\ \rho u I \end{pmatrix}_{rel}, \mathbf{G} = \begin{pmatrix} \rho v \\ \rho u v \\ \rho v^2 + p \\ \rho v w \\ \rho v I \end{pmatrix}_{rel}, \mathbf{H} = \begin{pmatrix} \rho w \\ \rho u w \\ \rho u w \\ \rho w^2 + p \\ \rho v I \end{pmatrix}_{rel}. \tag{2.4}$$

For an ideal gas with constant specific heat ratio γ, it can be shown that the pressure p is given by

$$p = (\gamma - 1)\rho[E_{rel} - \frac{1}{2}(u^2 + v^2 + w^2)_{rel} + \frac{1}{2}\Omega^2 R^2]. \tag{2.5}$$

In Equation (2.4), I is the rothalpy defined as

$$I = \frac{\rho E_{rel} + p}{\rho} = \frac{\gamma \rho E_{rel}}{\rho} - \frac{\gamma - 1}{2}(u^2 + v^2 + w^2)_{rel} + \frac{\gamma - 1}{2}(\Omega R)^2 \tag{2.6}$$

The vector $\mathbf{S}$ is a source term that includes the centripetal and Coriolis forces per unit volume, i.e.

$$\mathbf{S} = \begin{pmatrix} 0 \\ 0 \\ \rho(\Omega^2 y + 2\Omega w) \\ \rho(\Omega^2 z - 2\Omega v) \\ 0 \end{pmatrix}_{rel} \tag{2.7}$$

The system of fluid equations will be solved in Cartesian coordinates. However, it is more convenient to use a cylindrical coordinate system to apply boundary conditions. The relationship between cylindrical coordinates (x, θ, R) and Cartesian coordinates (x, y, z) is given by

$$y = R\sin\theta \tag{2.8}$$
$$z = R\cos\theta \tag{2.9}$$
$$R = \sqrt{y^2 + z^2} \tag{2.10}$$
$$\theta = \arctan\left(\frac{y}{z}\right) \tag{2.11}$$

The unit normals of the cylindrical coordinate system is expressed in terms of the unit normals of the Cartesian coordinate system as

$$\bar{e}_x = \bar{e}_x \tag{2.12}$$

$$\bar{e}_\theta = \bar{e}_y \cos\theta - \bar{e}_z \sin\theta \tag{2.13}$$

$$\bar{e}_r = \bar{e}_y \sin\theta + \bar{e}_z \cos\theta. \tag{2.14}$$

Using cylindrical coordinates, the vector of velocity in the absolute frame of reference, $\mathbf{V}_{abs} = (u_x, u_\theta, u_R)_{abs}$, is related to the one in the relative frame of reference, $\mathbf{V}_{rel} = (u_x, u_\theta, u_R)_{rel}$, by

$$\mathbf{V}_{abs} = \mathbf{V}_{rel} + \mathbf{V}_{\text{wheel}} \tag{2.15}$$

where $\mathbf{V}_{\text{wheel}}$ is the rotor wheel speed given by $\mathbf{V}_{\text{wheel}} = -\Omega R \bar{e}_\theta$. Hence, components of velocity are related as

$$u_{xabs} = u_{xrel} \tag{2.16}$$

$$u_{\theta abs} = u_{\theta rel} - \Omega R \tag{2.17}$$

$$u_{Rabs} = u_{Rrel} \tag{2.18}$$

2.3 Computational Coordinate System

In this work, the time-dependent or unsteady fluctuations in the flow are assumed to be small compared to the mean flow. This unsteadiness may arise from self-excited blade motions or upstream/downstream flow distortions called gusts.

Traditionally, computational grids for computing unsteady flows have been fixed in space. If the grid is fixed in space and the blade is vibrating, the pressure on the surface of the blade has to be extrapolated when the blade is not at its mean location. Making this extrapolation can cause large errors especially near the leading and trailing edges of the blade. To eliminate the difficulty of applying the boundary conditions in this work a different approach is used. In this approach the computational grid continuously moves and deforms with blades [7, 21, 22].

In this work, blade motion is assumed to be harmonic, with frequency ω. The physical coordinates (x, y, z, t) are related to the computational coordinates (ξ, η, ζ, τ) by

$$x(\xi, \eta, \zeta, \tau) = \xi + f(\xi, \eta, \zeta)e^{j\omega\tau} \tag{2.19}$$

$$y(\xi, \eta, \zeta, \tau) = \eta + g(\xi, \eta, \zeta)e^{j\omega\tau} \tag{2.20}$$

$$z(\xi, \eta, \zeta, \tau) = \zeta + h(\xi, \eta, \zeta)e^{j\omega\tau} \tag{2.21}$$

$$t(\xi, \eta, \zeta, \tau) = \tau \tag{2.22}$$

where (f, g, h) are amplitudes of displacement of the grid in the x, y and z directions respectively. On the boundaries of the blades, the vector (f, g, h) is the amplitude of the blade vibration. The computational coordinate system (ξ, η, ζ, τ) is the zeroth-order approximation to the physical coordinates (x, y, z, t). The mean or steady flow is computed in the computational coordinates (ξ, η, ζ).

A relationship between derivative operators in the physical coordinate system and derivative operators in the computational coordinate system is given by

$$\begin{pmatrix} \partial/\partial x \\ \partial/\partial y \\ \partial/\partial z \\ \partial/\partial t \end{pmatrix} = [\mathbf{J}] \begin{pmatrix} \partial/\partial \xi \\ \partial/\partial \eta \\ \partial/\partial \zeta \\ \partial/\partial \tau \end{pmatrix} = \begin{pmatrix} \xi_x & \eta_x & \zeta_x & \tau_x \\ \xi_y & \eta_y & \zeta_y & \tau_y \\ \xi_z & \eta_z & \zeta_z & \tau_z \\ \xi_t & \eta_t & \zeta_t & \tau_t \end{pmatrix} \begin{pmatrix} \partial/\partial \xi \\ \partial/\partial \eta \\ \partial/\partial \zeta \\ \partial/\partial \tau \end{pmatrix} \quad (2.23)$$

$$\begin{pmatrix} \partial/\partial \xi \\ \partial/\partial \eta \\ \partial/\partial \zeta \\ \partial/\partial \tau \end{pmatrix} = [\mathbf{J}]^{-1} \begin{pmatrix} \partial/\partial x \\ \partial/\partial y \\ \partial/\partial z \\ \partial/\partial t \end{pmatrix} = \begin{pmatrix} x_\xi & y_\xi & z_\xi & t_\xi \\ x_\eta & y_\eta & z_\eta & t_\eta \\ x_\zeta & y_\zeta & z_\zeta & t_\zeta \\ x_\tau & y_\tau & z_\tau & t_\tau \end{pmatrix} \begin{pmatrix} \partial/\partial x \\ \partial/\partial y \\ \partial/\partial z \\ \partial/\partial t \end{pmatrix} \quad (2.24)$$

where $[\mathbf{J}]$ is the Jacobian of the transformation.

Using Equations (2.19)-(2.22), one can express the matrix $[\mathbf{J}]^{-1}$ in terms of (f, g, h), so that

$$[\mathbf{J}]^{-1} = \begin{pmatrix} 1 + f_\xi & g_\xi & h_\xi & 0 \\ f_\eta & 1 + g_\eta & h_\eta & 0 \\ f_\zeta & g_\zeta & 1 + h_\zeta & 0 \\ f_\tau & g_\tau & h_\tau & 1 \end{pmatrix} \quad (2.25)$$

The matrix $[\mathbf{J}]$ is found by inverting the matrix $[\mathbf{J}]^{-1}$. The matrix $[\mathbf{J}]$ is given to first order by

$$[\mathbf{J}] = \begin{pmatrix} 1 - f_\xi & -g_\xi & -h_\xi & 0 \\ -f_\eta & 1 - g_\eta & -h_\eta & 0 \\ -f_\zeta & -g_\zeta & 1 - h_\zeta & 0 \\ -f_\tau & -g_\tau & -h_\tau & 1 \end{pmatrix} \quad (2.26)$$

The steady and unsteady grid generation technique will be discussed in Chapter 4. Note that for the gust response problems, moving grid terms (f, g, h) are equal to zero, and $[\mathbf{J}]$ is reduced to the identity matrix.

2.4 Linearization of the Euler Equations

Assuming that unsteadiness in the flow is small, each flow variable can be decomposed into a "steady" mean part and a small perturbation "unsteady" part. If ω is the frequency of an unsteady perturbation, then the flow variables can be represented as

$$\begin{align} \rho(\xi, \eta, \zeta, \tau) &= \bar{\rho}(\xi, \eta, \zeta) + \rho'(\xi, \eta, \zeta)e^{j\omega\tau} & (2.27) \\ \rho u(\xi, \eta, \zeta, \tau) &= \overline{\rho u}(\xi, \eta, \zeta) + (\rho u)'(\xi, \eta, \zeta)e^{j\omega\tau} & (2.28) \\ \rho v(\xi, \eta, \zeta, \tau) &= \overline{\rho v}(\xi, \eta, \zeta) + (\rho v)'(\xi, \eta, \zeta)e^{j\omega\tau} & (2.29) \\ \rho w(\xi, \eta, \zeta, \tau) &= \overline{\rho w}(\xi, \eta, \zeta) + (\rho w)'(\xi, \eta, \zeta)e^{j\omega\tau} & (2.30) \\ \rho E(\xi, \eta, \zeta, \tau) &= \overline{\rho E}(\xi, \eta, \zeta) + (\rho E)'(\xi, \eta, \zeta)e^{j\omega\tau} & (2.31) \end{align}$$

or in the more compact notation

$$\mathbf{U} = \overline{\mathbf{U}} + \mathbf{U}' e^{j\omega\tau}. \quad (2.32)$$

Here, $\overline{\mathbf{U}}$ is the vector of conservation variables representing the zeroth-order or mean flow field, and $\mathbf{U}'$ is the vector of small perturbation amplitudes of the conservation variables representing the first order unsteadiness in the flow field.

Similarly, the flux and source vectors can be expanded in a perturbation series. Taylor expanding about the mean flow, one finds that

$$\mathbf{F} = \overline{\mathbf{F}}(\overline{\mathbf{U}}) + \frac{\partial \mathbf{F}}{\partial \mathbf{U}}\Big|_{\overline{\mathbf{U}}} \mathbf{U}' e^{j\omega\tau} + \frac{\partial \mathbf{F}}{\partial \mathbf{X}}\Big|_{\overline{\mathbf{X}}} (f,g,h)^T e^{j\omega\tau} \qquad (2.33)$$

$$\mathbf{G} = \overline{\mathbf{G}}(\overline{\mathbf{U}}) + \frac{\partial \mathbf{G}}{\partial \mathbf{U}}\Big|_{\overline{\mathbf{U}}} \mathbf{U}' e^{j\omega\tau} + \frac{\partial \mathbf{G}}{\partial \mathbf{X}}\Big|_{\overline{\mathbf{X}}} (f,g,h)^T e^{j\omega\tau} \qquad (2.34)$$

$$\mathbf{H} = \overline{\mathbf{H}}(\overline{\mathbf{U}}) + \frac{\partial \mathbf{H}}{\partial \mathbf{U}}\Big|_{\overline{\mathbf{U}}} \mathbf{U}' e^{j\omega\tau} + \frac{\partial \mathbf{H}}{\partial \mathbf{X}}\Big|_{\overline{\mathbf{X}}} (f,g,h)^T e^{j\omega\tau} \qquad (2.35)$$

$$\mathbf{S} = \overline{\mathbf{S}}(\overline{\mathbf{U}}) + \frac{\partial \mathbf{S}}{\partial \mathbf{U}}\Big|_{\overline{\mathbf{U}}} \mathbf{U}' e^{j\omega\tau} + \frac{\partial \mathbf{S}}{\partial \mathbf{X}}\Big|_{\overline{\mathbf{X}}} (f,g,h)^T e^{j\omega\tau} \qquad (2.36)$$

where $\mathbf{X}$ and $\overline{\mathbf{X}}$ is the vector of spatial coordinates (x,y,z) and its mean value respectively. The first term on the right-hand side of Eqs. (2.33)-(2.36) represents the mean flux/source vector. In general this term is a function of the spatial coordinates (ξ, η, ζ) and the mean values of conservation variables $\overline{\mathbf{U}}$. This term is zeroth order in the expansion and is found by solving the steady equations. The second and the third terms on the right-hand side of Eqs. (2.33)-(2.36) are the first order terms arising from perturbations in the conservation variables and the motion of the computational mesh respectively.

The Jacobian matrices in Eqs. (2.33)-(2.36) are given by

$$\frac{\partial \mathbf{F}}{\partial \mathbf{U}}\Big|_{\overline{\mathbf{U}}} = \begin{pmatrix} 0 & 1 & 0 & 0 & 0 \\ -\overline{u}^2 + \frac{\gamma-1}{2}V_T & -(\gamma-3)\overline{u} & (1-\gamma)\overline{v} & (1-\gamma)\overline{w} & \gamma-1 \\ -\overline{uv} & \overline{v} & \overline{u} & 0 & 0 \\ -\overline{uw} & \overline{w} & 0 & \overline{u} & 0 \\ -\overline{u}(I - \frac{\gamma-1}{2}V_T) & I - (\gamma-1)\overline{u}^2 & (1-\gamma)\overline{uv} & (1-\gamma)\overline{uw} & \gamma\overline{u} \end{pmatrix} \qquad (2.37)$$

$$\frac{\partial \mathbf{G}}{\partial \mathbf{U}}\Big|_{\overline{\mathbf{U}}} = \begin{pmatrix} 0 & 0 & 1 & 0 & 0 \\ -\overline{uv} & \overline{v} & \overline{u} & 0 & 0 \\ -\overline{v}^2 + \frac{\gamma-1}{2}V_T & (1-\gamma)\overline{u} & -(\gamma-3)\overline{v} & (1-\gamma)\overline{w} & \gamma-1 \\ -\overline{vw} & 0 & \overline{w} & \overline{v} & 0 \\ -\overline{v}(I - \frac{\gamma-1}{2}V_T) & (1-\gamma)\overline{vu} & I - (\gamma-1)\overline{v}^2 & (1-\gamma)\overline{vw} & \gamma\overline{v} \end{pmatrix} \qquad (2.38)$$

$$\frac{\partial \mathbf{H}}{\partial \mathbf{U}}\Big|_{\overline{\mathbf{U}}} = \begin{pmatrix} 0 & 0 & 0 & 1 & 0 \\ -\overline{uw} & \overline{w} & 0 & \overline{u} & 0 \\ -\overline{vw} & 0 & \overline{w} & \overline{v} & 0 \\ -\overline{w}^2 + \frac{\gamma-1}{2}V_T & (1-\gamma)\overline{u} & (1-\gamma)\overline{v} & -(\gamma-3)\overline{w} & \gamma-1 \\ -\overline{w}(I - \frac{\gamma-1}{2}V_T) & (1-\gamma)\overline{uw} & (1-\gamma)\overline{vw} & I - (\gamma-1)\overline{w}^2 & \gamma\overline{w} \end{pmatrix} \qquad (2.39)$$

$$\frac{\partial \mathbf{S}}{\partial \mathbf{U}}\Big|_{\overline{\mathbf{U}}} = \begin{pmatrix} 0 & 0 & 0 & 0 & 0 \\ 0 & 0 & 0 & 0 & 0 \\ \Omega^2\eta & 0 & 0 & 2\Omega & 0 \\ \Omega^2\zeta & 0 & -2\Omega & 0 & 0 \\ 0 & 0 & 0 & 0 & 0 \end{pmatrix} \qquad (2.40)$$

$$\frac{\partial \mathbf{F}}{\partial \mathbf{X}}\bigg|_{\overline{\mathbf{X}}} = \begin{pmatrix} 0 & 0 & 0 \\ 0 & (\gamma-1)\overline{\rho}\Omega^2\eta & (\gamma-1)\overline{\rho}\Omega^2\zeta \\ 0 & 0 & 0 \\ 0 & 0 & 0 \\ 0 & (\gamma-1)\overline{\rho u}\Omega^2\eta & (\gamma-1)\overline{\rho u}\Omega^2\zeta \end{pmatrix} \tag{2.41}$$

$$\frac{\partial \mathbf{G}}{\partial \mathbf{X}}\bigg|_{\overline{\mathbf{X}}} = \begin{pmatrix} 0 & 0 & 0 \\ 0 & 0 & 0 \\ 0 & (\gamma-1)\overline{\rho}\Omega^2\eta & (\gamma-1)\overline{\rho}\Omega^2\zeta \\ 0 & 0 & 0 \\ 0 & (\gamma-1)\overline{\rho u}\Omega^2\eta & (\gamma-1)\overline{\rho u}\Omega^2\zeta \end{pmatrix} \tag{2.42}$$

$$\frac{\partial \mathbf{H}}{\partial \mathbf{X}}\bigg|_{\overline{\mathbf{X}}} = \begin{pmatrix} 0 & 0 & 0 \\ 0 & 0 & 0 \\ 0 & 0 & 0 \\ 0 & (\gamma-1)\overline{\rho}\Omega^2\eta & (\gamma-1)\overline{\rho}\Omega^2\zeta \\ 0 & (\gamma-1)\overline{\rho u}\Omega^2\eta & (\gamma-1)\overline{\rho u}\Omega^2\zeta \end{pmatrix} \tag{2.43}$$

$$\frac{\partial \mathbf{S}}{\partial \mathbf{X}}\bigg|_{\overline{\mathbf{X}}} = \begin{pmatrix} 0 & 0 & 0 \\ 0 & 0 & 0 \\ 0 & \overline{\rho}\Omega^2 & 0 \\ 0 & 0 & \overline{\rho}\Omega^2 \\ 0 & 0 & 0 \end{pmatrix} \tag{2.44}$$

where

$$V_T = \overline{u}^2 + \overline{v}^2 + \overline{w}^2 + (\Omega R)^2. \tag{2.45}$$

To linearize the Euler equations, one needs first to substitute the flow decomposition expressions, Eqs. (2.32)-(2.36), into the full Euler equations, Eq. (2.2). Collecting terms of zeroth order, one obtains the mean flow equations,

$$\frac{\partial \overline{\mathbf{F}}}{\partial \xi} + \frac{\partial \overline{\mathbf{G}}}{\partial \eta} + \frac{\partial \overline{\mathbf{H}}}{\partial \zeta} - \overline{\mathbf{S}} = 0. \tag{2.46}$$

These are just the original nonlinear steady Euler equations.

Collecting terms of first order, one finds the unsteady perturbation equations are given by

$$j\omega \mathbf{U}' + \frac{\partial}{\partial \xi}\left(\frac{\partial \overline{\mathbf{F}}}{\partial \overline{\mathbf{U}}}\mathbf{U}'\right) + \frac{\partial}{\partial \eta}\left(\frac{\partial \overline{\mathbf{G}}}{\partial \overline{\mathbf{U}}}\mathbf{U}'\right) + \frac{\partial}{\partial \zeta}\left(\frac{\partial \overline{\mathbf{H}}}{\partial \overline{\mathbf{U}}}\mathbf{U}'\right) - \frac{\partial \overline{\mathbf{S}}}{\partial \overline{\mathbf{U}}}\mathbf{U}' = \mathbf{b} \tag{2.47}$$

where the right-hand side $\mathbf{b}$ represents a source term arising from the moving grid terms. This source term $\mathbf{b}$ is given by

$$\mathbf{b} = j\omega(f, g, h) \cdot \nabla\overline{\mathbf{U}} + j\omega\frac{\partial \overline{\mathbf{U}}f}{\partial \xi} + j\omega\frac{\partial \overline{\mathbf{U}}g}{\partial \eta} + j\omega\frac{\partial \overline{\mathbf{U}}h}{\partial \zeta} +$$

$$\frac{\partial}{\partial \xi} \cdot \nabla\overline{\mathbf{F}} - \frac{\partial}{\partial \xi}\left(\frac{\partial \overline{\mathbf{F}}}{\partial \overline{\mathbf{X}}}(f, g, h)^T\right) + \frac{\partial}{\partial \eta} \cdot \nabla\overline{\mathbf{G}} - \frac{\partial}{\partial \eta}\left(\frac{\partial \overline{\mathbf{G}}}{\partial \overline{\mathbf{X}}}(f, g, h)^T\right)$$

$$+\frac{\partial}{\partial\zeta}\cdot\nabla\overline{\mathbf{H}}-\frac{\partial}{\partial\zeta}\left(\frac{\partial\overline{\mathbf{H}}}{\partial\overline{\mathbf{X}}}(f,g,h)^T\right)\quad-(f,g,h)\cdot\nabla\overline{\mathbf{S}}+\frac{\partial\overline{\mathbf{S}}}{\partial\overline{\mathbf{X}}}(f,g,h)^T \qquad (2.48)$$

Note that the source term **b** is a function only of the grid motion and the mean nonlinear flow. The grid motion terms are prescribed and the mean flow is known after solving the steady Euler equations, Eq. (2.46). Hence, the source term **b** can be computed once at the beginning of the computation of the unsteady flow.

Similarly, we can linearize the Euler equations in the integral form, Eq.(2.1). First, the differential volume and area are linearized. Up to this point, the differential volume and area have been written as dV and $d\mathbf{A}$ respectively. Using computational coordinates, the differential cell volume can be written as

$$dV = dx\,dy\,dz = (d\xi + df)(d\eta + dg)(d\zeta + dh) \qquad (2.49)$$

To first-order, this expression can be written as

$$dV = d\overline{V} + dV' = d\xi\,d\eta\,d\zeta + (df\,d\eta\,d\zeta + d\xi\,dg\,d\zeta + d\xi\,d\eta\,dh) \qquad (2.50)$$

Similarly, the differential cell area can be written as

$$d\mathbf{A} = d\overline{\mathbf{A}} + d\mathbf{A}' \qquad (2.51)$$

Substituting Eqs. (2.50)-(2.51) as well as the flow decomposition, Eq.(2.32)-(2.36), into the integral form of the Euler equations, Eq. (2.1), and collecting terms of zeroth order, one obtains the steady Euler equations

$$\iint_A (\overline{\mathbf{F}},\overline{\mathbf{G}},\overline{\mathbf{H}})\cdot d\overline{\mathbf{A}} - \iiint_V \overline{\mathbf{S}}\,d\overline{V} = 0 \qquad (2.52)$$

Collecting the first-order terms results in the integral form of the linearized Euler equations, i.e.

$$\iiint_V j\omega\mathbf{U}'d\overline{V} + \iint_A \left(\frac{\partial\overline{\mathbf{F}}}{\partial\overline{\mathbf{U}}}\mathbf{U}', \frac{\partial\overline{\mathbf{G}}}{\partial\overline{\mathbf{U}}}\mathbf{U}', \frac{\partial\overline{\mathbf{H}}}{\partial\overline{\mathbf{U}}}\mathbf{U}'\right)\cdot d\overline{\mathbf{A}} - \iiint_V \frac{\partial\overline{\mathbf{S}}}{\partial\overline{\mathbf{U}}}\mathbf{U}'d\overline{V}$$

$$= -\iiint_V j\omega\overline{\mathbf{U}}dV' + \iint_A j\omega\overline{\mathbf{U}}(f,g,h)\cdot d\overline{\mathbf{A}} - \iint_A (\overline{\mathbf{F}},\overline{\mathbf{G}},\overline{\mathbf{H}})\cdot d\mathbf{A}'$$

$$- \iint_A \left(\frac{\partial\overline{\mathbf{F}}}{\partial\overline{\mathbf{X}}}(f,g,h)^T, \frac{\partial\overline{\mathbf{G}}}{\partial\overline{\mathbf{X}}}(f,g,h)^T, \frac{\partial\overline{\mathbf{H}}}{\partial\overline{\mathbf{X}}}(f,g,h)^T\right)\cdot d\overline{\mathbf{A}}$$

$$+ \iiint_V \overline{\mathbf{S}}dV' + \iiint_V \frac{\partial\overline{\mathbf{S}}}{\partial\overline{\mathbf{X}}}(f,g,h)^T d\overline{V}. \qquad (2.53)$$

Chapter 3

Numerical Integration

In this chapter, the numerical method used in this report to solve the steady and linearized unsteady Euler equations is presented. In Section 3.2, the numerical methods used to generate the steady and unsteady grids are discussed. In Section 3.3, the modified Lax-Wendroff explicit scheme used to integrate the linearized Euler equations is developed. In Section 3.4, the stability condition of the scheme is discussed. In Section 3.5, the issues of numerical smoothing are addressed. The conservation and accuracy of the scheme is discussed in Sections 3.6, 3.7. In Section 3.8, the multiple grid technique used in this work to accelerate the convergence is presented. In Section 3.9, the differences between the solvers for the steady and linearized unsteady Euler equations are explained.

3.1 Nomenclature

A	area
$\mathbf{b}$	source term vector due to moving grid
E	total rotary internal energy per unit mass
$\mathbf{F, G, H}$	vector of flux variables
f, g, h	grid perturbations in the x, y and z directions
I	rothalpy
j	$\sqrt{-1}$
p	pressure
R	radius
$\mathbf{S}$	vector of source term (centripetal and Coriolis forces)
t	time
$\mathbf{U}$	vector of conservation variables
(u, v, w)	velocity vector in Cartesian coordinates
V	volume
x, y, z, t	Cartesian coordinate system - physical domain

δ	residual/correction of solution between two time levels
Δ	change of a quantity in time
$\epsilon^{(2)}, \epsilon^{(4)}$	solution dependent smoothing coefficients
ν_2, ν_4	user specified smoothing coefficients
$\lambda_\xi, \lambda_\eta, \lambda_\zeta$	Lagrange multipliers
ρ	density
ξ, η, ζ, τ	Cartesian coordinate system - computational domain
$\bar{\Omega}, \Omega$	angular velocity of a rotor shaft
ω	frequency
ψ	grid dependent weighting

$()^n$	n^{th} time level
$()^{(1)}$	related to the first order correction
$()^{(2)}$	related to the second order correction
$()'$	small perturbation quantity
$()^f$	related to the fine grid (multi-grid)
$()^c$	related to the coarse grid (multi-grid)
$\bar{()}$	mean (steady) quantity

3.2   Grid Generation

Before one can discretize the governing equations, one must generate a computational grid. The quality of a mesh is important for obtaining an accurate flow solution. Generally speaking, grids with smooth variations in cell volumes and with minimal amounts of shear are desirable.

In recent years, different approaches have been used to generate grid systems for arbitrary two and three-dimensional flow regions. These methods include conformal mapping [12, 36], algebraic methods [19, 57, 53], and partial differential equation techniques [59, 58]. In the present work, a modified version of an elliptic mesh generator developed by Thompson [59] is used. The principle behind this grid generator technique is to prescribe the boundary points in the physical domain and then map the specified computational grid into the irregular physical domain by solving an elliptic partial differential equation (PDE) with appropriate boundary conditions. The main advantage of this method is that the resulting grids are generally very smooth and one can control to some extent the amount of shear in the grid. The three most common types of grids in turbomachinery applications are C-grids, O-grids, and H-grids. C and O-grids are commonly used in steady flow calculations and provide good resolution around the airfoil. However, these grids lack resolution in the far-field to resolve acoustic, vortical, and entropic waves. H-grids provide uniformly good resolution throughout the computational domain. Since the present work is concerned with the flow-field in the entire domain including the far-field, H-grids have been chosen for calculations. Figs.3.1, 3.2 show an example of a computational grid for a three-dimensional turbomachinery blade.

For unsteady flow calculations involving blade motion, the complex amplitude of
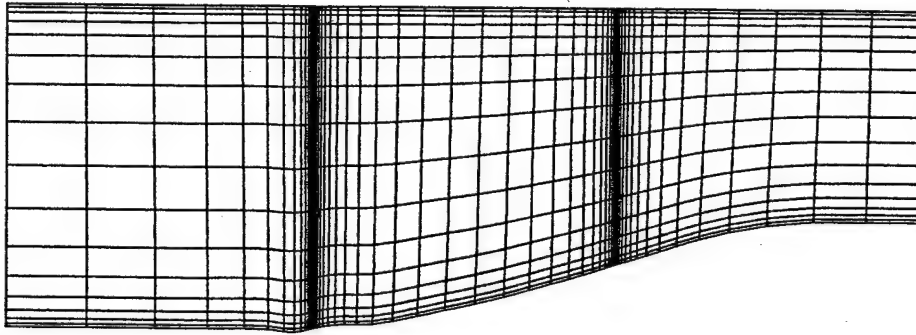
Figure 3.1: Side view of a blade row.
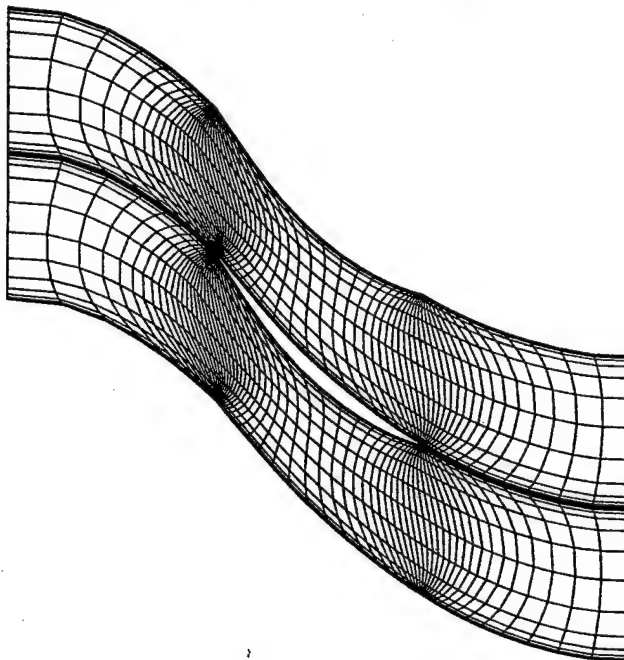
Figure 3.2: Mesh at the midspan.

the grid motion (f, g, h) at each node must be specified. For a given mode shape of a blade, the motion of the interior of the grid must be calculated. To provide a smooth variation in the grid displacement, an elliptic grid generator can be used. That is f, g, and h may be obtained as solutions to Laplace equation,

$$\nabla^2 f = 0 \tag{3.1}$$

$$\nabla^2 g = 0 \tag{3.2}$$

$$\nabla^2 h = 0. \tag{3.3}$$

Boundary conditions must be imposed on the boundaries of the computational grid. On the blade surfaces, the displacement of the grid must match the displacement of the blades. Upstream and downstream of the blades, the grid motion must satisfy the complex periodicity condition. On the hub and tip case there is no radial motion, however the grid may move tangent to these surfaces. In the far-field and along the interface boundaries, the grid motion terms are specified to be zero so that they do not complicate the implementation of the far-field and interface boundary conditions. A finite element scheme using eight-node isoparametric elements is used to discretize the equations, and the resulting system of equations is solved using Successive Line Over-Relaxation (SLOR) [3].

3.3   Modified Lax-Wendroff Integration Scheme

The numerical scheme implemented for both mean (steady) and unsteady flow calculations is an explicit time-marching Lax-Wendroff algorithm first introduced by Ni [47] and then, extended to three dimensions by Ni and Bogoian [48]. Some modifications to this scheme were introduced by Hall [27] and Saxer [54]. It is a second-order accurate scheme in space and in time.

The following development of the numerical scheme will be applied to the linearized Euler equations. For the moment, we will assume that the mean nonlinear flow, $\overline{\mathbf{U}}$, is known and the unsteady conservation variables, $\mathbf{U}'$, need to be computed.

The linearized Euler equations, Eqs. (2.47),(2.53), are written in the frequency domain, so that time does not appear explicitly. To take advantage of the explicit time-marching Lax-Wendroff algorithm, Ni and Sisto [49] proposed the pseudo-time technique. Using this technique, the unsteady conservation variables, $\mathbf{U}'$, are assumed to be functions of time. The full conservation variables now are given by

$$\mathbf{U}(\xi, \eta, \zeta, \tau) = \overline{\mathbf{U}}(\xi, \eta, \zeta) + \mathbf{U}'(\xi, \eta, \zeta, \tau)e^{j\omega\tau} \tag{3.4}$$

Using Eq. (3.4), the linearized Euler equations in differential form may be rewritten as

$$\frac{\partial \mathbf{U}'}{\partial \tau} + j\omega \mathbf{U}' + \frac{\partial \mathbf{F}'}{\partial \xi} + \frac{\partial \mathbf{G}'}{\partial \eta} + \frac{\partial \mathbf{H}'}{\partial \zeta} - \mathbf{S} = \mathbf{b} \tag{3.5}$$

where

$$\mathbf{F}' = \frac{\partial \overline{\mathbf{F}}}{\partial \overline{\mathbf{U}}}\mathbf{U}', \quad \mathbf{G}' = \frac{\partial \overline{\mathbf{G}}}{\partial \overline{\mathbf{U}}}\mathbf{U}', \quad \mathbf{H}' = \frac{\partial \overline{\mathbf{H}}}{\partial \overline{\mathbf{U}}}\mathbf{U}', \quad \mathbf{S}' = \frac{\partial \overline{\mathbf{S}}}{\partial \overline{\mathbf{U}}}\mathbf{U}'$$

The pseudo-time linearized Euler equations in the integral form are given by

$$\iiint_V \frac{\partial \mathbf{U}'}{\partial \tau} d\overline{V} + \iiint_V j\omega \mathbf{U}' d\overline{V} + \iint_A (\mathbf{F}', \mathbf{G}', \mathbf{H}') \cdot d\overline{\mathbf{A}} - \iiint_V \mathbf{S}' d\overline{V} = \mathbf{B} \qquad (3.6)$$

where the term $\mathbf{B}$ is the same as the right hand side of Eq. (2.53).

Since Eq. (3.5) is hyperbolic in time, it can be marched in time subject to appropriate boundary conditions. If these boundary conditions are independent of time, then as time advances the solution, $\mathbf{U}'$, will converge to time-independent values and $\partial \mathbf{U}'/\partial \tau$ will approach zero. In other words, the solution of the linearized Euler equations will be recovered.

The Lax-Wendroff algorithm is based on a Taylor series expansion in time for $\mathbf{U}'$. At the time level $n + 1$, the expansion for $\mathbf{U}'$ is given by

$$\mathbf{U}'^{n+1} = \mathbf{U}'^n + \Delta\tau \left(\frac{\partial \mathbf{U}'}{\partial \tau}\right)^n + \frac{1}{2}\Delta\tau^2 \left(\frac{\partial^2 \mathbf{U}'}{\partial \tau^2}\right)^n + O(\Delta\tau^3) \qquad (3.7)$$

Here $\Delta\tau$ is the time step size.

At this point, the linearized Euler equations are discretized on a computational mesh. The flow variables are located at the vertices of the hexahedral cells and are assigned according to an initial condition. The Fig.3.3 illustrates a fragment of a computational domain. In this figure, eight computational cells surrounding node 1 are denoted by A, B, C, D, E, F, G, H. The centers of these cells are located at the corners of pseudo-mesh cell P. Using Eq. (3.6), the first derivative of $\mathbf{U}'$ with respect to time at node 1 is approximated as

$$\frac{\partial \mathbf{U}'_1}{\partial \tau} \approx \frac{1}{V_1}\left[-\iint_{A_1}(\mathbf{F}', \mathbf{G}', \mathbf{H}') \cdot d\overline{\mathbf{A}} + \iiint_{V_1}(\mathbf{S}' - j\omega\mathbf{U}')d\overline{V} + \mathbf{B}\right] \qquad (3.8)$$

where V_1 is a control volume of pseudo-mesh cell P surrounding node 1. A_1 is the area of this cell.

Differentiating Eq. (3.6) with respect to time and multiplying the result by the time step $\Delta\tau$, one obtains

$$\iiint_V \Delta\tau \frac{\partial^2 \mathbf{U}'}{\partial \tau^2} d\overline{V} + \iiint_V j\omega \Delta\mathbf{U}' d\overline{V} + \iint_A (\Delta\mathbf{F}', \Delta\mathbf{G}', \Delta\mathbf{H}') \cdot d\overline{\mathbf{A}} - \iiint_V \Delta\mathbf{S}' d\overline{V} = 0$$
$$(3.9)$$

where

$$\Delta\mathbf{U}' = \frac{\partial \mathbf{U}'}{\partial \tau}\Delta\tau, \quad \Delta\mathbf{F} = \frac{\partial \overline{\mathbf{F}}}{\partial \overline{\mathbf{U}}}\Delta\mathbf{U}', \quad \Delta\mathbf{G} = \frac{\partial \overline{\mathbf{G}}}{\partial \overline{\mathbf{U}}}\Delta\mathbf{U}'$$

$$\Delta\mathbf{H} = \frac{\partial \overline{\mathbf{H}}}{\partial \overline{\mathbf{U}}}\Delta\mathbf{U}', \quad \Delta\mathbf{S} = \frac{\partial \overline{\mathbf{S}}}{\partial \overline{\mathbf{U}}}\Delta\mathbf{U}'. \qquad (3.10)$$

Using Eq. (3.9), the second derivative of $\mathbf{U}'$ with respect to time is approximated by

$$\frac{\partial^2 \mathbf{U}'_1}{\partial \tau^2}\Delta\tau \approx \frac{1}{V_1}\left[-\iint_{A_1}(\Delta\mathbf{F}', \Delta\mathbf{G}', \Delta\mathbf{H}') \cdot d\overline{\mathbf{A}} + \iiint_{V_1}(\Delta\mathbf{S}' - j\omega\Delta\mathbf{U}')d\overline{V}\right] \qquad (3.11)$$
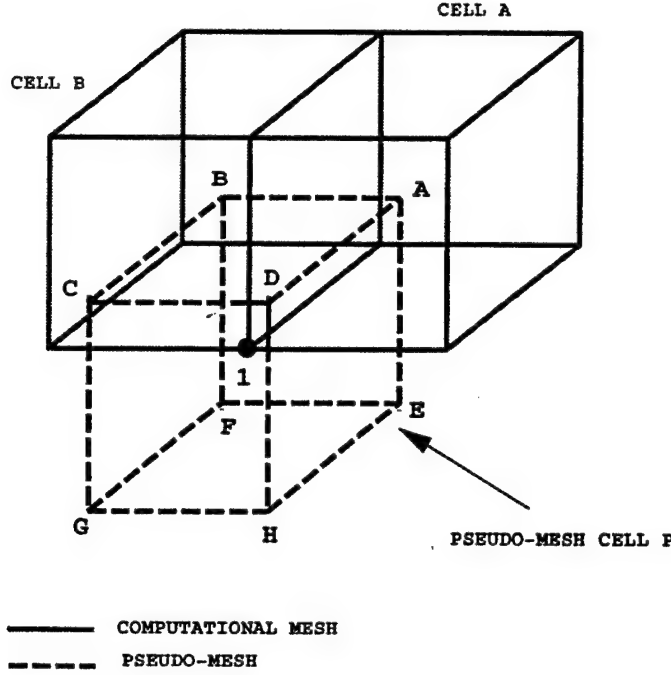
Figure 3.3: Control volume of pseudo-mesh cell P surrounding node 1.

After substitution Eqs. (3.11),(3.8) into Eq. (3.7), a correction to $\mathbf{U}'_1$ at $(n+1)$th time step, $\delta\mathbf{U}'_1 = \mathbf{U}_1'^{n+1} - \mathbf{U}_1'^n$, is given by

$$\delta\mathbf{U}'_1 \approx \frac{\Delta\tau_1}{V_1}\left[-\iint_{A_1}(\mathbf{F}',\mathbf{G}',\mathbf{H}')\cdot\overline{d\mathbf{A}} + \iiint_{V_1}(\mathbf{S}' - j\omega\mathbf{U}')\,d\overline{V} + \mathbf{B}\right]$$

$$+ \frac{\Delta\tau_1}{2\cdot V_1}\left[-\iint_{A_1}(\Delta\mathbf{F},\Delta\mathbf{G},\Delta\mathbf{H})\cdot\overline{d\mathbf{A}} + \iiint_{V_1}(\Delta\mathbf{S} - j\omega\Delta\mathbf{U}')d\overline{V}\right]. \qquad (3.12)$$

The two parts of Eq. (3.12) correspond to the first and second order corrections, which will be noted as $\delta\mathbf{U}_1'^{(1)}$ and $\delta\mathbf{U}_2'^{(1)}$ respectively. In this short-hand notation, Eq. (3.12) can be rewritten as

$$\delta\mathbf{U}'_1 = \delta\mathbf{U}_1'^{(1)} + \delta\mathbf{U}_1'^{(2)} \qquad (3.13)$$

For the convenience, both the first and second order corrections will be split into contributions from the eight computational cells of which node 1 is a corner, i.e.

$$\delta\mathbf{U}'_1 = \sum_{i=1}^{8\,\mathrm{cells}} \delta\mathbf{U}_{1i}'^{(1)} + \sum_{i=1}^{8\,\mathrm{cells}} \delta\mathbf{U}_{1i}'^{(2)}, \quad i = A, B, ..., H. \qquad (3.14)$$

The surface integral representing the first-order flux contribution to the correction (the first integral in the Eq. (3.12)) will be approximated as one eighth of the sum of the surface integrals over the computational cells of which node 1 is a corner. The volume integral in the first-order correction (the second integral in the Eq. (3.12)) will be represented as a sum of the products of the source terms taken in the middle

of the computational cells surrounding node 1 and one eighth of the corresponding volumes of these computational cells. As a result, the contribution to the first-order correction at node 1 from cell A is given by

$$\delta \mathbf{U}'^{(1)}_{1A} = \frac{1}{8} \frac{\Delta \tau_1}{V_1} \left[- \iint_{S_A} (\mathbf{F}', \mathbf{G}', \mathbf{H}') \cdot \overrightarrow{d\mathbf{A}} + (\mathbf{S}' - j\omega \mathbf{U}')_A V_A + \mathbf{B}_A \right] \quad (3.15)$$

where S_A and V_A are the area and the volume of cell A.

Eq.(3.15), when discretized, becomes

$$\delta \mathbf{U}'^{(1)}_{1A} = \frac{1}{8} \frac{\Delta \tau_1}{V_1} \left[- \sum_{I=1}^{6 \text{ faces}} [\mathbf{F}'_I A_{xI} + \mathbf{G}'_I A_{yI} + \mathbf{H}'_I A_{zI}] + \sum_{I=1}^{8 \text{ nodes}} \frac{1}{8} (\mathbf{S}' - j\omega \mathbf{U}')_I V_A + \mathbf{B}_A \right] \quad (3.16)$$

where A_{xI}, A_{yI} and A_{zI} are the projections of the face area I in the x, y and z directions respectively. The average fluxes of a face I, noted as $\mathbf{F}'_I$, $\mathbf{G}'_I$ and $\mathbf{H}'_I$, are computed as one fourth of the sum of the fluxes at four corner nodes of this face. The notation $\mathbf{B}_A$ refers to the discretized right hand side of Eq. (2.53). The first order contribution to node 1 from the remaining cells B, C, D, E, F, G, H are derived similarly.

To compute the second order correction, $\delta \mathbf{U}'^{(2)}_1$, at node 1, the first order changes $\Delta \mathbf{U}'$, $\Delta \mathbf{F}$, $\Delta \mathbf{G}$, $\Delta \mathbf{H}$, $\Delta \mathbf{S}$ are first computed at the centers of the computational cells surrounding node 1. The first order change $\Delta \mathbf{U}'$ for cell A is then given by

$$\Delta \mathbf{U}'_A = \frac{\Delta \tau_A}{V_A} \left[- \iint_{S_A} (\mathbf{F}', \mathbf{G}', \mathbf{H}') \cdot \overrightarrow{d\mathbf{A}} + \left(\frac{\partial \overline{\overline{\mathbf{S}}}}{\partial \overline{\overline{\mathbf{U}}}} \mathbf{U}' - j\omega \mathbf{U}' \right)_A V_A + \mathbf{B}_A dV \right] \quad (3.17)$$

Comparing Eq. (3.18) and (3.15), we obtain

$$\Delta \mathbf{U}'_A = 8 \frac{V_1}{\Delta \tau_1} \frac{\Delta \tau_A}{V_A} \delta \mathbf{U}'^{(1)}_{1A}. \quad (3.18)$$

The changes $\Delta \mathbf{F}_A$, $\Delta \mathbf{G}_A$, $\Delta \mathbf{H}_A$, $\Delta \mathbf{S}_A$ for cell A are computed as

$$\Delta \mathbf{F}_A = \left(\frac{\partial \overline{\mathbf{F}}}{\partial \overline{\overline{\mathbf{U}}}} \right)_A \Delta \mathbf{U}'_A, \quad \Delta \mathbf{G}_A = \left(\frac{\partial \overline{\mathbf{G}}}{\partial \overline{\overline{\mathbf{U}}}} \right)_A \Delta \mathbf{U}'_A, \quad \Delta \mathbf{H}_A = \left(\frac{\partial \overline{\mathbf{H}}}{\partial \overline{\overline{\mathbf{U}}}} \right)_A \Delta \mathbf{U}'_A,$$

$$\Delta \mathbf{S}_A = \left(\frac{\partial \overline{\mathbf{S}}}{\partial \overline{\overline{\mathbf{U}}}} \right)_A \Delta \mathbf{U}'_A \quad (3.19)$$

In Eq. (3.19) the Jacobians are evaluated using the mean value $\overline{\mathbf{U}}_A$, the cell-average of the eight nodes. For computational efficiency it is best not to actually compute the Jacobian matrices and perform the matrix-vector multiplication. Instead, the following equations are used

$$\Delta \mathbf{F}_A = \begin{pmatrix} \Delta(\rho u)' \\ \bar{u}\Delta(\rho u)' + \bar{\rho}\bar{u}\Delta u' + \Delta p' \\ \bar{u}\Delta(\rho v)' + \bar{\rho}\bar{v}\Delta u' \\ \bar{u}\Delta(\rho w)' + \bar{\rho}\bar{w}\Delta u' \\ \bar{u}(\Delta(\rho E)' + \Delta p') + \bar{\rho}\bar{I}\Delta u' \end{pmatrix}_A , \quad \Delta \mathbf{G}_A = \begin{pmatrix} \Delta(\rho v)' \\ \bar{v}\Delta(\rho u)' + \bar{\rho}\bar{u}\Delta v' \\ \bar{v}\Delta(\rho v)' + \bar{\rho}\bar{v}\Delta v' + \Delta p' \\ \bar{v}\Delta(\rho w)' + \bar{\rho}\bar{w}\Delta v' \\ \bar{v}(\Delta(\rho E)' + \Delta p') + \bar{\rho}\bar{I}\Delta v' \end{pmatrix}_A$$
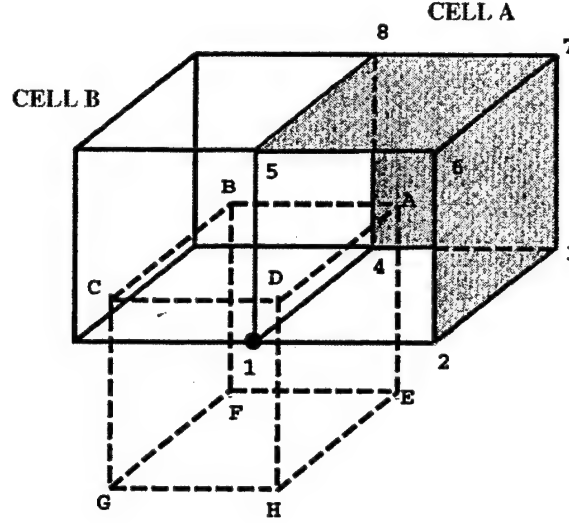
face	I	II	III	IV	V	VI
nodes	2376	1485	3487	1562	5678	1234

Figure 3.4: Contribution of cell A to the second order flux integration.

$$\Delta \mathbf{H}_A = \begin{pmatrix} \Delta(\rho w)' \\ \bar{w}\Delta(\rho u)' + \bar{\rho}\bar{u}\Delta u' \\ \bar{w}\Delta(\rho v)' + \bar{\rho}\bar{v}\Delta u' \\ \bar{w}\Delta(\rho w)' + \bar{\rho}\bar{w}\Delta u' + \Delta p' \\ \bar{w}(\Delta(\rho E)' + \Delta p') + \bar{\rho}\bar{I}\Delta u' \end{pmatrix}_A , \quad \Delta \mathbf{S}_A = \begin{pmatrix} 0 \\ 0 \\ \Omega^2 \bar{y}\Delta\rho - 2\Omega\Delta(\rho w)' \\ \Omega^2 \bar{y}\Delta\rho - 2\Omega\Delta(\rho w)' \\ 0 \end{pmatrix}_A$$

where

$$\begin{aligned}
\Delta \mathbf{U}'_A &= (\Delta\rho', \Delta(\rho u)', \Delta(\rho v)', \Delta(\rho w)', \Delta(\rho E)')_A^T \\
\Delta u' &= (\Delta(\rho u)' - \bar{u}\Delta\rho')/\bar{\rho} \\
\Delta v' &= (\Delta(\rho v)' - \bar{v}\Delta\rho')/\bar{\rho} \\
\Delta w' &= (\Delta(\rho w)' - \bar{w}\Delta\rho')/\bar{\rho} \\
\Delta p' &= (\gamma - 1)(\Delta(\rho E)' - \bar{u}\Delta(\rho u)' - \bar{v}\Delta(\rho v)' - \bar{w}\Delta(\rho w)' \\
&\quad + \frac{\Delta\rho'}{2}(\bar{u}^2 + \bar{v}^2 + \bar{w}^2 + \Omega^2 R^2))
\end{aligned}$$

The second-order flux contribution to node 1 from cell A (the third integral in Eq. (3.12)) is approximated as one fourth of the sum of integrals over I,III,V cell surfaces, see Fig. 3.4. The fourth integral in Eq. (3.12) is computed in the same manner as the volume integral in the first order correction term. The second-order contribution from cell A to node 1 is given by

$$\delta \mathbf{U}_{1A}'^{(2)} = \frac{\Delta\tau_1}{2 \cdot V_1}\left[-\frac{1}{4}\iint_{\text{faces I,III,V}}(\Delta\mathbf{F}, \Delta\mathbf{G}, \Delta\mathbf{H}) \cdot \overrightarrow{d\mathbf{A}} + \frac{1}{8}(\Delta\mathbf{S} - j\omega\Delta\mathbf{U}')_A V_A \right]$$

$$\approx \ -\frac{\Delta \tau_1}{8V_1} \left[\sum_{J=\text{I,III,V}} (\Delta \mathbf{F}_A A_{xJ} + \Delta \mathbf{G}_A A_{yJ} + \Delta \dot{\mathbf{H}}_A A_{zJ}) \right]$$

$$+ \ \frac{\Delta \tau_1}{2 \cdot 8 \cdot V_1} (\Delta \mathbf{S}_A - j\omega \Delta \mathbf{U}'_A) V_A \tag{3.20}$$

The total contribution to a change at node 1 from cell A is obtained by combining the Eqs. (3.16)-(3.18) and the Eq. (3.20), i.e.

$$\delta \mathbf{U}'_{1A} = \frac{1}{8} \frac{\Delta \tau_1}{V_1} \frac{V_A}{\Delta \tau_A} \left(1 - \frac{j\omega}{2} \Delta \tau_A \right) \Delta \mathbf{U}'_A$$

$$- \frac{1}{8} \frac{\Delta \tau_1}{V_1} \sum_{J=\text{I,III,V}} (\Delta \mathbf{F}_A A_{xJ} + \Delta \mathbf{G}_A A_{yJ} + \Delta \mathbf{H}_A A_{zJ}) + \frac{1}{16} \frac{\Delta \tau_1}{V_1} \Delta \mathbf{S}_A V_A$$

$$\tag{3.21}$$

Now that the contribution of cell A to node 1 is defined, the same procedure applies to the cells $B, ..., H$. The contribution of these cells to node 1 are given by

$$\delta \mathbf{U}'_{1B} = \frac{1}{8} \frac{\Delta \tau_1}{V_1} \frac{V_B}{\Delta \tau_B} \left(1 - \frac{j\omega}{2} \Delta \tau_B \right) \Delta \mathbf{U}'_B$$

$$- \frac{1}{8} \frac{\Delta \tau_1}{V_1} \sum_{J=\text{II,III,V}} (\Delta \mathbf{F}_B A_{xJ} + \Delta \mathbf{G}_B A_{yJ} + \Delta \mathbf{H}_B A_{zJ}) + \frac{1}{16} \frac{\Delta \tau_1}{V_1} \Delta \mathbf{S}_B V_B$$

$$\delta \mathbf{U}'_{1C} = \frac{1}{8} \frac{\Delta \tau_1}{V_1} \frac{V_C}{\Delta \tau_C} \left(1 - \frac{j\omega}{2} \Delta \tau_C \right) \Delta \mathbf{U}'_C$$

$$- \frac{1}{8} \frac{\Delta \tau_1}{V_1} \sum_{J=\text{II,IV,V}} (\Delta \mathbf{F}_C A_{xJ} + \Delta \mathbf{G}_C A_{yJ} + \Delta \mathbf{H}_C A_{zJ}) + \frac{1}{16} \frac{\Delta \tau_1}{V_1} \Delta \mathbf{S}_C V_C$$

$$\delta \mathbf{U}'_{1D} = \frac{1}{8} \frac{\Delta \tau_1}{V_1} \frac{V_D}{\Delta \tau_D} \left(1 - \frac{j\omega}{2} \Delta \tau_D \right) \Delta \mathbf{U}'_D$$

$$- \frac{1}{8} \frac{\Delta \tau_1}{V_1} \sum_{J=\text{I,IV,V}} (\Delta \mathbf{F}_D A_{xJ} + \Delta \mathbf{G}_D A_{yJ} + \Delta \mathbf{H}_D A_{zJ}) + \frac{1}{16} \frac{\Delta \tau_1}{V_1} \Delta \mathbf{S}_D V_D$$

$$\delta \mathbf{U}'_{1E} = \frac{1}{8} \frac{\Delta \tau_1}{V_1} \frac{V_E}{\Delta \tau_E} \left(1 - \frac{j\omega}{2} \Delta \tau_E \right) \Delta \mathbf{U}'_E$$

$$- \frac{1}{8} \frac{\Delta \tau_1}{V_1} \sum_{J=\text{I,III,VI}} (\Delta \mathbf{F}_E A_{xJ} + \Delta \mathbf{G}_E A_{yJ} + \Delta \mathbf{H}_E A_{zJ}) + \frac{1}{16} \frac{\Delta \tau_1}{V_1} \Delta \mathbf{S}_E V_E$$

$$\delta \mathbf{U}'_{1F} = \frac{1}{8} \frac{\Delta \tau_1}{V_1} \frac{V_F}{\Delta \tau_F} \left(1 - \frac{j\omega}{2} \Delta \tau_F \right) \Delta \mathbf{U}'_F$$

$$- \frac{1}{8} \frac{\Delta \tau_1}{V_1} \sum_{J=\text{II,III,VI}} (\Delta \mathbf{F}_F A_{xJ} + \Delta \mathbf{G}_F A_{yJ} + \Delta \mathbf{H}_F A_{zJ}) + \frac{1}{16} \frac{\Delta \tau_1}{V_1} \Delta \mathbf{S}_F V_F$$

$$\delta \mathbf{U}'_{1G} = \frac{1}{8} \frac{\Delta \tau_1}{V_1} \frac{V_G}{\Delta \tau_G} \left(1 - \frac{j\omega}{2} \Delta \tau_G \right) \Delta \mathbf{U}'_G$$

$$- \frac{1}{8} \frac{\Delta \tau_1}{V_1} \sum_{J=\text{II,IV,VI}} (\Delta \mathbf{F}_G A_{xJ} + \Delta \mathbf{G}_G A_{yJ} + \Delta \mathbf{H}_G A_{zJ}) + \frac{1}{16} \frac{\Delta \tau_1}{V_1} \Delta \mathbf{S}_G V_G$$

$$\delta \mathbf{U}'_{1H} = \frac{1}{8} \frac{\Delta \tau_1}{V_1} \frac{V_H}{\Delta \tau_H} \left(1 - \frac{j\omega}{2} \Delta \tau_H \right) \Delta \mathbf{U}'_H$$
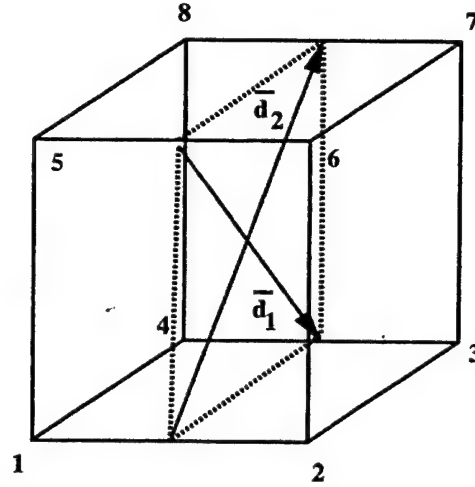
face	I	II	III	IV	V	VI
nodes	1458	2367	1256	3478	1234	5678

Figure 3.5: Average face I-II.

$$ - \frac{1}{8} \frac{\Delta \tau_1}{V_1} \sum_{J=I,IV,VI} (\Delta \mathbf{F}_H A_{xJ} + \Delta \mathbf{G}_H A_{yJ} + \Delta \mathbf{H}_H A_{zJ}) + \frac{1}{16} \frac{\Delta \tau_1}{V_1} \Delta \mathbf{S}_H V_H $$

$$(3.22)$$

The algorithms of computing cell volumes and areas are outlined in the Appendix A.

3.4   Numerical stability

Numerical stability sets an upper limit on the time step sizes that can be used for marching Eq. (3.5). Since we are only interested in finding a converged solution, the solution of the linearized Euler equations, Eq. (2.47), then we can use different time steps for different cells to accelerate the convergence. A local time step will be defined for each computational cell of a domain, and it will depend on a cell's geometry and the local flow conditions. The detailed discussion of stability condition for the modified Lax-Wendroff scheme is given in the Ref. [54]. Here only a brief outline of how to calculate the time step will be presented.

Consider cell A depicted in the Fig. 3.5. The average face between face I and face II of cell A is defined by the following two vectors

$$ \overrightarrow{d_1} = \frac{1}{2} (\xi_4 + \xi_3 - \xi_5 - \xi_6, \eta_4 + \eta_3 - \eta_5 - \eta_6, \zeta_4 + \zeta_3 - \zeta_5 - \zeta_6) $$

$$ \overrightarrow{d_2} = \frac{1}{2} (\xi_7 + \xi_8 - \xi_1 - \xi_2, \eta_7 + \eta_8 - \eta_1 - \eta_2, \zeta_7 + \zeta_8 - \zeta_1 - \zeta_2) $$

where (ξ_i, η_i, ζ_i) are the coordinates of node number i.

A unit vector perpendicular to the average face I-II, denoted as $\overrightarrow{n}_{I-II}$, is given by

$$\overrightarrow{n}_{I-II} = \frac{[\overrightarrow{d_1} \times \overrightarrow{d_2}]}{|[\overrightarrow{d_1} \times \overrightarrow{d_2}]|} \qquad (3.23)$$

The coordinates of the centers of faces I and II, noted as $(\xi_{c1}, \eta_{c1}, \zeta_{c1})$ and $(\xi_{c2}, \eta_{c2}, \zeta_{c2})$ respectively, are calculated as

$$\xi_{c1} = 0.25(\xi_1 + \xi_4 + \xi_5 + \xi_8) \qquad \xi_{c2} = 0.25(\xi_2 + \xi_3 + \xi_6 + \xi_7)$$
$$\eta_{c1} = 0.25(\eta_1 + \eta_4 + \eta_5 + \eta_8) \qquad \eta_{c2} = 0.25(\eta_2 + \eta_3 + \eta_6 + \eta_7)$$
$$\zeta_{c1} = 0.25(\zeta_1 + \zeta_4 + \zeta_5 + \zeta_8) \qquad \zeta_{c2} = 0.25(\zeta_2 + \zeta_3 + \zeta_6 + \zeta_7)$$

The average perpendicular distance between the faces I and II, denoted as D_{I-II}, is given by

$$D_{I-II} = (\xi_{c2} - \xi_{c1}, \eta_{c2} - \eta_{c1}, \zeta_{c2} - \zeta_{c1}) \cdot \overrightarrow{n}_{I-II}$$

If $\overrightarrow{V}_A$ is the average steady velocity vector and a_A is the average speed of sound for cell A, then the maximum time step for cell A is defined by

$$\Delta \tau_A \leq \min \left(\frac{D_{I-II}}{|\overrightarrow{V}_A \cdot \overrightarrow{n}_{I-II}| + a_A}, \frac{D_{III-IV}}{|\overrightarrow{V}_A \cdot \overrightarrow{n}_{III-IV}| + a_A}, \frac{D_{V-VI}}{|\overrightarrow{V}_A \cdot \overrightarrow{n}_{V-VI}| + a_A} \right) \qquad (3.24)$$

where the average quantities for faces III-IV and V-VI are computed in the similar way to those for faces I-II.

The time step at node 1 (see Fig. 3.3) that is a node of cells A, B, C, D, F, E, G, H is given by

$$\Delta \tau_1 = \min(\Delta \tau_A, \Delta \tau_B, \Delta \tau_C, \Delta \tau_D, \Delta \tau_E, \Delta \tau_F, \Delta \tau_G, \Delta \tau_H) \qquad (3.25)$$

3.5 Numerical smoothing

An artificial viscosity or smoothing operator must be added to the Lax-Wendroff scheme described in the Section 3.3 to prevent undesirable high-frequency waves in smooth flow regions, and to capture shocks for transonic flows. It can be shown, see for instance [60, 37], that the Lax-Wendroff finite difference approximation introduces a third-order dispersion error. As a result, non-physical oscillations known as odd-even decoupling modes are allowed as a part of numerical solution. To damp out these unwanted oscillations, a fourth-difference smoothing operator is introduced. In addition, a second-difference operator is used to stabilize the scheme in the vicinity of shocks.

The following sections discuss second and fourth difference smoothing operators. The development of these smoothing operators is built on previous work in Refs. [34, 54, 8].

3.5.1 Second-Difference Smoothing

Second difference smoothing is introduced by adding the term $\epsilon^{(2)}\nabla \cdot (\nabla \mathbf{U}')$ to the right-hand side of Eq. (3.5). Here $\epsilon^{(2)}$ is a smoothing coefficient. Discretizing, the correction due to the second order smoothing at node 1 (see Fig. 3.6) is given by

$$(\delta \mathbf{U}_1')_{\text{smth2}} = \left(\frac{\Delta\tau}{V}\right)_1 \sum_{i=1}^{8\,\text{cells}} \bar{\epsilon}_i^{(2)} \left(\frac{V}{\Delta\tau}\right)_i (\overline{\mathbf{U}}_i' - \mathbf{U}_1') \tag{3.26}$$

where $\bar{\epsilon}_i^{(2)}$ is the cell averaged smoothing coefficient and $\overline{\mathbf{U}}_i'$ is the cell averaged unsteady conservation variable vector. The correction $(\delta\mathbf{U}_1')_{\text{smth2}}$ is presented as a sum of contributions from eight cells of which node 1 is a corner. A cell averaged unsteady conservation variable vector is given by

$$\overline{\mathbf{U}}_i' = \frac{1}{8} \sum_{j=1}^{8\,\text{nodes}} \mathbf{U}_j' \tag{3.27}$$

where the summation is over all nodes of a cell. Similarly, a cell averaged smoothing coefficient [8] is given by

$$\bar{\epsilon}_1^{(2)} = \frac{1}{8} \sum_{j=1}^{8\,\text{nodes}} \epsilon_j^{(2)} \tag{3.28}$$

where

$$\epsilon_1^{(2)} = \nu_2 \left| \frac{\sum_{j=1}^{6\,\text{nodes}} \psi_j(p_j - p_1)}{\sum_{j=1}^{6\,\text{nodes}} \psi_j(p_j + p_1)} \right| \tag{3.29}$$

Here nodes at which quantities for summations are taken refer to nodes neighboring node 1, see Fig. 3.6. The coefficient ν_2 is a constant specified by a user. In the present study, it was set to 0.25. A symbol p denotes a mean (steady) pressure. The coefficient $\epsilon_1^{(2)}$ is constructed in a such way that it is close zero in the smooth flow regions and it is small and positive in the vicinity of a shock. ψ_j is a grid dependent weight that is designed to be close to unity to ensure an even dependence on all of the neighboring nodes. It is defined as $\psi_j = 1 + \Delta\psi_j$, where $\Delta\psi_j$ is defined from the minimization of a Laplacian L given by

$$L = \sum_{j=1}^{6\,\text{nodes}} (\Delta\psi_j)^2 \tag{3.30}$$

with the constraints

$$\mathcal{F}(\Delta\psi_j) = \sum_{j=1}^{6\,\text{nodes}} (1 + \Delta\psi_j)(\xi_j - \xi_1) = 0 \tag{3.31}$$

$$\mathcal{G}(\Delta\psi_j) = \sum_{j=1}^{6\,\text{nodes}} (1 + \Delta\psi_j)(\eta_j - \eta_1) = 0 \tag{3.32}$$

$$\mathcal{H}(\Delta\psi_j) = \sum_{j=1}^{6\,\text{nodes}} (1 + \Delta\psi_j)(\zeta_j - \zeta_1) = 0 \tag{3.33}$$
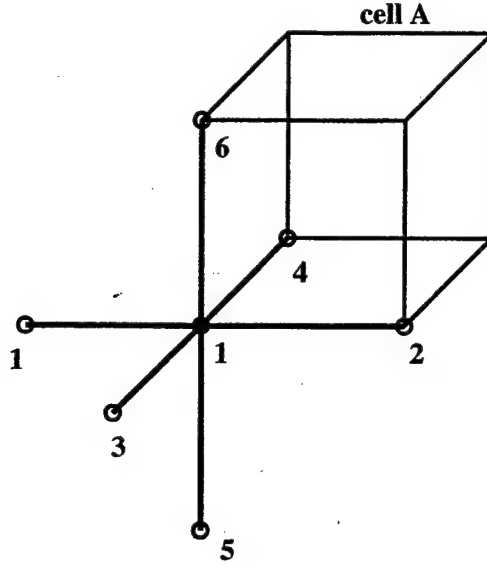
Figure 3.6: Stencil for pseudo-Laplacian.

The purpose of the constraint equations is to ensure that the smoothing operator has no effect on linear solutions on irregular meshes. The importance of this first was established by Lindquist and Giles [43].

To minimize the Laplacian L subject to constraints Eqs.(3.31)-(3.33), a Lagrange multiplier technique can be used. Using this technique, a Lagrange function, $\mathcal{L}$, is formed, i.e.

$$\mathcal{L}(\Delta\psi_j) = L - \lambda_\xi \mathcal{F} - \lambda_\eta \mathcal{G} - \lambda_\zeta \mathcal{H} \tag{3.34}$$

where $\lambda_\xi, \lambda_\eta, \lambda_\zeta$ are Lagrange multipliers. If the function L, Eq. (3.30), achieves a conditional extremum at the point $(\Delta\psi_1^*, \Delta\psi_2^*, ..., \Delta\psi_6^*)$, then

$$\frac{\partial \mathcal{L}}{\partial(\Delta\psi_j)}\Big|_{\psi_j^*} = 0, \quad j = 1, .., 6. \tag{3.35}$$

The conditions given by Eq. (3.35) are equivalent to

$$\Delta\psi_j^* = \lambda_\xi(\xi_j - \xi_1) + \lambda_\eta(\eta_j - \eta_1) + \lambda_\zeta(\zeta_j - \zeta_1), \quad j = 1, ..., 6 \tag{3.36}$$

The multipliers $(\lambda_\xi, \lambda_\eta, \lambda_\zeta)$ are found from Eqs.(3.31)-(3.33). After some algebra, one can show that

$$\lambda_\xi = \frac{-R_\xi(I_{\eta\eta}I_{\zeta\zeta} - I_{\eta\zeta}^2) + R_\eta(I_{\xi\eta}I_{\zeta\zeta} - I_{\xi\zeta}I_{\eta\zeta}) - R_\zeta(I_{\xi\eta}I_{\eta\zeta} - I_{\eta\eta}I_{\xi\zeta})}{I_{\xi\xi}(I_{\eta\eta}I_{\zeta\zeta} - I_{\eta\zeta}^2) - I_{\xi\eta}(I_{\xi\eta}I_{\zeta\zeta} - I_{\xi\zeta}I_{\eta\zeta}) + I_{\xi\zeta}(I_{\xi\eta}I_{\eta\zeta} - I_{\eta\eta}I_{\xi\zeta})}$$

$$\lambda_\eta = \frac{R_\xi(I_{\xi\eta}I_{\zeta\zeta} - I_{\xi\zeta}I_{\eta\zeta}) - R_\eta(I_{\xi\xi}I_{\zeta\zeta} - I_{\xi\zeta}^2) + R_\zeta(I_{\xi\xi}I_{\eta\zeta} - I_{\xi\eta}I_{\xi\zeta})}{I_{\xi\xi}(I_{\eta\eta}I_{\zeta\zeta} - I_{\eta\zeta}^2) - I_{\xi\eta}(I_{\xi\eta}I_{\zeta\zeta} - I_{\xi\zeta}I_{\eta\zeta}) + I_{\xi\zeta}(I_{\xi\eta}I_{\eta\zeta} - I_{\eta\eta}I_{\xi\zeta})} \tag{3.37}$$

$$\lambda_\zeta = \frac{-R_\xi(I_{\xi\eta}I_{\eta\zeta} - I_{\eta\eta}I_{\xi\zeta}) + R_\eta(I_{\xi\xi}I_{\eta\zeta} - I_{\xi\eta}I_{\xi\zeta}) - R_\zeta(I_{\xi\xi}I_{\eta\eta} - I_{\xi\eta}^2)}{I_{\xi\xi}(I_{\eta\eta}I_{\zeta\zeta} - I_{\eta\zeta}^2) - I_{\xi\eta}(I_{\xi\eta}I_{\zeta\zeta} - I_{\xi\zeta}I_{\eta\zeta}) + I_{\xi\zeta}(I_{\xi\eta}I_{\eta\zeta} - I_{\eta\eta}I_{\xi\zeta})}$$

where

$$R_\xi = \sum_{j=1}^{6 \text{ nodes}} (\xi_j - \xi_1), \quad R_\eta = \sum_{j=1}^{6 \text{ nodes}} (\eta_j - \eta_1), \quad r_\zeta = \sum_{j=1}^{6 \text{ nodes}} (\zeta_j - \zeta_1)$$

$$I_{\xi\xi} = \sum_{j=1}^{6 \text{ nodes}} (\xi_j - \xi_1)^2, \quad I_{\eta\eta} = \sum_{j=1}^{6 \text{ nodes}} (\eta_j - \eta_1)^2, \quad I_{\zeta\zeta} = \sum_{j=1}^{6 \text{ nodes}} (\zeta_j - \zeta_1)^2,$$

$$I_{\xi\eta} = \sum_{j=1}^{6 \text{ nodes}} (\xi_j - \xi_1)(\eta_j - \eta_1), \quad I_{\xi\zeta} = \sum_{j=1}^{6 \text{ nodes}} (\xi_j - \xi_1)(\zeta_j - \zeta_1),$$

$$I_{\eta\zeta} = \sum_{j=1}^{6 \text{ nodes}} (\eta_j - \eta_1)(\zeta_j - \zeta_1)$$

The optimum weights ψ_j for some distorted grids may differ significantly from unity. Holmes and Connel [34] suggested that the weights be limited to $0 \le \psi_i \le 2$.

Because the smoothing coefficient, $\epsilon_1^{(2)}$, defined in Eq.(3.29), depends only on the grid and steady background flow, it can be calculated just once and stored at every node of the computational domain.

3.5.2 Fourth-Difference Smoothing

Fourth difference smoothing is introduced by adding the term $-\epsilon^{(4)} \nabla \cdot [\nabla(\nabla^2 U')]$ to the right-hand side of Eq. (3.5). The correction at node 1 (see Fig. 3.6) due to this term is given by

$$(\delta \mathbf{U}'_1)_{\text{smth4}} = \left(\frac{\Delta\tau}{V} \right)_1 \sum_{i=1}^{8 \text{cells}} -\epsilon_i^{(4)} \left(\frac{V}{\Delta\tau} \right)_i (\overline{\mathbf{D}}_i^2 - \mathbf{D}_1^2) \tag{3.38}$$

where

$$\epsilon_i^{(4)} = \max[0, (\nu_4 - \overline{\epsilon}_i^{(2)})] \tag{3.39}$$

The coefficient ν_4 is a constant (usually, $\nu_4 = 0.002 - 0.005$). The term $\mathbf{D}_1^2$ is a pseudo-Laplacian operator based on the six edge nodes surrounding node 1 (see Fig. 3.6). It is defined as

$$\mathbf{D}_1^2 = \sum_{j=1}^{6 \text{nodes}} \psi_j (\mathbf{U}'_j - \mathbf{U}'_1) \tag{3.40}$$

where $\mathbf{U}'$ is the vector of unsteady conservation variables. $\overline{\mathbf{D}}_i^2$ is an averaged pseudo-Laplacian for a cell i. It is calculated as one eighth of a sum of pseudo-Laplacians at eight corner nodes of a cell i:

$$\overline{\mathbf{D}}_i^2 = \sum_{j=1}^{8 \text{nodes}} \frac{1}{8} \mathbf{D}_j^2. \tag{3.41}$$

The fourth difference smoothing is constructed in such a way that it is equal to zero in the regions of shocks where only second difference smoothing is needed to stabilize a solution.

The smoothing terms given by Eqs. (3.26) and (3.38) are calculated after the numerical integration routine and then added to the corrections obtained during the Lax-Wendroff integration.

3.6   Conservation

The Euler equations state the conservation laws of mass, momentum and energy. A finite-difference scheme that maintains the discretized version of the conservation statement exactly (except for round-off errors) for any number of grid points is *conservative*. It is important for a scheme to be conservative since this property guarantees the correct Rankine-Hugoniot shock jump relations and the correct treatment of other discontinuities such as contact surfaces.

The linearized Euler equations in the integral form are given by

$$\frac{d}{d\tau} \iiint_V \mathbf{U}' dV + \iint_A (\mathbf{F}', \mathbf{G}', \mathbf{H}') \cdot \overrightarrow{d\mathbf{A}} = \iiint_V \mathbf{Q} dV \qquad (3.42)$$

Here V denotes an arbitrary control volume with surface area A. The symbol $\mathbf{Q}$ denotes the source term of Eq. (3.5) and is equal to $\mathbf{S}' + \mathbf{b} - j\omega\mathbf{U}'$. The Lax-Wendroff scheme decomposes the domain into cells and approximates Eq. (3.42) by a discrete equation. This algorithm is proven to be numerically conservative [11] as long as

$$\sum_{j=1}^{\text{all nodes}} \left(\frac{V}{\Delta\tau} \delta\mathbf{U}' \right)_j = \sum [(\text{boundary fluxes}) + (\text{source terms})] \qquad (3.43)$$

where $\delta\mathbf{U}'_j$ is a total correction at node j, V_j is the volume of pseudo-cell around node j. The right hand side of Eq. (3.43) contains only the flux terms at the boundaries and the source terms. The flux terms inside domain cancel each other. This property often is referred to as the "telescoping property."

According to the present scheme a correction $\delta\mathbf{U}'_j$ at node j is equal to a sum of contributions from all surrounding cells (see Eq. (3.14)). These contributions consist of the first and second order corrections (Eq.(3.14)) and the smoothing terms (Eqs.(3.26),(3.38)). The left-hand side of Eq. (4.43) can be expanded as

$$\sum_{j=1}^{\text{all nodes}} \left(\frac{V}{\Delta\tau} \delta\mathbf{U} \right)_j = \sum_{i=1}^{\text{all cells}} [(1^{\text{st}}\text{order})_i + (2^{\text{nd}}\text{order})_i + (\text{smoothing})_i] \qquad (3.44)$$

After examining Eqs. (3.16) and (3.20) one can discover that the scheme is written such that the flux out of a particular cell across a particular face is equal an opposite to the flux out of the neighboring cell across the same face. Smoothing operators are constructed in a such way that the sum of smoothing contributions to the corner nodes of a cell is zero. Hence, Eq. (3.43) holds true and the scheme is conservative.
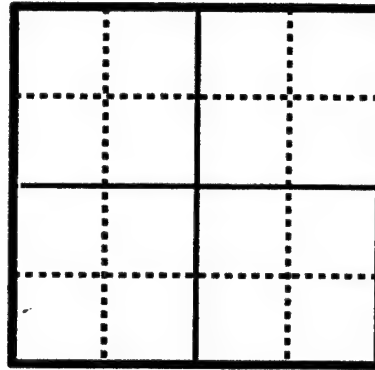
········· **fine grid (0th level)**

——————— **coarse grid (1st level)**

━━━━━━━ **coarse grid (2nd level)**

Figure 3.7: Generation multiple grids.

3.7 Accuracy

The discretization procedure described in Section 3.3 is spatially second-order accurate, except when second difference smoothing is active, in which case the scheme is first-order accurate. This is typical for schemes that use artificial viscosity to capture shocks.

3.8 Multi-Grid Acceleration Technique

To obtain accurate solutions, relatively fine grids must be used for computations. The computational work required to reach the convergence is strongly affected by the size of the computational domain and the number of cells. To make the computations both efficient and accurate, Ni [47] proposed a multiple-grid technique. In this technique, fine and coarse grids are used simultaneously to obtain a solution where the finest grid provides fine spatial accuracy and the coarse grid provides rapid convergence rates. To implement the technique, a series of grids of varying spatial resolution has to be generated. First, we generate a fine grid. The fine grid will be referred to as a "zeroth level." A higher level grid is constructed by removing every other grid plane in each of three directions. Fig. 3.7 depicts the process of obtaining coarse grids for multiple-grid technique. If, for example, the fine grid has $2^k + 1$ nodes in each direction, then k coarse grid levels can be constructed. In practice, the number of grids points in different directions will not be the same, in which case the maximum number of multiple-grid levels is dictated by the minimum of the number of multiple-grid levels allowable in each direction.

Once the Lax-Wendroff numerical integration has been performed on the zeroth (fine) level and the boundary conditions have been applied, the flow variables are
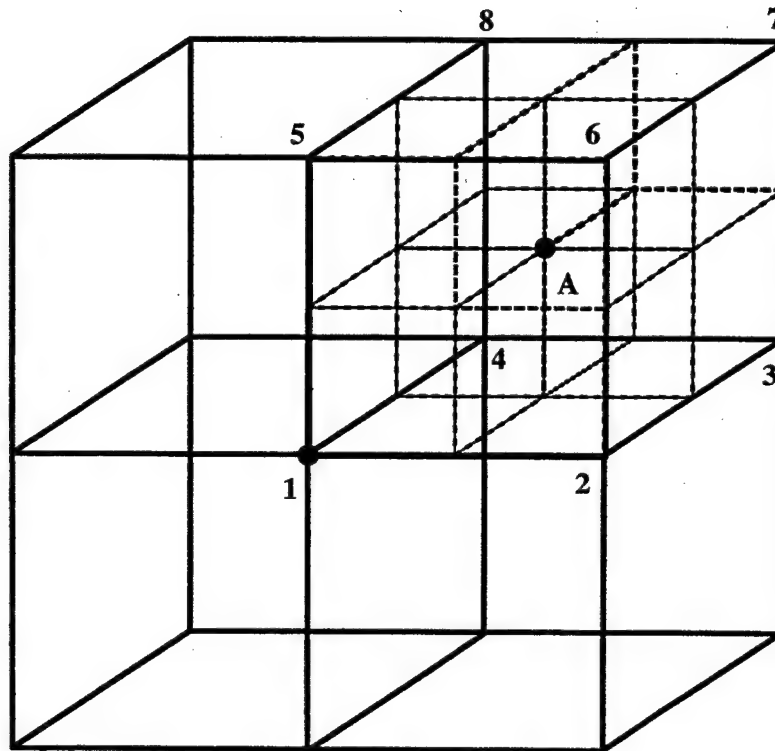
	coarse grid	face	1	2	3	4	5	6
-----	fine grid	nodes	2376	1485	3487	1562	5678	1234

Figure 3.8: Nomenclature used in multiple grid technique.

updated. The multiple-grid process then begins with the first level grid and proceeds with each successively coarser grid. As with the basic scheme, a multi-grid scheme is constructed in a way that all operations are performed on a cell by cell basis. See Fig. 3.8 for a description of the geometry associated with the multiple grid procedure. In this figure, the nodes of a cell of the first coarse grid level are numbered. The center of this cell is denoted by A. The first step of the multiple grid procedure is to transport the fine grid residuals to the coarse grid. The first-order change at the center of a cell A is [10, 27]

$$
\begin{aligned}
\Delta \mathbf{U}_A^c &= \delta \mathbf{U}_A^f + \frac{1}{8} \sum_{i=1}^{8\text{nodes}} \left[\delta \mathbf{U}_i^f - \frac{\Delta \tau_A}{2} (\Delta \mathbf{S}_i^c - j\omega\delta\mathbf{U}_i^f) \right] \\
&+ \frac{\Delta\tau_A}{8V_A} \sum_{J=1,3,5} (\Delta\mathbf{F}_1^c A_{xJ} + \Delta\mathbf{G}_1^c A_{yJ} + \Delta\mathbf{H}_1^c A_{zJ}) \\
&+ \frac{\Delta\tau_A}{8V_A} \sum_{J=2,3,5} (\Delta\mathbf{F}_2^c A_{xJ} + \Delta\mathbf{G}_2^c A_{yJ} + \Delta\mathbf{H}_2^c A_{zJ}) \\
&+ \frac{\Delta\tau_A}{8V_A} \sum_{J=2,4,5} (\Delta\mathbf{F}_3^c A_{xJ} + \Delta\mathbf{G}_3^c A_{yJ} + \Delta\mathbf{H}_3^c A_{zJ}) \\
&+ \frac{\Delta\tau_A}{8V_A} \sum_{J=1,4,5} (\Delta\mathbf{F}_4^c A_{xJ} + \Delta\mathbf{G}_4^c A_{yJ} + \Delta\mathbf{H}_4^c A_{zJ}) \\
&+ \frac{\Delta\tau_A}{8V_A} \sum_{J=1,3,6} (\Delta\mathbf{F}_5^c A_{xJ} + \Delta\mathbf{G}_5^c A_{yJ} + \Delta\mathbf{H}_5^c A_{zJ}) \\
&+ \frac{\Delta\tau_A}{8V_A} \sum_{J=2,3,6} (\Delta\mathbf{F}_6^c A_{xJ} + \Delta\mathbf{G}_6^c A_{yJ} + \Delta\mathbf{H}_6^c A_{zJ}) \\
&+ \frac{\Delta\tau_A}{8V_A} \sum_{J=2,4,6} (\Delta\mathbf{F}_7^c A_{xJ} + \Delta\mathbf{G}_7^c A_{yJ} + \Delta\mathbf{H}_7^c A_{zJ}) \\
&+ \frac{\Delta\tau_A}{8V_A} \sum_{J=1,4,6} (\Delta\mathbf{F}_8^c A_{xJ} + \Delta\mathbf{G}_8^c A_{yJ} + \Delta\mathbf{H}_8^c A_{zJ}) \qquad (3.45)
\end{aligned}
$$

where $\delta\mathbf{U}^f$ is the residual from the fine grid and vectors $\Delta\mathbf{F}^c, \Delta\mathbf{G}^c, \Delta\mathbf{H}^c, \Delta\mathbf{S}^c$ are computed as

$$
\Delta\mathbf{F}^c = \frac{\partial\mathbf{F}^f}{\partial\mathbf{U}^f}\delta\mathbf{U}^f, \quad \Delta\mathbf{G}^c = \frac{\partial\mathbf{G}^f}{\partial\mathbf{U}^f}\delta\mathbf{U}^f, \quad \Delta\mathbf{H}^c = \frac{\partial\mathbf{H}^f}{\partial\mathbf{U}^f}\delta\mathbf{U}^f, \quad \Delta\mathbf{S}^c = \frac{\partial\mathbf{S}^f}{\partial\mathbf{U}^f}\delta\mathbf{U}^f.
$$

A_{xJ}, A_{yJ}, and A_{zJ} in Eq. (3.45) are the projections of the area of face J in the x, y, and z directions respectively. Once the first-order change for a cell is determined the total changes at the nodes can be computed. The contribution to the total change at node 1 from the cell with a center A is given by

$$
\begin{aligned}
\delta\mathbf{U}_{1A}^c &= \frac{1}{8}\left(\Delta\mathbf{U}_A^c(1 - \frac{1}{2}j\omega\Delta\tau) + \frac{1}{2}\Delta\mathbf{S}_A^c\Delta\tau_A\right) \\
&- \frac{1}{8}\frac{\Delta\tau_A}{V_A}\sum_{J=1,3,5}(\Delta\mathbf{F}_A^c A_{xJ} + \Delta\mathbf{G}_A^c A_{yJ} + \Delta\mathbf{H}_A^c A_{zJ}). \qquad (3.46)
\end{aligned}
$$

The contributions to the change at node 1 from the cells with centers at $B, C, ..., H$ are computed in a similar way.

After the changes are computed, boundary conditions in the near field are applied. Then the changes at the fine grid are computed by linearly interpolating the coarse grid residuals. Then, boundary conditions at the far-field and the interface boundaries are applied. And finally, the solution is updated.

3.9 Steady Euler Analysis

In the previous sections, the solution of the linearized unsteady Euler equations has been discussed. In practice, of course, the steady Euler equations are solved first, as the steady solution is required before the linearized Euler equations can be solved. The numerical algorithm presented in the previous sections is based on marching the linearized unsteady Euler equations in pseudo time until the converged (steady state) is reached. The same algorithm is used for advancing the discretized nonlinear steady Euler equations, Eq. (2.2), to steady state. However, there are a few differences between the solution of the steady and unsteady flow solutions. First, the steady flow calculations are performed on the non-deforming (steady) grid so there is no source term associating with the moving grid. Second, for the steady flow, since local time steps depend on the mean flow conditions, they are calculated each iteration. Similarly, the second-order smoothing coefficients, Eq. (3.29), are determined at the each iteration since they depend on the mean flow pressure.

Chapter 4

Boundary Conditions

In this chapter, the boundary conditions required to solve numerically the conservation equations for an isolated blade row are developed. In Figure 4.1 a two-dimensional view of a computational domain is presented indicating the different types of boundary conditions. The boundaries are classified as being either near-field or far-field depending on their relative position to the blades. In the present work, the near-field boundary conditions include both solid surface and periodic boundary types whereas far-field boundaries include the inflow and the outflow boundaries.

Solid surface and periodic boundary conditions are presented in Subsections 4.2.1 and 4.2.2 respectively. Far-field boundary conditions are discussed in Section 4.3. One-dimensional non-reflective boundary conditions are presented in Subsection 4.3.1. Quasi-three-dimensional non-reflective boundary conditions are developed in Subsection 4.3.2. Implementation of reflective boundary conditions for the present mean (steady) flow solver is discussed in Subsection 4.3.3.

4.1 Nomenclature

a	speed of sound
(f, g, h)	grid perturbations in x, y, and z directions
$\mathbf{n}$	outward unit normal
p	pressure
$\mathbf{R}$	position vector
$[\mathbf{T}], [\mathbf{T}]^{-1}$	matrix of left and right eigenvectors
$\mathbf{U}$	vector of conservation variables
(u, v, w)	velocity vector in Cartesian coordinates
(u_x, u_θ, u_R)	velocity vector in cylindrical coordinates
$\mathbf{W}$	vector of characteristic variables

x, θ, r, t	cylindrical coordinate system - physical domain
ρ	density
ρ_T	total density
σ	interblade phase angle
$\bar{\Omega}, \Omega$	angular velocity of a rotor shaft
ω	frequency
θ_G	angular blade to blade gap
$()'$	small perturbation quantity
$\overline{()}$	circumferential average
$()_p$	refers to primitive variables

4.2 Near-Field Boundary Conditions

4.2.1 Solid Surface Boundary Condition

Solid surface boundary conditions are applied at the blade's surfaces and on the hub and tip casings. First, it is assumed that the computational grid at the wall is a stream-surface of the flow. To obtain the proper values of the flow variables corrections, it is assumed that there is a "ghost" cell inside the solid surface. In practice, the changes computed during Lax-Wendroff integration at the solid walls are doubled to produce the proper effect. Second, the solid wall boundary condition specifies that there is no flow through the surface. For an inviscid model, this means that the normal velocity of the fluid at the solid surface must equal to the normal velocity of this surface. Hence,

$$(u, v, w) \cdot \mathbf{n}(s_1, s_2, \tau) - \frac{\partial \mathbf{R}(s_1, s_2, \tau)}{\partial \tau} \cdot \mathbf{n}(s_1, s_2, \tau) = 0 \qquad (4.1)$$

where s_1 and s_2 are two directions in which the surface is splined, $\mathbf{n}(s_1, s_2, \tau)$ is a unit-normal to body surface, (u, v, w) is the velocity vector, and the vector $\mathbf{R}(s1, s_2, \tau)$ describes the location of a point of a solid surface (see Fig 4.2). To perform the linearization of the condition, Eq. (4.1), we decompose the parameters as

$$\begin{aligned} \mathbf{R}(s_1, s_2, \tau) &= \overline{\mathbf{R}}(s_1, s_2) + (f, g, h)e^{j\omega\tau} & (4.2) \\ \mathbf{n}(s_1, s_2, \tau) &= \overline{\mathbf{n}}(s_1, s_2) + \mathbf{n}'e^{j\omega\tau} & (4.3) \\ (u, v, w) &= (\overline{u}, \overline{v}, \overline{w}) + (u', v', w')e^{j\omega\tau} & (4.4) \end{aligned}$$

where $\overline{\mathbf{R}}(s_1, s_2)$ is the mean location of a point of a solid surface, (f, g, h) are the amplitudes of solid surface vibration, $\overline{\mathbf{n}}$ is the mean normal vector, $\mathbf{n}'$ is the perturbation of a normal vector, $(\overline{u}, \overline{v}, \overline{w})$ is the steady velocity vector. After linearization, the steady part of Eq. (4.1) is given by

$$(\overline{u}, \overline{v}, \overline{w}) \cdot \overline{\mathbf{n}} = 0, \qquad (4.5)$$
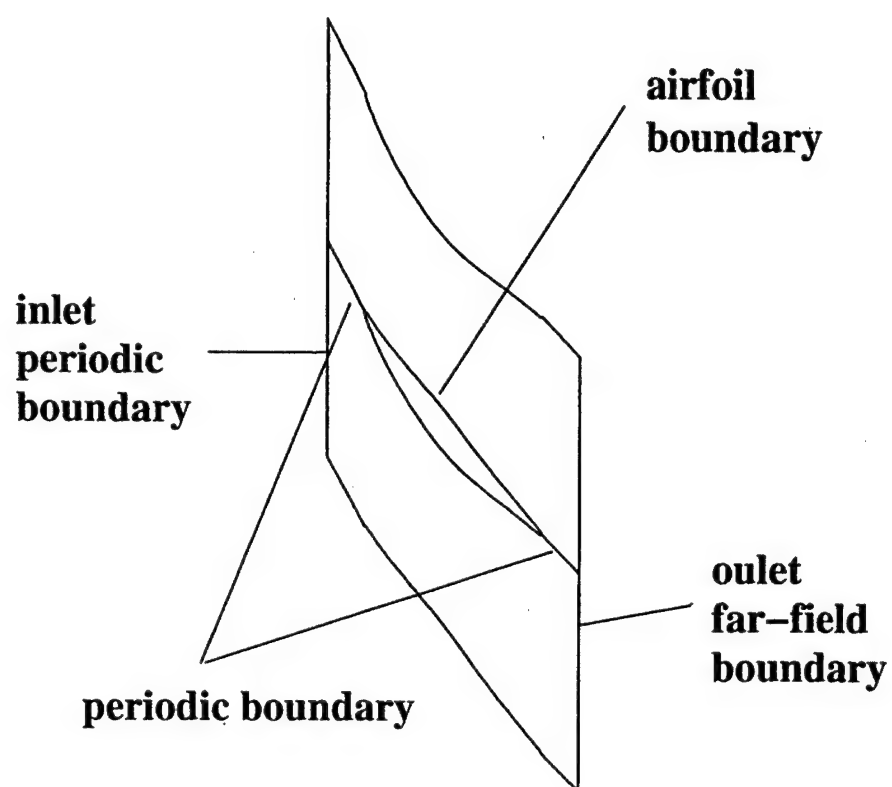
Figure 4.1: Identification and location of numerical boundary types in computational domain.
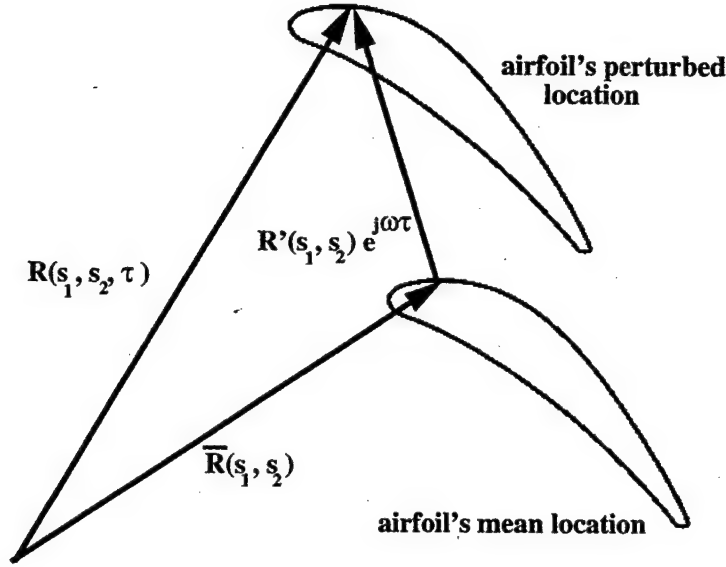
Figure 4.2: Illustration of position vectors for vibrating airfoil.

and the unsteady part is given by

$$(u', v', w') \cdot \overline{\mathbf{n}} = -(\overline{u}, \overline{v}, \overline{w}) \cdot \mathbf{n}' + j\omega(f, g, h) \cdot \overline{\mathbf{n}}. \tag{4.6}$$

To compute the steady and perturbed normals, consider two directions, s_1 and s_2, in which the solid surface is splined. The cross product of derivatives of a position vector with respect to the spline direction results in the normal (unnormalized) vector to the surface, $\mathbf{n}_{\text{surf}}$, i.e.

$$\mathbf{n}_{\text{surf}} = \left(\frac{\partial \overline{\mathbf{R}}}{\partial s_1} + \frac{\partial \mathbf{R}'}{\partial s_1} \right) \times \left(\frac{\partial \overline{\mathbf{R}}}{\partial s_2} + \frac{\partial \mathbf{R}'}{\partial s_2} \right) \tag{4.7}$$

To the first-order, vector, $\mathbf{n}_{\text{surf}}$, is given by

$$\mathbf{n}_{\text{surf}} \approx \overline{\mathbf{n}}_{\text{surf}} + \mathbf{n}'_{\text{surf}} = \frac{\partial \overline{\mathbf{R}}}{\partial s_1} \times \frac{\partial \overline{\mathbf{R}}}{\partial s_2} + \left(\frac{\partial \overline{\mathbf{R}}}{\partial s_1} \times \frac{\partial \mathbf{R}'}{\partial s_2} + \frac{\partial \mathbf{R}'}{\partial s_2} \times \frac{\partial \overline{\mathbf{R}}}{\partial s_2} \right) \tag{4.8}$$

where the zeroth-order and first-order terms are denoted by $\overline{\mathbf{n}}_{\text{surf}}$ and $\mathbf{n}'_{\text{surf}}$ respectively. Next, to compute the unit normal and the perturbation of the unit normal, vectors $\overline{\mathbf{n}}_{\text{surf}}$ and $\mathbf{n}'_{\text{surf}}$ must be normalized by the magnitude of $\overline{\mathbf{n}}_{\text{surf}}$. In addition, the component of the perturbation of the unit vector in the $\overline{\mathbf{n}}_{\text{surf}}$ direction must be removed to prevent stretching of the grid from inducing an upwash. Finally, the expressions for unit mean and perturbed normals are given by

$$\overline{\mathbf{n}} = \frac{\overline{\mathbf{n}}_{\text{surf}}}{|\overline{\mathbf{n}}_{\text{surf}}|}, \quad \mathbf{n}' = \frac{\mathbf{n}'_{\text{surf}}}{|\overline{\mathbf{n}}_{\text{surf}}|} - \left(\frac{\mathbf{n}'_{\text{surf}}}{|\overline{\mathbf{n}}_{\text{surf}}|} \cdot \frac{\overline{\mathbf{n}}_{\text{surf}}}{|\overline{\mathbf{n}}_{\text{surf}}|} \right) \frac{\overline{\mathbf{n}}_{\text{surf}}}{|\overline{\mathbf{n}}_{\text{surf}}|}. \tag{4.9}$$

4.2.2 Periodic Boundary Condition

In this work, we consider only circumferentially periodic flows. This assumption permits one to model an entire cascade while numerically simulating the flow in a single blade passage. For the mean flow, the periodicity condition is given by

$$\overline{U}(\xi, \theta, R) = \overline{U}(\xi, \theta + \theta_G, R) \tag{4.10}$$

where $\overline{U}$ is the vector of conservation variables in the cylindrical coordinates and θ_G is the angular blade to blade gap.

In this analysis, we assume the unsteady flowfield can be modeled as a small harmonic perturbation about the mean (steady) flowfield. Since the governing equations for an unsteady flowfield are linear, then the response of the blade row to arbitrary blade motions or gusts may be determined by decomposing the disturbance into a sum of traveling wave modes. Each mode will have a unique frequency, ω, and a phase shift over one blade pitch (the *interblade phase angle*), σ. Because linear solutions can be superposed, the total response of the blade row is equivalent to the sum of the responses to each of individual modes. Therefore, without loss of generality, only one traveling mode need to be considered at a time. The periodicity condition of an unsteady linearized flow is given by

$$U'(x, \theta + \theta_G, R) = U'(x, \theta, R)e^{j\sigma}. \tag{4.11}$$

4.3 Far-Field Boundary Conditions

In this section, the implementation of the far-field boundary conditions will be discussed for steady and unsteady flow calculations. Typically, far-field boundaries are placed close to the blades to reduce computational resources. Ideally, the far-field boundary conditions for unsteady flows should allow all outgoing unsteady disturbances to pass out of the domain without being reflected. These conditions are referred to as non-reflecting boundary conditions. Full one and two dimensional non-reflecting boundary conditions have been developed in recent years [18, 23, 25]. In this work, quasi-three-dimensional non-reflecting boundary conditions are implemented according to Giles and Saxer [54].

For the steady analysis, the far-field boundary conditions enforce the desired inflow (the total pressure, the total density, the circumferential and radial components of velocity) and outflow (the static pressure) operating conditions.

4.3.1 One-Dimensional Nonreflecting Boundary Conditions

A one dimensional boundary condition is the simplest model for non-reflective far-field boundaries. In this model it is assumed that there is no grid motion in the far-field, which means that in the far-field the computational coordinates are the same as the physical coordinates. The next assumption is that the variations in the unsteady flowfield in the radial and circumferential directions are small, i.e. $\partial/\partial\theta \approx \partial/\partial r \approx 0$. In addition, it is assumed that the effects due to rotation are small, so that the source

terms are ignored. Based on these assumptions the unsteady Euler equations can be written in cylindrical coordinates as

$$\frac{\partial \mathbf{U}'}{\partial t} + \frac{\partial \mathbf{F}'}{\partial x} = 0. \tag{4.12}$$

It is also assumed that the steady flow does not vary in the axial direction in the far field. Eq. (4.12) then becomes

$$\frac{\partial \mathbf{U}'}{\partial t} + \frac{\partial \overline{\mathbf{F}}}{\partial \overline{\mathbf{U}}} \frac{\partial \mathbf{U}'}{\partial x} = 0 \tag{4.13}$$

or in primitive variable form

$$\frac{\partial \mathbf{U}'}{\partial t} + [\mathbf{A}]\frac{\partial \mathbf{U}'}{\partial x} = 0 \tag{4.14}$$

where

$$\mathbf{U}'_p = \begin{pmatrix} \rho' \\ u' \\ u'_\theta \\ u'_R \\ p' \end{pmatrix}, \quad [\mathbf{A}] = \begin{pmatrix} \bar{u} & \bar{\rho} & 0 & 0 & 0 \\ 0 & \bar{u} & 0 & 0 & \frac{1}{\bar{\rho}} \\ 0 & 0 & \bar{u} & 0 & 0 \\ 0 & 0 & 0 & \bar{u} & 0 \\ 0 & \gamma\bar{p} & 0 & 0 & \bar{u} \end{pmatrix}.$$

The far-field behavior of the system can be examined by performing an eigenanalysis of the matrix [$\mathbf{A}$]. Eq. (4.14) can be decoupled by premultiplying the equation by the matrix of left eigenvectors $\mathbf{T}$ given by

$$[\mathbf{T}] = \begin{pmatrix} 0 & 1 & 0 & 0 & -1/\bar{\rho}\bar{a} \\ 0 & 1 & 0 & 0 & 1/\bar{\rho}\bar{a} \\ 1 & 0 & 0 & 0 & -1/\bar{a}^2 \\ 0 & 0 & 0 & 1 & 0 \\ 0 & 0 & 1 & 0 & 0 \end{pmatrix}. \tag{4.15}$$

Eq. (4.14) then becomes

$$\frac{\partial \mathbf{W}}{\partial t} + [\Lambda]\frac{\partial \mathbf{W}}{\partial x} = 0. \tag{4.16}$$

Here [Λ] is a diagonal matrix given by

$$\Lambda = [\mathbf{T}][\mathbf{A}][\mathbf{T}]^{-1} = \begin{pmatrix} \bar{u} - \bar{a} & 0 & 0 & 0 & 0 \\ 0 & \bar{u} + \bar{a} & 0 & 0 & 0 \\ 0 & 0 & \bar{u} & 0 & 0 \\ 0 & 0 & 0 & \bar{u} & 0 \\ 0 & 0 & 0 & 0 & \bar{u} \end{pmatrix}, \tag{4.17}$$

and

$$\mathbf{W} = [\mathbf{T}]\mathbf{U}'_p \tag{4.18}$$

are the characteristic variables (eigenvalues).

In Eq. (4.17) each diagonal component of $[\Lambda]$ is equal to the propagation speed of each of the five associated characteristic waves. Positive eigenvalues correspond to downstream traveling waves and negative eigenvalues correspond to upstream traveling waves. For axially subsonic flows ($\bar{u} < \bar{a}$), there are four downstream moving characteristic waves and one upstream moving wave.

The first characteristic of Eq. (4.16) can be written as

$$w_1 = u' - \frac{p'}{\bar{\rho}\bar{a}}. \tag{4.19}$$

This characteristic denotes an upstream traveling pressure wave. Similarly, the second characteristic is given by

$$w_2 = u' + \frac{p'}{\bar{\rho}\bar{a}} \tag{4.20}$$

and physically is a downstream traveling pressure wave. The third characteristic,

$$w_3 = \rho' - \frac{p'}{\bar{a}^2}, \tag{4.21}$$

is an entropy wave. The fourth and the fifth characteristics are given by

$$w_4 = u'_R \tag{4.22}$$

$$w_5 = u'_\theta, \tag{4.23}$$

and physically are vorticity waves. The entropy and vorticity waves convect downstream with the mean flow. The velocity of their propagation is equal to the axial velocity of the mean flow, $\bar{u}$.

Far-field boundary conditions are applied after each step of the basic numerical integration algorithm at every node of the far-field boundaries. First, at the $(n+1)$st time level after the Lax-Wendroff integration, the estimated solution is computed as

$$\mathbf{U}'^{(n+1)}_{\text{p old}} = \mathbf{U}'^n_{\text{p}} + \delta\mathbf{U}'^n_{\text{p old}} \tag{4.24}$$

where the subscript "old" refers to a value of a variable after the Lax-Wendroff integration, but before applying the far-field boundary conditions. Next, the "old" values of characteristic variables are obtained by $\mathbf{W}_{\text{old}} = [\mathbf{T}]\mathbf{U}'_{\text{p old}}$. The next step is to eliminate downstream traveling waves in case of the inlet far-field boundary, and upstream traveling pressure wave in case of the outlet far-field boundary. This is accomplished by setting corresponding characteristic values to zero, i.e

$$w_{i\,\text{new}} = 0 \quad @\,\text{inlet, if} \quad i = 2,...,5$$
$$w_{i\,\text{new}} = 0 \quad @\,\text{outlet, if} \quad i = 1$$

Then, the "new" values of solution, $\mathbf{U}'^{(n+1)}_{\text{p new}}$, are obtained, i.e.

$$\mathbf{U}'^{(n+1)}_{\text{p new}} = [\mathbf{T}]^{-1}\mathbf{W}_{\text{new}} \tag{4.25}$$

The "new" changes at the $(n+1)$st time level are given by

$$\delta\mathbf{U}'^{(n+1)}_{\text{p new}} = \mathbf{U}'^{(n+1)}_{\text{p new}} - \mathbf{U}'^n_{\text{p}}. \tag{4.26}$$

4.3.2 Quasi-Three Dimensional Analytical Nonreflecting Boundary Conditions

The quasi-three dimensional approach for the implementation of far-field boundary conditions is based on a two-dimensional linearized Euler analysis by Hall and Crawley [23]. Hall's two-dimensional boundary conditions were applied at every radial station making the analysis "quasi-three-dimensional". In this analysis we assume that the flow variations are small in the radial direction and that there is no grid motion in the far-field. Also we neglect rotational effects. Incorporating these assumptions into the linearized Euler equations in cylindrical coordinates, one obtains

$$\frac{\partial \mathbf{U}'}{\partial t} + \frac{\partial}{\partial x}\left(\frac{\partial \overline{\mathbf{F}}}{\partial \overline{\overline{\mathbf{U}}}}\mathbf{U}'\right) + \frac{1}{r}\frac{\partial}{\partial \theta}\left(\frac{\partial \overline{\mathbf{G}}}{\partial \overline{\overline{\mathbf{U}}}}\mathbf{U}'\right) = 0 \qquad (4.27)$$

Additionally it is assumed that the steady flow does not vary in the axial and circumferential directions in the far-field. Equation (4.27),then, becomes

$$\frac{\partial \mathbf{U}'}{\partial t} + \frac{\partial \overline{\mathbf{F}}}{\partial \overline{\overline{\mathbf{U}}}}\frac{\partial \mathbf{U}'}{\partial x} + \frac{1}{r}\frac{\partial \overline{\mathbf{G}}}{\partial \overline{\overline{\mathbf{U}}}}\frac{\partial \mathbf{U}'}{\partial \theta} = 0 \qquad (4.28)$$

or in primitive variable form

$$\frac{\partial \mathbf{U}'_p}{\partial t} + [\mathbf{A}]\frac{\partial \mathbf{U}'_p}{\partial x} + \frac{1}{r}[\mathbf{B}]\frac{\partial \mathbf{U}'_p}{\partial \theta} = 0 \qquad (4.29)$$

where

$$\mathbf{U}'_p = \begin{pmatrix} \rho' \\ u' \\ u'_\theta \\ u'_R \\ p' \end{pmatrix}, \quad [\mathbf{A}] = \begin{pmatrix} \overline{u} & \overline{\rho} & 0 & 0 & 0 \\ 0 & \overline{u} & 0 & 0 & \frac{1}{\overline{\rho}} \\ 0 & 0 & \overline{u} & 0 & 0 \\ 0 & 0 & 0 & \overline{u} & 0 \\ 0 & \gamma\overline{p} & 0 & 0 & \overline{u} \end{pmatrix}, \quad [\mathbf{B}] = \begin{pmatrix} \overline{u}_\theta & 0 & \overline{\rho} & 0 & 0 \\ 0 & \overline{u}_\theta & 0 & 0 & 0 \\ 0 & 0 & \overline{u}_\theta & 0 & \frac{1}{\overline{\rho}} \\ 0 & 0 & 0 & \overline{u}_\theta & 0 \\ 0 & 0 & \gamma\overline{p} & 0 & \overline{u}_\theta \end{pmatrix}$$

We can decompose the unsteady flow, $\mathbf{U}'_p$, at each radial station into Fourier harmonics since it is circumferentially periodic. The Fourier representation of a solution, $\mathbf{U}'_p$, is given by

$$\mathbf{U}'_p(x, \theta, r, t) = \sum_{m=-\infty}^{\infty} \mathbf{U}'_{pm}(r)e^{j[\omega t + k_m x + (\sigma + 2\pi m)\theta/\theta_G]} \qquad (4.30)$$

where ω is the frequency, σ is the interblade phase angle and k_m is a spatial wave number to be determined.

The first step in finding spatial wave numbers k_m is the substitution of Eq. (4.30) into Eq. (4.29):

$$\sum_{m=-\infty}^{\infty} (\omega[\mathbf{I}] + k_m[\mathbf{A}] + \frac{\beta_m}{r}[\mathbf{B}])\mathbf{U}'_{pm}e^{j(\omega t + k_m x + \beta_m \theta)} = 0 \qquad (4.31)$$

Here $[\mathbf{I}]$ is the identity matrix and $\beta_m = (\sigma + 2\pi m)/\theta_G$. For Eq. (4.31) to hold true, each term in the series must independently vanish, hence

$$(\omega[\mathbf{I}] + k_m[\mathbf{A}] + \frac{\beta_m}{r}[\mathbf{B}])\mathbf{U}'_{p_m} = 0 \tag{4.32}$$

or

$$-[\mathbf{A}]^{-1}(\omega[\mathbf{I}] + \frac{\beta_m}{r}[\mathbf{B}])\mathbf{U}'_{p_m} = k_m\mathbf{U}'_{p_m} \tag{4.33}$$

Since ω and β_m are prescribed quantities, Eq. (4.33) is an eigenvalue problem for the eigenvalue k_m and the corresponding right eigenvector $\mathbf{U}'_{p_m}$. For the construction of the non-reflecting boundary conditions, we will need to know the left eigenvectors, which satisfy the equation

$$-\mathbf{U}'^L_m[\mathbf{A}]^{-1}(\omega[\mathbf{I}] + \frac{\beta_m}{r}[\mathbf{B}]) = k_m\mathbf{U}'^L_m \tag{4.34}$$

Note that the right eigenvector is a column vector and the left eigenvector is a row vector. The eigenvalue problem, Eqs. (4.33)-(4.34), is solved analytically. For each fixed m there are five eigenvalues and five corresponding left and right eigenvectors.

A critical step in the construction of boundary conditions is to separate eigensolutions of the eigenvalue problem, Eqs. (4.33)-(4.34), into incoming and outgoing modes. Once the spatial wave numbers k_m are known, this is accomplished by looking at the group velocity, $V_G = -\frac{\partial \omega}{\partial k_x}$. A positive group velocity corresponds to a wave traveling downstream, a negative group velocity corresponds to a wave traveling upstream.

The first eigenvalue and corresponding left eigenvector are given by

$$k_{1m} = \frac{-\bar{u}(\omega + \frac{\beta_m \bar{u}_\theta}{r}) - \bar{a}\sqrt{\frac{\beta_m^2}{r^2}(\bar{u}^2 + \bar{v}_\theta^2 - \bar{a}^2) + 2\frac{\beta_m}{r}\omega\bar{u}_\theta + \omega^2}}{\bar{u}^2 - \bar{a}^2} \tag{4.35}$$

$$\mathbf{U}'^L_{1m} = \left(0, \quad \frac{\beta_m \bar{u}_\theta}{r} + \omega, \quad -\frac{\beta_m \bar{u}}{r}, \quad 0, \quad -\frac{\sqrt{\frac{\beta_m^2}{r^2}(\bar{u}^2 + \bar{v}_\theta^2 - \bar{a}^2) + 2\frac{\beta_m}{r}\omega\bar{u}_\theta + \omega^2}}{\bar{\rho}\bar{a}}\right) \tag{4.36}$$

This pair defines **an upstream traveling pressure wave**, provided $\bar{u} < \bar{a}$. When the wave number, k_{1m}, switches from real to complex, the propagation behavior of this pressure wave changes. When the wave number is real, the amplitude of this wave is constant. When the wave number is complex, the amplitude is decaying exponentially as x decreases. The division point between these two behaviors (the square root term in Eq. (4.35) is equal to zero) is called *the acoustic resonance point.* Constant amplitude waves are referred to as superresonant or cut-on, while decaying waves are referred to as subresonant or cut-off.

The second eigenvalue and corresponding left eigenvector of Eq.(4.34) are given by

$$k_{2m} = \frac{-\bar{u}(\omega + \frac{\beta_m \bar{u}_\theta}{r}) + \bar{a}\sqrt{\frac{\beta_m^2}{r^2}(\bar{u}^2 + \bar{v}_\theta^2 - \bar{a}^2) + 2\frac{\beta_m}{r}\omega\bar{u}_\theta + \omega^2}}{\bar{u}^2 - \bar{a}^2} \tag{4.37}$$

$$\mathbf{U}'^L_{2m} = \left(0, \quad \frac{\beta_m \bar{u}_\theta}{r} + \omega, \quad \frac{-\beta_m \bar{u}}{r}, \quad 0, \quad \frac{\sqrt{\frac{\beta_m^2}{r^2}(\bar{u}^2 + \bar{v}_\theta^2 - \bar{a}^2) + 2\frac{\beta_m}{r}\omega\bar{u}_\theta + \omega^2}}{\bar{\rho}\bar{a}}\right) \tag{4.38}$$

This pair defines **a downstream traveling pressure wave.**

The third set eigenvalue and left eigenvector correspond to **a traveling downstream entropy wave**

$$k_{3m} = -\frac{\beta_m \bar{u}_\theta / r + \omega}{\bar{u}} \tag{4.39}$$

$$\mathbf{U'}_{3m}^L = (\ 1, \ \ 0, \ \ 0, \ \ 0, \ \ -\frac{1}{\bar{a}^2} \ ) \tag{4.40}$$

The fourth and the fifth eigenvalues and left eigenvectors correspond to **traveling downstream vorticity waves.**

$$k_{4m} = k_{5m} = -\frac{\beta_m \bar{u}_\theta / r + \omega}{\bar{u}} \tag{4.41}$$

$$\mathbf{U'}_{4m}^L = (\ 0, \ \ 0, \ \ 0, \ \ 1, \ \ 0 \ ) \tag{4.42}$$

$$\mathbf{U'}_{5m}^L = (\ 0, \ \ \frac{\beta_m \bar{u}}{r}, \ \ \frac{\beta_m \bar{u}_\theta}{r} + \omega, \ \ 0, \ \ \frac{\beta_m}{\bar{\rho} r} \ ) \tag{4.43}$$

Note that the entropy and vorticity waves are cut-on since $k_{3m}, k_{4m},$ and k_{5m} are always real.

Before constructing non-reflective boundary condition, let us recall that left and right are orthogonal. It can be shown that if a left eigenvector $\mathbf{U'}_{jm}^L$ corresponds to an eigenvalue k_{jm} and a right eigenvector $\mathbf{U'}_{im}^R$ corresponds to an eigenvalue k_{im}, then

$$\mathbf{U'}_{jm}^L \mathbf{U'}_{im}^R = 0 \ \ \text{if} \ \ i \neq j$$

$$\mathbf{U'}_{jm}^L \mathbf{U'}_{im}^R = 1 \ \ \text{if} \ \ i = j. \tag{4.44}$$

After all eigenvalues and eigenvectors are known, we can present each Fourier harmonic of a solution as a sum of its five eigenmodes. Four of these eigenmodes travel downstream, and one eigenmode travels upstream. To make a far-field boundary non-reflective, one must exclude from a solution all waves traveling inside the computational domain. More specifically, Eq. (4.30) can be rewritten in a form:

$$\mathbf{U'}_p(x, \theta, r, t) = \sum_{m=-\infty}^{\infty} \mathbf{U'}_{p_m}(x, r) e^{j(\omega t + \beta_m \theta)} = \sum_{m=-\infty}^{\infty} \sum_{i=1}^{5} a_{im} \mathbf{U'}_{im}^R(r) e^{j(\omega t + k_{m_i} x + \beta_m \theta)} \tag{4.45}$$

where the index i refers an eigenmode number i, $\mathbf{U'}_{im}^R$ is its right eigenvector, and a_{im} is the amplitude of this eigenmode. To make a far-field boundary nonreflective one has to set the amplitudes a_{im} to zero for the waves entering the computational domain, i.e. a_{im} $(i = 2, 3, 4, 5)$ is set to zero for an upstream boundary and a_{1m} is set to zero for a downstream boundary. If one multiplies a Fourier coefficient $\mathbf{U'}_{p_m}$ by a left eigenvector $\mathbf{U'}_{jm}^L$, one obtains

$$\mathbf{U'}_{jm}^L \mathbf{U'}_{p_m} = \sum_{i=1}^{5} a_{im} \mathbf{U'}_{jm}^L \mathbf{U'}_{im}^R e^{j(\omega t + k_{mi} x + \beta_m \theta)} = a_{jm} e^{j(\omega t + k_{mi} x + \beta_m \theta)} \tag{4.46}$$

Here the orthogonality of left and right eigenvectors, Eq. (4.44), was used. Eq. (4.45) shows that setting an amplitude a_{jm} to zero is equivalent to setting the quantity $\mathbf{U'}_{jm}^L \mathbf{U'}_{p_m}$ to zero.

The detailed discussion of the numerical implementation of quasi-three-dimensional boundary condition follows.

Discretization of an unsteady far-field boundary condition

The following operations are performed at each radial station at a far-field boundary.

- Compute circumferentially averaged steady flow quantities.

- Update the unsteady solution after the Lax-Wendroff integration and smoothing routines. Go from conservation variables to primitive variables.

- Calculate the Fourier coefficients, $\mathbf{U'}_{p_m}(x, r)$, of an unsteady flow, $\mathbf{U'}_p(x, \theta, r)$. Typically, a finite number $m_{\max}$ of Fourier harmonics is considered. For clarity, let us rewrite the first part of Eq. (4.45) as

$$\mathbf{U'}_p(x, \theta, r) = \sum_{m=-m_{\max}}^{m_{\max}} \mathbf{U'}_{p_m}(x, r) e^{j\beta_m \theta} \tag{4.47}$$

Here the left hand side $\mathbf{U'}_p(x, \theta, r)$ is known. It is the earlier updated unsteady solution vector. A vector $\mathbf{U'}_{p_m}(x, r)$ has to be determined. To compute it, we have to invert a matrix $\mathbf{L}_{im} = \{e^{j\beta_m \theta_i}\}$, where $i = 1, ..., J_{\max} - 1$ and $m = -m_{\max}, ..., m_{\max}$. $J_{\max}$ is a number of grid points in the circumferential direction. Note that the first dimension of the matrix $\mathbf{L}$ is equal to $J_{\max} - 1$ because the first and the last grid points in the circumferential direction are periodic. Since the matrix $\mathbf{L}$ is not square, a pseudoinversion is used to invert it. A pseudoinverted matrix $\mathbf{L}$ is given by

$$\mathbf{L}^{-1} = (\bar{\mathbf{L}}^T \mathbf{L})^{-1} \bar{\mathbf{L}}^T \tag{4.48}$$

where the symbol $\bar{\mathbf{L}}^T$ stands for a conjugated and transposed matrix $\mathbf{L}$.

- For each m a vector $\mathbf{U'}_{p_m}(x, r)$ is multiplied from the left by a matrix $\mathbf{T}$ the rows of which are the left eigenvectors:

$$\mathbf{W}_m = [\mathbf{T}]\mathbf{U'}_{p_m}(x, r) \tag{4.49}$$

$$[\mathbf{T}] = \begin{pmatrix} 0 & \frac{\beta_m \bar{u}_\theta}{r} + \omega & -\frac{\beta_m \bar{u}}{r} & 0 & -\frac{\sqrt{\frac{\beta_m^2}{r^2}(\bar{u}^2 + \bar{v}_\theta^2 - \bar{a}^2) + 2\frac{\beta_m}{r}\omega \bar{u}_\theta + \omega^2}}{\bar{\rho}\bar{a}} \\ 0 & \frac{\beta_m \bar{u}_\theta}{r} + \omega & \frac{-\beta_m \bar{u}}{r} & 0 & \frac{\sqrt{\frac{\beta_m^2}{r^2}(\bar{u}^2 + \bar{v}_\theta^2 - \bar{a}^2) + 2\frac{\beta_m}{r}\omega \bar{u}_\theta + \omega^2}}{\bar{\rho}\bar{a}} \\ 1 & 0 & 0 & 0 & -\frac{1}{\bar{a}^2} \\ 0 & 0 & 0 & 1 & 0 \\ 0 & \frac{\beta_m \bar{u}}{r} & \frac{\beta_m \bar{u}_\theta}{r} + \omega & 0 & \frac{\beta_m}{\bar{\rho}r} \end{pmatrix} \tag{4.50}$$

where $\mathbf{W}_m$ is a vector $(\mathbf{W}_m = (w_{1m}, w_{2m}, w_{3m}, w_{4m}, w_{5m})^T)$.

- To exclude waves entering the computational domain specify $w_{im} = 0$, $i = 2, 3, 4, 5$ for the inlet boundary, and $w_{1m} = 0$ for the outlet boundary.

- Compute new values for Fourier coefficients as

$$\mathbf{U}'_{p_m \text{new}} = [\mathbf{T}]^{-1}\mathbf{W}_m \tag{4.51}$$

where $[\mathbf{T}]^{-1}$ is an inverted matrix of left eigenvectors $[\mathbf{T}]$.

- Compute new values of primitive variables as

$$\mathbf{U}'_p(x, \theta_i, r)_{\text{new}} = \sum_{m=-m_{\max}}^{m_{\max}} \mathbf{U}'_{p_m \text{new}}(x, r) e^{j\beta_m \theta_i} \tag{4.52}$$

4.3.3 Steady Reflecting Boundary Conditions

In the present work, the steady solution is obtained by advancing the governing equations in pseudo time until a steady state is reached, hence far-field boundary conditions are applied at each time level. At a far-field boundary at a given radius r a steady solution at the $(n+1)$st time level (after applying the Lax-Wendroff integration, but before applying the far-field boundary conditions) is given by

$$\overline{\mathbf{U}}_{\text{old}}^{n+1}(x, r, \theta) = \overline{\mathbf{U}}^n(x, r, \theta) + \delta\overline{\mathbf{U}}_{\text{old}}^{n+1}(x, r, \theta). \tag{4.53}$$

The subscript "old" refers to a value of variable before applying the far-field boundary conditions.

Since the solution is spatially periodic ($\overline{\mathbf{U}}^{n+1}(x, r, \theta) = \overline{\mathbf{U}}^{n+1}(x, r, \theta + \theta_G)$), it can be decomposed into Fourier harmonics as

$$\overline{\mathbf{U}}_{\text{old}}^{n+1}(x, r, \theta) = \sum_{m=-\infty}^{m=\infty} \overline{\mathbf{U}}_{m \text{ old}}^{n+1}(x, r) e^{j2\pi m \frac{\theta}{\theta_G}}. \tag{4.54}$$

Here $\overline{\mathbf{U}}_{m \text{ old}}^{n+1}(x, r)$ is the amplitude of the m-th Fourier harmonic of the solution. In practice, a finite number $m_{\max}$ of harmonics is kept in the sum in Eq. (4.54). We assume that in the far-field region the m-th harmonic ($m \neq 0$) of a flow is a small perturbation about a circumferentially averaged mean flow. All harmonics with $m \neq 0$ should be non-reflective. Quasi-three-dimensional conditions described in the previous section are implemented for each harmonic $\overline{\mathbf{U}}_{m \text{ old}}^{n+1}(x, r)$, $m \neq 0$ with $\omega = 0$ and $\beta_m = 2\pi m/\theta_G$. A steady background flow is assumed to be equal to the zeroth harmonic of a solution at the nth time level.

At the inlet and exit boundaries we specify physical quantities that correspond to the time-averaged values expected during operation. At the inlet boundary we specify the total pressure, $p_{T \text{ spec}}$, the total density, $\rho_{T \text{ spec}}$, the radial, $u_{R \text{ spec}}$, and tangential, $u_{\theta \text{ spec}}$, components of velocity. The total density, ρ_T, and the total pressure, p_T, are given by

$$\rho_T = \bar{\rho}(1 + \frac{\gamma - 1}{2}M_{\text{abs}}^2)^{\frac{1}{\gamma-1}} \tag{4.55}$$

$$p_T = \bar{p}(1 + \frac{\gamma - 1}{2}M_{\text{abs}}^2)^{\frac{\gamma}{\gamma-1}} \tag{4.56}$$

where M_{abs} is the Mach number computed in the absolute frame of reference. At the exit boundary we specify the static pressure, $p_{exit\,spec}$. To insure that a circumferentially averaged mean steady flow matches the specified values, a correction to the estimated mean flow, $\overline{\mathbf{U}}_{0\,old}^{(n+1)}(x,r) = (\bar{\rho}, \bar{u}, \bar{u}_\theta, \bar{u}_R, \bar{p})_{old}^{(n+1)}$, has to be made. For this, one-dimensional reflective boundary conditions are applied at the inlet and outlet boundaries at each radial station.

The change in the mean steady flow at the $(n+1)$st time level at the inlet boundary is determined by matching the specified inlet flow values and by keeping unchanged the upstream traveling pressure wave. Assuming that the change is small comparing to the mean flow, one obtains

$$
\begin{pmatrix} \rho_{T\,spec} - \rho_T^n \\ p_{T\,spec} - p_T^n \\ u_{\theta\,spec} - u_\theta^n \\ u_{R\,spec} - u_R^n \\ \delta u_{old} - \frac{\delta p_{old}}{\bar{\rho}\bar{a}} \end{pmatrix}_{inflow} \approx \begin{pmatrix} \frac{\partial\bar{\rho}_T}{\partial\bar{\rho}} & \frac{\partial\bar{\rho}_T}{\partial\bar{u}} & \frac{\partial\bar{\rho}_T}{\partial\bar{u}_\theta} & \frac{\partial\bar{\rho}_T}{\partial\bar{u}_R} & \frac{\partial\bar{\rho}_T}{\partial\bar{p}} \\ \frac{\partial\bar{p}_T}{\partial\bar{\rho}} & \frac{\partial\bar{p}_T}{\partial\bar{u}} & \frac{\partial\bar{p}_T}{\partial\bar{u}_\theta} & \frac{\partial\bar{p}_T}{\partial\bar{u}_R} & \frac{\partial\bar{p}_T}{\partial\bar{p}} \\ 0 & 0 & 1 & 0 & 0 \\ 0 & 0 & 0 & 1 & 0 \\ 0 & 1 & 0 & 0 & -1/(\bar{\rho}\bar{a}) \end{pmatrix}_{inflow}^n \begin{pmatrix} \delta\bar{\rho} \\ \delta\bar{u} \\ \delta\bar{u}_\theta \\ \delta\bar{u}_R \\ \delta\bar{p} \end{pmatrix}_{new}^{n+1}
$$

(4.57)

where $\delta u_{old} = \bar{u}_{old}^{n+1} - \bar{u}^n$ and $\delta p_{old} = \bar{p}_{old}^{n+1} - \bar{p}^n$ are the changes in the mean axial velocity and the mean static pressure at the $(n+1)$st time level before applying far-field boundary conditions. The derivatives of the total pressure and the total density with respect to the flow primitive variables are calculated using Eqs. (4.55)-(4.56). From Eq. (4.57) the new changes in mean steady flow at the $(n+1)$st time level are computed and the new mean steady flow is given by

$$
\overline{\mathbf{U}}_{0\,new}^{n+1} = \overline{\mathbf{U}}_0^n + \delta\overline{\mathbf{U}}_{0\,new}^{n+1}
$$

(4.58)

At the outflow boundary, the new changes in mean steady flow are determined from the requirement that the static pressure has a prescribed value. One specifies an average exit pressure $\bar{p}_{out\,spec}$ at a certain radius (usually at the hub casing). Then, static pressure is computed as a function of radius along the span using a radial equilibrium condition, given by

$$
\frac{\partial\bar{p}_{out\ spec}}{\partial r} = \bar{\rho}\frac{(\bar{u}_\theta)_{abs}^2}{r}.
$$

(4.59)

The change in the mean steady flow at the (n+1)st time level at the outlet boundary is determined by matching the specified static pressure and by keeping unchanged the downstream traveling pressure wave, the entropy wave and the two vorticity waves. Similarly to the inlet boundary, the new changes in mean steady flow at the $(n+1)$st time level are obtained from the equations:

$$
\begin{pmatrix} p_{spec} - p^n \\ \delta u_{old} + \frac{\delta p_{old}}{\bar{\rho}\bar{a}} \\ \delta\rho_{old} - \frac{\delta p_{old}}{\bar{a}^2} \\ \delta u_{\theta\,old} \\ \delta u_{R\,old} \end{pmatrix}_{outflow} \approx \begin{pmatrix} 0 & 0 & 0 & 0 & 1 \\ 0 & 1 & 0 & 0 & 1/(\bar{\rho}\bar{a}) \\ 1 & 0 & 0 & 0 & -1/\bar{a}^2 \\ 0 & 0 & 1 & 0 & 0 \\ 0 & 0 & 0 & 1 & 0 \end{pmatrix}_{outflow}^n \begin{pmatrix} \delta\bar{\rho} \\ \delta\bar{u} \\ \delta\bar{u}_\theta \\ \delta\bar{u}_R \\ \delta\bar{p} \end{pmatrix}_{new}^{n+1}
$$

(4.60)

Once the new changes are obtained, the mean steady flow is updated at the outflow boundary using Eq. (4.58).

The final solution at the $(n+1)$st time level is given by

$$\overline{U}_p^{n+1}(x,r) = \sum_{m=-\infty}^{m=\infty} \overline{U}_{p\,m\,\text{new}}^{n+1} e^{j2\pi m \frac{\theta}{\theta_G}}. \tag{4.61}$$

where $\overline{U}_{p\,m\,\text{new}}^{n+1}$ are the new amplitudes of Fourier harmonics of the solution.

Chapter 5

Coupling of Multiple Blade Rows

The behavior of unsteady flows through multistage machines and the numerical method used to model these flows are discussed in this chapter. An incoming gust or blade vibration creates an initial fluid mode disturbance that travels through the fluid. When this initial disturbance encounters a blade row, the blade row reflects, transmits, and scatters the fluid mode into a set of outgoing fluid modes. When these outgoing modes encounter other blade rows, the process repeats. In addition, frequencies of these modes are shifted as they are viewed in the frames of reference of neighboring blade rows because adjacent blade rows (rotors and stators) move relative to each other. Eventually multiple waves at certain frequencies and spatial wave numbers are excited in the fluid. The unsteady flow is modeled as a sum of these waves.

In Section 5.2, the generation of unsteady pressure, vorticity, and entropy waves in the fluid flow resulting from an initial unsteady disturbance is explained. In Section 5.3, the numerical algorithm for multiple blade rows is outlined. The inter-row boundary conditions are discussed in Section 5.4.

5.1   Nomenclature

B	number of blades in a row
k_0	nodal diameters of initial excitation
N	nodal diameters
p	pressure
$\mathbf{u}$	vector of conservation variables
(u_x, u_θ, u_R)	velocity vector in cylindrical coordinates
x, R, θ, t	cylindrical coordinate system - physical domain

ρ	density
σ	interblade phase angle
$\bar{\Omega}, \Omega$	angular velocity of a rotor shaft
ω	frequency
θ_G	angular blade to blade gap
$()'$	small perturbation quantity
$\overline{()}$	circumferential average

5.2 Spinning Mode Generation

To illustrate the physical process to be modeled, let us consider just one stage which includes a stator and a rotor as shown in Fig. 5.1. The relative motion is provided by the rotor shaft spinning at the rotational frequency, Ω. The relative and fixed coordinate systems are denoted by (x, θ, R) and (x', θ', R') respectively. The stator has B_1 blades, while the rotor contains B_2 blades.

Suppose that the rotor blades vibrate with frequency ω_0 and small amplitude. The resulting unsteadiness in the flow is assumed to be small compared to the mean flow and will be governed by the linearized Euler equations. Therefore, unsteady solutions may be superposed and we can decompose the motion of the rotor into a sum of traveling wave modes to analyze each traveling mode separately. Hence, without loss of generality, we can assume that the rotor blades vibrate with frequency ω_0 and k_0 nodal diameters. As a result of this vibration, pressure, vortical, and entropy waves with frequency ω_0 will radiate away from the rotor. These radiated waves will satisfy the complex periodicity condition given by

$$\mathbf{U}'(x, \theta, R)e^{j\sigma_0} = \mathbf{U}'(x, \theta + \theta_{G2}, R) \tag{5.1}$$

where $\mathbf{U}'$ is the complex amplitudes of the unsteady perturbation conservation variables, and θ_{G2} is the angular blade to blade gap in the rotor. The interblade phase angle of the motion, σ_0, is given by

$$\sigma_0 = \frac{2\pi k_0}{B_2} \tag{5.2}$$

The unsteady flow upstream and downstream of the rotor satisfying the periodicity condition, Eq. (5.1), can be presented in the form of Fourier series, i.e.

$$\mathbf{u}'(x, \theta, R, t) = \sum_{k=-\infty}^{\infty} \mathbf{U}'_k(x, R)e^{j[\omega_0 t + (k_0 + kB_2)\theta]} \tag{5.3}$$

where k takes on all integer values. Each component of the sum, Eq. (5.3), will be referred to as a spinning mode. The kth spinning mode has $N = k_0 + kB_2$ nodal diameters.

Due to the relative motion of blade rows, waves expressed in the moving frame of reference of the rotor will experience a frequency shift when viewed in the fixed
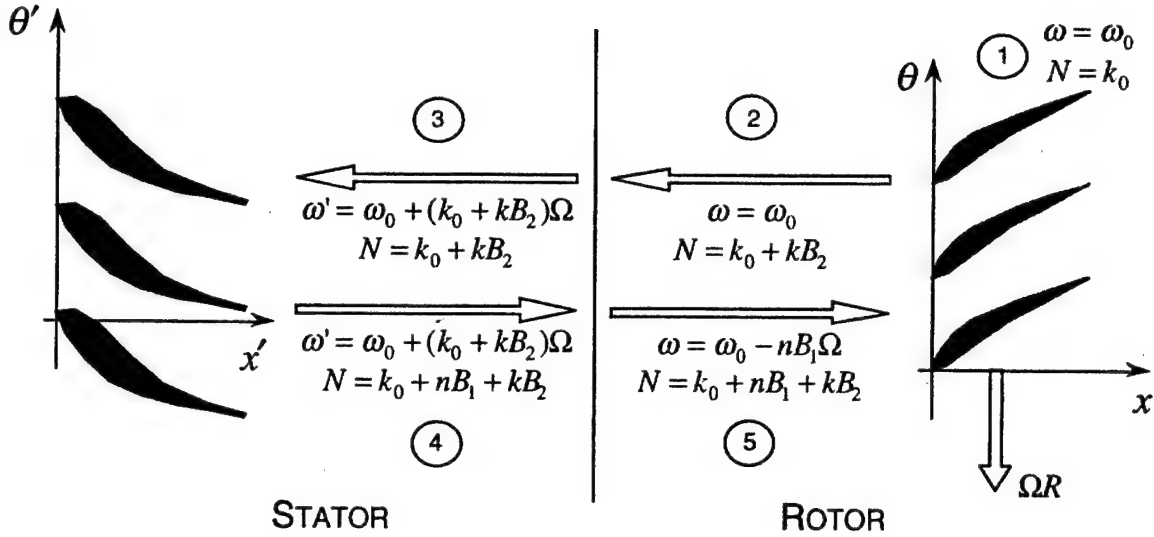
Figure 5.1: Spinning mode generation.

frame of reference of the stator. This phenomenon of frequency shifting is known as the Doppler effect. In our example, the coordinate transformation is given by

$$x' = \Delta x + x, \quad \theta' = -\Omega t + \theta, \quad R' = R \tag{5.4}$$

where Δx is the axial distance between the leading edges of the stator and the rotor. Substitution of Eq. (5.4) into Eq. (5.3) gives

$$\mathbf{u}'(x', \theta', R', t) = \sum_{k=-\infty}^{\infty} \mathbf{U}'_k(x' - \Delta x, R') e^{j[\omega' t + (k_0 + k B_2)\theta']}, \tag{5.5}$$

where $\omega' = \omega_0 + (k_0 + k B_2)\Omega$. Note, that the original frequency ω_0 is shifted to the frequency $\omega' = \omega_0 + (k_0 + k B_2)\Omega$ when viewed in the stator frame of reference. In particular, each wave leaving the rotor is viewed in the stator frame of reference at a different frequency. As a result of the subsequent interaction with the stator, each of these waves excite additional waves which radiate away from the stator. These radiated waves will have the same phase shift over one blade pitch as the incident wave. Hence, the solution can be expressed as

$$\mathbf{u}'(x', \theta', R', t) = \sum_{n=-\infty}^{\infty} \sum_{k=-\infty}^{\infty} \mathbf{U}'_{kn}(x' - \Delta x, R) e^{j[\omega' t + (k_0 + n B_1 + k B_2)\theta']} \tag{5.6}$$

where $\omega' = \omega_0 + (k_0 + k B_2)\Omega$. When viewed in the rotor frame of reference, the waves have the form

$$\mathbf{u}'(x, \theta, R, t) = \sum_{n=-\infty}^{\infty} \sum_{k=-\infty}^{\infty} \mathbf{U}'_{kn}(x, R) e^{j[\omega t + (k_0 + n B_1 + k B_2)\theta]} \tag{5.7}$$

where now $\omega = \omega_0 - n B_1 \Omega$. Note, that the frequency of waves as viewed in the rotor frame does not depend on k. Therefore, the original disturbance with frequency ω_0

and k_0 nodal diameters has scattered into a number of discrete nodal diameters and has shifted into a number of discrete frequencies. Note that the mode numbers n and k, wheel speed, blade count, original frequency and nodal diameters determine the frequency and the nodal diameters of a spinning mode.

The previous example of spinning modes generated in a turbomachinery stage can be extended to machines with several blade rows. Consider $nmax$ blade rows with $B_1, ..., B_{nmax}$ blades respectively. Even numbered blade rows are rotors rotating at the angular frequency Ω; odd numbered blade rows are stators. If the initial disturbance with (ω_0, k_0) starts in any of the rotors, the possible nodal diameters and frequencies can be expressed as

$$N = k_0 + n_1 B_1 + n_2 B_2 + ... + n_{nmax} B_{nmax} \tag{5.8}$$

$$\omega_i = \omega_0 + (k_0 + ... + n_{i-2} B_{i-2} + n_i B_i + n_{i+2} B_{i+2} + ...)\Omega \tag{5.9}$$

$$\omega_j = \omega_0 - (... + n_{j-2} B_{j-2} + n_j B_j + n_{j+2} B_{j+2} + ...)\Omega \tag{5.10}$$

where i and j are blade row numbers, where i is odd and j is even. The indices n take on all integer values.

Furthermore, individual spinning modes will be identified by a set of indices n_i which are needed to define the nodal diameters and the frequency of a mode, see Eqs. (5.8-5.10). The fundamental mode, the mode that is excited initially, will be associated with a set of indices given by $n_i = 0$, with $i = 1, .., nmax$.

It has been shown that an initial excitation with a specific frequency and an interblade phase angle leads to an excitation of an infinite number of spinning modes. In practice, the sums describing the unsteady small perturbation solution, as in Eqs. (5.6-5.7), are truncated to a finite number of modes. We assume that including more spinning modes does not significantly change the unsteady response of the fundamental spinning mode.

When choosing spinning modes for a model, one should always include the fundamental mode. Then, the indices n_i are varied to create more modes. The modes with lower nodal diameters are added first. While adding more modes to the model, it is necessary to satisfy the connectivity condition. For instance, in a single stage, the fundamental mode $(0,0)$ excites the modes $(a,0)$ and $(0,b)$ where a and b are any non-zero integers. Modes $(a,0)$ and $(0,b)$ excite the modes (a,b). If the mode (a,b) is needed in the model, then at least one mode from sets $(a,0)$, $(0,b)$ must be kept to provide a connection between (a,b) and $(0,0)$ modes. Apart from these rules, choosing an appropriate set of spinning modes for a given machine is as much art as science.

5.3 Outline of the Method

Having described the mechanism of spinning mode generation, we will now outline the numerical approach for computing the unsteady flow through a multiple blade row machine using time-linearized CFD techniques.

To begin, we generate a computational mesh for each blade row of a given multistage configuration. Because both mean steady and small perturbation unsteady flows satisfy complex periodicity conditions in the circumferential direction, we only need to generate grid for a single blade to blade passage of each blade row. We generate the three-dimensional grids so that there is the same number of grid points in the radial direction for all blade rows and the radii of the radial stations at the interface boundaries are equal on both sides. These grid features simplify coupling of the solutions at the inter-row boundaries.

The second step is to compute the mean steady flow through the whole machine. Our technique is based on the previously described method for a single blade row. We march the full Euler equations in pseudo-time simultaneously for all blade rows. The circumferentially averaged mean flow variables are matched at each of the radial stations of the inter-row boundary after every time step. A detailed discussion of how solutions are matched at the inter-row boundaries is deferred until the next section.

Once the mean steady solution has been computed, we can linearize the Euler equations. We define a set of spinning modes, each with a different frequency and interblade phase angle to find a small perturbation unsteady solution. The flows associated with each of these spinning modes are found in parallel for an entire computational domain using the method developed for a single blade row. At each iteration of the flow solver, information is exchanged among the various spinning modes at the inter-row computational boundaries (see Section 5.4). This iteration procedure is continued until a converged solution is obtained.

5.4 Interface Boundary Conditions

To begin, we first discuss the steady flow interface boundary conditions. At the stator/rotor interface, mass, momentum and energy must be conserved. The objective of the interface boundary conditions is to make the flux of these quantities out of the stator equal to the flux into the rotor. To achieve this, the following circumferentially averaged flow quantities are matched at the each fixed radius,

$$\bar{\rho}_{\text{stator}} = \bar{\rho}_{\text{rotor}} \tag{5.11}$$

$$\bar{u}_{\text{stator}} = \bar{u}_{\text{rotor}} \tag{5.12}$$

$$\bar{u}_{\theta\text{stator}} = \bar{u}_{\theta\text{rotor}} + \Omega R \tag{5.13}$$

$$\bar{u}_{R\text{stator}} = \bar{u}_{R\text{rotor}} \tag{5.14}$$

$$\bar{p}_{\text{stator}} = \bar{p}_{\text{rotor}} \tag{5.15}$$

The rotor wheel speed ΩR is introduced into the condition matching circumferential velocities, because relative flow variables are used in the flow calculations. Note that similar matching equations can be written for the circumferential averages of conservation variables.

Inter-row boundary conditions are applied after the Lax-Wendroff integration and smoothing routines. The primitive flow variables at time level n and the computed changes at time level $n + 1$ are decomposed into Fourier components at the interface

boundary at each radial station for both stator and rotor, i.e.

$$\mathbf{U}_p^n(x, \theta, R) = \sum_{m=-m_{\max}}^{m=m_{\max}} \overline{\mathbf{U}}_m^n(x, R) e^{j2\pi m \frac{\theta}{\theta_G}} \tag{5.16}$$

$$\delta\mathbf{U}_p^{n+1}(x, \theta, R) = \sum_{m=-m_{\max}}^{m=m_{\max}} \overline{\delta\mathbf{U}}_m^{n+1}(x, R) e^{j2\pi m \frac{\theta}{\theta_G}} \tag{5.17}$$

where $m_{\max}$ is the number of Fourier harmonics one chooses to keep. The zeroth harmonics in Eqs. (5.16)-(5.17) equal to the circumferential average of a quantity at a given radius. For Eqs. (5.11)-(5.15) to hold true, the "new" zeroth harmonic changes at the $(n+1)$st time level are computed as

$$\overline{\delta\rho_0}^{n+1}{}_{\text{NEW}}|_{\text{stator}} = \overline{\delta\rho_0}^{n+1}|_{\text{stator}} + \overline{\delta\rho_0}^{n+1}|_{\text{rotor}} + \overline{\rho_0^n}|_{\text{rotor}} - \overline{\rho_0^n}|_{\text{stator}} \tag{5.18}$$

$$\overline{\delta\rho_0}^{n+1}{}_{\text{NEW}}|_{\text{rotor}} = \overline{\delta\rho_0}^{n+1}{}_{\text{NEW}}|_{\text{stator}} - \overline{\rho_0^n}|_{\text{rotor}} + \overline{\rho_0^n}|_{\text{stator}} \tag{5.19}$$

$$\overline{\delta u_{\theta 0}}^{n+1}{}_{\text{NEW}}|_{\text{stator}} = \overline{\delta u_{\theta 0}}^{n+1}|_{\text{stator}} + \overline{\delta u_{\theta 0}}^{n+1}|_{\text{rotor}} + \overline{u_{\theta 0}^n}|_{\text{rotor}} - \overline{u_{\theta 0}^n}|_{\text{stator}} + R\Omega \tag{5.20}$$

$$\overline{\delta u_{\theta 0}}^{n+1}{}_{\text{NEW}}|_{\text{rotor}} = \overline{\delta u_{\theta 0}}^{n+1}{}_{\text{NEW}}|_{\text{stator}} - \overline{u_{\theta 0}^n}|_{\text{rotor}} + \overline{u_{\theta 0}^n}|_{\text{stator}} - R\Omega \tag{5.21}$$

The "new" changes of the zeroth harmonic of the axial velocity, the radial velocity, and the static pressure are computed similarly to Eqs. (5.18)-(5.19).

To allow circumferential variations in the flow variables, the quasi-three-dimensional non-reflective boundary conditions are applied to the non zero harmonics of changes (see Secs.4.2.2-4.2.3). Once the "new" changes to all Fourier harmonics are found, we compute the "new" changes for primitive variables according to Eq. (5.17).

In the unsteady flow calculation code spinning modes are coupled similarly to the circumferential average flow (the zeroth Fourier harmonic) of the steady flow. The quasi three-dimensional non-reflective boundary conditions are applied to those Fourier harmonics which are not coupled. To illustrate, consider a single stage (see Fig. 5.1) with four spinning modes retained in the model: $(n, k) = (0, 0), (0, 1), (1, 0)$, and $(1, 1)$. The linearized Euler equations are solved simultaneously for the following pairs of frequency and an interblade phase angle for the stator and rotor blade rows,

STATOR   ROTOR

$[\omega_0 + k_0\Omega, 2\pi k_0/B_1]$ $[\omega_0, 2\pi k_0/B_2]$

$[\omega_0 + (k_0 + B_2)\Omega, 2\pi(k_0 + B_2)/B_1]$ $[\omega_0 - B_1\Omega, 2\pi(k_0 + B_1)/B_2]$

After the Lax-Wendroff integration and smoothing routines the computed changes to the flow variables are decomposed into Fourier components at the interface boundary at each radial station. Frequencies and nodal diameters of these Fourier components are given by

STATOR   ROTOR

$$\omega_0 + k_0\Omega, \quad \begin{cases} \dots \\ k_0 - 2B_1 \\ k_0 - B_1 \\ \mathbf{k_0} \\ \mathbf{k_0 + B_1} \\ k_0 + 2B_1 \\ \dots \end{cases} \qquad \omega_0, \quad \begin{cases} \dots \\ k_0 - 2B_2 \\ k_0 - B_2 \\ \mathbf{k_0} \\ \mathbf{k_0 + B_2} \\ k_0 + 2B_2 \\ \dots \end{cases}$$

$$\omega_0 + (k_0+B_2)\Omega, \quad \begin{cases} \dots \\ k_0 + B_2 - 2B_1 \\ k_0 + B_2 - B_1 \\ \mathbf{k_0 + B_2} \\ \mathbf{k_0 + B_2 + B_1} \\ k_0 + B_2 + 2B_1 \\ \dots \end{cases} \qquad \omega_0 - B_1\Omega, \quad \begin{cases} \dots \\ k_0 + B_1 - 2B_2 \\ k_0 + B_1 - B_2 \\ \mathbf{k_0 + B_1} \\ \mathbf{k_0 + B_1 + B_2} \\ k_0 + B_1 + 2B_2 \\ \dots \end{cases}$$

Here nodal diameters of spinning modes which are coupled are in bold. For these modes we match perturbations in density; axial, circumferential, radial components of velocity; and pressure as in Eqs. (5.18)-(5.21). For the rest of modes quasi-three-dimensional boundary conditions are applied to prevent their reflections from the interface boundary.

Chapter 6

Code Validation and Results

To validate the present multistage method and to demonstrate the significance of multistage effects in turbomachinery, a number of test cases are examined in this chapter. Section 6.1 presents results for two-dimensional multistage configurations. In Section 6.2, the present method is validated against a three-dimensional semi-analytical multistage method for a case of a stage composed of flat helical plate blades. Section 6.3 presents multistage results for a typical modern high pressure axial compressor.

6.1 Two-Dimensional Configurations

6.1.1 Flat Unloaded Plates

The first test case is one and one-half stage machine ($stator_1$/rotor/$stator_2$) composed of flat-plate airfoils that do no steady turning. The configuration is depicted in Fig. 6.1. The ratio of blades in the three blade rows is 16:20:25. The specifications of the geometry and the mean steady flow parameters are given in Table 6.1. In this table, the relative quantities are associated with the rotor frame of reference and the absolute quantities with the stator frame of reference. All lengths are nondimensionalized by the chord c of the blades of the middle row, velocities by the relative steady velocity V_{rel}, densities by the mean steady density $\bar{\rho}$, and pressures by the quantity $\bar{\rho}V_{rel}^2$. The nondimensional axial gap between $stator_1$ and rotor is 0.25; the nondimensional axial gap between rotor and $stator_2$ is 0.2.

The driving unsteady aerodynamic excitation to this one and one-half stage system is the plunging motion of the middle blade row with a unit plunging velocity, $\dot{h}$, at a reduced frequency, ω, of 0.5. The interblade phase angle, σ, is varied from $-180°$ to $180°$. Calculations are carried out using zero (uncoupled case), one (fundamental), eleven and twenty seven spinning modes as grouped in Table 6.2. Figure 6.2 shows the resulting fundamental spinning mode of unsteady lift on the middle blade row as a function of the forcing phase angle. The results are compared to the results obtained using the Coupled Mode Method (CMM) of Hall and Silkowski [56]. CMM is a two-dimensional multistage method which is based on modeling an individual blade row as a matrix of reflection/transmission coefficients. For the current case
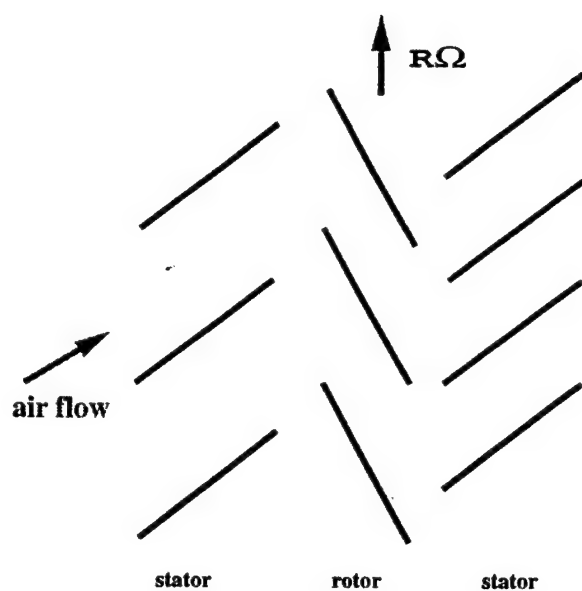
Figure 6.1: Flat Unloaded Plates. Mean Flow Path.

Table 6.1: Flat Unloaded Plates. Geometry and mean flow properties. $R\Omega = 1.25$.

| Parameter	Stator	Rotor	Stator
Blade Count	16	20	25
Gap	1.00	0.80	0.64
Chord	1.25	1.00	0.80
Stagger,deg	37.522	-60.000	37.522
Static pressure	1.458	1.458	1.458
Absolute total pressure	2.022	2.022	2.022
Relative total pressure	1.666	1.666	1.666
Static density	1.000	1.000	1.000
Absolute total density	1.263	1.263	1.263
Relative total density	1.100	1.100	1.100
Relative velocity	1.00	1.00	1.00
Absolute velocity	0.63	0.63	0.63
Relative Mach number	0.700	0.700	0.700
Absolute Mach number	0.441	0.441	0.441
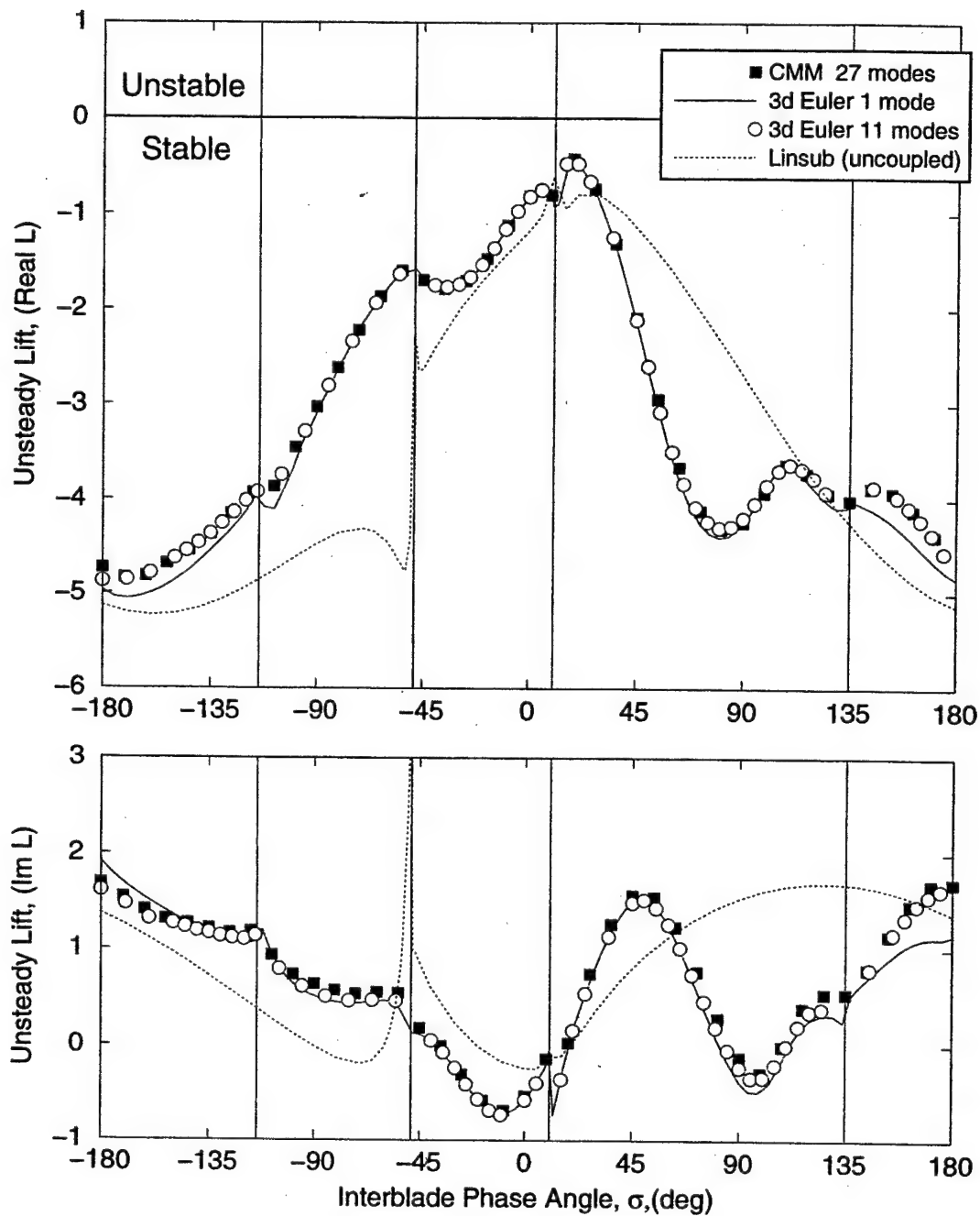
Figure 6.2: Multistage machine with flat plate unloaded airfoils. Unsteady fundamental spinning mode of lift for middle blade row. Plunging excitation of middle row at $\omega = 0.5$ and $-180° \leq \sigma \leq 180°$. Lift is nondimensionalized by $\bar{\rho}V_{rel}hc$.

Table 6.2: Indices of spinning modes used for a coupled analysis. $N = n_1 B_1 + n_2 B_2 + n_3 B_3$

Mode	n_1	n_2	n_3	Mode	n_1	n_2	n_3
1	0	0	0	14	-1	-2	1
2	0	0	-1	15	1	-2	1
3	0	-1	0	16	-1	1	-1
4	-1	0	0	17	0	2	0
5	0	1	-1	18	0	-2	1
6	1	-1	0	19	1	0	-1
7	-1	1	0	20	-1	2	-1
8	0	-1	1	21	1	-2	1
9	1	0	0	22	-1	0	1
10	0	1	0	23	0	2	-1
11	0	0	1	24	1	-1	1
12	-1	0	-1	25	-1	2	0
13	0	-2	0	26	1	2	-1
				27	1	0	1

these coefficients were calculated using LINSUB [61], a code which is based on semi-analytical approach for determining the unsteady aerodynamic response of a linear flat plate cascade. Uncoupled results in Figure 6.2 were obtained for the middle blade row in the isolation using LINSUB.

As nondimensionalized here, the aerodynamic work per cycle is proportional to the real part of the unsteady lift. Therefore, if the real part of the unsteady lift becomes positive, this would represent negative aerodynamic damping. In the absence of any structural damping, flutter would occur. Figure 6.2 shows the substantial differences between the aerodynamic damping of a blade row in isolation and in the presence of neighboring blade rows. There are regions in which the amount of damping is significantly reduced or increased for the coupled case as compared to the uncoupled one. Clearly, multistage effects should not be neglected in an unsteady aerodynamic analysis for flutter stability or forced response.

Note that the large difference in the damping occurs in the regions with $\sigma \leq -48.5°$ and $\sigma \geq 10.4°$. Over these regions the pressure waves of the fundamental mode are cutoff, which means that the amplitudes of these waves are decaying exponentially as the axial distance from the vibrating blade row increases. Since the distances between blade rows are relatively short, the decaying pressure waves are still strong when they are reflected by the neighboring blade rows. These reflected pressure waves alter the unsteady response of the middle (vibrating) blade row.

The lift curves shown in Fig. 6.2 have distinct slope discontinuities. These discontinuities correspond to the acoustic resonance points, which are shown by vertical lines. The curve corresponding to the uncoupled case has resonances at $\sigma = -48.5°$

and $\sigma = 10.4°$. These are the resonance points of the fundamental mode. The one mode coupling case shows two additional resonance points at $\sigma = -114.3°$ and $\sigma = 135.1°$. These are the resonances of spinning modes with indices $(n_1, n_2, n_3) = (1, 0, 0), (-1, 0, 0)$. These two spinning modes belong to the scatter group that is excited by the fundamental mode in the first blade row. Hence, they influence the unsteady response of the fundamental mode. There are more resonance points in the 11 mode case. These points are not indicated in Fig. 6.2.

Next, Figure 6.2 shows a mode convergence study. In our example, a solution obtained with eleven modes is very close to a solution obtained with twenty seven modes. In other words, the solution is "mode converged", becuase the addition of more modes does not change the solution. Also when the convergence is achieved, the solution becomes periodic. For example, the one mode coupling solution at $\sigma = 180°$ does not equal the solution at $\sigma = -180°$. As more modes are included, however, this periodicity is achieved. Finally, note that for this case keeping only one fundamental mode in the coupled calculations is enough to obtain a good estimation of the unsteady lift.
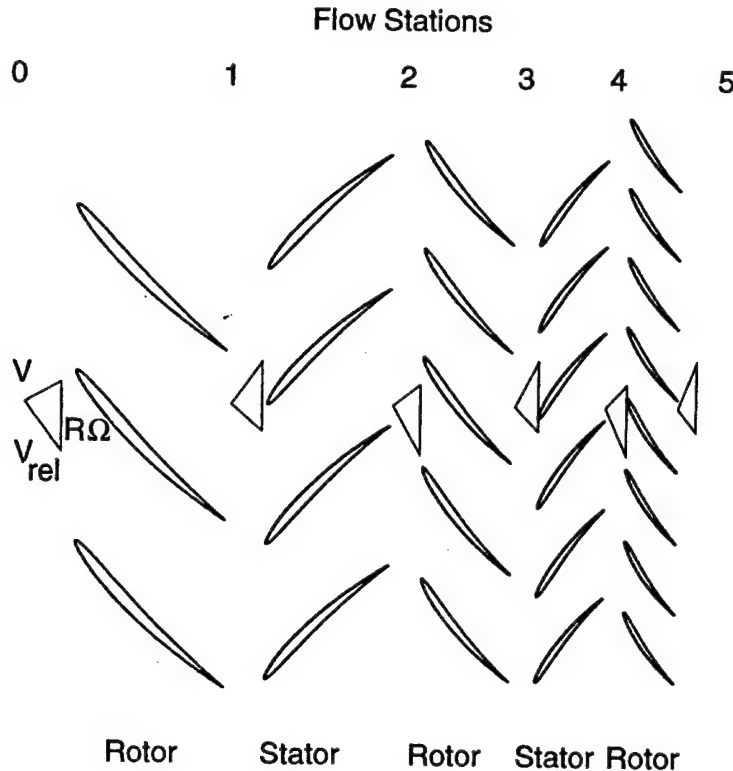
Flow Stations

Figure 6.3: 2D Linear Compressor.

6.1.2 Two-Dimensional Compressor

In this section, we consider compressible flows in the (two-dimensional) two and one-half stage linear compressor section shown in Fig. 6.3. This test case was designed to be representative of current axial flow compressors. The airfoils of each blade row of the compressor are NACA four digit series airfoils, for which a description can be found in the Ref. [1]. The specific geometry for the compressor is given in Table 6.3. As before, lengths are nondimensionalized by the chord c of the rotor blades of the middle rotor, velocities by the relative inflow velocity V_{rel} at station 2, and pressures by the quantity $\bar{\rho}V_{rel}^2$ at station 2.

First, the steady flow is computed through all five blade rows using the steady multistage code. The computational grid used for this calculation was an H-grid with 57×17 grid points (57 nodes in the streamwise direction, and 17 nodes in the circumferential direction) for each blade row. The same computational grid was used to compute the steady and unsteady flow solutions. The computational grid for the middle three blade rows is shown in Fig. 6.4. Shown in Fig. 6.5 is the computed steady pressure distribution on the surface of the blades of the middle blade row. For the cases considered, the flow through the multistage compressor is entirely subsonic.

The first unsteady case examined is similar to the case for the flat plate airfoil geometry described in the previous section. Only the middle three blade rows are considered. The blades of the middle rotor are prescribed to vibrate in plunge normal to the chord with a reduced frequency, ω, of 0.5 for a range of interblade phase angles,

Table 6.3: 2D Linear Compressor. Geometry and mean flow properties. $R\Omega = 1.25$.

Parameter	Rotor	Stator	Rotor	Stator	Rotor
Airfoil	NACA 3.5,506	NACA 4.5,506	NACA 4.5,506	NACA 4.5,506	NACA 4.5,506
Blade Count	13	16	20	25	31
Gap	1.231	1.000	0.800	0.640	0.516
Chord	1.539	1.250	1.000	0.800	0.645
Stagger, deg	-44.0	43.0	-49.5	52.0	-55.0
Axial gap	0.31	0.25	0.2	0.16	
Inlet Static pressure	0.939	1.213	1.458	1.797	2.131
Exit static pressure	1.213	1.458	1.797	2.131	2.524
Inlet Total pressure, abs	1.180	1.666	1.666	2.346	2.346
Inlet Total pressure, abs	1.473	1.473	2.022	2.022	2.739
Inlet Static density	0.730	0.877	1.000	1.161	1.312
Inlet Flow Angle, rel deg	-52.0	-40.0	-60.0	-45.	-65.5
Inlet Flow Angle, abs deg	28.6	53.5	37.5	62.3	47.3
Inlet Relative Velocity	1.112	0.744	1.000	0.609	0.919
Inlet Absolute Velocity	0.780	0.959	0.630	0.926	0.562
Inlet Relative Mach number	0.829	0.535	0.700	0.414	0.609
Inlet Absolute Mach number	0.581	0.689	0.441	0.629	0.373
Exit static pressure	1.213	1.458	1.797	2.131	2.524

σ. The blade rows are coupled using zero, one, 11, and 27 spinning modes (see Table 6.2). The zero mode case corresponds to an isolated blade row.

Figure 6.6 shows the unsteady lift associated with the fundamental spinning mode on the reference airfoil of the middle blade row. The lift for the coupled cases is seen to be significantly different than the lift for the uncoupled case. The calculations also demonstrate mode convergence. Like the flat plate airfoil case, the model with one (fundamental) mode gives a good estimate of unsteady lift for almost the entire range of interblade phase angles. This fact is very important, because keeping just one fundamental mode decreases significantly the CPU time required to compute the unsteady multistage response.

Figure 6.7 shows the unsteady lift associated with the fundamental mode computed for different placements of the interface boundaries for one mode case. Note that the computed lift is virtually unaffected by the position of the interface boundary indicating that the interface boundary conditions have been properly implemented.

Finally, we include the first and last blade rows to create a full two and one-half stage machine. Figure 6.8 compares the unsteady lift on the reference airfoil of the middle blade row for the models with three and five blade rows. Just the fundamental spinning mode is used to couple the blade rows. The results are nearly the same for both cases indicating that only the closest neighboring blade rows make a significant contribution to the unsteady response of the middle blade row.
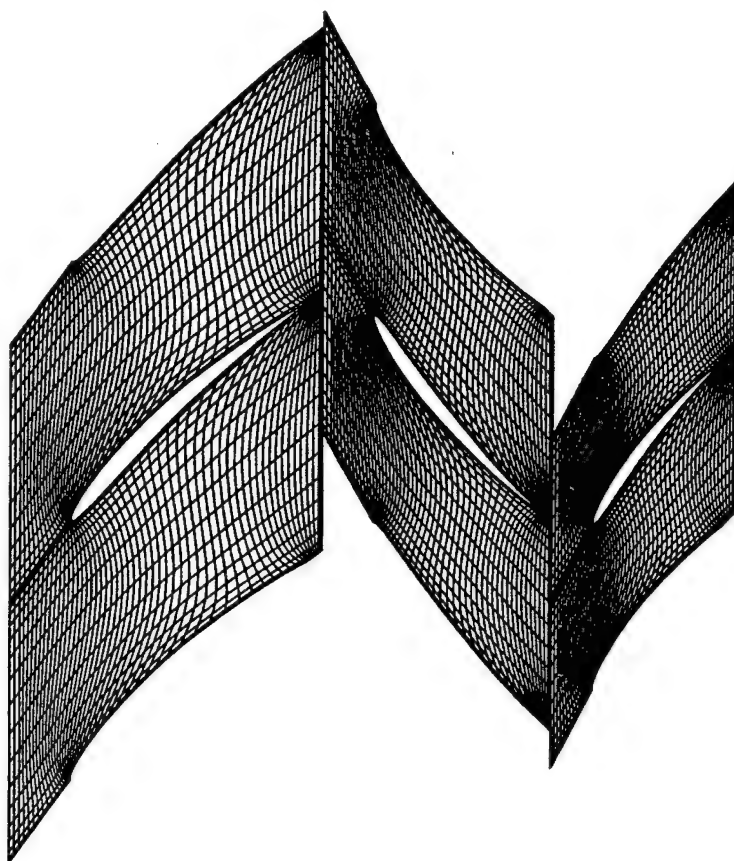
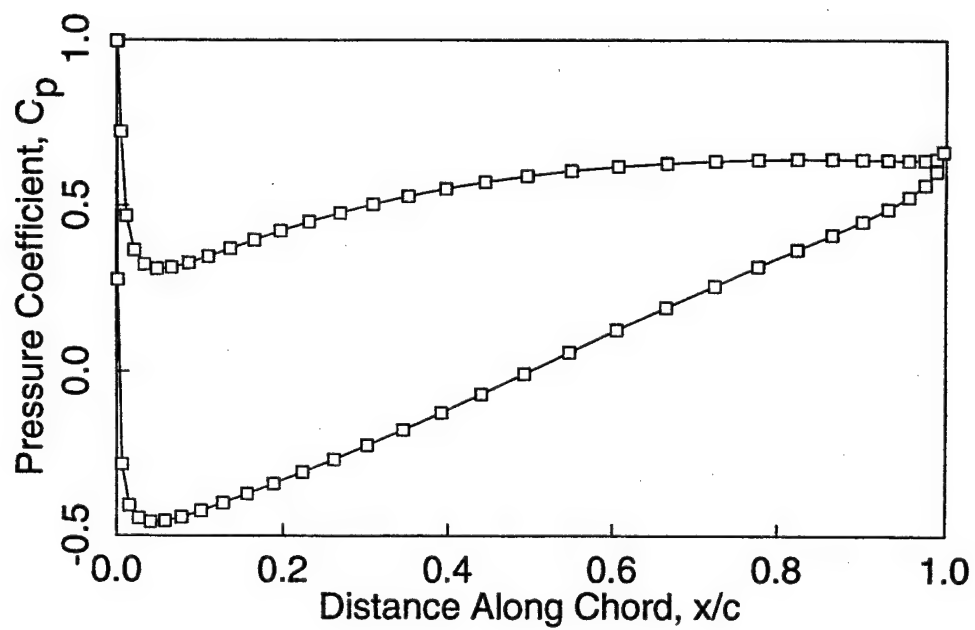Figure 6.4: 2D Linear Compressor. Computational Mesh.

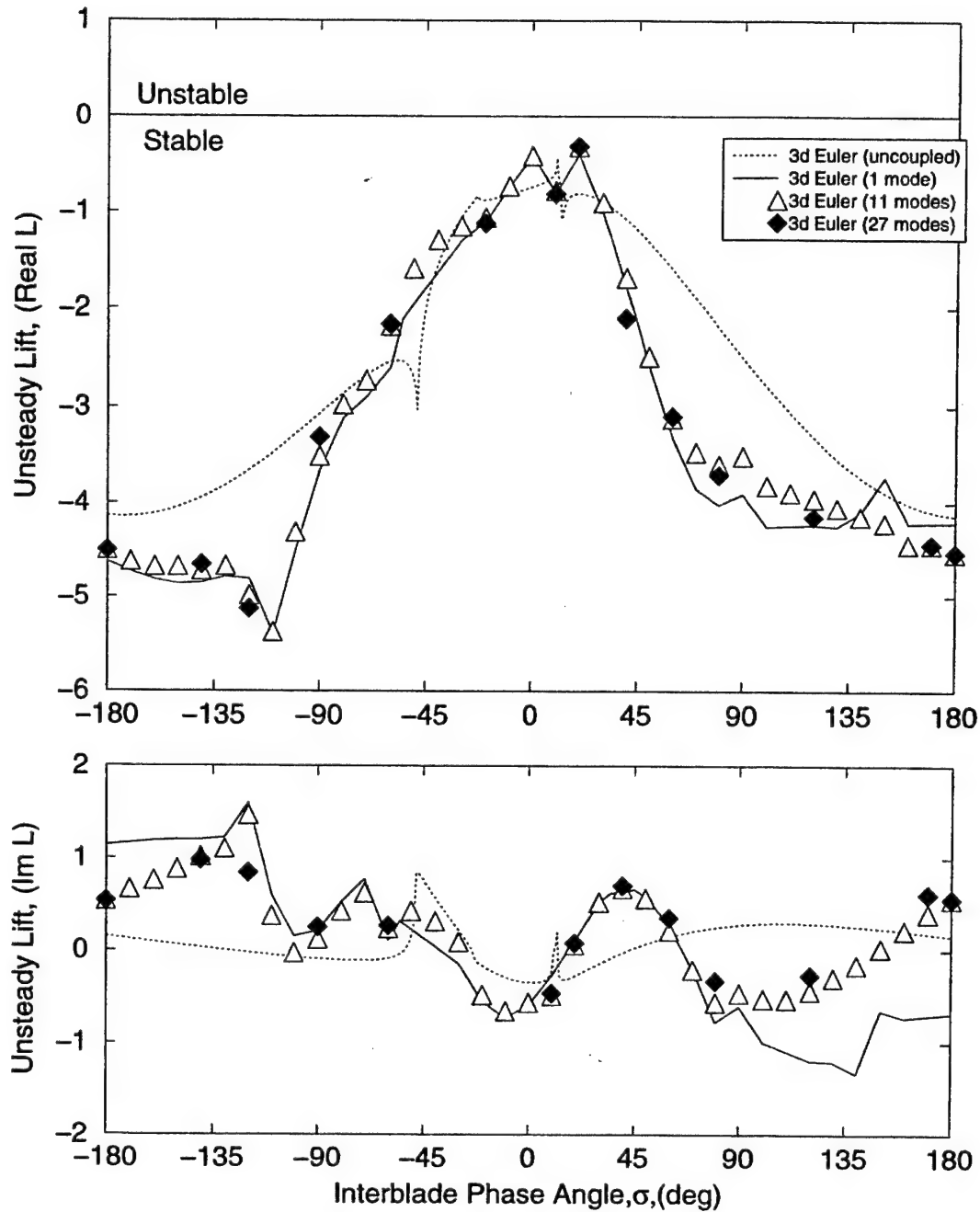Figure 6.5: 2D Linear Compressor. Pressure Coefficient in the middle blade row.

Figure 6.6: 2D Linear Compressor (3 blade rows). Unsteady fundamental spinning mode of lift for middle blade row. Plunging excitation of middle row at $\omega = 0.5$ and $-180° \leq \sigma \leq 180°$. Lift is nondimensionalized by $\bar{\rho}V_{rel}\dot{h}c$.
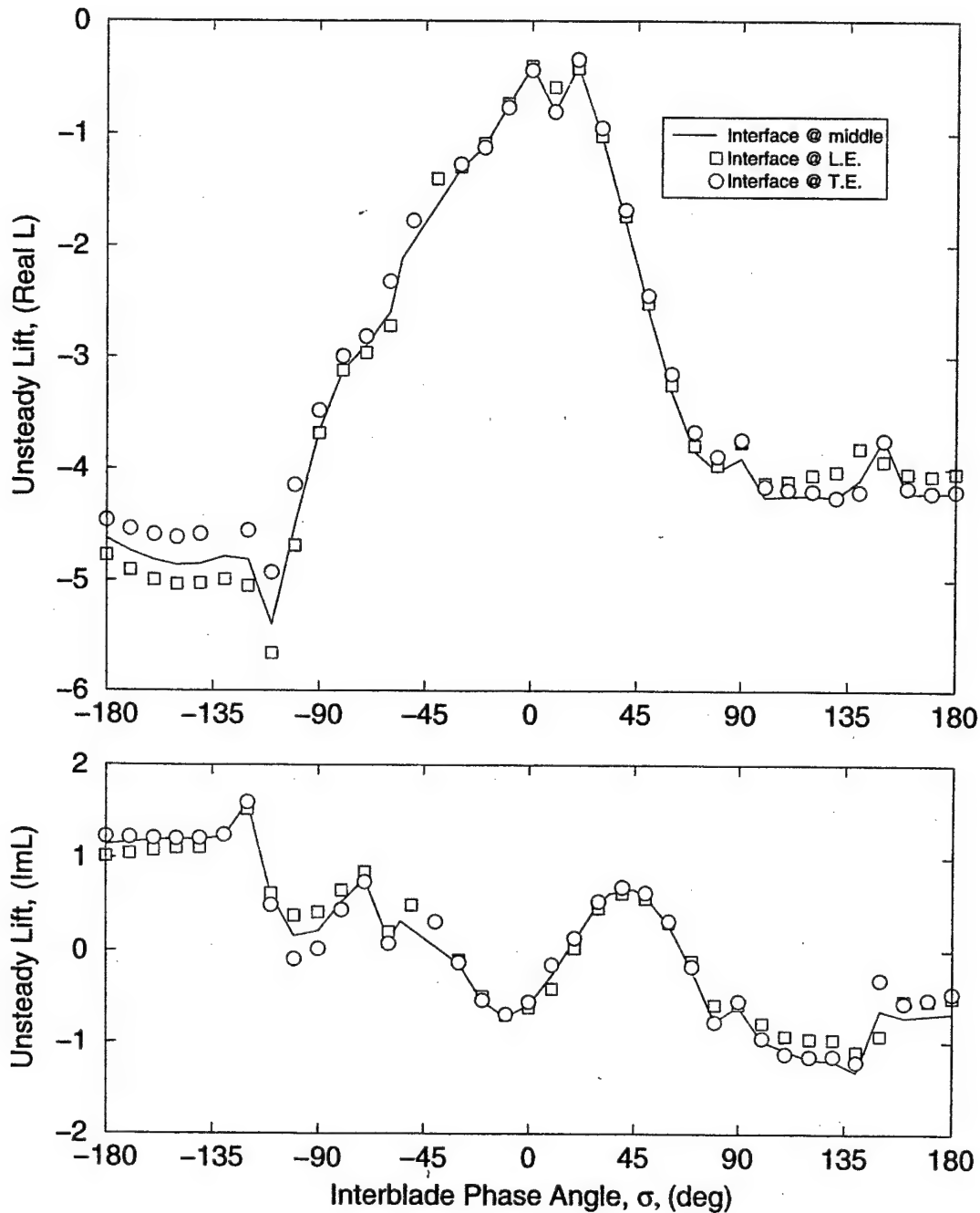
Figure 6.7: 2D Linear Compressor (3 blade rows). Different placements of interface boundary. Unsteady fundamental spinning mode of lift for middle blade row. Plunging excitation of middle row at $\omega = 0.5$ and $-180° \leq \sigma \leq 180°$. Lift is nondimensionalized by $\bar{\rho} V_{rel} \dot{h} c$.
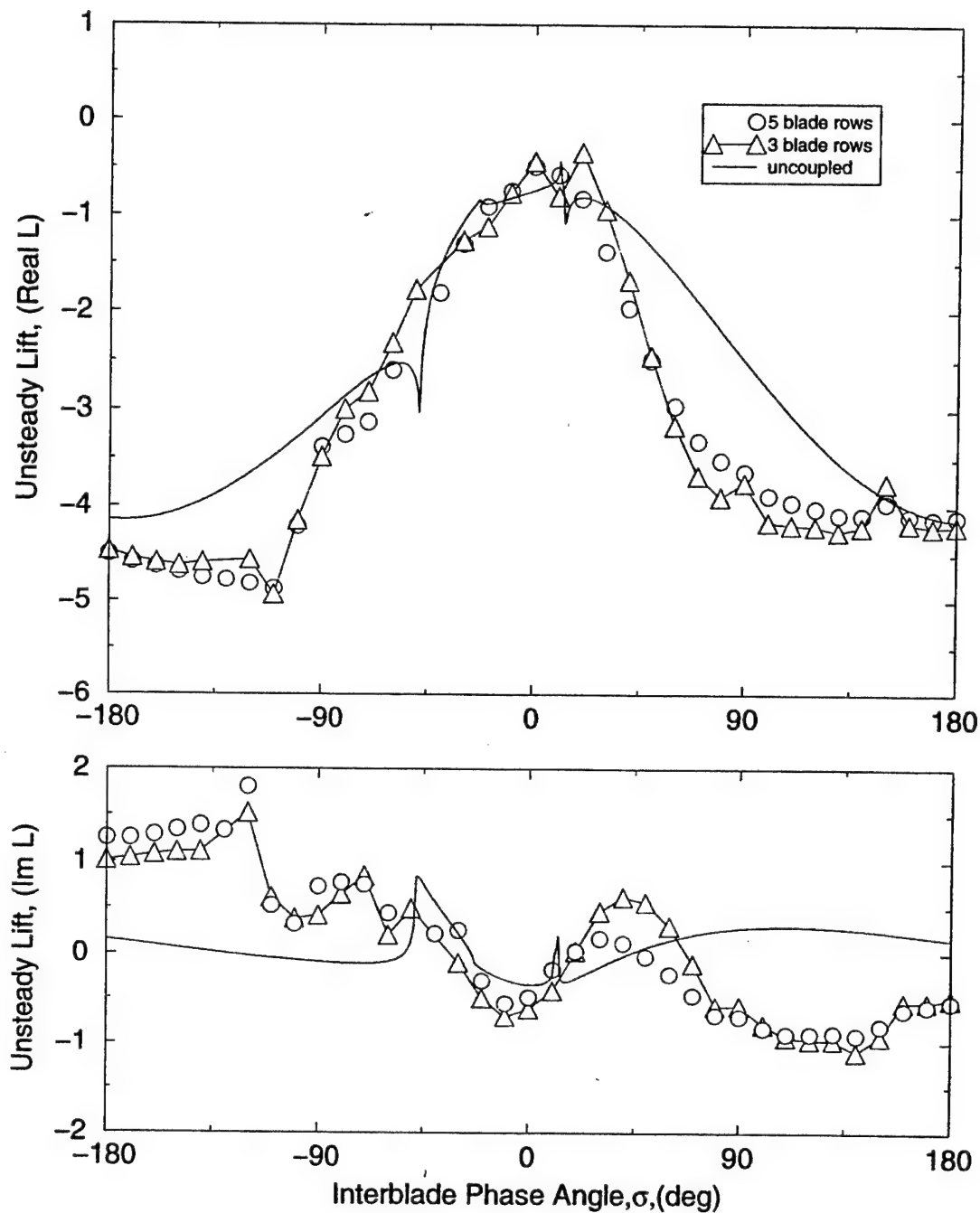
Figure 6.8: 2D Linear Compressor. Comparison of models with different number of blade rows. Unsteady Fundamental spinning mode of lift for middle blade row. Plunging excitation of middle row at $\omega = 0.5$ and $-180° \leq \sigma \leq 180°$. Lift is nondimensionalized by $\bar{\rho}V_{rel}\dot{h}c$.

6.2 Three-Dimensional Flat Plates

To further validate the present method, in this section, the linearized multistage Euler computational results are compared to Namba's unsteady three-dimensional multistage semi-analytical analysis [45]. The configuration considered here is one stage (rotor/stator). The blades are helical surfaces with zero steady pressure loading. The rotor has 38 blades, while the stator contains 50 blades. In the following, lengths are nondimensionalized by the tip radius r_T, velocities by the axial velocity U, densities by the steady density $\bar{\rho}$, and pressures by the quantity $\bar{\rho}U^2$. Axial chords of blades are assumed constant along the span. The nondimensional axial chord of the rotor c_{a1} is 0.11203, whereas that of the stator c_{a2} is 0.12566. The axial gap between the blade rows is $c_{a1}/2$. The nondimensional rotation rate of the rotor, Ω, is 1.73205. The geometry of this multistage configuration is summarized in Table 6.4.

The blades of the rotor are vibrating in plunge with a reduced frequency, ω, of 1.0 based on local chord and local relative flow velocity. Note that ratio of local chord to local relative flow velocity does not vary along the span for this configuration. The displacement of the blade is normal to the local blade chord, and its radius-dependent amplitude is given by

$$a(r) = c_{a1}h_1(r)/\sqrt{1 + \Omega^2 r^2} \tag{6.1}$$

where $h_1(r)$ denotes the spanwise distribution of amplitude of a cantilever beam for the first bending mode.

The unsteady aerodynamic response was computed using zero and nine modes (see Table 6.6). The zero mode case corresponds to an isolated blade row (no inter-row coupling). Figure 6.9 shows the computed unsteady pressure difference across the rotor surface at the tip, middle span, and the hub stations for an interblade phase angle, σ, $20\pi/38$. Note that there is a substantial difference in unsteady pressure distribution for the coupled and uncoupled cases. Next, we compare the present coupled mode analysis to the Namba's semi-analitycal multistage method in Fig. 6.10. Note that there is a good agreement between the two methods. These results show that the linearized multistage Euler method produces accurate predictions for the unsteady responses of a three-dimensional multistage configurations with three-dimensional (that is, radial) mode shapes.

Table 6.4: 3D Flat Plates. Geometry and mean flow properties.

Parameter	Rotor	Stator
Blade Count	38	50
Tip radius	1.	1.
Hub radius	0.5	0.5
Axial Chord	0.11023	0.12566
Axial Mach number	0.35	0.35
Flow angle @ hub, (deg)	40.89338	0.
Flow angle @ tip, (deg)	60.	0.

Table 6.5: Mode shape function of circumferential bending displacement, $h_1(r)$.

r	$h_1(r)$
0.50000	0.0
0.58333	0.04512
0.66667	0.16559
0.75000	0.33962
0.83333	0.54705
0.91667	0.77104
1.00000	1.00000

Table 6.6: Indices of spinning modes used for a coupled analysis. $N = n_1 B_1 + n_2 B_2$

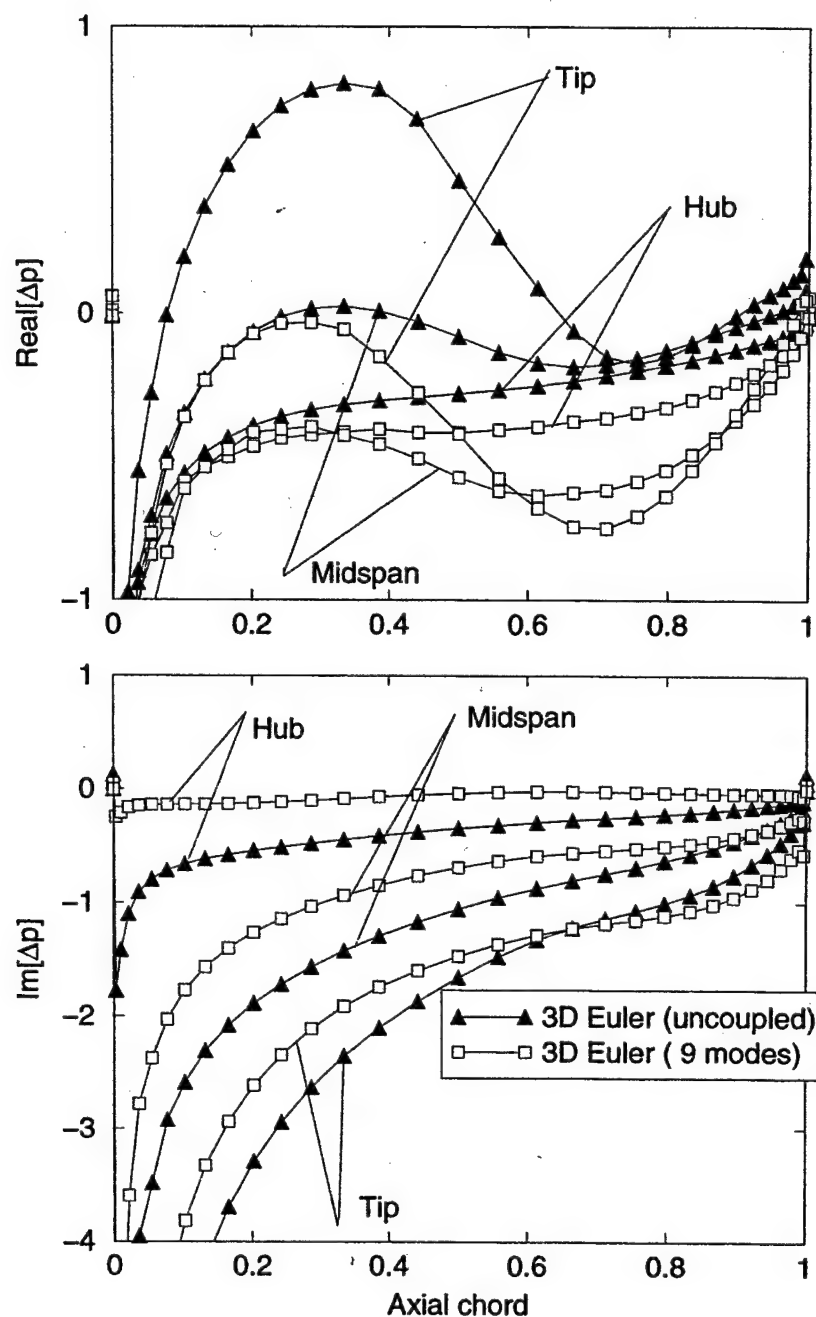| Mode	n_1	n_2	Mode	n_1	n_2
1	0	0	6	-1	1
2	-1	0	7	1	1
3	1	0	8	1	-1
4	0	-1	9	1	1
5	0	1			

Figure 6.9: Comparison of the coupled and uncoupled solutions for a stage composed of annular flat plates. Bending vibration of rotor at $\omega = 1.0$ and $\sigma = 94.7368°$. The unsteady pressure is nondimensionalized by $\bar{\rho}U^2$.
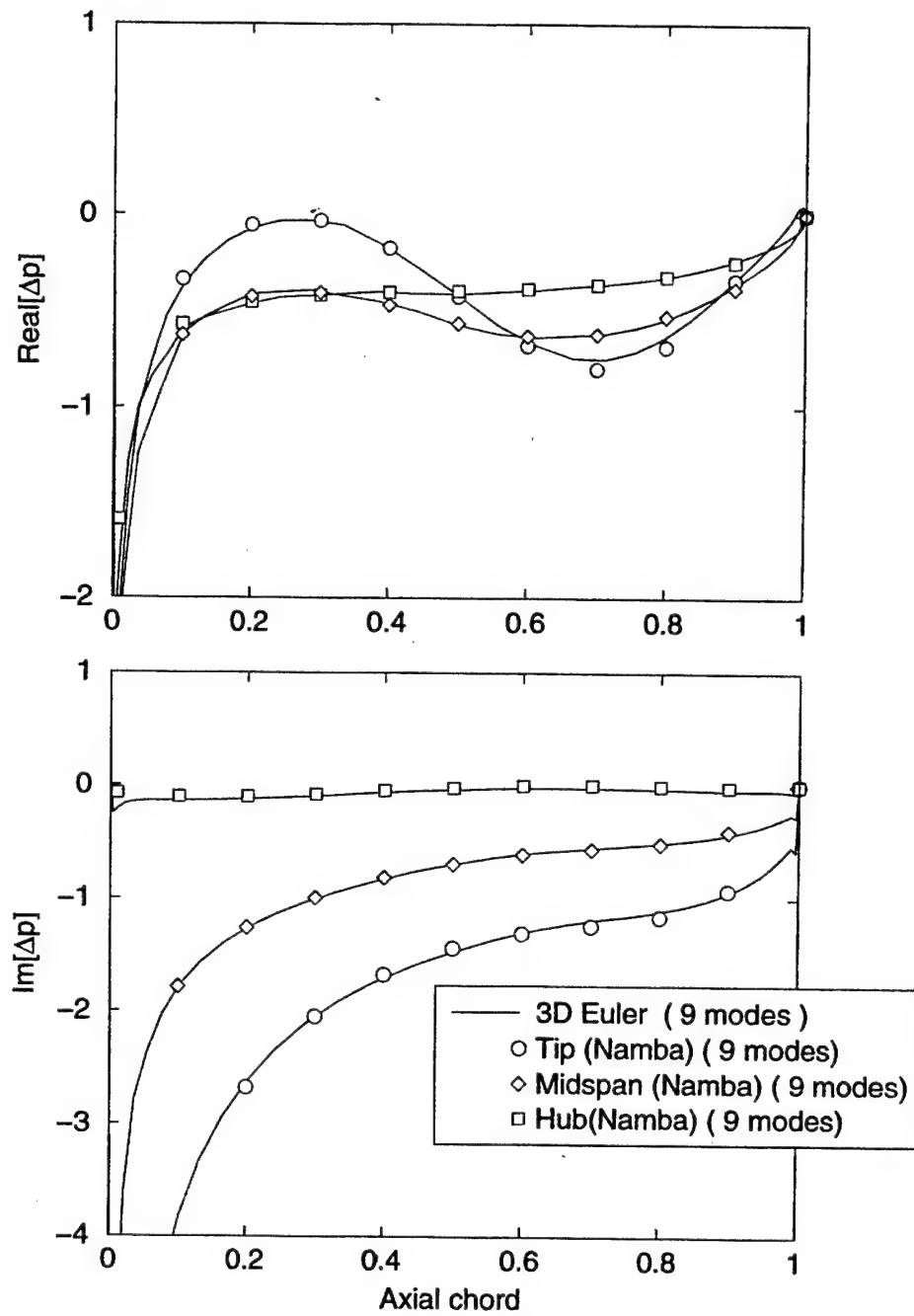
Figure 6.10: Comparison of three-dimensional linearized Euler solution to Namba's semi-analitical three-dimensional multistage method. Bending vibration of rotor at $\omega = 1.0$ and $\sigma = 94.7368°$. The unsteady pressure is nondimensionalized by $\bar{\rho}U^2$.
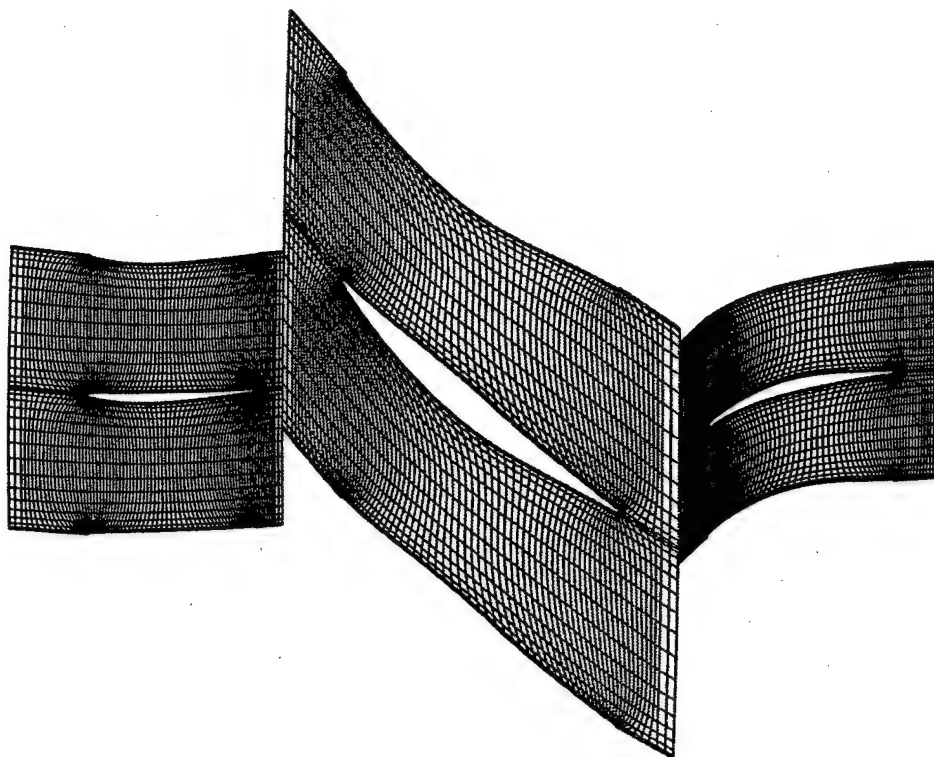
Figure 6.11: 3D Compressor. Computational grid at the middle span.

6.3 Modern Three-Dimensional Compressor

The next configuration considered is a section of a modern axial high pressure compressor. The flow through the front three blade rows is examined. These are the inlet guide vanes (IGV), and the first stage, rotor (R1) and stator (S1).

The operating condition considered is close to the design point of the compressor. Table 6.7 shows some typical parameters of the mean flow for this case.

First, the mean (steady) flow is calculated using the three-dimensional steady flow code. The computational grid used for this calculation was an H-grid with $81 \times 17 \times 17$ grid points (81 nodes in the streamwise direction, 17 nodes in circumferential direction, and 17 points in radial direction). The grid is generated for only a single blade passage of each blade row, because the flow is periodic in circumferential direction. Figure 6.11 shows a computational grid at the midspan.

When the mean (steady) flow is computed, we only specify the flow parameters in the far-field. In particular, the circumferential averages of the total pressure, the total density, the circumferential and radial components of velocity are specified along the span at the inlet of the inlet guide vanes. The static pressure is specified on the hub at the exit of the stator. Figure 6.12 shows the mean static pressure contours at the midspan. Of particular interest is the behavior of the solution near the interface boundaries and in the far-field. The pressure contours are seen to pass smoothly out these boundaries without reflection demonstrating the effectiveness of the boundary conditions. Note that the pressure contours do not match at the interface boundaries,
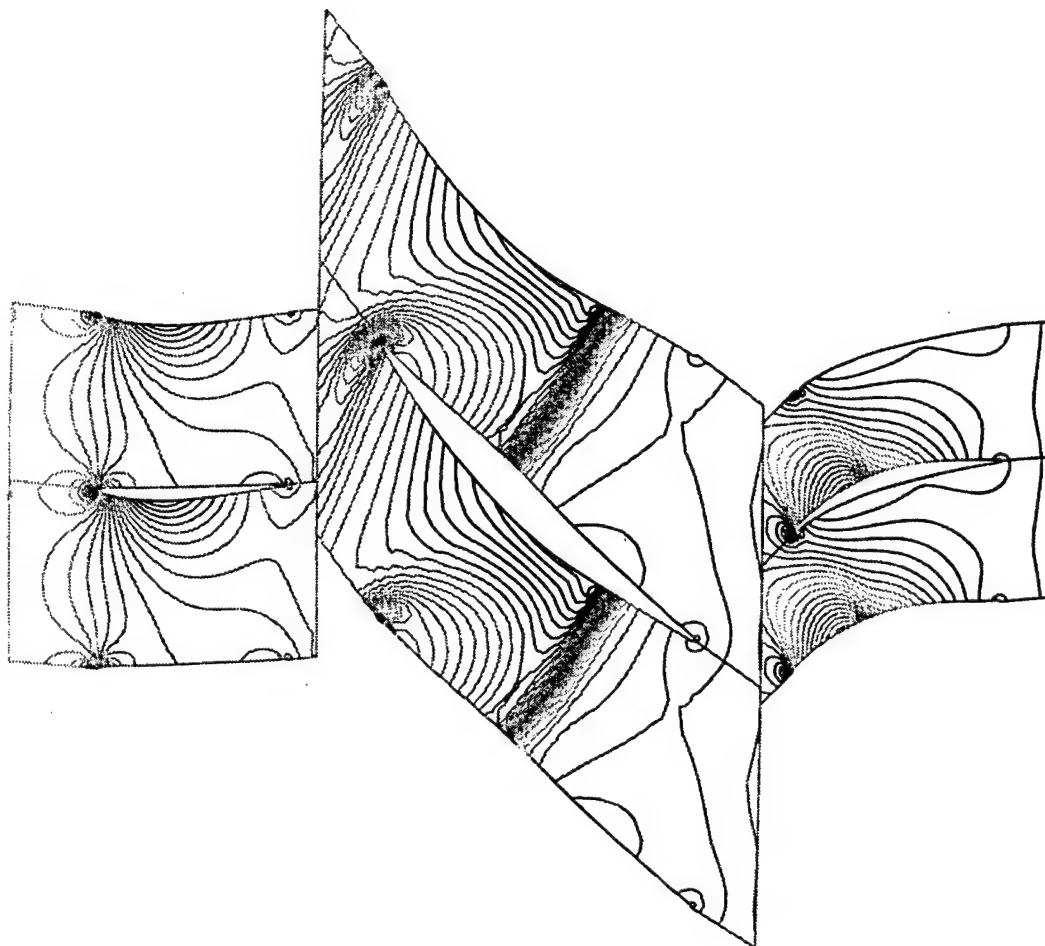
Figure 6.12: 3D Compressor. Static pressure contours at the middle span at design conditions.

because only the circumferential averages of the flow variables are matched at the inter-row boundaries during the flow calculations.

Now consider the case where the rotor blades vibrate in plunge with the first-bending mode shape with a reduced frequency, ω, of 0.37 based on the upstream rotor relative velocity and rotor chord at the tip. The unsteady aerodynamic response was computed with zero, one, and seven spinning modes for a range of interblade phase angles.

Figure 6.13 shows the computed unsteady pressure on the surface of the rotor at the midspan station for the case where a single mode is used to couple the three blade rows. Also shown is the unsteady pressure distribution for the uncoupled case. One can integrate the unsteady pressure distribution on the surface of the blade to obtain the aerodynamic work per cycle. Fig. 6.14 shows the aerodynamic work per cycle associated with the fundamental mode on a rotor blade for a range of interblade phase angles. The aerodynamic work per cycle for the coupled cases is seen to be substantially different than that for the uncoupled case.

Similar calculations were performed for the case where the rotor blades vibrate in
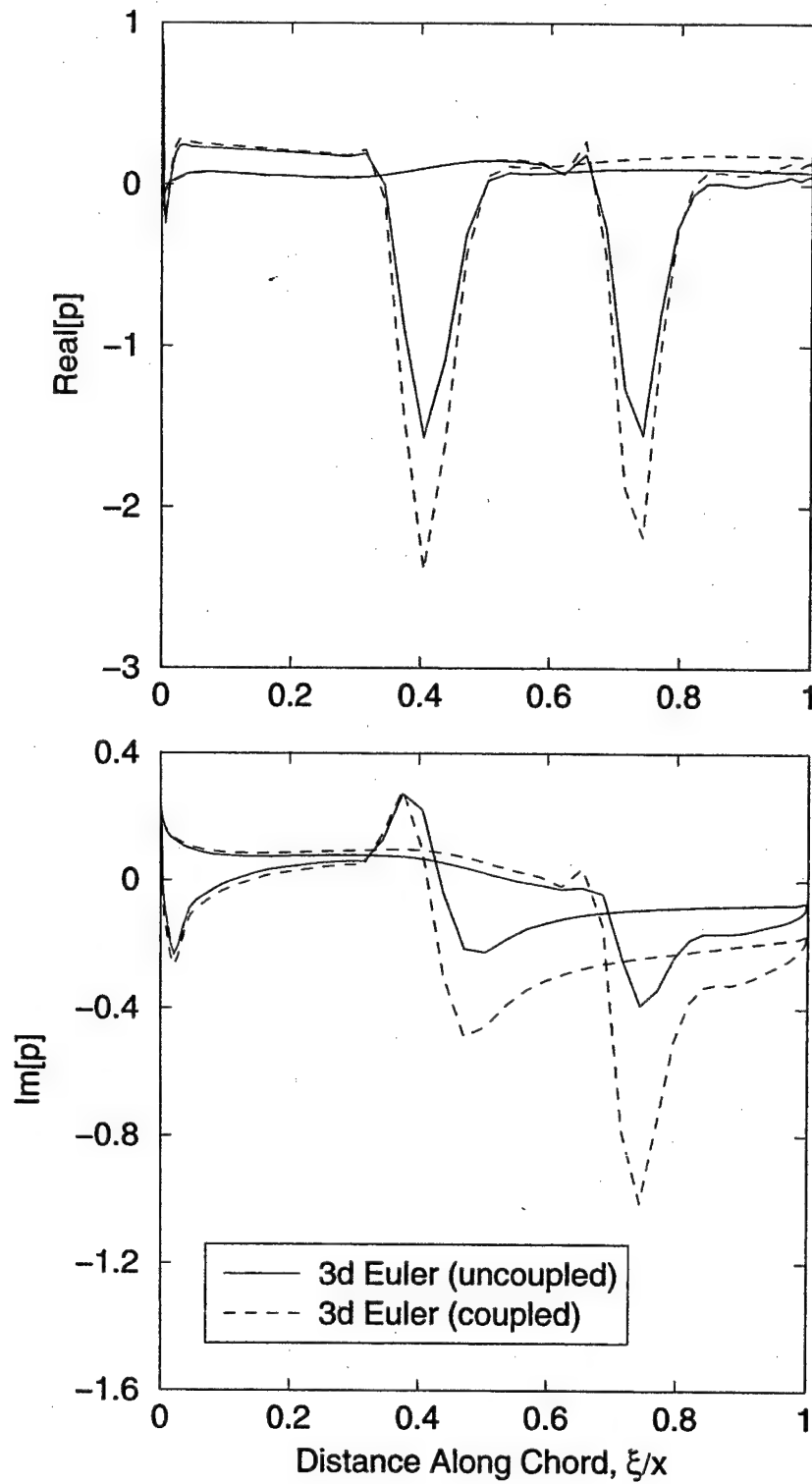
Figure 6.13: 3D Compressor. Fundamental harmonic of unsteady surface pressure on the rotor at the middle span. First bending mode of vibration of the rotor at $\omega = 0.37$ and $\sigma = -30.857140°$.

Table 6.7: 3D Compressor. Mean flow properties.

Parameter	IGV	R1	S1
Inlet mean Mach @ midspan, abs	0.505	0.572	0.776
Inlet mean Mach @ midspan, rel	1.121	1.103	0.715
Inlet mean total pressure @ midspan, abs	1.000	0.993	1.743
Inlet mean static pressure @ midspan	0.840	0.795	1.170
Outlet mean static pressure @ midspan	0.795	1.170	1.363

the first-torsional mode shape with a reduced frequency, ω, of 1.09. The aerodynamic work per cycle for the coupled and uncoupled cases is shown in Fig. 6.15. Note that in both Figs. 6.14 and 6.15, the mode convergence is observed. Like before, the model with one fundamental mode gives an estimate of aerodynamic damping very close to that obtained using multiple spinning modes.

Figures 6.16, 6.17 show typical convergence histories of the computer code for steady and unsteady calculations (one mode) for one and one-half stage of three-dimensional compressor. The lines in these figures correspond to calculations with a different number of levels of multigrid. The computations were performed on a single processor Silicon Graphics workstation with an R10000 processor. The unsteady code requires around 1000 iterations and about 60 minutes of CPU time to converge when a single mode is used to couple three blade rows. Typically, a computational time required for a solution to converge is roughly proportional to the number of grid nodes and to the number of modes one keeps in the model.
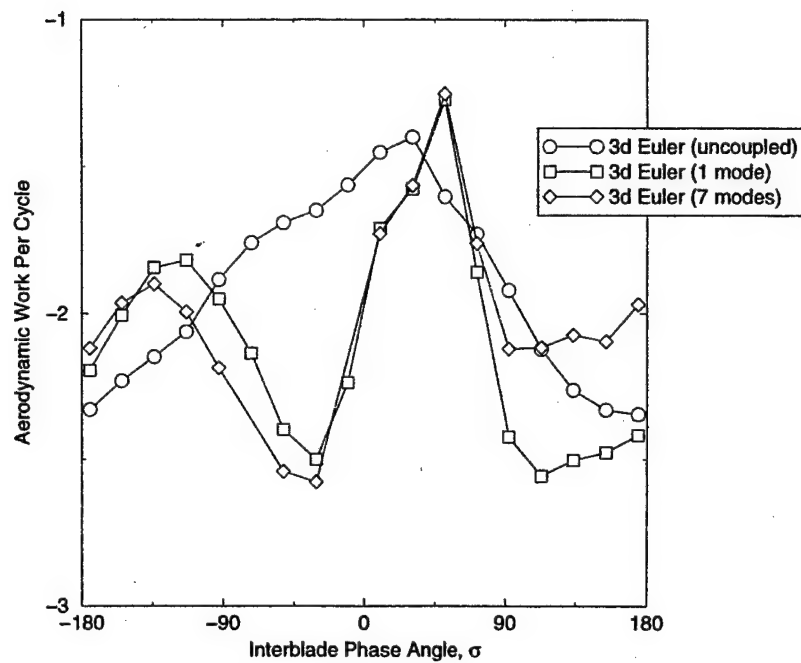
Figure 6.14: 3D Compressor. Fundamental spinning mode of aerodynamic work per cycle on the rotor. First bending mode of vibration of the rotor at $\omega_{tip} = 0.37$
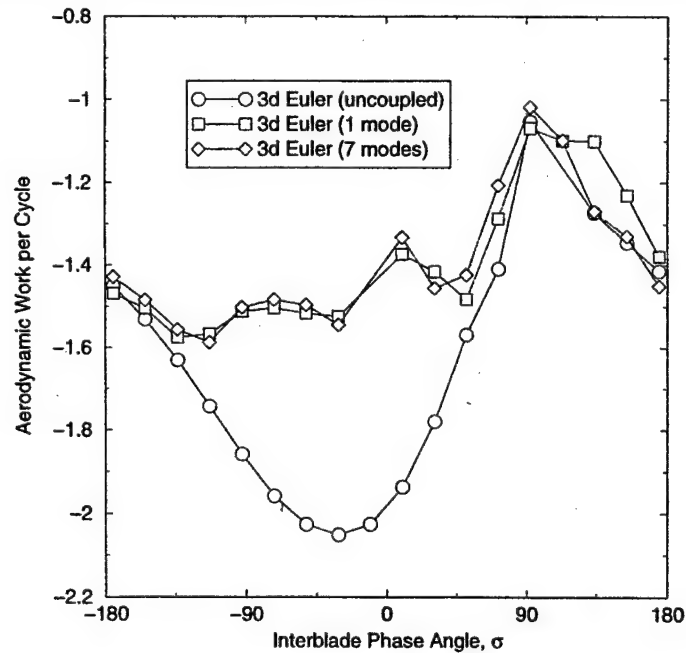

Figure 6.15: 3D Compressor. Fundamental spinning mode of aerodynamic work per cycle on the rotor. First torsional mode of vibration of the rotor at $\omega_{tip} = 1.09$
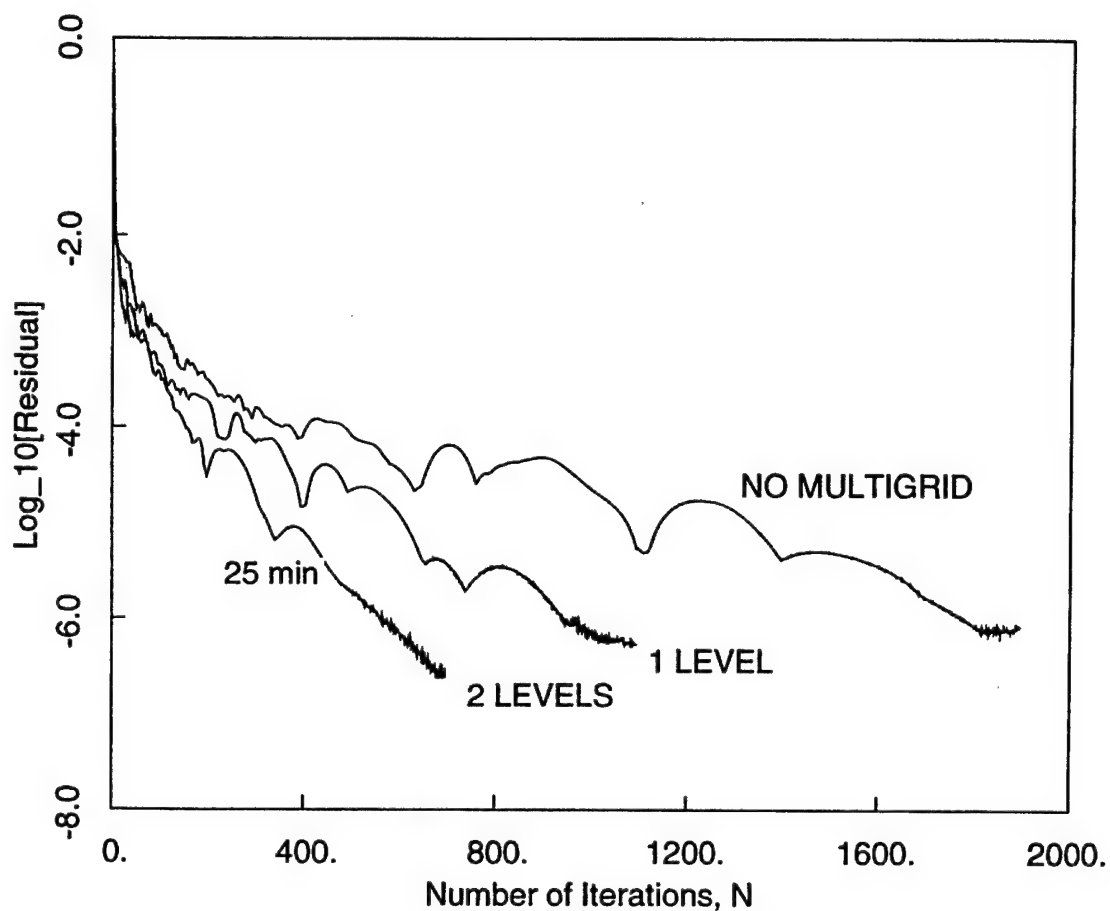
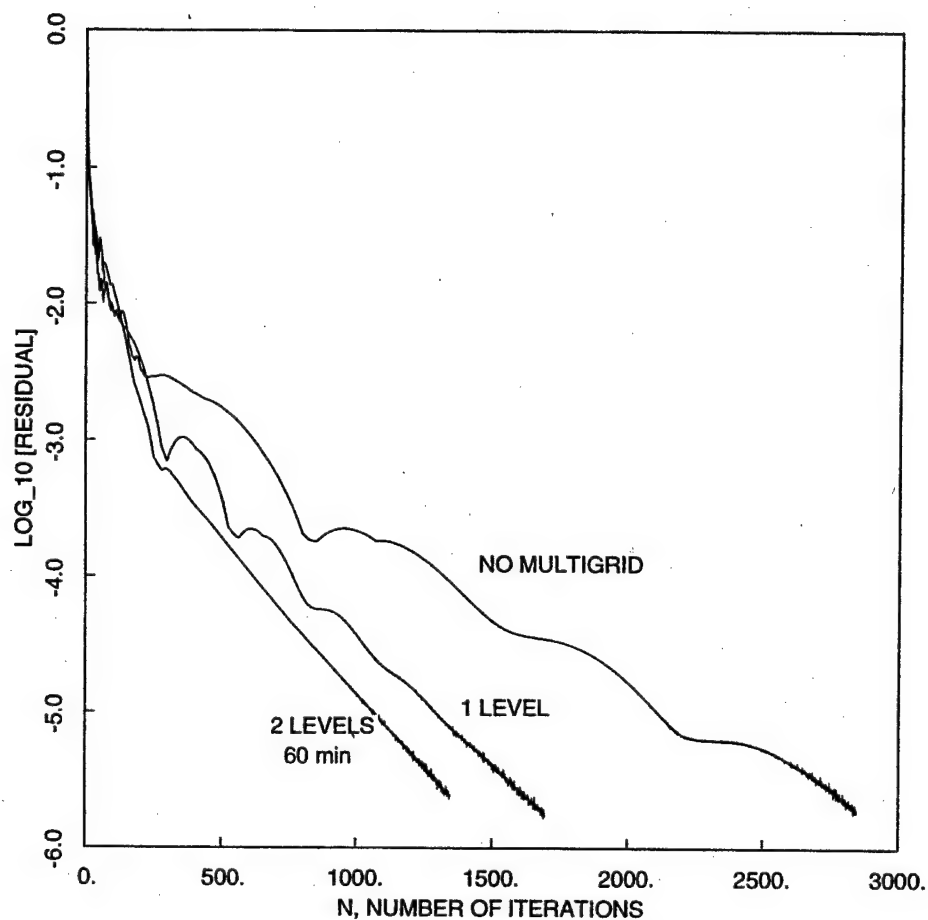Figure 6.16: 3D Compressor. Steady code convergence history. Grid: IGV(81×17×17), R1(81×17×17), S1(81×17×17). Total number of nodes 70,227.

Figure 6.17: 3D Compressor. Unsteady code convergence history for one mode coupling case. Grid: IGV(81×17×17), R1(81×17×17), S1(81×17×17). Total number of nodes 70,227.

Chapter 7

Conclusions and Suggested Future Work

7.1 Summary and Conclusions

An accurate and efficient method for solving three-dimensional unsteady flow problems in multistage turbomachinery has been presented. To obtain accurate estimates of the unsteady aerodynamic response of modern turbomachinery blades, one needs to model multistage effects, because stator and rotor blades are closely spaced in real compressors and turbines. Three-dimensional effects are also important, because modern turbomachinery contain large amounts of bow, sweep and have highly three-dimensional vibratory mode shapes producing unsteady lift distributions not well predicted by the traditional strip theory and quasi-three-dimensional approaches.

The method in this report is based on the time-linearized Euler approach; work is underway to extend the method to the three-dimensional Navier-Stokes equation. Using the current method, the flow through a turbomachinery is decomposed into a time-averaged nonlinear flow plus a small unsteady perturbation flow resulting from blade vibration or an incoming gust. The unsteady fluctuation part of the flow is assumed to be harmonic and circumferentially periodic. Because adjacent blade rows (rotors and stators) move relative to one another, an initial unsteady disturbance at a given frequency and nodal diameters is shifted and scattered into a multiplicity of frequencies and nodal diameters. In the present method, the unsteady flow is identified with a set of fluid modes called "spinning modes," each with a different frequency and an interblade phase angle. All these modes are computed for each blade row in parallel, using a time-linearized CFD techniques developed for an isolated blade row. At each iteration of the flow solver, the information is exchanged among various modes of the solution at the inter-row boundaries. This is accomplished by decomposing the solution into circumferential Fourier modes and then by matching the appropriate Fourier modes across inter-row boundary. The technique described for coupling adjacent blade rows is computationally efficient and can be easily implemented for both two- and three-dimensional flows.

In the present analysis, we solve for the flow in two steps. First, the steady Euler equations are solved to obtain the mean "steady" flow. Second, the unsteady time-

linearized Euler equations, obtained by linearizing the full Euler equations about the mean operating condition, are solved to obtain the unsteady perturbation flow. Because the pertubation flow is harmonic in time ($e^{j\omega}$), the time derivative operator $\partial/\partial t$ can be replaced by the constanst $j\omega$. Thus, for both the steady and unsteady flow problems, time does not appear explicitly in the governing equations. An artificial time dependence (pseudo-time) is introduced so that traditional time-marching can be used to solve both the nonlinear steady and linearized unsteady Euler equations. These equations do not have to be marched time-accurately, because only the "steady-state" solution is desired. Thus, multiple-grid and local time stepping are used to accelerate the convergence rate of the numerical algorithm, making the method nearly two orders of magnitude faster than conventional time-accurate simulations.

For problems where the source of unsteadiness is the vibration of rotor or stator blades, a deformable grid that conforms to the motion of the moving blades is used instead of a computational grid fixed in space. Hence, no extrapolation terms are required to apply the boundary conditions or to compute the unsteady pressure on the surface of the vibrating blade. The motion of the grid is assumed to be a small harmonic perturbation about the mean grid location. Substitution of this deforming grid assumption into the nonlinear Euler equations results in an inhomogeneous term in the time-linearized Euler equations. The use of a deformable grid increases the accuracy of the solution, particularly near the surface of the blades.

Non-reflecting boundary conditions need to be imposed at the far-fields to eliminate spurious reflections of outgoing waves. These boundary conditions enable the computational grid far-field boundaries to be placed fairly close to the blades without affecting the resultant unsteady flowfield. Quasi-three-dimensional nonreflecting boundary conditions were implemented in this report.

Results of the present method were presented for both linear and annular geometries. The accuracy of the technique was validated against existing two and three-dimensional methods. The computed results showed that the interactions between blade rows can significantly influence the unsteady surface pressure distributions on a blade and, therefore, the aerodynamic damping of a blade. This is an important result because most current models do not account for multistage effects, and thus may significantly over or under predict aerodynamic damping. The calculations in the present report show that aerodynamic damping could be predicted using just a few spinning modes. We observe a convergence of the unsteady aerodynamic response of the fundamental mode of the unsteady solution as more spinning modes are added to the model. In fact, for most flutter calculations in this work, a good estimation of aerodynamic damping can be obtained by keeping only the fundamental spinning mode. This is a very encouraging conclusion, because the computational cost is proportional to the number of spinning modes in the model.

Next, it was shown for a case of a linear cascade that the two neighboring stator blade rows adjacent to a rotor have the strongest influence on the unsteady aerodynamic response of the rotor. The next nearest blade rows are less important, but still have a modest influence. By modeling only the nearest blade rows instead of all the blade rows of a multistage machine, the computational time is significantly reduced.

For the reasons discussed above, the present unsteady analysis is computationally

very efficient compared to nonlinear time-marching multistage solvers, requiring one to two orders of magnitude less computer time. This efficiency makes the present analysis a viable design tool of turbomachinery blade rows.

7.2   Ongoing and Future Work

Although the present work has demonstrated the advantages of the multistage linearized Euler method, some issues remain to be resolved before the method can be fully exploited in aeroelastic design. For example, the effects of other engine components, e.g., fan inlets, should be incorporated into the present model.

A current Duke University graduate student and a post-doctoral researhcer are working to convert the multistage Euler analysis to a multistage Navier-Stokes analysis. A number of modifications to the previous computer code are required if the code is to model viscous flows. First, the original computational code used an H-grid structure. H-grids, while relatively simple to use in a CFD code, do not have adequate resolution to resolve boundary layers, especially near the leading and trailing edges of an airfoil. Therefore, we are implementing using an H-O-H grid structure, with an O-grid around the airfoils, with H-grid extensions upstream and downstream of the O-grids. We now have a single blade row Navier-Stokes code that uses an H-O-H grid structure. We have included the additional viscous terms in the Navier-Stokes, including Reynolds stress terms modeled using the Spalart-Allmaras turbulence model. We are currently in the process of debugging this analysis, and hope to have both steady and linearized unsteady three-dimensional viscous analysis capability within the next two months. (This work will continue under a NASA sponsored GUIde III project.)

In addition, to improve our understanding of the physics of unsteady flows, the development of an efficient technique for implementing fully three-dimensional nonreflecting far-field boundary conditions is desirable. These conditions would allow us to model cases with radial modes that do not decay, i.e., superresonant and subresonant cases with slowly decaying mode shapes. One promising approach has already been formulated by Hall et al. [25], where the radial eigenmodes are calculated numerically.

It would also be useful to make comparisons between results obtained using the present linearized method and by other nonlinear methods to determine the boundary where linear unsteady aerodynamic analyses are not viable and fully nonlinear modeling is required.

Finally, the speed of the present method can be increased. Since the integration of the equations on the grids for the different blade rows can be performed in parallel, the algorithm is easily parallelized for calculations on computers with multiple processors.

Appendix A

Cell Volume and Face Area

The volume of an hexahedral cell can be computed very efficiently using the method described by Kordulla [40]. For instance, with reference to Fig. A.1, the volume, V, of the cell is given by

$$V = \frac{1}{6}\mathbf{r}_{71} \cdot [(\mathbf{r}_{31} \times \mathbf{r}_{24}) + (\mathbf{r}_{61} \times \mathbf{r}_{52}) + (\mathbf{r}_{81} \times \mathbf{r}_{45})] \tag{A.1}$$

where $\mathbf{r}_{71} = (x_7 - x_1, y_7 - y_1, z_7 - z_1)$ and the rest vectors $\mathbf{r}_{31}, \mathbf{r}_{24}, \mathbf{r}_{61}, \mathbf{r}_{52}, \mathbf{r}_{81}, \mathbf{r}_{45}$ are defined in a similar way. The first-order perturbation series for vector $\mathbf{r}_{71}$ is given by

$$\mathbf{r}_{71} = \bar{\mathbf{r}}_{71} + \mathbf{r}'_{71} = (\xi_7 - \xi_1, \eta_7 - \eta_1, \zeta_7 - \zeta_1) + (f_7 - f_1, g_7 - g_1, h_7 - h_1)e^{j\omega\tau} \tag{A.2}$$

where (ξ, η, ζ) is the mean location of a point and (f, g, h) is the amplitude of a point vibration.

To compute the mean cell volume, $\bar{V}$, and the perturbation in the cell volume, V', substitute the first-order perturbation series for $\mathbf{r} = \mathbf{r} + \mathbf{r}'$ into Eq. (A.1). Collection of the zeroth-order terms results in the mean cell volume,

$$\bar{V} = \frac{1}{6}\bar{\mathbf{r}}_{71} \cdot [(\bar{\mathbf{r}}_{31} \times \bar{\mathbf{r}}_{24}) + (\bar{\mathbf{r}}_{61} \times \bar{\mathbf{r}}_{52}) + (\bar{\mathbf{r}}_{81} \times \bar{\mathbf{r}}_{45})] \tag{A.3}$$

Collection of the first-order terms results in the perturbation in the cell volume,

$$V' = \frac{1}{6}\bar{\mathbf{r}}_{71} \cdot [(\bar{\mathbf{r}}_{31} \times \mathbf{r}'_{24}) + (\mathbf{r}'_{31} \times \bar{\mathbf{r}}_{24}) + (\bar{\mathbf{r}}_{61} \times \mathbf{r}'_{52})$$
$$+ (\mathbf{r}'_{61} \times \bar{\mathbf{r}}_{52}) + (\bar{\mathbf{r}}_{81} \times \mathbf{r}'_{45}) + (\mathbf{r}'_{81} \times \bar{\mathbf{r}}_{45})]$$
$$+ \frac{1}{6}\mathbf{r}_{71} \cdot [(\bar{\mathbf{r}}_{31} \times \bar{\mathbf{r}}_{24}) + (\bar{\mathbf{r}}_{61} \times \bar{\mathbf{r}}_{52}) + (\bar{\mathbf{r}}_{81} \times \bar{\mathbf{r}}_{45})] \tag{A.4}$$

The area of the cell face is equal to half the cross product of the two diagonal vectors, $\mathbf{r}_{13}$ and $\mathbf{r}_{24}$ (see Fig. A.1),

$$\mathbf{A} = \frac{1}{2}[\mathbf{r}_{13} \times \mathbf{r}_{24}] \tag{A.5}$$

Since the grid is moving, each vector has a mean part and a perturbation part. Hence, to the first-order cell area is given by

$$\mathbf{A} \approx \bar{\mathbf{A}} + \mathbf{A}' = \frac{1}{2}(\bar{\mathbf{r}}_{13} \times \bar{\mathbf{r}}_{24}) + \frac{1}{2}[(\bar{\mathbf{r}}_{13} \times \mathbf{r}'_{24}) + (\mathbf{r}'_{13} \times \bar{\mathbf{r}}_{24})]. \tag{A.6}$$

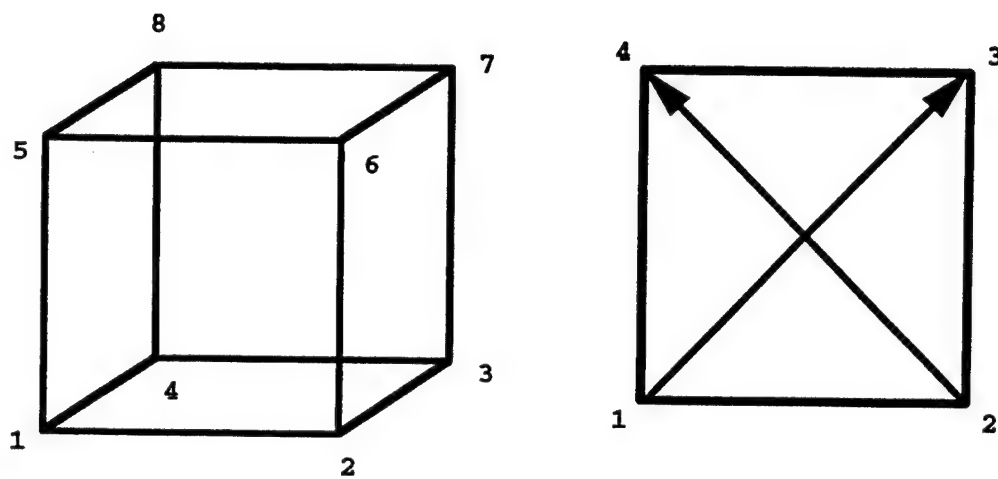Figure A.1: Typical Computational Cell and Cell Face.

Appendix B

Aerodynamic Work per Cycle

Nomenclature

A	surface area of a blade
j	$\sqrt{-1}$
$\overrightarrow{\mathbf{n}}$	outward unit normal vector
p	pressure
t	time
$\overrightarrow{\mathbf{V}}$	vector of unsteady velocity
W_{cycle}	aerodynamic work per cycle
ω	frequency of vibration
$\text{Re}()$	real part of complex expression
$\overline{()}$	mean (steady) part of quantity
$()'$	small perturbation (unsteady) part of quantity
$()_r$	real part of complex expression
$()_i$	imaginary part of complex expression

An important quantity for an aerodynamic analysis is the unsteady aerodynamic work done on the blade. If this work is positive, then the blade extracts the energy from the flow. If this energy is greater than the energy dissipated by the structural damping, then the motion is unstable. On the other hand, if the aerodynamic work per cycle is negative, then the blade motion is damped by the resulting unsteady aerodynamic load and the motion is stable.

The unsteady aerodynamic work per cycle is defined as the integral over one vibratory cycle of the product of unsteady force (pressure times area) and unsteady velocity:

$$W_{\text{cycle}} = - \int\limits_0^{2\pi/\omega} \int\limits_A \text{Re}(p)\text{Re}(\overrightarrow{\mathbf{V}}) \cdot \text{Re}(\overrightarrow{\mathbf{n}}) dA dt \qquad (B.1)$$

where p is the unsteady pressure, $\overrightarrow{\mathbf{V}}$, the unsteady velocity of the blade surface, $\overrightarrow{\mathbf{n}}$, the outward unit normal vector, A, the surface area of the blade.

The quantities of the Eq. (B.1) are decomposed into their mean (steady) part plus a small harmonically varying perturbation (unsteady) part as in the following

$$
\mathrm{Re}(p) = \bar{p} + \mathrm{Re}[(p'_r + jp'_i)e^{j\omega t}] = \bar{p} + p'_r \cos(\omega t) - p'_i \sin(\omega t) \tag{B.2}
$$

$$
\mathrm{Re}(\vec{V}) = \bar{V} + \mathrm{Re}[(V'_r + jV'_i)e^{j\omega t}] = \bar{V} + V'_r \cos(\omega t) - V'_i \sin(\omega t) \tag{B.3}
$$

$$
\mathrm{Re}(\vec{n}) = \bar{n} + \mathrm{Re}[(n'_r + jn'_i)e^{j\omega t}] = \bar{n} + n'_r \cos(\omega t) - n'_i \sin(\omega t). \tag{B.4}
$$

After substituting Eqs. (B.2)-(B.4) into Eq. (B.1) one obtains

$$
W_{\mathrm{cycle}} = - \int_0^{2\pi/\omega} \int_A [\bar{p} + p'_r \cos(\omega t) - p'_i \sin(\omega t)]
$$

$$
[\bar{V} + V'_r \cos(\omega t) - V'_i \sin(\omega t)] \cdot [\bar{n} + n'_r \cos(\omega t) - n'_i \sin(\omega t)] dA dt. \tag{B.5}
$$

In the expression (B.5) the order of integration can be reversed. Also recall that $\bar{V} \cdot \bar{n} = 0$ (see Eq. (4.5)). After the integration with respect to time one has

$$
W_{\mathrm{cycle}} = -\frac{\pi}{\omega} \int_A \left(\bar{V} \cdot [p'_r n'_r + p'_i n'_i] + \bar{n} \cdot [p'_r V'_r + p'_i V'_i] + \bar{p}[n'_r \cdot V'_r + n'_i \cdot V'_i] \right) dA. \tag{B.6}
$$

Bibliography

[1] I. H. Abbot and A. E. von Doenhoff. *Theory of Wing Sections*. Dover, 1959.

[2] J.J. Adamczyk and M.E. Goldstein. Unsteady flow in a supersonic cascade with subsonic leading edge locus. *AIAA Journal*, 16(12):1248–1254, 1978.

[3] W.F. Ames. *Numerical Methods for Partial Differential Equations*. Academic, New York, 1977.

[4] J.D. Jr. Anderson. *Fundamentals of Aerodynamics*. McGraw-Hill Book Company, 1984.

[5] D.H. Buffum. Blade row intercation effects on flutter and forced response. Paper No. AIAA-93-2084; also NASA Technical Memorandum 106438.

[6] W. S. Clark and K. C. Hall. A numerical model of stall flutter in cascades. Presented at the ASME 40th Gas Turbine and Aeroengine Congress and Exposition, Houston, TX, 1995.

[7] W.S. Clark. Prediction of unsteady flows in turbomachinery using the linearized Euler equations on deforming grids. Master's thesis, Duke University, 1992.

[8] W.S. Clark. *Investigation of Unsteady Viscous Flows In Turbomachinery Using A Linearized Navier-Stokes Analysis*. PhD thesis, Duke University, 1998.

[9] W.S. Clark. A time-linearized Navier-Stokes analysis of stall flutter. *Journal of Turbomachinery*, 122:467–476, 2000.

[10] J.F. III Dannenhoffer. *Grid Adaptation for Complex Two-Dimensional Transonic Flows*. PhD thesis, MIT, 1987.

[11] John F. Dannenhoffer and Giles Michael B. Convergence acceleration through the use of time inclining. AIAA-89-0096. Presented at the 27th Aerospace Sciences Meeting, Reno, NV, January 9-12, 1989.

[12] R.T. Davis. Numerical methods for coordinate generation based on Schwarz-Christoffel transformations. AIAA Paper 79-1463, 1979.

[13] W.N. Dawes. Toward improved throughflow capability: the use of three-dimensional viscous flow solvers in multistage environment. *Journal of Turbomachinery*, 114:8–17, 1992.

[14] J.D. Denton. The calculation of three-dimensional viscous flow in multistage turbomachines. *Journal of Turbomachinery*, 114:18–26, 1992.

[15] J.D. Denton and U.K. Singh. Time marching methods for turbomachinery flow calculations. VKI-LEC-SER-1979-7,VKI.

[16] G. A. Gerolymos. Advances in the numerical integration of the three-dimensional Euler equations in vibrating cascades. *Journal of Turbomachinery*, 115:781–790, 1993.

[17] M. B. Giles. Calculation of unsteady wake/rotor interaction. *Journal of Propulsion and Power*, 4(4):356–362.

[18] M. B. Giles. Non-reflecting boundary conditions *AIAA Journal*, 28:2050–2058, December 1990.

[19] W. Gordon and C. Hall. Construction of curvilinear coordinate systems and application to mesh generation. *International Journal Numerical Methods Eng.*, 7:461–477, 1973.

[20] E.J. Hall and R.A. Delaney. Investigation of advanced counter rotation blade configuration concepts for high speed turboprop systems. NASA CR 187126.

[21] K. C. Hall. Deforming grid variational principle for unsteady small disturbance flows in cascades. *AIAA Journal*, 31(5):891–900, 1993.

[22] K. C. Hall and W. S. Clark. Linearized Euler prediction of unsteady aerodynamic loads in cascades. *AIAA Journal*, 31(3):540–550, 1993.

[23] K. C. Hall and E. F. Crawley. Calculation of unsteady flows in turbomachinery using the linearized Euler equations. *AIAA Journal*, 27:777–787, 1989.

[24] K. C. Hall and C. B. Lorence. Calculation of three-dimensional unsteady flows in turbomachinery using the linearized harmonic Euler equations. *Journal of Turbomachinery*, 115(4):800–809, 1993.

[25] K. C. Hall, C. B. Lorence, and W. S. Clark. Nonreflecting boundary conditions for linearized unsteady aerodynamic calculations. AIAA-93-0882. Presented at the AIAA 31st Aerospace Sciences Meeting, Reno, NV, January 11-14, 1993.

[26] K.C. Hall and P.D. Silkowski. The influence of neighboring blade rows on the unsteady aerodynamic response of cascades. *Journal of Turbomachinery*, 119:85–93, 1997. ASME Paper 95-GT-35.

[27] M.G. Hall. Cell-vertex multigrid schemes for solution of the Euler equations. Royal Aircraft Establishment, Technical Report No.2029, 1985.

[28] D.B. Hanson. Unsteady coupled cascade theory applied to the rotor/stator interaction noise problem. DGRL/AIAA Paper, 92-02-084, 1992.

[29] D.B. Hanson. Mode trapping in coupled 2d cascades-acoustic and aerodynamic results. AIAA Paper No. 93-4417, 1993.

[30] L. He. Three-dimensional time-marching inviscid and viscous solutions for unsteady flows around vibrating blades. ASME paper 93-GT-92.

[31] L. He and J.D. Denton. Inviscid-viscous coupled solution for unsteady flows through vibrating blades. Parts 1,2. ASME Papers 91-GT-125,126.

[32] D. G. Holmes and H. A. Chuang. 2D linearized harmonic Euler flow analysis for flutter and forced response. H. Atassi, editor, *Unsteady Aerodynamics, Aeroacoustics, and Aeroelasticity of Turbomachines and Propellers*, pages 213–230. Springer-Verlag, New York, 1993.

[33] D.G. Holmes, B.E. Mitchell, and Lorence C.B. Three-dimensional linearized Navier-Stokes calculations for flutter and forced response. Presented at the 8th International Symposium on Unsteady Aerodynamics, Aeroacoustics, and Aeroelasticity of Turbomachines and Propellers, Stockholm, Sweden, 1997.

[34] D.G. Holmes and Connell S.D. Solution of the 2-D Navier-Stokes equations on unstructured adaptive grids. *AIAA*, Paper 89-1932-CP, 1989.

[35] D. L. Huff, T. W. Swafford, and T. S. R. Reddy. Euler flow predictions for an oscillating cascade using a high resolution wave-split scheme. ASME Paper 91-GT-198, 1991.

[36] D.C. Ives. Conformal grid generation. J.F. Thompson, editor, *Numerical Grid Generation, Proceedings of a Symposium on the Numerical Generation of Curvilinear Coordinate Systems and Their Use in the Numerical Solution of Partial Differential Equations*, pages pp. 107–130. Elsevier, New York.

[37] J.C. Strikwerda. *Finite Differences Schemes and Partial Differential Equations*. Wadsworth & Brooks/Cole, Belmont, CA, 1989.

[38] Verdonm J.M. and McCune J.E. Unsteady supersonic cascade in subsonic axial flow. *AIAA Journal*, 13(2):193–201, 1975.

[39] S. Kaji and T. Okazaki. Generation of sound by rotor-stator interaction. *J. Sound and Vibration*, 13(3):281–307.

[40] W. Kordulla and M. Vinokur. Efficient computation of volume in flow prediction. *AIAA Journal*, 21:917–918, 1983.

[41] He L. An Euler solution for unsteady flows around oscillating blades. *ASME Journal of Turbomachinery*, 112:714–722, 1990.

[42] H.W. Liepmann and A. Roshko. *Elements of Gasdynamics*. John Wiley and Sons, Inc., 1957.

[43] D. R. Lindquist and M. B. Giles. On the validity of linearized euler equations with shock capturing. *AIAA Journal*, 32:46–53, 1994.

[44] C. B. Lorence. An investigation of three-dimensional unsteady flows in turbomachinery using the linearized Euler equations. Master's thesis, Duke University, 1991.

[45] Namba M., Yamasaki N., and Nishimura S. Unsteady aerodynamic force on oscillating blades of contra-rotating annular casacdes. Presented at ISUAAAT2000.

[46] T. Nagashima and D.S. Whitehead. Linearized supersonic unsteady flow in cascades. In *Reports and Memoranda No. 3711, Aeronautical Research Coucil,London*.

[47] R.H. Ni. A multiple grid scheme for solving the Euler equations. *AIAA Journal*, 20(11):1565–1571, November 1982.

[48] R.H. Ni and R.H. Bogoian. Prediction of 3-D multi-stage turbine flow field using a multiple-grid Euler solver. *AIAA Paper 89-0203*, 1989.

[49] R.H. Ni and F. Sisto. Numerical computation of nonstationary aerodynamics of flat plate cascades in compressible flow. *Transactions of the ASME:Journal of Engineering for Power*, 98:165–170, 1976.

[50] M. M. Rai. Navier-Stokes simulations of rotor/stator interaction using patched and overlaid grids. *Journal of Propulsion and Power*, 3(5):387–396, sept.-oct. 1987.

[51] M. M. Rai. Three-dimensional Navier-Stokes simulations of turbine rotor-stator interaction: Part i – methodology. *Journal of Propulsion and Power*, 5(3):307–311, 1989.

[52] M. M. Rai. Three-dimensional Navier-Stokes simulations of turbine rotor-stator interaction: Part ii – results. *Journal of Propulsion and Power*, 5(3):312–319, 1989.

[53] A. Rizzi and L.-E. Eriksson. Transfinite mesh generation and damped euler equation algorithm for transonic flow around wing-body configuration. *Proc. AIAA 5th Computational Fluid Dynamics Conference*, pages 43–69.

[54] Andre P. Saxer. A numerical analysis of 3-d inviscid stator/rotor interactions using non-reflecting boundary conditions. Gas Turbine Laboratory Report 209, MIT, March 1992.

[55] P.D. Silkowski. *A Coupled Mode Method for Multistage Aeroelastic and Aeroacoustic Analysis of Turbomachinery*. PhD thesis, Duke University, 1996.

[56] P.D. Silkowski and K.C. Hall. A coupled mode analysis of unsteady multistage flows in turbomachinery. *Journal of Turbomachinery*, 120:410–421, 1998. ASME Paper,97-GT-186.

[57] R.E. Smith and B.L. Weigel. Analytic and approximate boundary fitted coordinate systems for fluid flow simulation. AIAA Paper 80-0192, 1980.

[58] J.L. Steger and R.L. Sorenson. Use of hyperbolic partial differential equations to generate body fitted coordinates. *Numerical Grid Generation Techniques*, pages 463–478. NASA Conference Publication 2166.

[59] J. F. Thompson, F. C. Thames, , and C. W. Mastin. Automatic numerical generation of body-fitted curvilinear coordinate system for field containing any number of arbitrary two-dimensional bodies. *Journal of Computational Physics*, pages 299–319, July 1974.

[60] L.N. Trefethen. Dispersion, dissipation and stability. D.F.Griffiths and G.A.Watson, editors, *Numerical Analysis*, 1986.

[61] D. S. Whitehead. Classical two-dimensinal methods. M.F. Platzer and F. O. Carta, editors, *AGARD* Manual on Aeroelasticity in Axial-Flow Turbomachines, Unsteady Turbomachinery Aerodynamics, volume 1 of *AGARD-AG-298*, chapter 2. 1987.

[62] D.S. Whitehead. The vibration of cascade blades treated by actuator disc methods. *Proc. I. Mech. E.*, 173:555, 1959.

[63] D.S. Whitehead. Bending flutter of unstalled cascade blades at finite deflection. Aeronautical Research Council, London, Reports and Memoranda 3386, 1962.